

SHEDDING NEW LIGHT ON OLD DATA
FINDING NEW RESULTS FOR EXOPLANET SCIENCE IN ARCHIVAL DATA
CHRISTINA HEDGES



THIS DISSERTATION IS SUBMITTED FOR THE DEGREE OF DOCTOR OF PHILOSOPHY

Institute of Astronomy, Cambridge
Murray Edwards College – University of Cambridge

April 2017

SUMMARY

In this thesis I discuss four studies carried out during my PhD at Cambridge relating to using large, public data sets to find new and exciting exoplanet science. The first of these is discussed in Chapter 2, where I present my database of molecular absorption cross sections. These were developed using public molecular transition line-lists (from the ExoMol group). I use them to find limitations in the modelling of exoplanet atmospheres due to pressure broadening. Pressure broadening, where collisions between molecules in atmospheres cause a Lorentzian broadening of molecular transitional lines, is little understood in the field. In this chapter I consider its effects on real exoplanet atmosphere observations, both with current and future instruments. I show that pressure broadening may affect future observations of exoplanets in the JWST era. Pressure broadening primarily affects cooler, small exoplanets such as Earth analogues.

In Chapter 3 I present the pipeline I have developed to reduce HST WFC₃ spectra of exoplanet hosts during transits to create transmission spectra. This code corrects several instrumental systematics, from varying dark signal in the detector to sub-pixel shifts in the target position over time. By creating a pipeline to process all targets, regardless of observing strategy, systematics are dealt with uniformly and different planets' spectra can be meaningfully compared. I show that the height of the water feature in 30 unique exoplanets' transmission spectra is strongly correlated with the most simplistic absorption model. I use this to predict a list of the best future targets for observations with HST WFC₃ to find water.

In Chapter 4 I discuss my work with the stellar spectra from WFC₃, which utilise the sub-pixel shifts in target position to oversample the spectra and increase the resolution. I have compared these exoplanet host stellar spectra with stellar models to investigate how well stellar atmosphere models describe the near IR. I find a small discrepancy in temperature when WFC₃ alone is used to assess the stellar temperature, particularly with cooler stars. I attribute this firstly to an error in the WFC₃ sensitivity curve and secondly to an inaccuracy in models of cool, small stars due to molecular absorption.

In Chapter 5 I present my work on K2 light curve data using machine learning to find young stellar objects that display unusual, transit-like behaviour. These objects are known as dipper stars due to their distinctive occultations with depths of 10-50% in flux and very fast orbital periods of a few hours to a few days. Such large occultations are difficult to explain and are currently attributed to material at the inner edge of the protoplanetary disk. This behaviour is often variable and aperiodic, suggesting that the occulting material is changing in morphology on the time scale of a single orbit. Using python's scikit-learn I have developed a code that utilises a Random Forest algorithm to classify stars in K2 Campaign Field 2 and distinguish these objects from other types of variables, such as eclipsing binaries and pulsating stars. This method has proved very successful and has allowed me to nearly quadruple the number of known dipper candidates in the Upper Scorpius and ρ Ophiuchus clusters.

ACKNOWLEDGEMENTS

Working towards this thesis has been challenging. At many times in this process astronomy has not been the path of least resistance, and it has been difficult to get to the end. It was hard work to get here, and I am pleased I have stayed and chosen to continue in this field. That certainly would not have been the case without many of my excellent mentors and colleagues. I would like to thank a few of them here, though I hope you all already know how grateful I am to you.

I would like to show my sincere appreciation for my supervisor Simon Hodgkin, who has provided support and mentoring to me throughout my PhD. You have been a truly wonderful teacher, improving not only scientific technique but my confidence and enthusiasm. You've put in so much time, care and attention into my education, I can't tell you how much I value all your input.

I have had other excellent mentors at the IoA including Vasily Belokurov, Grant Kennedy and Thomas Masseron. To everyone at the IoA I am so grateful for your help in my education, and so sorry for popping up at your doors and emailing you at all hours with so many questions.

I must thank my college, and specifically my college tutor Dr. Alex Piotrowski. The college has supported me through my PhD and has stood by me through difficulties in the department. Alex, you particularly have made it so I could keep going and attain my PhD. Thank you for lending me your time and advice to keep my head above water. Without your support, the last year of my PhD would have been insurmountable.

I would also like to thank my family for supporting and encouraging me through the PhD. It has been demanding, thank you for being so patient with me. I've wanted this for so long and it's only through your encouragement that I pursue science that I am here. I promise, I will leave school soon.

I am so thankful to have a good friend in Scott Thomas who helped keep my morale so high throughout all my time at Cambridge. From getting me interested in python to conference trips in Switzerland, having you around has been a blast. Thank you in particular for your excellent advice on writing style, I've done my best to use your advice in the pages that follow.

I am very grateful to my good friends Bjoern, Dominika and Matt. You've made living in Cambridge some of the most fun I've had, I'm sorry I never stopped whining about writing this monster thesis. I'm even more sorry that I won't be around to repay the favours of encouragement and support back to you all. To all the students at the IoA, I'm grateful we went through this together. Thank you all for putting up with my incessant whining about codes not running, data reduction and thesis writing. I promise that I will put all my new found skills to good use, and make sure all your encouragement and time was worth it.

Christina Hedges April 2017

PREFACE

This dissertation is the culmination of work from my PhD in astronomy at the University of Cambridge from October 2013 to March 2017 under the direction of my supervisor Dr. Simon Hodgkin. Chapter 2 uses work from my published paper on pressure broadening in 2016 (Hedges and Madhusudhan, 2016) and 5 uses work from my second paper (which is currently in prep) on classifying young stellar objects with machine learning. Many passages from these works are quoted verbatim and many figures are exact reproductions. This dissertation is the result of my own work and includes nothing which is the outcome of work done in collaboration except as declared in the Preface and specified in the text. It is not substantially the same as any that I have submitted, or, is being concurrently submitted for a degree or diploma or other qualification at the University of Cambridge or any other University or similar institution except as declared in the Preface and specified in the text. I further state that no substantial part of my dissertation has already been submitted, or, is being concurrently submitted for any such degree, diploma or other qualification at the University of Cambridge or any other University or similar institution except as declared in the Preface and specified in the text. This thesis (discounting the bibliography, acknowledgements, table of contents and figure captions) does not exceed 60,000 words.

CONTENTS

I	INTRODUCTION	1
1	INTRODUCTION	3
1.1	An Overview of Exoplanets	3
1.2	Methods in Exoplanet Discovery	7
1.2.1	The Transit Method	7
1.2.2	Radial Velocity	12
1.2.3	Other Methods	14
1.2.4	Planets Parameters are Derived from Stellar Parameters	15
1.2.5	Biases in Planet Surveys	15
1.2.6	The Future of Exoplanet Detection	16
1.3	Finding Planets in the Data	17
1.3.1	Confirming Exoplanet Signals	18
1.4	Exoplanet Atmospheres	18
1.4.1	Characterising Transiting Exoplanet Atmospheres	19
1.4.2	Characterising Non Transiting Exoplanet Atmospheres	23
1.4.3	Clouds and Hazes	24
1.4.4	Biosignatures	25
1.4.5	Future of Atmospheric Characterisation of Planets	25
1.5	This Thesis	26
1.5.1	A Data Driven Approach to Exoplanet Study	27
II	PRESSURE IN EXOPLANET ATMOSPHERES USING PUBLIC MOLECULAR DATA	29
2	THE EFFECTS OF PRESSURE BROADENING ON EXOPLANET ATMOSPHERES	31
2.1	Introduction	31
2.1.1	Line List Sources	32
2.2	Line Broadening	32
2.2.1	Broadening Profiles	33
2.2.2	Evaluating the Voigt Profile	34
2.2.3	Availability of Broadening Parameters	36
2.3	Generating Cross-Sections	37
2.3.1	Line Intensities and Partition Functions	37
2.3.2	Cross-Sections from Line Intensities	40
2.4	Optimal Resolution and Cut off of Broadening Profile	41
2.4.1	Effect of Profile Grid Resolution	41
2.4.2	Effect of Profile Evaluation Width	44
2.5	Effect of Pressure Broadening on Cross sections	44
2.5.1	Definition of Change Due to Broadening	44
2.5.2	Line-by-line versus Mean Broadening Parameters	46
2.5.3	Effect of Spectral Resolution	46
2.5.4	Effect of Broadening Agent	49
2.6	Effect of Pressure Broadening on Transmittance	52
2.7	Cross-Section Database	56
2.8	Discussion and Summary	56
III	EXOPLANET AND STELLAR SPECTRA FROM HST WFC3	61
3	BUILDING A UNIFORM REDUCTION OF HST WFC3 TRANSMISSION SPECTRA	63
3.0.1	A Sequence of Exoplanet Atmosphere Spectra	64
3.1	Hubble Space Telescope	64
3.1.1	Hubble Programs and Treasury Data	65
3.1.2	Wide Field Camera 3	66

3.1.3	Spatial Scan	70
3.2	Data	71
3.2.1	Data Description	71
3.2.2	How to Reduce HST Data	75
3.2.3	Calibrations from STScI	76
3.2.4	Pixel Level Corrections	77
3.3	Spectral and Spatial Drift in HST WFC	79
3.3.1	Stretch as a Function of Row	83
3.3.2	Oversampling And Removing The Stellar Spectrum	84
3.3.3	Shifts for All Exoplanet Targets	85
3.3.4	Effects of Shift Corrections	87
3.3.5	Variable Scan Rate	87
3.4	Flux Calibration and Wavelength Solution	88
3.4.1	Flux Calibration	88
3.4.2	Wavelength Calibration	89
3.5	Corrections Applied to Light Curves	89
3.5.1	White Light Curves	90
3.5.2	Residual Shift Trends	90
3.5.3	Residual Background Trends	93
3.5.4	Divide Out Of Transit (OOT) Method	93
3.6	Transmission Spectra	94
3.7	Data Validation	96
3.7.1	Internal Consistency	97
3.7.2	Consistency with Literature Results	97
3.7.3	Out-of-Transit Testing	105
3.8	Results	106
3.8.1	A spectral sequence of Exoplanet Transmission Spectra	109
3.8.2	Comparative Exoplanetology	112
3.9	Conclusions	118
3.10	Acknowledgements	122
4	RETRIEVING STELLAR TEMPERATURES IN THE IR	123
4.1	Introduction	123
4.1.1	Importance of Accurate Stellar Parameters	124
4.2	Methods of Stellar Parameter Retrieval	124
4.2.1	Comparison of methods	125
4.3	Data: Stellar Spectra	126
4.3.1	Literature Temperature Values	131
4.3.2	Checking WFC ₃ Calibration with 2MASS	131
4.4	Spectral Models	132
4.4.1	Known Problem with Stellar Models and Cool Stars	133
4.5	Temperature Estimates using WFC ₃	133
4.5.1	Inaccuracy in WFC ₃ Data	134
4.5.2	Testing WFC ₃ Calibration with NICMOS	136
4.5.3	Dividing Through by Common Slope	139
4.6	Discussion	140
IV	FINDING YOUNG DIPPER STARS IN K2 DATA WITH MACHINE LEARNING	143
5	FINDING DUSTY DIPPER STARS WITH MACHINE LEARNING	145
5.1	Introduction	145
5.2	K2 Observations	148
5.3	Upper Scorpius and ρ Ophiuchus	150
5.4	Building a Machine Learning Algorithm	151
5.4.1	Training Sample	152
5.4.2	ML Performance	153
5.4.3	Features	154

5.5	Dipper Candidates	161
5.5.1	Top 10 Features	161
5.5.2	F1 Score	162
5.6	Measuring Dip Parameters	162
5.6.1	Periodicity	165
5.6.2	Dip Parameters	167
5.7	Dipper Characteristics	167
5.7.1	Comparison with Ansdell 2015	168
5.7.2	Comparing Dipper Samples By Cluster	169
5.7.3	Orbital Distance to Inner Disk Edge	177
5.8	Burster Stars	182
5.9	Summary	182
V	CONCLUSIONS	187
6	CONCLUSIONS	189
6.1	Atmospheric Pressure Broadening	189
6.2	Exoplanet IR Spectra	190
6.2.1	Stellar IR Spectra	191
6.3	Dipper Stars	192
6.4	Future Prospects	194
VI	APPENDIX	195
6.5	Appendix A	197
6.6	Appendix B	199
	BIBLIOGRAPHY	216

Part I

INTRODUCTION

INTRODUCTION

The field of exoplanet study is unusually young in astronomy. In 20 short years we've moved from scepticism of the existence of exoplanets, to knowledge of a select few, to enormous surveys and hunts for earth analogues. Now, we are confident there are planets around most main sequence stars¹. This field of study is not only new, but fast growing. With new dedicated instruments coming online in the next few years we will be able to detect thousands more exoplanets around bright stars. This will enable further exoplanet characterisation, including measuring the radii and masses of planets accurately and taking spectra of their atmospheres. As the field continues to develop and instruments improve, we will be able to push towards detecting weather systems, surface structure and eventually biosignatures on distant planets.

¹ see; *Cassan et al. (2012)*; *Fressin et al. (2013)*

Studying exoplanets allows us to better understand how planets form, what they are made from and what conditions are like on their surfaces. The variety of exoplanets can help us understand the formation methods for planets, the effects of migration and the occurrence rates of planets of different sizes. Studying exoplanets can help us understand our own solar system (though there are currently no known solar system analogues). Comparing the architecture of the solar system to those around other stars allows us to investigate whether we are in a unique or unusual position. We can therefore investigate whether planets like our own are common, or whether the Earth is a rarity amongst the planet population.

Over the past few years a new field of study in exoplanet astronomy has begun: the study of exoplanet atmospheres (see *Snellen et al. (2010)*; *Deming et al. (2013a)*). Measurements of atmospheres are difficult, due to small signals and bright host stars (see Section 1.4) but allow unprecedented measurements of exoplanets. Obtaining atmospheric measurements allows us to quantify the abundance of molecular species, observe clouds on planets outside our solar system and model the different surface conditions of exoplanets. Atmospheric study is a tool to enable us to better characterise worlds beyond our own.

In this thesis I will investigate publicly available, archival data to study several aspects of exoplanet science. I take a data driven approach to this work, bringing together data from large surveys and libraries. This includes databases of molecules used for atmospheric chemistry, archival HST stellar spectra and K2 survey data. In this chapter I will introduce some of the basics of exoplanet study, including detection methods and atmospheric characterisation. I will also introduce some of the necessary physics and geometry for the following chapters. A summary of the contents of this thesis is given in Section 1.5.

1.1 AN OVERVIEW OF EXOPLANETS

The first exoplanets were discovered more than 20 years ago, with *Wolszczan and Frail (1992)* finding a planet around a pulsar star. The first detection of a planet around a main sequence star quickly followed in *Mayor and Queloz (1995)*. Since then the number of known exoplanets has soared. Figure 1.4 shows the exponential increase in planet discovery over the last 20 years. This surge in planets has allowed us to learn more about how planets form and migrate.

PLANET FORMATION AND MIGRATION Planets are formed out of protoplanetary disks around stars. As discussed in the reviews by *Larson (2003)* and *Li et al. (2014)*, stars form from the collapse of large molecular clouds. Properties such as the magnetic field strength in the gas and the core rotation rate effect the formation of the

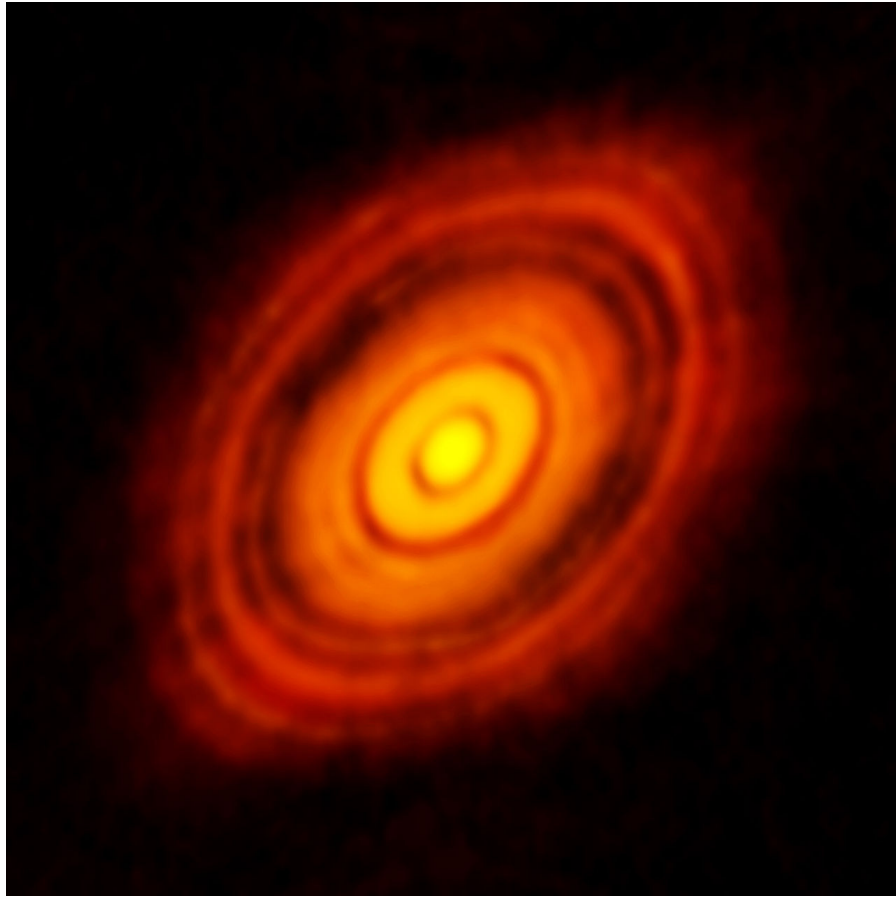


Figure 1.1: ALMA 1mm observation of HL Tau from ALMA Partnership et al. (2015), a young star with a protoplanetary disk at 140 pc. The dark rings in the disk have been used to inform models of disk evolution and planet formation, for examples see Meru et al. (2014); Flock et al. (2015) and the references therein.

² Li et al. (2014)

³ See; Alexander, Clarke, and Pringle (2006); Carpenter et al. (2006); Kennedy and Kenyon (2009); Kennedy et al. (2017)

⁴ See; Meru et al. (2014); Flock et al. (2015)

final system, from the number of stars to the properties of the circumstellar disk.² It is from this disk that planets are eventually able to form. The link between star formation and disks and the processes by which disks evolve are complex.³ This young stage of stellar evolution is difficult to observe as it is obscured when the star is young and is a very short lived period of stellar life.

Recently, it has been possible to begin to image some of the closest and brightest protoplanetary disks using the ALMA at 1.25mm. ALMA Partnership et al. (2015) observed structure in the disk of T Tauri star HL Tau, showing dark rings that have been attributed to a variety of processes including planet formation⁴. Stephens et al. (2014) discuss the properties of the magnetic field in the disk of HL Tau, suggesting that the accretion mechanisms of the disk in young stars is still poorly understood.

While it is possible to observe the region where photo evaporation drives disk evolution with these methods, it is much harder to observe the inner region of the disk, where accretion occurs onto the star. Interferometric methods can probe into the inner disk region, but observations are limited for the smallest scales. (For examples across a range of disk sizes see Millan-Gabet et al. (2006).) However, structures such as disk warps and accretions streams are present at the inner edge of disks, which alter the light curves of these objects. This presents an alternative method to observe this inner region and model the structure of disks. For example, objects known as 'dippers' show rapid and often aperiodic variation due to dust obscuring the host star at the inner edge of the disk. Similarly 'bursters' undergo accretion events last-

ing days due to accretion of inner disk material (see Chapter 5 for more). Kennedy et al. (2017) discusses some of the disk behaviours that cause light curves of stars to show variability including small scale dippers and large scale Herbig Ae/Be stars.

A schematic of the evolution of a protoplanetary disk is given in Figure 1.2. As discussed in Williams and Cieza (2011), these disks are made up mostly of gas with a small fraction of solids ('dust') left over from star formation. The solids settle into the dust midplane over a few Myrs. The gas is accreted onto the star or evaporated by solar winds and radiation pressure, leaving behind planetesimals in the plane of the disk. These are the small building blocks that accrete to form planets. The protoplanetary disk stage lasts for 10-100 Myrs before dissipating.

The laws that govern the growth of grains into planetesimals are complex. Grains of different sizes and velocities impact each other in a variety of ways, either sticking, bouncing or breaking apart (see Birnstiel, Fang, and Johansen (2016) for a review of these processes). Once these small dust grains have grown to large enough sizes they can begin to hold onto atmospheres. Gas giants can form when cores reach $\sim 10M_{\text{earth}}$, after which they accrete an atmosphere of gas from the primordial gas disk ("core accretion")⁵. Smaller planets that do not reach this mass are unable to hold onto the large atmosphere of gas that causes the run-away growth in gas giants.

⁵ Armitage (2007)

Once planets have formed they are initially interacting with the remaining gas disk. The force the gas exerts on the planets causes them to migrate, as the planets exchange angular momentum with the disk (see Armitage (2007) and the references therein). Once this disk evaporates the planets are then able to interact with each other. The architecture of the system may be unstable on long time scales, causing planet-planet scattering to occur. This can lead to four scenarios: 1) The separation between two planets increases until the system is stable 2) A planet is ejected 3) The planets collide 4) One or more planets impact the star or become close enough for tidal interactions to significantly alter its orbit. Such events can leave hallmarks on the system architecture, such as eccentric orbits, high inclination, planets that rotate out of the orbital plane or very close in planets. These mechanisms have been used to explain some of the more unusual planets that have been found⁶.

⁶ e.g.; Nagasawa, Ida, and Bessho (2008)

EXOPLANETS GREAT AND SMALL Different formation processes and migration histories can cause different planets types to form; from small terrestrial planets, to ice giants, to gas giants. The prevalence of each size of planet can be used to inform models of planetary formation. See the review by Mordasini et al. (2010) which discusses the different theories of planet formation for terrestrial and gas planets. Exoplanet surveys have shown us that the planets found in the solar system are not the only types of exoplanets that can form. The Kepler mission in particular has highlighted the spread of different planet types, as shown in Figure 1.3. There are many planets that have been found in between the mass range of Earth and Neptune. These are termed super-Earths and we have no examples in the solar system, despite them being one of the most common planet types⁷.

⁷ Chen and Kipping (2017)

There is a second class of planet that is particularly unusual and dissimilar to the solar system: hot Jupiters. They orbit close to their host star, causing the planet to become hot, with temperatures $\gtrsim 1000\text{K}$. Their orbits usually last $\lesssim 10$ days and are often circularised by the tidal interactions with the host star.⁸ This planet type is extremely useful for follow up observations of atmospheres (see Section 1.4 and the review of atmosphere observations of hot exoplanets by Heng and Showman (2015)). However, they are one of the rarest types of planet, with $\lesssim 2\%$ of FGK stars hosting a hot Jupiter. Wright et al. (2012) Hot Jupiters have only been found in large numbers largely due to observational biases and selection effects (see Section 1.2.5).

⁸ Batygin, Bodenheimer, and Laughlin (2016)

Despite having found many exoplanets, there are currently no solar system analogues, (planets that have the same mass, radius and orbital period as any of the solar system planets.) This is almost certainly due to observational bias (see Kipping and Sandford (2016) for a review of observation bias for the transit method and the

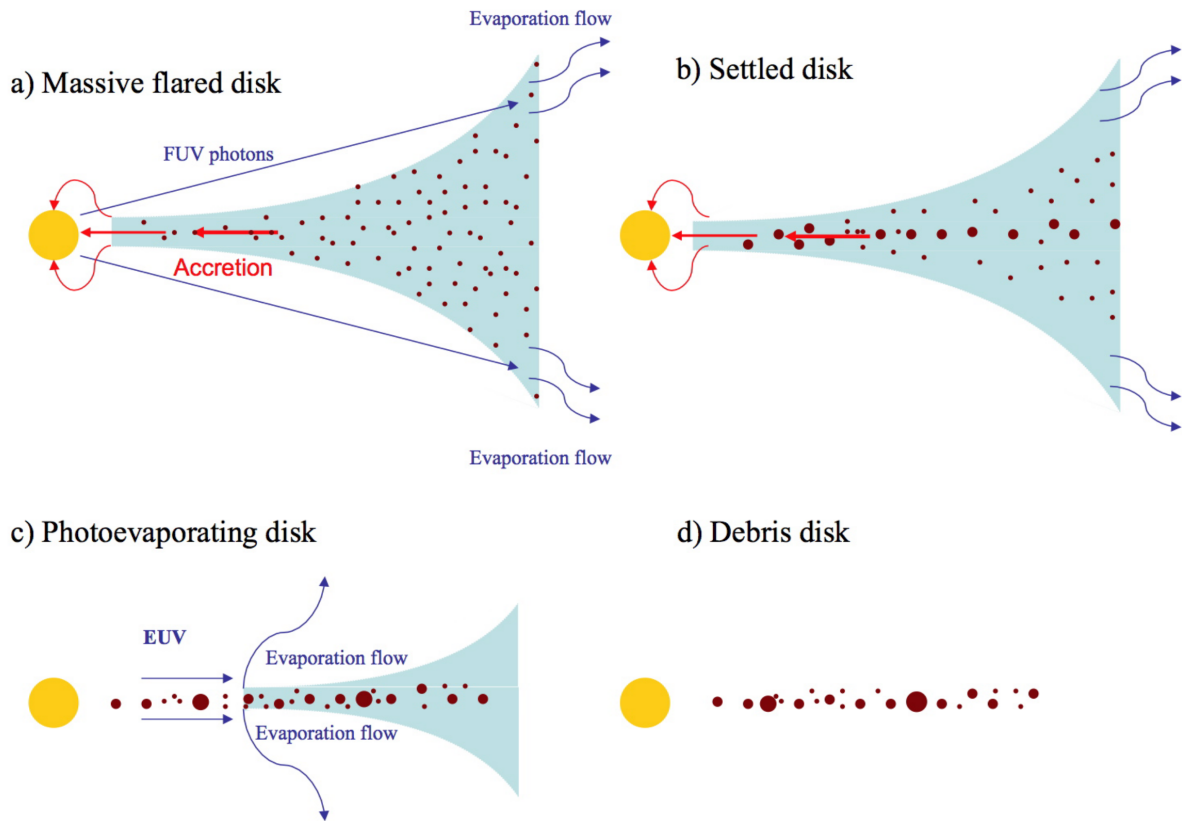


Figure 1.2: Schematic of protoplanetary disk evolution taken from Williams and Cieza (2011). The initial disk of gas and dust is both accreting onto the star and being photo-evaporated by the UV emission of the star. Dust grains settle into the core of the disk and grow in size. As the material at the inner edge of the disk is accreted onto the star, photo-evaporation becomes more dominant and a gap forms. Finally the gas disk is blown off by photo-evaporation and the debris remains at around 10 Myrs. These planetesimals go on to form planets over the next 100 Myrs.

Sizes of Kepler Planet Candidates

As of July 23, 2015

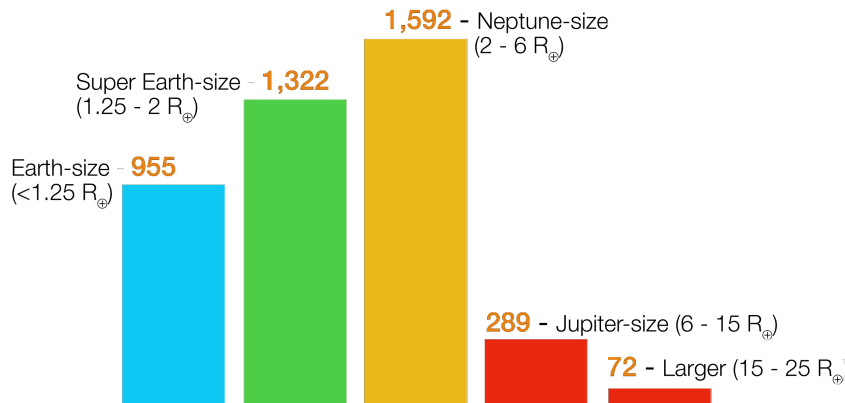


Figure 1.3: Number of each planet size found by the Kepler mission as of July 2015. This chart would suggest that super-Earths are a common type of planet, despite there being no examples of them in the solar system. This also suggests Neptune-sized planets are common. However, this graph is subject to observational biases, as discussed in Section 1.2.5.

discussion in Section 1.2.5). As we increase our capabilities for exoplanet detection we will likely find evidence of solar system analogues around sun-like stars.

1.2 METHODS IN EXOPLANET DISCOVERY

In this thesis I am concerned primarily with planets discovered by the transit method, which is discussed below. I also rely on the results of radial velocity surveys, which provide the exoplanet mass estimates needed to calculate atmospheric properties. I will introduce the radial velocity method in brief in Section 1.2.2. There are many other methods used for finding exoplanet (see Section 1.2.3). However, the transit method and the radial velocity method are most easily applied in large surveys and to date have been the most successful planet hunting methods. This is shown in Figure 1.4. The two large spikes in that figure in 2014 and 2016 are due to two data releases from the Kepler mission of hundreds of planets.

1.2.1 The Transit Method

A transit is an occultation event, where an exoplanet moves between a star and the observer. This causes a small drop in the observed flux from the star. If the star is observed during a transit, the relative change in flux can be used to infer the radius of the planet. The frequency and duration of the transits is used to infer the orbital distance. An example of the geometry of a transit light curve is given in Figure 1.5. In this section I will discuss some of the planet parameters that can be found using the transit method.

TRANSIT PROBABILITY For a transit to be visible the planet must pass directly between the star and the observer. As such, there are some orbital inclinations where

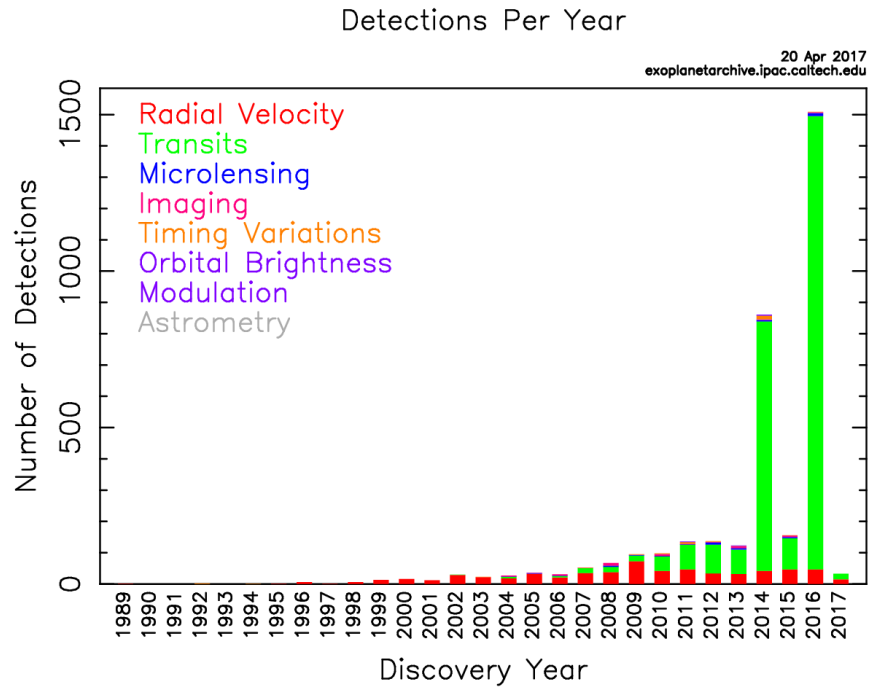


Figure 1.4: Distribution of exoplanet discoveries by method. (Accessed on April 20th 2017 from NASA Exoplanet Archive.) The two peaks in 2014 and 2016 correspond to large releases of transit data from the Kepler mission. The transit method and the radial velocity method produce the highest number of planet detections.

Transit method

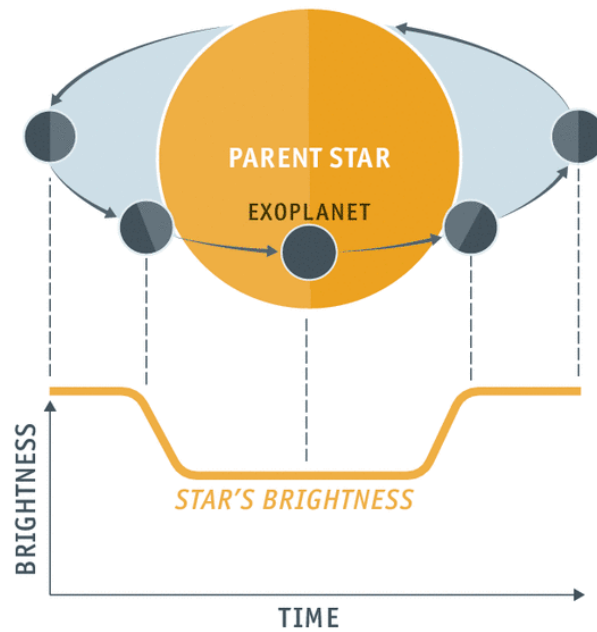


Figure 1.5: Geometry of a transit light curve. If the inclination of the planets orbital plane is 90° the planet will cross the surface of the star. The planet causes a drop in light proportional to its area, as shown in Equation 9. Graphic taken from the Economist.com's graphics library.

a transit will never occur. The probability that a planet will transit (assuming systems are uniformly distributed in inclination) is given as

$$p \approx \frac{R_* + R_p}{a} \quad (1)$$

where R_* is the star radius, R_p is the planet radius and a is the orbital separation. (See Read, Wyatt, and Triaud (2017) and the references therein for a derivation of the transit probability for both single and multiple planets.) The probability is greatly increased by having planets that orbit closer to the star. Due to it's distance, the Earth would have a transit probability of less than 1% if observed in a random orientation.

ORBITAL DISTANCE The transit method requires that we observe for a long period of time, to maximise the chances that a transit will occur. From Kepler's third law we know the period of a planet to be related to its orbital distance and stellar host mass by the following equation

$$P^2 = \frac{4\pi a^3}{G(M_* + M_p)} \approx \frac{4\pi a^3}{GM_*} \quad (2)$$

where P is the orbital period, M_* is the mass of the star and M_p is the mass of the planet. As the orbital distance increases so does the orbital period. To calculate the orbital distance of the planet based on the period we simply rearrange Equation 7 to find a .

For the Earth orbital the period is 365 days, and so to observe an Earth like planet transiting we would require at least 365 days of continuous observation. However, in order to confirm that the event is periodic we would require at least 3-4 transits to be observed. In order to detect a planet at 1 AU from a sun-like star we would require at least four years of continuous observation. Because of this, planets with short orbital periods are preferred by the transit method.

EQUILIBRIUM TEMPERATURE Using the period of the transits we can also find the orbital distance by rearranging Equation 7 and using estimates of the stellar mass. Based on this distance we can calculate the equilibrium temperature of the planet (which is the temperature it would be if it were only heated by the star). From the Stefan-Boltzmann law we know that the luminosity of a black-body is given by

$$L = 4\pi R^2 \sigma T^4 \quad (3)$$

where R is the radius of the object and T is its temperature. The luminosity received by a planet is

$$L_p = \frac{\pi R_p^2}{4\pi a^2} 4\pi R_*^2 \sigma T_*^4 (1 - A) \quad (4)$$

where T_* is the temperature of the star, σ is the Stephan-Boltzmann constant and A is the fraction of luminosity that is reflected away from the planet, referred to as the albedo. We can substitute in the Stephan-Boltzmann to find the temperature of the planet

$$R_p^2 \sigma 4\pi T_{eq}^4 = \frac{\pi R_p^2}{4\pi a^2} 4\pi R_*^2 \sigma T_*^4 (1 - A) \quad (5)$$

$$T_{eq}^4 = \frac{L_*}{16\pi \sigma a^2} (1 - A) \quad (6)$$

Based on Equation 6 it is clear that the temperature for close in planets is high. Large, close in planets such as HD209458b and HD189733b can reach temperatures of 1500K or more.

This equilibrium temperature can be used to characterise the planet. For example, the Habitable Zone for a system is defined as the region where a planet could host liquid water, based on its T_{eq} . Using the period of the planet transits and the stellar parameters we can calculate whether the planet would be in the Habitable Zone. To observe in the Habitable Zone but still benefit from short orbital periods and

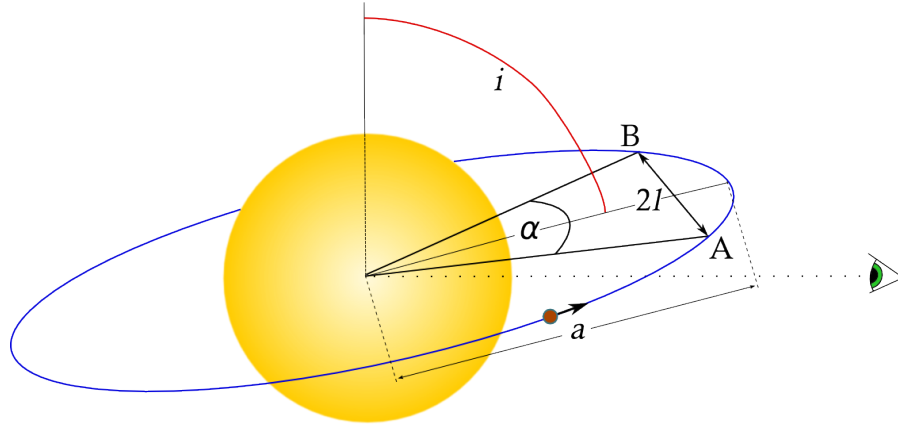


Figure 1.6: Geometry of a transit event. Here we are interested in the time it would take for a planet to travel from A to B. The angle i is the orbital inclination and the angle α is the angle that the planet sweeps out during a transit. l is the projected distance that the planet crosses during the transit. Figure taken from paulanthonywilson.com.

frequent transits, the luminosity of the star should be reduced. This is done by observing cooler, smaller stars. For example the TRAPPIST-1 system has recently been detected, with 7 exoplanets in a single system around an ultra-cool dwarf, three of which are in the habitable zone⁹.

⁹ Gillon et al. (2017)

TRANSIT DEPTH The transit method provides us with a measure the cross sectional area of the planet with respect to the star. The change in the luminosity of the star is

$$\delta = \frac{L_{*,\text{no transit}} - L_{*,\text{transit}}}{L_{*,\text{no transit}}} \quad (7)$$

where L_* is the luminosity of the star. We can substitute in the Stephan-Boltzmann law for the luminosity of the star, assuming a black body, to find

$$\delta = \frac{\pi R_*^2 \sigma T_*^4 - (\pi R_*^2 - \pi R_p^2) \sigma T_*^4}{\pi R_*^2 \sigma T_*^4} \quad (8)$$

This simplifies to

$$\delta = \frac{R_p^2}{R_*^2} \quad (9)$$

which is the fractional change in brightness during a transit. We can measure the radius of the star either from interferometry or model fitting to stellar spectra or photometry (see Chapter 4) or using methods such as asteroseismology and stellar evolution models. Using the stellar radius and the transit depth we can then calculate the radius of the planet.

The transit depth for exoplanets tends to be small, particularly for terrestrial planets. For Earth the transit depth is 1×10^{-4} , where as for Jupiter the transit depth is 1×10^{-2} .

TRANSIT DURATION The duration of the transit can be used to establish the distance to the transiting body. The transit duration is simply given as

$$T_{\text{dur}} = \frac{d}{v} \quad (10)$$

where d is the distance that the planet travelled in front of the star at velocity v . For the simplest case of a circular orbit

$$v = \frac{2\pi a}{P} \quad (11)$$

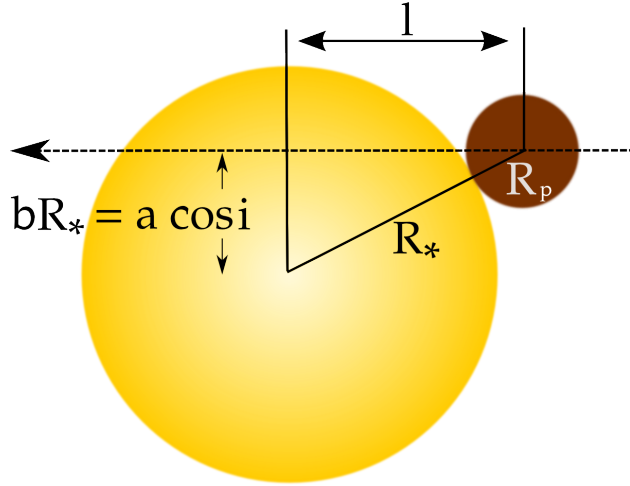


Figure 1.7: Geometry of the path a planet will take during a transit. The transit duration will be the time it takes to cross a distance $2l$. Note varying the orbital inclination i alters the distance, and so the crossing time. The maximum crossing time is at $i = 90^\circ$. Figure taken from paulanthonywilson.com.

where a is again the orbital distance and P is the orbital period. The distance d that the planet travels is shown in Figure 1.6 (the arc through points A to B)

$$d = \frac{\alpha}{2\pi} 2\pi a = \alpha a \quad (12)$$

where α is the angle the planet travels through while transiting. The transit time is therefore

$$T_{\text{dur}} = \frac{P}{2\pi a} \alpha a = \frac{P\alpha}{2\pi} \quad (13)$$

To calculate the angle α we must first calculate the distance l , the projected distance across the surface of the star. This is shown in Figure 1.7.

The distance across the stellar surface the planet will cross depends on the orbital inclination. If $i=90^\circ$ the planet will cross a length of $2\pi R_*$. However if the inclination is slightly higher or lower it will cross a shorter length, as shown in Figure 1.6. The distance is based on the impact parameter b which is the projected distance between the planet centre and the stellar centre exactly at the transit mid-point. The impact parameter is given by

$$b = \frac{a \cos(i)}{R_*} \quad (14)$$

The projected distance that the planet crosses over the star l is shown in Figure 1.7. This is simply

$$l = \sqrt{(R_* + R_p)^2 - (bR_*)^2} \quad (15)$$

From Figure 1.6, the angle α is now

$$\alpha = 2 \sin^{-1} \left(\frac{l}{a} \right) \quad (16)$$

$$\alpha = 2 \sin^{-1} \left(\frac{\sqrt{(R_* + R_p)^2 - (bR_*)^2}}{a} \right) \quad (17)$$

Substituting this value of α into Equation 13 gives us the final transit duration in terms of the planet and stellar radii and the orbital distance

$$T_{\text{dur}} = \frac{P}{\pi} \sin^{-1} \left(\frac{\sqrt{(R_* + R_p)^2 - (bR_*)^2}}{a} \right) \quad (18)$$

Following the prescriptions from Kipping (2010) and the references therein the reader can find more detailed derivations of the transit duration for eccentric orbits and derivations of the shape of the transit curve. The transit duration for the earth is 12 hours, where as for Jupiter the transit would last 32 hours due to its longer orbital period. The transit shape is also useful for inference. The ingress and egress shapes (the slopes at the entry and exit points of the transit) can also be used to infer properties about the transiting body such as optical thickness (for example see Kennedy et al. (2017)).

LIMB DARKENING The base of the transit in Figure 1.5 is curved slightly inwards towards the transit centre. This is due to the process of ‘limb darkening’. The atmospheres of stars are optically thin, and stars’ temperatures increase as you move closer to their cores. When observing the centre of a star we reach an optical depth of one (where the star becomes opaque) at a layer deep in the star. This deep layer is hotter than outer layers, making the star appear ‘bluer’ at the centre, (with a black body curve peaking at shorter wavelengths.) At the limbs, due to the curvature of the star, the same path length does not reach as deep a layer. This causes us to see a cooler part of the star. This cooler part seen at the limbs of the star is both dimmer and redder. The severity effect depends on the temperature of the host star and the wavelength that the observation was made in. Transit models (such as from Mandel and Agol (2002)) include quadratic parameters for limb darkening to account for this effect, which causes curvature at the base of the transit.

1.2.1.1 *Strengths and Weaknesses of Transit Method*

The transit depth measurement is simple in theory, but often more complicated in practice. These signals are small, particularly where the planet itself is small. This requires high precision to confirm above the shot noise. The ratio of the radius of the Earth to the Sun is 0.01. Based on Equation 9, if we were to observe the earth around a sunlike star, the change in transit depth would be 1×10^{-4} , or 100 ppm. To observe 100 ppm with a signal-to-noise ratio of 5 we would require precision of 20 ppm. Kepler’s precision never reached this level, with a precision of 39ppm for the brightest targets. However, beyond simple shot noise there are other noise sources in the light curve, such as star spots. These cool patches on the star surface are much lower temperature than their surroundings, causing them to be darker. As the star rotates, these spots modulate the brightness of the star, causing a noise that can easily wash out variability from small planets or alter transit shapes.

The transit probability limits this method; the chances of observing a transit are small. The need for multiple transits also limits the method. These problems are overcome by observing as many stars as possible, for as long as possible. This increases the chance that a planet will transit while we are observing. Survey missions such as Kepler¹⁰ and CoRoT¹¹ from space and WASP¹², MEarth¹³ and HATnet¹⁴ from the ground have used this approach. The Kepler survey alone observed 145,000 main sequence stars at visual magnitudes between 8 and 17 over 3 years. This has lead to 4,496 planet candidates being discovered by the mission (see Figure 1.4. These surveys all observe over many months and years to maximise the probability of a planet transiting.

The transit method has proved very beneficial in the hunt for exoplanets. However, it is limited in the information that it can provide on it’s own. For example, it is unable to measure the mass of exoplanets. For that we must turn to a new method: radial velocity.

1.2.2 *Radial Velocity*

The radial velocity (RV) method relies on the orbit of the planet causing the star to move. The star and planet orbit a common centre of mass, which causes the star’s spectrum to be doppler shifted. If the spectra of the star are taken at different points

¹⁰ Batalha et al. (2013)

¹¹ Baglin and Vauclair (2000)

¹² Cameron et al. (2007)

¹³ Berta, Irwin, and Charbonneau (2013)

¹⁴ Bakos et al. (2007)

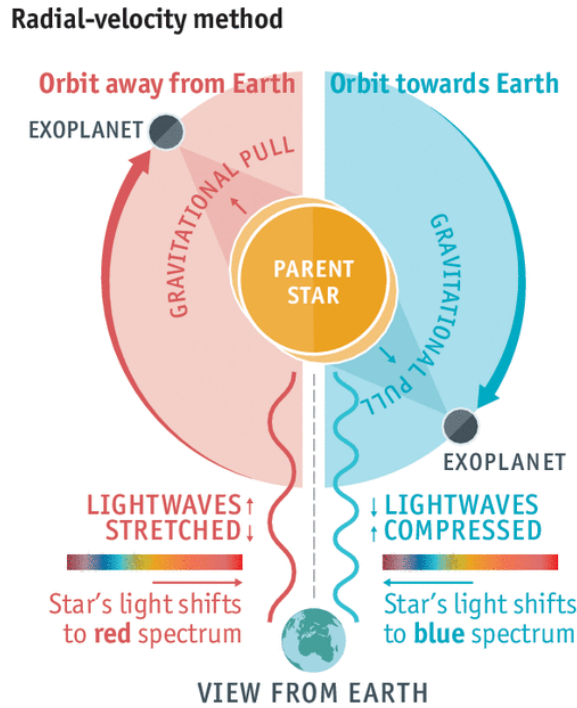


Figure 1.8: Geometry of a radial velocity signal. Here the planet and star orbit a common centre of mass which causes the star to move with respect to the observer. The change in the velocity of the star over time can then be used to infer the presence of a planet and find its mass. This graphic has been taken from the Economist.com's graphics library.

during the planet orbit, the phase folded velocity of the star forms a sinusoid in the circular case (an example of this is shown in Figure 1.9). The velocity is blue shift as the planet is travelling towards the observer and red-shifted as the planet is travelling away. This is shown in Figure 1.8.

The derivation of radial velocity parameters is shown in many works, for example Lovis and Fischer (2010). Following that work it can be shown that (for circular orbits)

$$K_* = \left(\frac{2\pi G}{P} \right)^{\frac{1}{3}} \frac{M_p \sin(i)}{(M_* + M_p)^{\frac{2}{3}}} \quad (19)$$

where K_* is the maximum velocity of the star. G is the gravitational constant and P is the orbital period of the planet. The change to the star velocity is directly proportional to $\sin(i)$ where i is the inclination. We see at face-on geometries ($i=0^\circ$) the maximum velocity $K_* = 0$. We see it is also dependent on the mass of the host star, with lower mass stars causing higher maximum velocities.

The RV method provides a crucial component the transit method was lacking: the mass of the planet. By combining the mass and the radius of the planet we can estimate the mean density. From the mean density we can estimate the composition (e.g. whether it is made from hydrogen, metals, silicates etc). We can also estimate parameters such as the scale height of the atmosphere (see Section 1.4).

RV measurements require us to take high resolution spectra in order to resolve the spectral lines. This is done with ground based facilities such as the HARPS spectrograph (High Accuracy Radial velocity Planet Searcher)¹⁵ which has a precision of 1m/s. This precision is easily enough to detect a Jupiter mass planet at 1 AU (which would have $K_* = 28\text{m/s}$) but not enough to detect an Earth at 1 AU (which would have $K_* = 0.1\text{m/s}$). Detections of RV signals also require many repeat observations in order to sample the velocity at many points during the planets orbit.

¹⁵ Mayor et al. (2003)

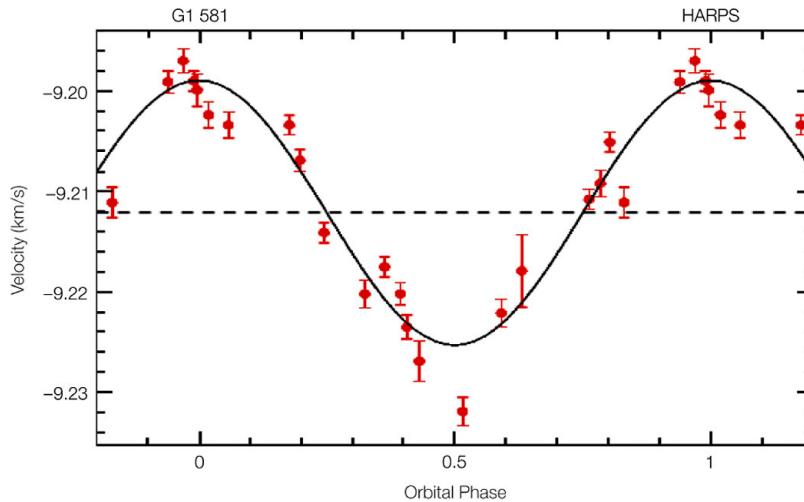


Figure 1.9: Example of a radial velocity curve for a red dwarf star G1 581. The circular orbit of the second mass in the system causes the curve to be sinusoidal with a period of 6 days and $K_* = 13 \text{ m/s}$. This graphic has been taken from the ESO public images archive.

This method is limited by two main factors; the mass estimate from the method is always the minimum mass, and the mass is always derived from the stellar mass. The maximum doppler shift is produced when the system is edge on to the observer (which is the case in Figure 1.8). As the inclination of the system decreases to zero (face-on to the observer) the magnitude of the doppler shift reduces. When the system is face-on to the observer, there is no movement in the line of sight and the planet is not visible. As the inclination for the system is rarely known for planets, Equation 19 can only ever give us a minimum mass estimate. However, if we have a case where a planet also transits the inclination of the system is known (based on the impact parameter) and the RV method can give us an accurate mass estimate. Using these two methods in conjunction gives us the most information about a planet possible. However, RV follow-up is time intensive and costly.

1.2.3 Other Methods

There are several other methods to find exoplanet signals. These methods have not produced the quantity of exoplanets that the RV and transit methods have, as shown in Figure 1.4. However, they are able to explore parameter space that these two methods are lacking. Notably, some of these methods (e.g. micro-lensing and direct imaging) are better suited to observing long period exoplanets.

Of particular interest is astrometry, where a stars movements on the sky due to an orbiting mass are used to infer the presence of a planet. The star and the planet orbit a common centre of mass, and the motion of the host star around this centre can be observed to change over time. Astrometry is useful for finding planets on wide separations, as they cause the largest motion in the host star (although observations must be made over many years to find such motion). This makes it a complementary technique to observing transits or radial velocity, which are both more sensitive to short period planets. With the *Gaia* mission accurately measuring star positions and velocities, astrometry is likely to reveal a great deal of new planet candidates. Perryman et al. (2014) discuss astrometry with *Gaia* and suggest that up to 70,000 planets could be found over the missions 10 year life time.

Other methods such as Transit Timing Variations (TTVS) give insight into multiplicity in exoplanet systems. In TTVS the transit of a planet becomes slightly aperiodic due to the presence of another mass in the system. This is used to infer the presence of other masses such as planets and companions.

Other discovery methods include Pulsar timing (which was used to discover the first exoplanet¹⁶) where the regular period of a pulsar is doppler shifted due to an orbiting planet and Microlensing, where a planet close to a lensing star temporarily increases the signal from a gravitational lens. These methods all produce a low number of planets (see Figure 1.4) and are harder to do with large surveys, due to the rarity of amenable targets.

These methods all have their own drawbacks and advantages. This thesis only focuses on transiting exoplanets, but other methods are useful for characterising planets. For example, it is possible to directly image planets, though the conditions needed for this are restrictive: the planet must be bright and far from the host star in this method. The star light is blocked and the signals for the surrounding planets are found above the background noise. This has worked for a select few targets. (For example HR8799, which has four planets that are very young and retain formation heat, making them observable)¹⁷. Observing young, giant planets so far from their host star allows us to learn more about how systems form and evolve¹⁸.

¹⁶ Wolszczan and Frail (1992)

¹⁷ Marois et al. (2008)

¹⁸ Dodson-Robinson et al. (2009); Meru and Bate (2010)

1.2.4 Planets Parameters are Derived from Stellar Parameters

With the above methods, one drawback is clear: all planet parameters are derived from their host stars. The transit depth and duration are both dependent on the mass and radius of the stars. The mass of a planet in the radial velocity method is derived only with respect to the host star mass. This presents a problem for exoplanet astronomers, as accurate and precise stellar parameters can be hard to obtain. Largely, the measurement of stellar parameters relies on comparisons of photometry and optical spectra to stellar atmosphere and evolution models. In some cases we are able to use independent methods such as interferometry (if we have very bright stars) and asteroseismology (if we have long, high cadence time series) to measure stellar mass and radii. However, without first accurately understanding the stellar properties we are limited in what we can learn about exoplanets.

1.2.5 Biases in Planet Surveys

In the above sections I have discussed the advantages and disadvantages of two methods for detecting exoplanets. In each method there are 'detection biases' that skew the derived sample towards a preferred parameter space. This is illustrated in Figure 1.10, where all current exoplanets with mass estimates are plotted against their orbital period. More details on the biases of these methods can be found in literature, particularly in the review of statistics in exoplanets by Udry and Santos (2007).

There is clearly a skew in the transit method towards shorter period exoplanets. We are biased towards short periods because they occur more frequently. This allows us to detect them using the shortest amount of time. Large radii planets are also preferentially selected as they cause this largest change in the transit signal (see Equation 9). The highest mass planets also tend to have larger radii on average, particularly where gas giants begin to form (which are lower density). This creates a bias towards low density planets with large radii and short orbital periods. Not only do short orbital period planets transit more frequently, but their shorter orbital distances increases the transit probability as shown in Equation 1

There is a bias in the RV method towards high mass exoplanets as shown in Figure 1.10. This is clear from Equation 19, where high mass planets cause the largest maximum velocity. The radial velocity method also requires stars to be bright in order to collect enough photons to accurately measure the stellar spectral lines. Most RV planets have been detected around stars brighter than 9th magnitude (see Figure

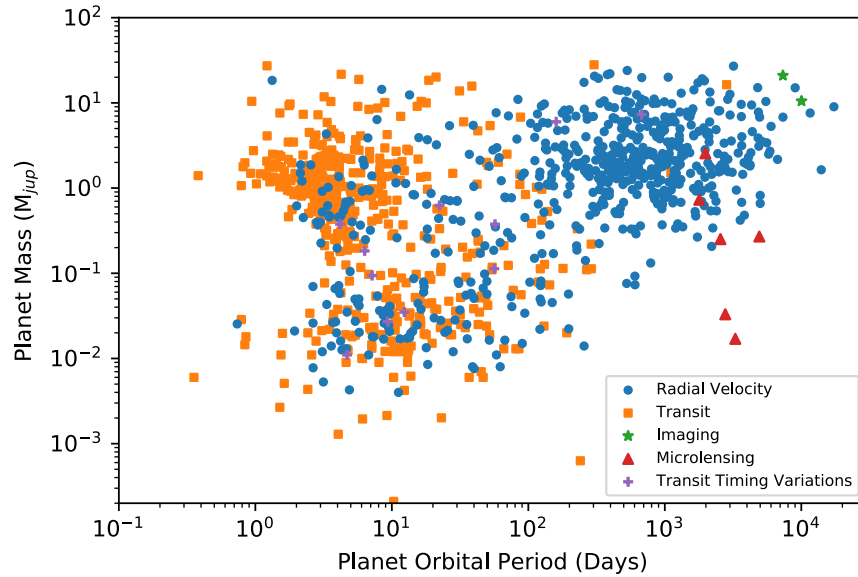


Figure 1.10: Mass/ period diagram for known exoplanets that have mass estimates. These have been split into their discovery methods. The transit method and radial velocity method have been the most fruitful. It is clear that each method is biased, with both being more biased towards larger planet. Few exoplanets have been discovered by other methods. (Data accessed from NASA Exoplanet Archive in April 2017.)

1.11). As very short period planets are quite rare and RV searches are not as deep as transit searches, there are fewer RV short period exoplanets.

Based on these biases it can be difficult to accurately quantify the underlying distribution of exoplanet types. However, by understanding and quantifying the biases in these methods we can gain an understanding of the true distribution of exoplanets. The study of the underlying occurrence rates of planets has been undertaken by many works (for example Burke et al. (2015); Foreman-Mackey, Hogg, and Morton (2014); Dong and Zhu (2013)), with a goal of estimating η_{Earth} (the frequency of Earth-like planets). This goal will become easier in the future with detection missions TESS and PLATO expanding the known set of exoplanets, particularly around nearby bright stars.

A DESERT OF NEPTUNES In Figure 1.10 there appears to be a reduced number of exoplanets at short periods (1-10 days) and Neptune masses. This has been noted in literature as a desert of short-period Neptune planets (see Mazeh, Holczer, and Faigler (2016) and the references therein). Features such as these can be used to better understand the underlying formation mechanisms of planets, since certain planet types are clearly penalised.

1.2.6 The Future of Exoplanet Detection

There are several exoplanet detection surveys online, actively hunting for planets, particularly using the transit method. While the Kepler mission has ended due to faults with the spacecraft, it has been repurposed into K2 which continues to provide light curves for planet hunters. New ground-based survey NGTS (Next Generation Transit Survey)¹⁹ is currently taking data, searching for Earth-like and Neptune-like planets around $\sim 40,000$ stars brighter than 13th magnitude. The TRAPPIST mission (Transiting Planets and Planetesimals Small Telescope)²⁰ has recently proved successful by finding 7 small planets around an M star. It searches for transits around cool, small stars (which maximises the transit depth as shown in Equation 9). The

¹⁹ Chazelas et al. (2012)

²⁰ Gillon et al. (2017)

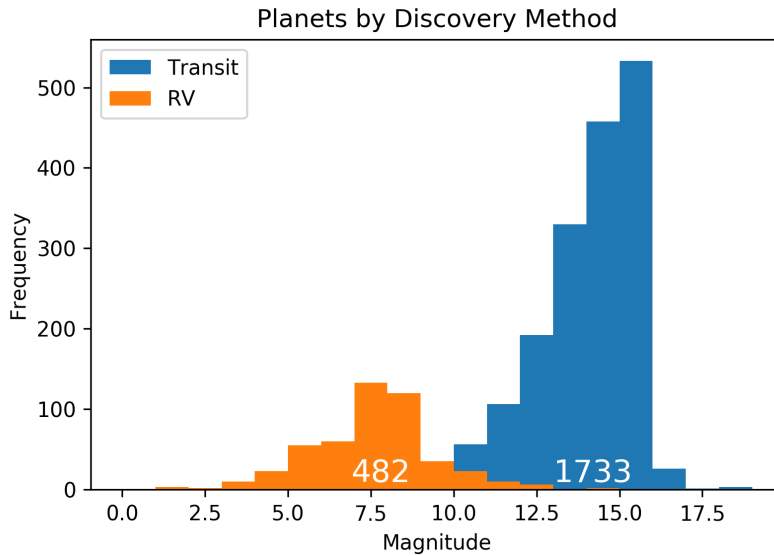


Figure 1.11: Brightness in magnitude of all exoplanet host stars discovered with either transit or RV method. Many more planets have been discovered with the transit method to date. The Kepler spacecraft has provided the majority of the transit planets, and had a magnitude limit of 18th mag (though usually apertures were not placed over stars dimmer than 16th). The magnitude limit is softer (larger planets can be confirmed around dimmer stars) but largely RV cannot be used for stars dimmer than ~ 9 th magnitude.

SPECULOOS mission (Search for habitable Planets Eclipsing ULtra-cOOl Stars)²¹ will follow on from the success of TRAPPIST and continue to search for planets around small stars.

²¹ Gillon et al. (2013)

Other instruments are also being developed and implemented that do not use the transit method. The ESPRESSO instrument (Echelle SPectrograph for Rocky Exoplanet- and Stable Spectroscopic Observations)²² is a next generation radial velocity instrument that will shortly come online on the VLT. This will greatly help the effort to characterise small planets with mass estimates. Project 1640²³ is a new direct imaging instrument that will be able to image Jupiter sized planets around nearby stars and take spectra of them.

²² Pepe et al. (2010)

²³ Roberts et al. (2009)

There are two large, dedicated exoplanet missions coming online in the near future. TESS (Transiting Exoplanet Survey Satellite) in 2018 and PLATO (Planetary Transits and Oscillations of stars) in 2025. PLATO is expected to observe up to a million stars, and TESS is expected to observe 200,000. ²⁴ Kepler's occurrence rates of super Earth planets at short periods ($P < 10$ days) is 0.2%. We would therefore expect TESS to find ~ 400 short period super Earths and PLATO to find ~ 2000 . These targets are particularly good for follow-up with atmospheric observations and RV observations as they are larger and transit often.

²⁴ Rauer et al. (2014); (2014)

These missions will drastically increase the known set of exoplanets and crucially increase the sample around bright stars. Bright stars allow the possibility of follow-up observations of atmospheres and, in some cases, direct imaging.

1.3 FINDING PLANETS IN THE DATA

With the advent of so many survey missions providing huge quantities of data (particularly the Kepler mission which has provided three years of data on 145,000 stars) the next question is how we should go about finding exoplanet signals. Jenkins et al. (2010) discusses in detail how the automatic processing for Kepler initially

cleaned light curves and vetted stars, finding ‘threshold crossing events’ that should be further investigated. This is done by finding highly periodic events based on template matching in frequency space (see Batalha et al. (2013) and the references therein for a detailed explanation of this process). Any detections of 7σ or greater that occur multiple times are then taken for further analysis. A transit model from Mandel and Agol (2002) is then fit to the data and light curves are visually inspected.

There are other ways to search for exoplanets including searching through periodograms and using Box-Least-Squares fitting (see the large sample of exoplanet light curve fitting tools, for example Akeson et al. (2013a); Paunzen and Vanmunster (2016); Hartman and Bakos (2016)). Recently, more effort has gone into automatically classifying and measuring transit signals using machine learning. For example, McCauliff et al. (2015) (who proposes automating the search for threshold-crossing events) and Thompson et al. (2015) (who uses machine learning to identify transit shapes in light curves). Distinguishing these small signals reliably over the noise of the star, (which may also be a variable star) is an open problem in the field. With more data coming in the future from transit surveys, finding fast and reliable ways to classify light curves will become crucial.

1.3.1 *Confirming Exoplanet Signals*

When using the transit method, transit signals must be ‘confirmed’. This process attempts to confirm that the signal is from a planet and is not a false positive. The easiest way to do this is to confirm them with radial velocity follow up. However, this is often difficult as the stars must be bright, and there are a great deal of exoplanets to follow up on (see Figure 1.11). Batalha et al. (2013) discusses the process for confirming exoplanets using statistics from the Kepler mission and attempting to rule out false positive such as eclipsing binaries. Coughlin et al. (2014) discusses in detail the process for identifying false positives in Kepler data and finds that 12% of KOIs (Kepler Objects of Interest) are false positives.

1.4 EXOPLANET ATMOSPHERES

Over the past 15 years it has become possible to not only detect the presence of exoplanets, but begin to analyse them through their atmospheric composition. Understanding the composition of atmospheres allows us to investigate many aspects of exoplanets. We can model atmospheric circulation and study the variety of atmosphere compositions. If the atmosphere is primordial (with the same composition as the protoplanetary disk it formed from) the atmosphere can be used to infer properties about the exoplanets formation history. If the atmosphere is not primordial it will contain chemistry from geological processing in the planet, giving valuable insight into the composition and even geology of the planet.

In the solar system all planets (and even dwarf planets such as Pluto) have atmospheres, although some are more tenuous than others. It does not seem a stretch to assume that many (or even most) exoplanets also have atmospheres. However solar system planets also usually exhibit clouds and weather patterns. Clouds can become a problem for this technique as they are opaque and sit high in the atmosphere. They block light from being transmitted through the atmosphere and set a ‘floor’ on the minimum transit depth. This limits the contrast between wavelengths where molecules absorb strongly and regions where the atmosphere is mostly transmissive. I will discuss clouds and hazes in exoplanet atmospheres in Section 1.4.3.

We can use observations of exoplanet atmospheres as well as mass and radius estimates to characterise some of their properties. One useful example is the scale height of the exoplanet. This is used to estimate how thick the atmosphere around a planet may be.

SCALE HEIGHT The atmosphere becomes less dense as you move further from the surface of the planet. The height of the atmosphere is measured in scale heights H . This quantity is the height from the surface such that the pressure of the atmosphere has fallen off by a factor of e . Scale height is given as

$$H = \frac{kT}{\mu g} \quad (20)$$

where k is Boltzmann's constant, T is the temperature of the surface of the planet, μ is the mean molecular mass in proton masses and g is the surface gravity. The true atmosphere has a non-uniform density, becoming much more tenuous at the top of the atmosphere. Using Seager and Sasselov (2000) we can approximate that this true atmosphere is equivalent to a uniform gas layer of 5 scale heights with uniform density.

There is an important factor of μ in the scale height equation. μ is the mean molecular weight of the atmosphere scaled by the proton mass. For molecular hydrogen this would be $\mu = 2 \times 1.66 \times 10^{-24}$. μ is where we would encode the information about the atmosphere composition. For Earth-like planets we would expect an atmosphere containing molecules such as N_2 and a μ value of the order 30 proton masses. For hot Jupiters, where we expect the atmosphere to be mostly molecular hydrogen and helium, μ would be 2. We can use this to calculate the approximate scale height for Earth and a hot Jupiter such as HD209458b.

$$H_{\text{Earth}} = \frac{N \times 1.38 \times 10^{-23} \times 255}{30 \times 9.8} = 42.5\text{km} \quad (21)$$

$$H_{\text{HJup}} = \frac{N \times 1.38 \times 10^{-23} \times 1200}{2 \times 30} = 1000\text{km} \quad (22)$$

For Earth the scale height is much lower, due to the larger μ and lower temperature, even though it is smaller and has a low surface gravity.

The hot Jupiter has a large scale height as it is highly irradiated. The scale height is a useful metric for comparing planets and judging whether they would be strong candidates for atmosphere observations. Figure 1.12 shows the mass radius diagram of known exoplanets with lines of constant surface gravity drawn. High scale height planets, which are the strongest candidates for atmosphere observation, lie at the top edge of this distribution.

1.4.1 Characterising Transiting Exoplanet Atmospheres

After the initial discoveries of exoplanets, Seager and Sasselov (2000) proposed a method of observing exoplanet atmospheres: transmission spectroscopy. The principle of transmission spectroscopy is relatively simple; when an exoplanet with an optically thin atmosphere passes in front of its host star during a transit some fraction of stellar light must pass through this atmosphere. Some of this light will be transmitted and some will be absorbed by the molecules present in the atmosphere. When taking a spectrum of the star during transit, if the stellar spectrum is accurately removed, what remains must contain the spectrum transmitted through the atmosphere. This process was then observed in Charbonneau et al. (2001) where the Sodium doublet at 589.3nm was observed in the atmosphere of exoplanet HD209458b. In the years since significant strides have been made in characterising exoplanets in this way.

The geometry of transmission spectra is shown in Figure 1.13. As discussed in Section 1.2.1 the signals required for searching for exoplanets are very small. This is compounded in transmission spectroscopy, where we are attempting to detect the change in radius of the planet due to molecular absorption in different wavelengths. Because of this, only the brightest targets are used. (All planets observed with HST to retrieve transmission spectra have been magnitude 12 or brighter.)

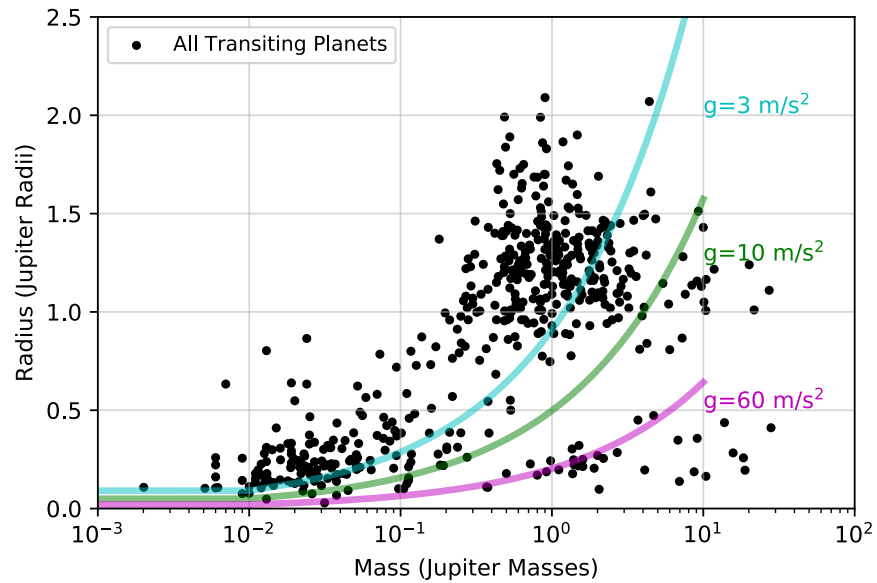


Figure 1.12: Mass/radius diagram for exoplanets with lines of constant surface gravity g . High scale height planets will lie above the cyan line as these are the least dense planets. Planets with shorter periods also have higher scale heights.

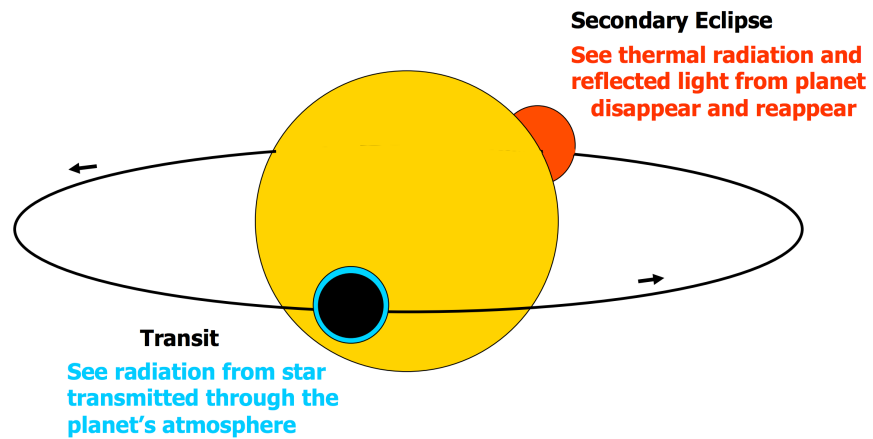


Figure 1.13: Diagram of exoplanet transit geometry as used for exoplanet atmospheres. The light transmitted through the atmosphere during transit can be used to take a spectrum of the atmosphere. The reflected light from eclipse can be used to estimate the properties of the atmosphere. The phase curve can be useful for finding hot spots. (Figure from Sara Seagar and Heather Knutson.)

Transmission spectroscopy provides us with the possibility to detect water using fairly short observations. However, due to the nature of the geometry it requires that we wait for the planet to transit. This limits the sample that can be observed to those planets that are short period enough to have frequent transits. For particularly small planets, many observations can be stacked in order to increase the signal-to-noise ratio. This adds to the bias towards short period planets. A further shortcoming of this method is that it is only viable for planets that do in fact transit, which reduces the sample that can be used.

GROUND-BASED OR SPACE-BASED? More than 1000 HST orbits have been spent on characterising exoplanet atmospheres using transmission spectroscopy in the IR (see Chapter 3). Treasury programs of HST data have enabled the largest census of exoplanet atmospheric spectra to date and several water detections in exoplanet atmospheres have been made.²⁵ Spitzer has also provided longer wavelength follow-up in the mid-IR²⁶. Further, a great deal of effort and telescope hours have been used for transmission spectroscopy using ground based facilities including the Magellan and Keck telescopes.²⁷ These two regimes have their own strengths and weaknesses. From the ground we can obtain high resolution spectra of the transiting exoplanet across a wide range of wavelengths. However, we are limited by the atmosphere both in terms of seeing and in terms of water absorption. The absorption from telluric water makes it impossible to measure water abundance in exoplanet atmospheres from the ground. From space we are free from the atmosphere and can observe water. However, we are much more limited in wavelength resolution. The two current resources at our disposal, HST and Spitzer, have narrow coverage in the near and mid-IR as well as very low resolution ($R < 30$). This combines to make our observations degenerate, with atmospheric models able to fit transmission spectra with several molecules. However, recently more work is being done to combine observations from several sources. For example the work from Sing et al. (2016) combines two HST instruments and ground based observations. By combining the two sources we can alleviate degeneracies and better constrain the abundances of more molecules.

²⁵ Deming et al. (2013a); Knutson et al. (2014a); Kreidberg et al. (2014c); Ehrenreich et al. (2014); de Wit et al. (2016)

²⁶ Demory et al. (2013); Stevenson et al. (2014b); Wakeford et al. (2017)

²⁷ Crossfield et al. (2013); Bean et al. (2013)

1.4.1.1 Beyond Transmission Spectroscopy

In cases of short period, large planets the transit method can provide more than just transit observations. Large planets can reflect a higher percentage of the planet light, and they also emit an amount of thermal radiation. This is usually small compared to the stars radiation, though with small dim stars this is not always the case. As the planet moves from transit towards the furthest point in the orbit, it increasingly reflects more starlight back to the observer. This causes the brightness of the star to increase and decrease sinusoidally, which is known as a phase curve. Once the planet reaches the furthest point and goes behind the star this reflected light is temporarily blocked. This reduces the flux from the system temporarily in an 'eclipse' (see Figure 1.13). These two effects can allow us to measure the planets reflectivity. The eclipse depth is given below, based on the emitted light of the planet compared to the emitted light of the star.

$$\delta_{ecl} = \frac{R_p^2}{R_*^2} \frac{\int B_\lambda(T_{eq}) d\lambda}{\int F_\lambda d\lambda} + r \quad (23)$$

where B_λ is a blackbody curve for the planet and T_{eq} is the equilibrium temperature of the planet. r is the amount of light reflected by the planet which is given by

$$r = A \frac{R_p^2}{a^2} \quad (24)$$

where A is the planet albedo, which is the fraction of energy that is reflected. (A high albedo will increase the eclipse depth.)

In some cases phase curves also allow us to identify hot spots, or particularly bright regions of the planet surface. These occur when a planet is tidally locked, causing one side to permanently face the host star. The addition of an atmosphere with strong winds can displace this hot spot²⁸. This phenomenon has been used to measure exoplanet atmospheres and surface brightness, notably in Wasp-43b²⁹, where a full phase curve was obtained with HST's Wide Field Camera 3 instrument.

²⁸
²⁹ Kataria
et al. (2015a)

1.4.1.2 Effect of Adding an Atmosphere

In working with exoplanet transmission spectra it is beneficial to have an appreciation for the size of signal we are trying to detect. We can calculate the size of this signal from simple transit geometry. For this purpose we will consider a planet during transit with a thin atmospheric layer. This layer will become optically thick in some wavelengths and optically thin in others, depending upon the molecular absorption. An optically thick atmosphere will slightly increase the radius of the planet, increasing the transit depth δ given by Equation 9 from the sections above. To establish the effect of the atmosphere we can consider the change in effective radius of the planet caused by an optically thick layer. The addition of this atmosphere layer will give us a new effective radius of the form

$$R'_p = R_p + NH \quad (25)$$

where H is the height of the atmosphere and $N = 5$. The new equation for transit depth taking into account the new effective radius is

$$\delta_{\text{atm}} = \frac{(R_p + NH)^2}{R_*^2} \quad (26)$$

The difference in the transit depth from introducing this atmosphere layer (Δ) is then

$$\Delta = \delta_{\text{atm}} - \delta = \frac{(R_p + NH)^2}{R_*^2} - \frac{R_p^2}{R_*^2} \quad (27)$$

$$\Delta = \frac{2R_p NH + N^2 H^2}{R_*^2} \quad (28)$$

where we assume $R \gg H$ giving

$$\Delta \approx \frac{2R_p NH}{R_*^2} = \delta \times \frac{2NH}{R_p} \quad (29)$$

From this we can lastly calculate the change in the transit depth during the transit when an atmosphere is introduced

$$\delta_{\text{atm}} - \delta = \delta \times \frac{H}{R_p} = \frac{R_p^2}{R_*^2} \times \frac{H}{R_p} \quad (30)$$

Substituting in the scale height values and radii for the planets from above we find

$$\delta_{\text{atm, Earth}} - \delta_{\text{Earth}} \approx 0.6 \text{ ppm} \quad (31)$$

$$\delta_{\text{atm, HJup}} - \delta_{\text{HJup}} \approx 150 \text{ ppm} \quad (32)$$

While we have utilised a μ value to quantify the mean molecular mass of the atmosphere we have not used any wavelength dependence. In reality we would observe the atmosphere across multiple different wavelengths where molecular features would absorb or transmit light, depending on the molecular transition lines. Any molecular feature will cause structure in the transmission spectrum as a function of wavelength.

The analysis of exoplanet atmospheres also relies on molecules that absorb strongly being present in high abundance. The addition of a molecular absorber creates a contrast between the optically thin atmosphere (where there is low absorption) and the

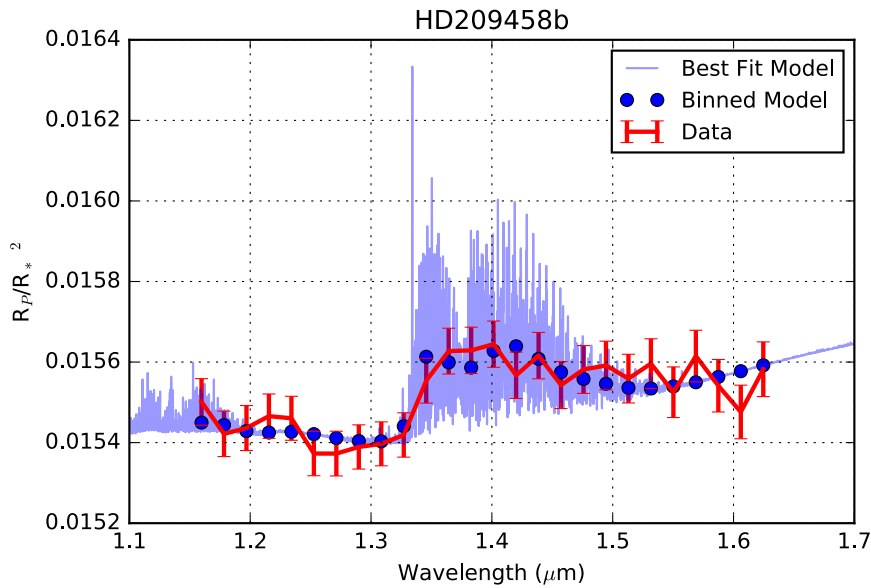


Figure 1.14: Transmission spectrum for HD209458b using the reduction discussed in this work with an atmospheric model fit using atmospheric retrieval code BART. The water feature at $1.34\mu\text{m}$ is clearly seen in this exoplanet atmosphere. The model is much higher resolution than the data and is binned down to the observation resolution.

optically thick atmosphere (where there is high absorption). This makes observations of atmospheres with molecular absorbers high in their atmospheres attractive to atmospheric modellers. Figure 1.14 shows an example; at $1.34\mu\text{m}$ the water molecules absorb strongly, creating an absorption feature. At $1.1\mu\text{m}$ - $1.25\mu\text{m}$ however the spectrum is fairly flat. This contrast allows the water abundance to be constrained in models.

The signal that we are trying to detect is exceptionally small. Even in the most optimistic case of a hot Jupiter with a thick atmosphere, signals will likely never exceed a few hundred ppm. When hunting for signals from exoplanet atmospheres astronomers must use techniques where their signal to noise is high. Even with some of the best instruments available this is often difficult. Currently detecting the atmosphere of a super-Earth planet is pushing the limits of what can be achieved just from these physical limitations. Observers focus their attention on planets that have the highest chance of a detection of an atmospheric signal. Based on their large scale heights hot Jupiter targets and larger exoplanets are often chosen for this reason. (For example, see Figure 3.1 in Chapter 3.) Some smaller planets such as GJ1214b have been observed with a great many Hubble orbits. However, no atmospheric signal has been detected and the spectrum retrieved is flat.³⁰

³⁰ Berta et al. (2012)

1.4.2 Characterising Non Transiting Exoplanet Atmospheres

It is possible to observe spectra of an exoplanet atmosphere without using a transiting planet. A high resolution technique for deriving exoplanet atmosphere signals from non-transiting planets has been developed using ground-based instruments.³¹ The method utilises the motion of the planet and high resolution spectra of the combine star-planet system. Rather than detecting the transmission through the atmosphere, this method directly detects the atmospheric signal. An observation of the stellar spectrum is taken multiple times as the planet orbits. The stellar spectrum is able to be isolated and removed, from all observations (as it is constant). Telluric lines are also removed. The remaining planet signal is then observed as it is Doppler shifted as the planet orbits the star. This allows a spectrum to be built and template

³¹ Snellen et al. (2010); Birkby et al. (2013); de Kok et al. (2013)

spectra to be cross matched. The signal to noise ratio is increased by summing up multiple lines of the same molecule. Many observations of CO have been made this way using the CRIRES instrument on the VLT including HD209458b and τ Bootis b (e.g. see Snellen et al. (2010); Brogi et al. (2012)). An example of a spectrum for one of these observations is given in Figure 1.15.

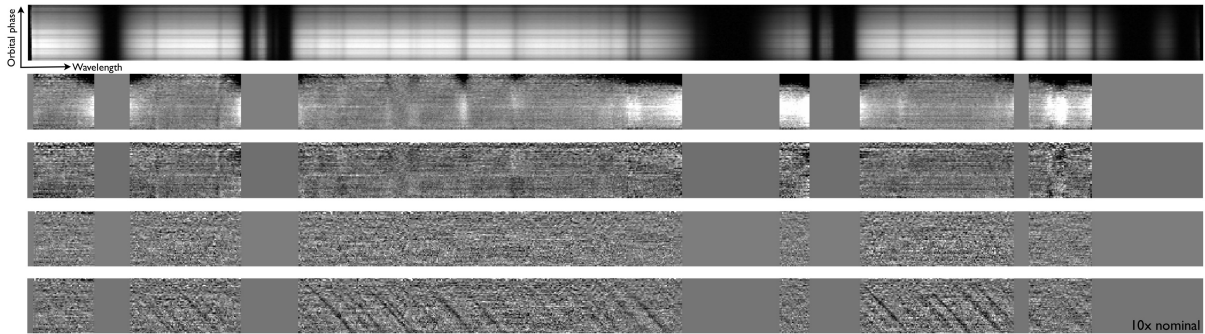


Figure 1.15: Schematic of the method for directly observing exoplanet atmospheres, as discussed by Birkby et al. (2013) (Figure taken from that work.) The top panel shows the original data containing the stellar light, telluric lines and planet signal, with spectral axis as the x axis and time increasing up the y axis. Next two panels show the different corrections applied to remove the stellar and telluric signals (grey portions are completely blocked by telluric absorption.) The fourth panel shows the final spectrum, which should only contain signals from the exoplanet atmosphere. The last panel shows the same data with the expected CO template injected at 10x the expected value to show how the signal of the exoplanet motion would present in the spectra.

There are some drawbacks to this method. As with the transmission spectroscopy method, it requires the signal from the planet be bright in order to obtain enough photons, and so this method has only been attempted with a handful of planets to date. Spectra are required at many different points during the planet orbit in order to see the change in the line positions over time and isolate it from the stellar spectrum. This can make observations expensive. However, this method can be used on non-transiting planets, greatly increasing the sample of nearby planets where atmospheric characterisation can be obtained (since transit probabilities are small as discussed in Section 1.2.1).

1.4.3 Clouds and Hazes

While this simple calculation gives an estimate of the signal size, the addition of clouds or hazes could alter the retrieved values significantly. Clouds are opaque and can sit high in the atmosphere. Based on giant planets in the solar system clouds are common and we would expect them in many exoplanets. However, with the effects of heating and tidal locking for hot Jupiters it is difficult to model how clouds may manifest. High level clouds are opaque across all wavelengths, essentially creating a floor to the possible measurements of the planet radius, reducing the amount of optically thin material that can cause the transmission spectrum. Unfortunately this massively limits our ability to observe exoplanet atmospheres in transmission. However, other methods may prove more beneficial. For example, if looking at a planet in eclipse varying clouds can alter the albedo of a planet which could potentially be detectable.³² Beyond clouds there are also particulate hazes which can affect results. These hazes are modelled with Rayleigh scattering and have a strong wavelength dependence. They block the light in a similar way to clouds, creating a limit in the observed transmission spectrum.

Figure 1.16, taken from Sing et al. (2015), shows an example of how these atmospheric features can affect the final spectrum. We see firstly the effect of a hazy atmosphere increasing the opacity at bluer wavelengths due to the strong wavelength dependence of Rayleigh scattering. This causes the atmosphere to be much more optically thick in the visual than in the IR. Secondly the effect of a cloudy atmosphere is shown where the cloud deck limits the contrast between the absorption features

³² Marley et al. (2013)

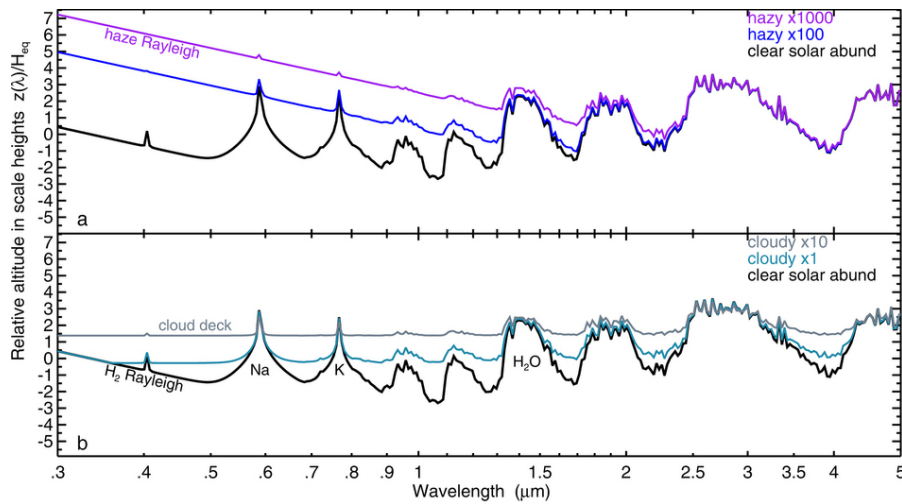


Figure 1.16: Example of the effects of different atmospheric features taken from Sing et al. (2015) who discusses a comparison of the atmosphere of several hot Jupiters. The addition of a cloud layer raises the effective surface of the planet, reducing the height of any molecular features. A strong haze adds a steep Rayleigh scattering slope with a strong wavelength dependence.

and the continuum level. The addition of clouds makes observations of absorption features much lower signal to noise and also inhibits abundance measurements from atmospheric modelling.

1.4.4 Biosignatures

Atmospheric characterisation is an important tool to understand more about these worlds, allowing us to compare chemistry outside the solar system to chemistry with in it, and potentially to look for biosignatures. Biosignatures are observables that indicate life. Most of these signatures are degenerate with other chemical or geological abiotic processes. For example, methane is produced by life on earth making it a biosignature, however it is also produced by geological processes. The most useful biosignatures are only present due to life. O_2 and O_3 are much more useful, particularly in the context of Earth. The level of Oxygen is driven much higher than its natural value due to life on Earth. It is harder to produce O_2 and O_3 using geological processing. However, the amount of each of these is fairly small and requires great precision to detect. From the ground the E-ELT will be able to detect Oxygen on an Earth like planet with a dozen transits³³, though even around a small star this would take many years and be extremely costly. By using ground-based and space-based instruments in conjunction with multiple transits, it may be possible to begin to detect biomarkers such as O_3 , H_2O and CO_2 around planets in the habitable zone using ten or more transits.³⁴

³³ Snellen et al. (2013)

³⁴ Hedelt et al. (2013)

1.4.5 Future of Atmospheric Characterisation of Planets

In the next few years there will be two new space based missions that will drastically improve our characterisations of atmospheres. Firstly CHEOPS (CHAracterising EXOPlanets Satellite) will be a small telescope which will launch in the next few years. CHEOPS will provide much better radii measurements for planets that have been discovered from the ground.

JWST will also launch in the next few years. The NIRSpec and MIRI instruments will provide near-IR observations from 1–20 μm at resolutions of up to $R=3000$. A longer wavelength coverage allows absorption from many different molecular species to be measured at once. This gives the extra information needed to fit atmospheric

models and retrieve molecular abundance estimates. This will drastically improve our capabilities with transmission spectra, not only by increasing the sampling of the absorption features but by breaking degeneracies in atmospheric models. For JWST to be effective at characterising exoplanets, it will require transiting targets around bright stars. These will be provided by missions such as TESS, as discussed in Section 1.2.6.

1.5 THIS THESIS

Due to the rapid expansion of the field of exoplanets models are often catching up with the rate of discovery and data release. New planets are discovered regularly, (there are 3458 confirmed planets at time of writing). Models for planet formation, structure and atmospheres have been created and improved greatly in recent years, and there is a wealth of data to apply them to. On top of this our computing capabilities improve, and data is processed faster and more accurately with new algorithms. This leaves lots of gains to be made in old data by revisiting it with state of the art techniques.

In the field of exoplanet study we are moving beyond just detecting exoplanets and into characterising them. The precision needed for this is extreme, requiring many hours of follow up observations to measure masses and observe atmospheric spectra. Characterising exoplanets is difficult and expensive, with most exoplanet parameters having large errors and most spectra having limited coverage. To properly understand exoplanets we must handle the data carefully and reduce instrument systematics where possible.

In this thesis I will address two sides of exoplanet study; the gains we can make in exoplanet characterisation by using 'big data' and the new techniques we can use for discovering unusual light curves. I will split this into four chapters answering the following questions.

ARE WE PREPARED FOR THE FUTURE OF EXOPLANET OBSERVATION? Atmospheric models all rely on input data based on molecular absorption. The model in Figure 1.14 requires the temperature and wavelength dependent absorption cross section of water to calculate how much light the atmosphere absorbs. This data is readily available online from sources such as HITRAN, HITEMP and ExoMol. However, this data is also dependent on pressure, a factor that comes into atmospheric modelling. Currently pressure broadening at the molecular level is ignored by atmospheric models. This is largely due to observations of exoplanet atmospheres being low resolution. However, in the future with JWST we will improve our observational quality. In my first chapter I test whether the inclusion of pressure broadening at the molecular level will cause changes to the transmission spectrum of exoplanets large enough to observe and model. This work was published in Hedges and Madhusudhan (2016)

WHAT CAN WE LEARN ABOUT EXOPLANET ATMOSPHERES AS AN ENSEMBLE? HST Wide Field Camera 3 has been used to observe more than 30 exoplanet atmospheres, with more than 1000 orbits devoted to transmission spectra. To date, no one has reduced this entire set as a complete sample. In this chapter I will create a bespoke pipeline to reduce all WFC3 spatial scan data of exoplanet atmospheres and produce a sequence of transmission spectra from water-rich to water-poor. Using the molecular cross sections from the previous chapter I will be able to assess whether this sequence is consistent with simple molecular absorption by water. Analysing all spectra together allows me to investigate whether the atmospheric signals paint a consistent picture of absorption in exoplanet atmospheres.

ARE STELLAR PARAMETERS (AND SO EXOPLANET PARAMETERS) ROBUST IN THE NEAR IR? Stellar parameters are key in measuring the radii, masses and temperatures of exoplanets. They can often be difficult to measure in absolute terms. Using the sample of stellar spectra observed by HST from the previous chapter I will derive stellar temperatures based on stellar atmosphere models. Using these parameters I will project the expected error in exoplanet parameters. The accuracy of stellar atmosphere models in the IR is not well understood. By testing the accuracy of measuring stellar parameters in the IR on final exoplanet measurements I will be able to investigate whether more accurate IR models are needed.

CAN WE IMPROVE CLASSIFICATION OF LIGHT CURVES OF UNUSUAL OBJECTS USING MACHINE LEARNING? There are several large surveys of light curve data available currently, with several new missions coming online in the next decade. As the amount of data increases we require state-of-the-art search algorithms to find and classify objects. In this chapter I will use a Random Forest algorithm to search for and classify 'dipper' stars. These stars undergo short period occultation events on time scales of hours to days. They are very deep events, reducing the star flux by up to 50%. While these occultation events are not due to planets, they are similar in geometry to transits. I have chosen these objects as they are not only scientifically interesting, but hard to classify by eye. They also show much stronger variation than exoplanets, making them a good test case for machine learning algorithms. These objects are also young and will inform us about the processes that occur in protoplanetary disks. By creating a machine learning algorithm I will be able to test the classification probability of this unusual object and compare it with literature classifications by eye. This will allow me to test whether Random Forests can be used to improve the known sample of this unusual object. In theory, similar algorithms could be applied for search for any type of variable, from eclipsing binaries even down to exoplanets.

1.5.1 *A Data Driven Approach to Exoplanet Study*

With the modern age of computing power and precision instruments, astronomy is becoming a data intensive pursuit. The volume of data we can obtain is growing, and the computing power at our hands to process it is growing too. While it is possible to make new observations with the vast range of instruments available, there is also a wealth of data available for many astronomical purposes, archived for public use. In this thesis, I will focus on using archived public data to find new and exciting science.

All of the projects presented here use data that is freely and readily available to build new scientific insights for exoplanet characterisation and time series analysis. I intend to release the results from several of my projects online as libraries for public use. These will include a library of pressure broadened atmospheric cross sections, with plots showing their major absorption features. I will also release the stellar spectra I have produced, as they are very useful for stellar modellers to calibrate models and creating synthetic exoplanet atmosphere observations. These will be made available shortly after I submit my PhD.

Part II

PRESSURE IN EXOPLANET ATMOSPHERES USING
PUBLIC MOLECULAR DATA

THE EFFECTS OF PRESSURE BROADENING ON EXOPLANET ATMOSPHERES

2.1 INTRODUCTION

In recent years it has become possible to observe high-precision atmospheric spectra of a variety of exoplanets. High-precision observations with the HST Wide Field Camera 3 (WFC3) in the near-infrared (1.1-1.7 μm) have led to unambiguous detections of H_2O in several hot Jupiter atmospheres³⁵. The high photometric precisions of HST WFC3 spectra have allowed constraints on the H_2O abundances in these atmospheres, despite the modest resolution ($R \sim 10$ -100; depending on spectral binning).³⁶ It has also become possible to detect molecules such as H_2O and CO in atmospheres of hot Jupiters using very high resolution ($R = 10^5$) infrared Doppler spectroscopy with large, ground-based facilities³⁷. High-resolution and high-precision spectra have been reported for young giant planets on large orbital separations discovered via direct imaging from the ground. This has led to detections of several molecules, including H_2O , CO and CH_4 ³⁸. The field will be further revolutionised with upcoming facilities including JWST ($R \sim 1000 - 3000$) and several large ground-based facilities such as the E-ELT ($R \sim 10^5$).

The accuracy of atmospheric models is the key to interpreting observations of exoplanet atmospheres. In this Chapter I will discuss one aspect of atmospheric models that affects their accuracy: molecular absorption cross sections. There are many sources of error in models that are not discussed here; the physics involved is complex and there are many assumptions made on the astrophysical system and the chemistry. However, it is possible to quantify the errors from the fundamental inputs to these atmospheric models. These inputs are the behaviour of molecular absorbers, which comes in the form of a molecular cross section. Cross sections describe the amount of light a molecule will absorb as a function of wavelength. These are used to build the opacity of an atmospheric layer. Any inaccuracies in these fundamental inputs will limit the accuracy of an atmospheric model, regardless of the physical or chemical assumptions. With improving observational data quality it is important to examine the uncertainties in these model inputs.

In this work I investigate various factors involved in computing cross sections from molecular line lists. I discuss each aspect of the construction of the cross sections and where errors can be introduced. I compare different data sources, temperatures, pressures, broadening agents, evaluation widths and resolutions. I have also generated a database of cross sections with only thermal broadening included for comparison with those including pressure broadening. The cross sections generated span a wide range of pressures (10^{-4} - 100 atm) and temperatures (300 - 3500 K) that are relevant for exoplanet atmospheres and sub-stellar objects. I intend to release these cross sections online for public use shortly after submitting this thesis.

There are a wide array of future instruments that will observe exoplanet atmospheres in a new, detailed light. To benefit from these instruments we must be prepared, with thorough and accurate knowledge of basic inputs to atmospheric models. The James Webb Space Telescope (JWST) is scheduled for launch in 2018 and will host several instruments in the infra-red range. NIRSPEC and MIRI spectrographs will hold significance for the characterisation of exoplanet atmospheres. NIRSPEC will encompass the 0.6-5 μm range using three overlapping bands. MIRI will be a broadband instrument, stretching from 5-20 μm in wavelength. NIRSPEC will have a spectral resolution ranging up to $R=1400$ -3600 for its highest resolution grating and MIRI will achieve $R \approx 3000$. This is a drastic increase in my current capabilities with HST which warrants an investigation into our current modelling inputs.

³⁵ Deming et al. (2013b); McCullough et al. (2014); Kreidberg et al. (2014a); Madhusudhan et al. (2014a)

³⁶ Kreidberg et al. (2014a); Madhusudhan et al. (2014a)

³⁷ Snellen et al. (2010); Brogi et al. (2012)

³⁸ Konopacky et al. (2013)

³⁹ Snellen
et al. (2010); Brogi
et al. (2012)

From the ground, the CRIRES instrument on the VLT has been used extensively to study exoplanet atmospheres.³⁹ The instrument provides a resolution of $R=100,000$ which can be used for detailed observations of prominent absorption features such as CO. At such high resolutions the line profiles themselves can be resolved. In the distant future the E-ELT will be available, with a resolution of $R=100,000$ and be highly capable of atmospheric characterisation for exoplanets. Based on these instruments I present my tests of cross sections at a range of resolutions of $R=100, 1000, 3000, 10,000$ and $100,000$, encompassing the resolutions of current and future instruments.

2.1.1 Line List Sources

⁴⁰ Rothman
et al. (1998); Rothman
et al. (2013)

Significant progress has been made in recent years to generate molecular absorption line lists for molecules of relevance to exoplanet atmospheres. One of the largest and most well established of all the repositories for molecular line lists is the HITRAN database, which has been updated every few years⁴⁰. The HITRAN database has been mainly used for terrestrial applications and predominantly includes molecules of importance for the Earth's atmosphere. HITRAN is only valid at temperatures $\lesssim 300$ K. Because of this low temperature these data are less applicable for the most currently observable exoplanet atmospheres. Higher temperature line lists are provided by the newer HITEMP database, which contains fewer molecules but many more transitions for each⁴¹. HITEMP currently covers OH, NO, CO, CO₂ and H₂O which are particularly useful for hot Jupiter atmospheres, accurate up to temperatures of 4000K. More recently, the ExoMol database has begun addressing the deficit of data available for molecules of astrophysical importance at high temperatures⁴². They cover a wide range of molecules and continue to expand their data.

⁴¹ Rothman
et al. (2010)

⁴² Tenmyson and
Yurchenko (2012)

In this work I use many sources of line lists for inputs to generate cross sections. (I make comparisons across different sources in the sections below.) In this work I focus on HITRAN, HITEMP and ExoMol. These databases of molecular transitions are given in a variety of formats. Each source contains the key parameters (e.g. Einstein coefficients, degeneracies, energy levels, etc.) and a method for obtaining the line positions ν and the line intensities $S(T)$ for a given temperature T . They cover a wide spectral range, typically spanning the visible to mid-IR (e.g. $\sim 0.5 \mu\text{m}$ to $\sim 30 \mu\text{m}$), although this can vary between the different molecules.

Sources range in their completeness, with some containing fewer transitions than others. Lack of completeness leads to less reliable cross section data for two reasons. Firstly, gaps in the wavenumber coverage cause some features to be missed from the cross section. Secondly, lines of lower intensity which are missed can contribute significantly to the cross section when summed. As such accurate cross sections require the most complete lists of molecular transitions.

The complete list of molecules used in this work including all sources for data is given in Table 2.1. Many different line list sources were chosen, particularly for water, for comparison to investigate how completeness effects the resulting cross section.

2.2 LINE BROADENING

Molecular transition lines in spectra are often broadened by external factors such as heating in the atmosphere. Exoplanet atmospheres span a wide range of temperatures ($\sim 400 - 3000$ K) and dynamical parameters (e.g. wind speeds, and orbital and spin rotation rates) ranging from tidally locked close-in planets to young giant planets on wide orbital separations. The diversity of physical conditions in exoplanet atmospheres can lead to different types and degree of line broadening. The two prominent sources of line broadening in planetary atmospheres are thermal (Doppler) broadening and pressure (collisional) broadening⁴³. Thermal Doppler broadening is caused by the line-of-sight thermal velocity distribution of molecules at a given

⁴³
Chamberlain (1978);
Mihalas, Auer, and
Mihalas (1978);
Seager and
Deming (2010)

temperature in the planetary atmosphere. Pressure broadening is induced by collisions between chemical species with the collision frequency being a strong function of pressure.

Other sources of broadening can be prevalent depending on the planetary properties and observing geometry. In principle, natural broadening due to the intrinsic uncertainty in energy levels is always present, but is negligible compared to other broadening mechanisms discussed above. Further broadening and shifting of spectral lines can be caused by rotation of the planet and strong winds. This is especially important for close-in hot Jupiters observed in transmission⁴⁴. Finally, rotational broadening due to the spin of the planet can also be significant, especially for exoplanets that are not tidally locked such as those on wide orbital separations⁴⁵. I do not investigate these broadening mechanisms here, however the same methods presented below could be used to create cross sections broadened by these mechanisms.

⁴⁴ Spiegel, Haiman, and Gaudi (2007); Miller-Ricci Kempton and Rauscher (2012); Showman et al. (2013)

⁴⁵ Snellen et al. (2014)

2.2.1 Broadening Profiles

Under the assumption of a Maxwell-Boltzmann thermal velocity distribution the Doppler broadening takes the form of a Gaussian profile. Pressure broadening is represented by a Lorentzian profile. The Doppler and Lorentzian broadening profiles are given below in wavenumbers in cm^{-1} .

$$f_D(\nu - \nu_0) = \frac{1}{\gamma_G \sqrt{\pi}} \exp\left(-\frac{(\nu - \nu_0)^2}{\gamma_G^2}\right) \quad (33)$$

$$f_P(\nu - \nu_0) = \frac{1}{\pi} \frac{\gamma_L}{(\nu - \nu_0)^2 + \gamma_L^2} \quad (34)$$

where ν_0 is the centroid in wavenumbers, γ_G I define as the Doppler width and γ_L is the Lorentzian pressure broadening half-width at half-maximum (HWHM) both in units of cm^{-1} . These are given by works such as Hill, Yurchenko, and Tenynson (2013); Rothman et al. (1998):

$$\gamma_G = \sqrt{\frac{2k_B T}{m}} \frac{\nu_0}{c} \quad (35)$$

$$\gamma_L = \left(\frac{T_{ref}}{T}\right)^n P \sum_b \gamma_{L,b} p_b \quad (36)$$

where P is pressure in atm, T is the temperature in Kelvin, T_{ref} is the reference temperature (usually 296K), p_b is the partial pressure of the broadening agent, n is a temperature scaling factor and $\gamma_{L,b}$ indicates the Lorentzian HWHM due to a specific broadening molecule in units of $\text{cm}^{-1}/\text{atm}$. Here k_B is the Boltzmann constant, m is the mass of the molecule in grams and c is the speed of light in cm/s . Here, \sum signifies the sum over all the broadening parameters for each broadening medium.

Pressure broadening is typically harder to evaluate than thermal broadening for two reasons. Firstly, the line-by-line pressure broadening parameters $n(\nu)$ and $\gamma(\nu)$ are typically unavailable for most molecules⁴⁶. Secondly, the Lorentzian has extensive wings which can result in a significant amount of the intensity being distributed far from the line centre. In cases of extreme broadening this can significantly increase the impact of high intensity transitions across a wide wavelength range, where they influence neighbouring low intensity transitions.

Figure 2.1 shows a comparison between the Doppler HWHM ($\gamma_G \sqrt{\ln 2}$) and the Lorentzian HWHM over the P-T space of interest in this work. This gives an approximation of where each profile contributes most significantly. However, as the two profiles are quite different, it is hard to make a thorough comparison. A Gaussian profile contains most information in the core, where as the Lorentzian has extended wings. As expected, at low pressures thermal (Gaussian) broadening provides a significant contribution to the final profile core, whereas at high pressures pressure (Lorentzian)

⁴⁶ Freedman, Marley, and Lodders (2008); Freedman et al. (2014)

Profile Widths Across Temperature-Pressure Space

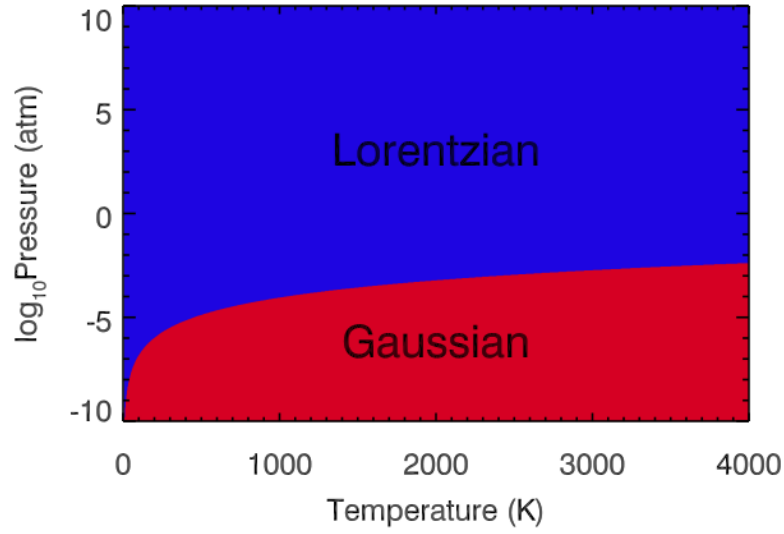


Figure 2.1: Comparison of widths of line cores of Gaussian vs Lorentzian profiles in pressure-temperature space. The red (blue) region represents P-T space where the HWHM of a Gaussian (Lorentzian) profile is wider than that of a Lorentzian (Gaussian) profile. The Gaussian profile is wider at low pressures and the Lorentzian at high pressures, as expected.

broadening is stronger. Closer to the boundary between these two regimes, both broadening mechanisms are likely to contribute significantly to the core of the profile. Due to the extended wings of the Lorentzian it is generally advisable to consider both broadening contributions, even when the Lorentzian HWHM is narrow in comparison to the Gaussian.

2.2.2 Evaluating the Voigt Profile

The joint contributions due to thermal and pressure broadening are modelled using a Voigt profile. This is a convolution of the Gaussian and Lorentzian profiles, given as

$$f_{\nu}(\nu - \nu_0) = \int_{-\infty}^{\infty} f_G(\nu' - \nu_0) f_L(\nu - \nu') d\nu'. \quad (37)$$

The issue of how best to evaluate the Voigt profile is a well known problem in the field. The profile must be calculated accurately and quickly for a wide range of Lorentzian and Gaussian profiles for potentially millions of transitions. The two parameters used for generating the profile are

$$u = \frac{\nu - \nu_0}{\gamma_G} \quad (38)$$

$$a = \frac{\gamma_L}{\gamma_G} \quad (39)$$

where u is the distance from the profile centroid and a is the ratio of the Lorentzian and Gaussian widths⁴⁷. To be able to calculate the Voigt function accurately u must be evaluated over many orders of magnitude to encompass the relevant temperature and pressure region.

The Voigt function is given as

$$f_{\nu}(\nu, \gamma_G, \gamma_L) = H(a, u) \quad (40)$$

⁴⁷ Zaghoul (2007)

where as above γ_G and γ_L are the widths of the Gaussian and Lorentzian widths and ν denotes wavenumber. Here,

$$H(a, u) = \frac{1}{\pi} \int_{-\infty}^{\infty} \frac{ae^{-t^2}}{(u-t)^2 + a^2} dt. \quad (41)$$

From formula 7.4.13 in⁴⁸

$$\int_{-\infty}^{\infty} \frac{ye^{-t^2}}{(x-t)^2 + y^2} dt = \pi \text{Rw}(x + iy), \quad (42)$$

⁴⁸ Abramowitz and Stegun (1964)

where

$$w(z) = e^{-z^2} \text{erfc}(-iz), \quad (43)$$

where erfc is the complimentary error function

$$\text{erfc}(z) = 1 - \text{erf}(z), \quad (44)$$

where erf is the error function

$$\text{erf}(z) = \frac{2}{\sqrt{\pi}} \int_0^z e^{-t^2} dt. \quad (45)$$

From this we can see that

$$f_\nu(\nu, \gamma_G, \gamma_L) = \text{Rw}(u + ia) \quad (46)$$

The function $w(z)$ is known as the Faddeeva function and here is calculated using the Faddeeva package⁴⁹. The characteristic width of the Voigt function is investigated by⁵⁰. Using coefficients from this work I define the Voigt width γ_V with the approximation

$$\gamma_V \approx 0.5346\gamma_L + \sqrt{0.2166\gamma_L^2 + \gamma_G^2}. \quad (47)$$

This Voigt width is used in later sections to approximate the width of the combination of the two profile types.

Several numerical methods have been proposed to compute the Voigt profile accurately and efficiently over different regions of parameter space⁵¹. I implement the Voigt profile using a method based on the complex error function or Faddeeva function⁵². This is a fast and accurate method with the relevant libraries publicly available. In this work I use the Faddeeva package from S. G. Johnson (2012). The Faddeeva package includes *Algorithm 916* from Zaghoul and Ali (2011) which is also employed in Grimm and Heng (2015) and found to be fast and effective. I find this package gives computational speeds of less than 2 ms per profile. I use a sampling rate of 6 points per Voigt width, which is much finer than my required final resolution. I evaluate the Voigt profile to 500 Voigt widths around the centroid to accurately capture the information in the Lorentzian wings, as the derived cross sections are critically dependent on this evaluation width. (Rising to 1000 Voigt widths at pressures of 1 atm and above.) This is discussed in more detail in Section 2.4.2.

⁴⁹ S. G. Johnson (2012)
⁵⁰ Olivero and Longbothum (1977)

⁵¹ Schreier (2011)

⁵² S. G. Johnson (2012)

Ngo et al. (2012) shows that there is some deviation in reality from the Voigt profile in real atmospheric broadening through comparisons with experimental data on pressure broadening. This is due to the change in velocity of the broadening agent particle by the collision with the broadening agent. This affects the profile shape, the width of the profile and shifts the line in wavelength. Here I have used only the standard Voigt profile and have not investigated further in terms of profile shape. It would be possible to change to a more sophisticated profile and regenerate molecular cross sections if it were found to be an important factor. These deviations due to the velocity of the particles undergoing collisions are of the order of a few percent and I do not expect a more physically accurate Voigt profile shape to impact my results.

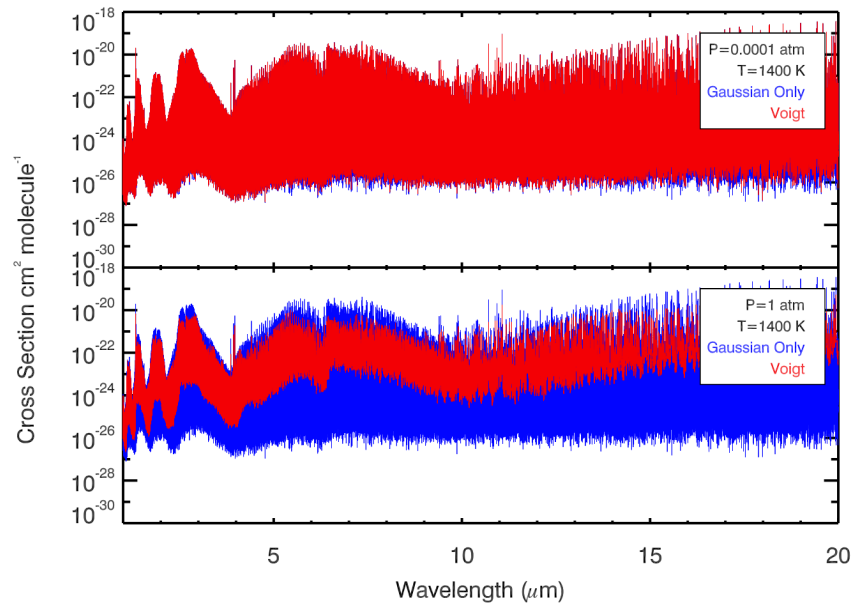


Figure 2.2: Comparison of purely thermally-broadened H_2O cross sections (blue) with cross sections including both thermal and pressure broadening using a Voigt profile (red) at the native line spacing of 0.01 cm^{-1} . A combination of the two broadening types brings extensive wings from the Lorentzian component which brings up the level of the continuum.

Figure 2.2 shows a comparison between cross sections for H_2O generated with only thermal broadening and those generated with a full Voigt profile including both thermal and pressure broadening. It is clear that the Voigt profile has a significant effect on the low intensity lines, and increases the overall continuum of the molecular cross sections, especially where pressure is high.

2.2.3 Availability of Broadening Parameters

Pressure broadening parameters are not yet readily available for all molecules of relevance to exoplanet atmospheres, despite their critical importance.⁵³ The parameters required for computing pressure broadening are the Lorentzian HWHM (γ_L) for the required broadening agents and the temperature-scaling parameter (n) for each line in the line list (as shown in Equation 36). These parameters are hard to determine. In recent years, significant efforts have been dedicated towards generating pressure broadening parameters for exoplanetary applications, particularly with a focus on broadening molecules such as H_2 . Useful parameters for important molecules can be found in works such as Li et al. (2015) and Faure et al. (2013), where pressure broadening coefficients are made available.

Theoretical calculations of pressure broadening parameters are time consuming and not well understood for a wide range of molecules or broadening agents, particularly at high temperatures. Methods have been explored by⁵⁴ and used to generate the HITRAN database. For example, Complex Robert-Bonamy (CRB) calculations are used as discussed in⁵⁵, where values are also verified experimentally. Molecular line lists in the HITRAN data base do contain pressure broadening parameters for self-broadening and air-broadening, but are typically relevant only to low temperature atmospheres ($\sim 300 \text{ K}$). For high temperature exoplanet atmospheres pressure broadening data is still scarce. This is particularly true for H_2 -rich atmospheres, which are the most observable. Typically, state-of-the-art line lists such as ExoMol are computed under zero pressure conditions.

⁵³ Freedman, Marley, and Lodders (2008); Freedman et al. (2014)

⁵⁴ Gamache et al. (1997); Gamache, Laraia, and Lamouroux (2011)

⁵⁵ Gamache, Lynch, and Neshyba (1998); Gamache et al. (2012)

In this work I use only air and self broadening provided by HITEMP and HITRAN and the PS 1997 list for water from Partridge and Schwenke (1997), which contains H₂ broadening⁵⁶. I focus on H₂O as it is the most well studied molecule currently available with a large variety of line list sources and three different broadening molecules available to test: H₂O, N₂ and H₂. H₂O is one of the best measured molecules in exoplanet atmospheres to date.

⁵⁶ Partridge and Schwenke (1997)

Where values are not available we are forced to turn to experiments and other line list sources. Where detailed, line-by-line pressure broadening values are not available from ExoMol I use the mean of pressure broadening values available from other sources (e.g. HITRAN) and apply this to every line. While this approach is not ideal, in some cases it is the only option. For example, the YT10to10 line list for CH₄ is has high completion and is valid at high temperatures, making it a useful asset for modelling of exoplanet atmospheres. However, it does not include line-by-line pressure broadening parameters. The CH₄ HITRAN list has line-by-line pressure broadening values but only a small fraction of the molecular transitions and is only valid at room temperature. In this case I apply the mean of the HITRAN broadening parameters to the YT10to10 list to estimate the effect of broadening with on CH₄ at high temperatures. I refer to this approach as taking ‘mean broadening’ parameters. I will discuss the consequences of this compromise in Section 2.5.2. Table 2.1 shows which molecules have detailed broadening available and which only have mean broadening. For each case where detailed broadening parameters are available a mean case has also been investigated in order to make a comparison.

2.3 GENERATING CROSS-SECTIONS

I compute molecular cross sections over a wide range of pressures (P) and temperatures (T) relevant for exoplanet atmospheres. My grid in P-T space is shown in Table 2.2. For each point in P-T each cross section will usually be calculated multiple times, using different broadening parameter or line lists source. Interpolation could be used on the cross sections if a cross section was required between these points. Interpolation between the nearest pressure and temperature values is discussed in⁵⁷. In this section, I describe the procedure I use to compute cross sections.

⁵⁷ Hill, Yurchenko, and Tennyson (2013)

2.3.1 Line Intensities and Partition Functions

The generation of cross sections requires the intensity of each transition to be accurately calculated. Most line list databases give Einstein coefficients for each transition with degeneracies and energies for each state. These can be converted into line intensities as showed in Rothman et al. (2013). The line intensity is given by

$$S_{i,j}(T_{ref}) = \frac{A_{i,j}}{8\pi c \nu_{i,j}^2 Q(T_{ref})} g_i e^{-hcE_j/k_B T_{ref}} (1 - e^{-hc\nu_{i,j}/k_B T_{ref}}) \quad (48)$$

where $A_{i,j}$ is the Einstein coefficient for spontaneous emission for the transition between states i and j , g_i is the upper state degeneracy, E_j is the lower state energy in cm^{-1} and $\nu_{i,j}$ is the transition frequency between i and j , also in cm^{-1} and finally h is Planck’s constant. Here, $Q(T_{ref})$ is the partition function at the required reference temperature. When an intensity is given at a reference temperature, usually 296 K, it can be converted to an intensity at any temperature using

$$S_{i,j}(T) = S_{i,j}(T_{ref}) \frac{Q(T_{ref})}{Q(T)} \frac{\exp(-hcE_j/k_B T)}{\exp(-hcE_j/k_B T_{ref})} \frac{[1 - \exp(-hc\nu_{i,j}/k_B T)]}{[1 - \exp(-hc\nu_{i,j}/k_B T_{ref})]}. \quad (49)$$

This gives the intensity of a transition in units of $\text{cm}^{-1}/(\text{molecule cm}^{-2})$.

As shown in equations 48 and 49 the partition function scales the line intensities. The partition function gives a measure of the number of the molecules of a gas are

Molecule	Source	Broadening Agent	Max T (K)
H ₂ O	BT ₂ ¹	Self, Air	3000K
H ₂ O	HITEMP ²	Self, Air	4000K
H ₂ O	HITRAN ³	Self, Air	296K
H ₂ O	PS (1997) ⁴	H ₂	-
CO ₂	HITEMP	Self, Air	4000K
CO ₂	HITRAN	Self, Air	296K
CO	HITEMP	Self, Air	4000K
CO	HITRAN	Self, Air	296K
OH	HITEMP	Self, Air	4000K
OH	HITRAN	Self, Air	296K
NO	HITEMP	Self, Air	4000K
NO	HITRAN	Self, Air	296K
CH ₄	YT10to10 ⁵	Self, Air	2000K
CH ₄	HITRAN	Self, Air	296K
NH ₃	BYTe ⁶	Self, Air	1600K
NH ₃	HITRAN	Self, Air	296K
HCN	Harris ⁷	Self, Air	4000K
HCN	HITRAN	Self, Air	296K
C ₂ H ₂	HITRAN	Self, Air	296K

Table 2.1: Molecules used to generate cross section database and all line list sources, including which broadening agents are given. (Note HITRAN is recommended at room temperature of 296K.) Here I choose many different sources to compare the effect that completion has on my final cross sections.

- 1 Barber et al. (2006)
- 2 Rothman et al. (2010)
- 3 Rothman et al. (2013)
- 4 Partridge and Schwenke (1997)
- 5 Yurchenko and Tennyson (2014)
- 6 Yurchenko, Barber, and Tennyson (2011)
- 7 Harris et al. (2006)

T (K)	300	400	500	600	700	800	900
-	1000	1200	1400	1600	1800	2000	2500
-	3000	3500					
P (atm)	0.0001	0.001	0.01	0.1	1	10	100

Table 2.2: Pressure-Temperature grid for cross sections. Values between these points could be interpolated by the user to allow a finer grid. These points have been chosen as they represent observable temperatures and pressures of currently known exoplanets.

in the ground state compared with all other states. This ratio of state populations increases with temperature, as it becomes more likely to find particles in higher energy states. This is intrinsically linked to the energy of each transition, which makes the partition function unique for each molecule. The partition function is given by

$$Q(T) = \sum_j g_j e^{-E_j/k_B T} \quad (50)$$

where g_j is the lower state degeneracy and E_j is the lower state energy as described in Eq. 48. To calculate a partition function in this way the spectral information of the molecule must be complete. Missing transitions result in an inaccurate partition function, which will not be representative (especially at high temperatures). Information on how partition functions are calculated for ExoMol can be found in Tennyson and Yurchenko (2012). Errors in the partition function may cause discrepancies that are small when considering individual cross sections at particularly high temperatures. Models of atmospheres require cross sections at many different temperatures to be included in computing the final spectrum. This allows for different temperatures and pressures as a function of height in the atmosphere. This will cause any errors in the cross section from the partition function to become compounded by many layers of an inhomogeneous atmosphere.

In this work, partition functions have either been adopted from existing databases or computed using the TIPS code⁵⁸. The ExoMol database provides partition functions for use with each molecular line list. The HITRAN database uses the TIPS code to create partition functions between 70K-3000K. There can be some discrepancies between partition functions from different sources, particularly at high temperatures. I use extrapolation to find the partition function values at higher temperatures. In my case this only affected my highest temperature point of T=3500K. At this temperature many of the line lists are unreliable and incomplete. I use this temperature point only as an edge case for atmospheric modellers and do not recommend trusting it as much as the lower temperature points.

Using a line list at a temperature greater than recommended by the source is possible using the partition function. At low temperatures many transitions are low intensity and can be ignored without greatly effecting the final result. However, as temperature increases these low intensity lines begin to contribute more considerably. Low intensity lines become much stronger as these states populate at high temperatures. Any lines that are omitted (because of an incomplete list) begin to significantly affect the cross section. Because of this, errors in the cross section can arise if line lists are used above their recommended temperatures. (These temperatures are given in the last column of Table 2.1.) With the exception of NH₃ and CH₄, the ExoMol and HITEMP line lists provide coverage up to and beyond the temperature grid used in this work. The HITRAN sources, used primarily for earth applications, are only valid at room temperature.

⁵⁸ Fischer et al. (2003)

Wavenumber Range [cm^{-1}]	Grid spacing $\Delta\nu$ [cm^{-1}]
10-100	10^{-5}
100-1000	10^{-4}
1000-10000	10^{-3}
10000-30000	10^{-2}

Table 2.3: Table from Hill, Yurchenko, and Tennyson (2013) giving the staggered spacing of the grid for used for line mapping. Here I present an alternative adaptive grid spacing which is given in Equation 51.

2.3.2 Cross-Sections from Line Intensities

Cross sections are derived from line intensities by first broadening with the appropriate profile. This is followed by binning the result to the desired spectral resolution. This allows the cross section to be easily manipulated and read into atmospheric codes quickly. This is a general approach followed by several recent studies⁵⁹, albeit with minor differences in implementation. Here I discuss my implementation. The differences from other works are discussed in Section 2.4.

⁵⁹ Hill, Yurchenko, and Tennyson (2013)

Computing the cross sections from line intensities involves three steps as follows, for a given temperature (T) and pressure (P). Firstly, the Voigt profile (f_ν) is computed at a high resolution in order to accurately evaluate each individual line profile, as described in Section 2.2.2. The spacing of this fine grid, here referred to as the ‘sub-grid’, is given as

$$\Delta\nu = \frac{\gamma_\nu(\nu = 500, T, P, m)}{6} \quad (51)$$

where $\gamma_\nu(\nu = 500, T, P, m)$ is the HWHM of a Voigt profile at $\nu = 500 \text{ cm}^{-1}$. This samples each Voigt width with 6 points. I find this provides the resolution and accuracy necessary with optimal computational speed, as discussed in more detail in Section 2.4. This sub-grid spacing is a function of T, P and molecular mass, making it specific to the molecule concerned.

Secondly, the cross section is computed at each point on the sub-grid described above for every spectral line. The cross section $\sigma(\nu)$ of a transition between states i and j at a certain pressure (P) and temperature (T) is given by

$$\begin{aligned} \sigma_{i,j,P,T}(\nu) &= S_{i,j,P,T} \frac{f_\nu(\nu)}{\int_{-\infty}^{\infty} f_\nu(\nu) d\nu} \\ &\approx S_{i,j,P,T} \frac{f_\nu(\nu)}{\int_{\nu_{i,j} - \frac{\Delta\nu_c}{2}}^{\nu_{i,j} + \frac{\Delta\nu_c}{2}} f_\nu(\nu) d\nu} \end{aligned} \quad (52)$$

in units of $\text{cm}^{-1}/\text{molecule}$ where $S_{i,j,P,T}$ is the line intensity and $f_\nu(\nu)$ is the Voigt function with broadening parameters corresponding to the line at the given P and T. $\nu_{i,j}$ is the wave number of the line centre and $\Delta\nu_c$ is the extent of the profile to which the line wings are evaluated. For a given line I use a $\Delta\nu_c$ value of 500 Voigt widths (250 around the line centroid), which I find to be optimal, as discussed in Section 2.4. The integral is evaluated up to this cut off and normalises the profile. Evaluating up to this cut off effectively folds in the intensity from the missing wings that are not evaluated back into the profile, ensuring no intensity is missed.

Finally, the high-resolution cross section described above is binned to a final cross section grid. This has a coarser spacing for saving on storage space. The final cross section grid spacing is still high resolution at 10^{-2} cm^{-1} which corresponds to a resolution of R=100,000 or greater. When a lower resolution cross section grid is desired, this high-resolution grid can be binned down further in frequency-space or wavelength-space as required. The mid points between adjacent bins are selected and all values within these bounds are averaged, giving the binned down contribution at each wavelength on the grid.

In this work I apply a cut in intensity to only evaluate high intensity lines. This method is also adopted in the field⁶⁰. This provides a reduction in computation time with minimal effect on accuracy; very low intensity lines contribute little to the final cross section even at high resolution. I apply a cut off at $10^{-30} \text{ cm}^{-1}/(\text{molecule cm}^{-2})$ in intensity across all line lists, with the exception of BYTe and YT10to10 line lists for NH_3 and CH_4 respectively. Due to their large size the cut off was increased to $10^{-26} \text{ cm}^{-1}/\text{molecule cm}^{-2}$.

⁶⁰ Rothman
et al. (2013)

2.4 OPTIMAL RESOLUTION AND CUT OFF OF BROADENING PROFILE

A high resolution grid is needed to accurately sample the contribution from the broadening profile. However, a high resolution also influence the computational cost. It is desirable to adopt the coarsest grid possible while obtaining enough accuracy, to ensure a reasonable computation time. Several recent studies have adopted different prescriptions for the grid, in the particular context of molecular cross sections for exoplanetary applications⁶¹. In this section, I systematically investigate the effect of both the profile grid resolution and extent of the profile wings on the cross sections to determine optimal values for these parameters.

⁶¹ Hill, Yurchenko,
and Tennyson (2013);
Grimm and
Heng (2015)

2.4.1 Effect of Profile Grid Resolution

In this work I present a grid resolution that is adaptive with the equivalent width of the Voigt profile for a given transition. This is given in Eq 47. This approach allows for optimal computational time while ensuring high accuracy of the cross sections. In this formulation the grid in frequency space I use to evaluate the Voigt profile (sub-grid) is defined by Eq. 51. Evaluating this spacing at $\nu = 500 \text{ cm}^{-1}$ gives a conservative estimate of the width of a Voigt profile where the Gaussian component is narrowest. (See Equation 35.) This also corresponds to a wavelength of $20 \mu\text{m}$ which is the longest wavelength of interest in the present work. This is the upper wavelength limit of the infrared observations of exoplanet atmospheres for instruments such as MIRI on JWST. The necessary grid spacing can become very wide at high pressures ($P \gtrsim 1 \text{ atm}$) where the equivalent width of the Voigt profile becomes large. Therefore, I place an upper-limit of 0.01 cm^{-1} on the grid spacing. The grid can become no coarser than this.

This spacing is coarser than that used in some previous studies, but is optimised for computational time and accuracy in computing cross sections. For example the spacing used in Hill, Yurchenko, and Tennyson (2013), as shown in Table 2.3 and referred to here as a staggered grid, is finer than the grid employed here. This is in part due to that work concerning only thermal broadening where their profile is Gaussian and much narrower requiring finer grid spacing to accurately assess. Figure 2.3 shows a comparison between the spacing of my adaptive grid and the staggered grid for a representative temperature of 1000 K. Both grids are much finer than the Voigt width for each pressure case, (upper panel). While a fine grid spacing gives highly accurate profiles using the staggered grid can lead to unnecessarily high resolution, especially in the limit of high pressures where the profiles become inherently very broad. This can be computationally expensive particularly for high pressures. The grid I propose in Eq. 51, referred to here as an adaptive grid as its spacing with changes in pressure, uses fewer points at higher pressures to overcome this problem while preserving the accuracy.

To create an accurate cross section we need to accurately represent the transition. The broadening profile must have a normalised area of 1. This ensures we neither underestimate or overestimate the contribution of the transition. To normalise the profiles I compute the area under the curve using a simple trapezium rule. When a profile is only sparsely evaluated this approach will tend to a greater area estimation, producing a lower intensity contribution from each line profile after normalisation.

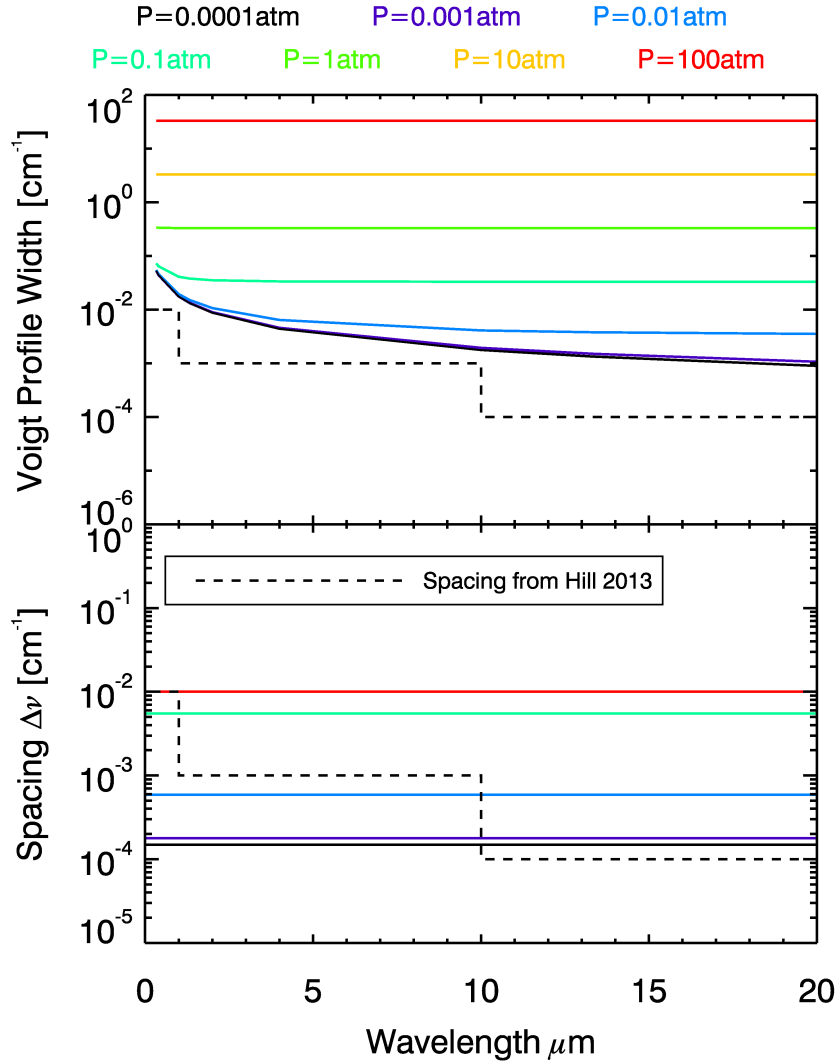


Figure 2.3: Comparison of grid spacing in my adaptive grid with that in the staggered grid from Table 2.3 of Hill, Yurchenko, and Tennyson (2013) for different pressures. Top: The coloured lines show the Voigt profile widths at different pressures and a representative temperature of 1000 K. The staggered grid spacing is shown in dashed line for reference, demonstrating that the grid spacing is well below the Voigt profile width for pressures down to 10^{-4} atm. Bottom: The coloured lines show the adaptive grid spacing I use. For high pressures (≥ 1 atm), the minimum spacing is fixed at 10^{-2} cm^{-1} as profiles become very broad. While my grid spacing is coarser than the staggered grid spacing for high pressures the resultant effect on the cross sections is small, as shown in Fig. 2.4. Note that a single value of broadening width and temperature scaling has been adopted for this figure.

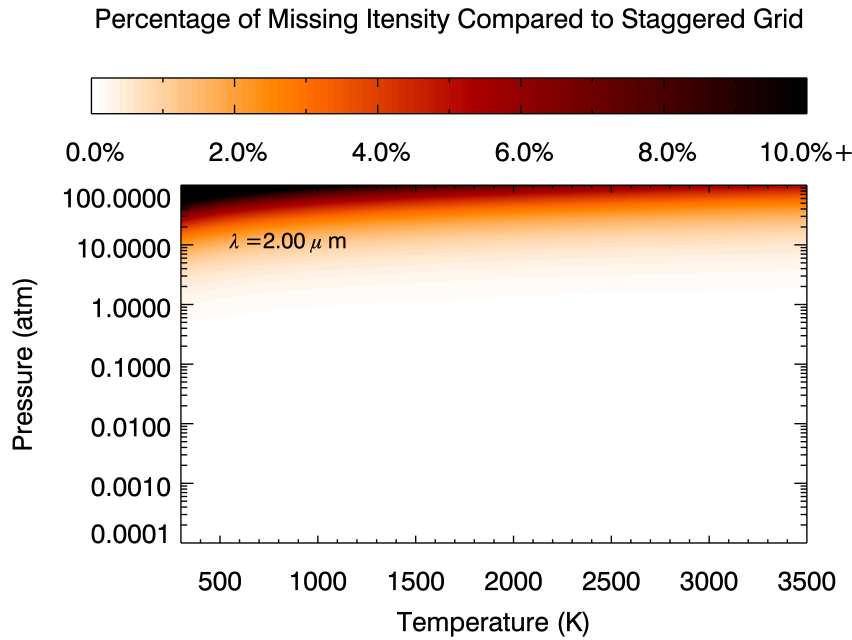


Figure 2.4: Comparison of adaptive grid with staggered grid from Table 2.3 . Voigt profiles are mapped to a fine grid from equation 51. The integrated area under the profile for the adaptive case is compared with that for the staggered case to produce this result. Only pressures of ~ 100 atm are affected significantly by the resolution of the adaptive grid beyond a few percent. Below 1 atm the difference is $\approx 0.2\%$ or less.

This results in a small percentage of “missing” intensity. To test the validity of my approach I analyse this amount of missing intensity in a single profile when calculated using the adaptive grid compared with the finer, staggered grid from Hill, Yurchenko, and Tennyson (2013). This is done for each T and P point. The results are shown in Figure 2.4.

In order to test my adaptive grid and how well it approximates the Voigt profile it is compared with the staggered grid using a wide cut off of $\Delta\nu_c=100\text{ cm}^{-1}$ wavenumbers for each pressure and temperature case. Here I take one profile per T and P point and map to each grid. The profiles are generated in the same way as in section 2.2.2. Any difference in the profiles will effect the integrated area, which is used for normalisation. I consider the staggered grid to be high enough resolution in all cases that it will produce an accurate area estimation. The comparisons have been conducted over a range of wavelengths but here I select a representative wavelength of $\lambda = 2\mu\text{m}$ for illustration. The difference in the final output of these grids is very small, with $\lesssim 0.2\%$ of intensity missing at $P < 1$ atm. At $P=10$ atm a maximum of 2% of the original intensity is missed at low temperatures. The largest differences found are $\sim 10\%$ for pressures of 100 atm. I find that in such cases the cut off chosen $\Delta\nu_c$ is too narrow for the extreme case of $P=100$ atm. Such high pressures are not directly observable for exoplanet atmospheres, based on this difference I recommend that pressures of $\gtrsim 10$ atm are not used. For the 10^{-4} to 10 atm pressure range I find the adaptive grid to be very accurate, particularly after binning to the final output grid with a spacing of 0.01 cm^{-1} which corresponds to a spectral resolution of $R=10^5$ - 10^6 at $\lambda < 10\text{ }\mu\text{m}$.

2.4.2 Effect of Profile Evaluation Width

In order to accurately account for the contribution of the line wings the broadening profile must be evaluated over a wide enough range centred on the line centre. However, due to computational efficiency this must be finite. The edge up to which the profiles are evaluated is referred to here as a cut off value ($\Delta\nu_c$), as discussed in section 2.3.2. This cut off value determines the extent of evaluation of the profile as well as its normalisation as described in Eq. 52. The choice of $\Delta\nu_c$ has already been noted in the field as an important factor in computing cross sections⁶². A common approach is to apply a cut off in wavenumber, with values ranging between 10 and 100 cm^{-1} , especially for high pressures as discussed by Sharp and Burrows (2007). Another approach is to take a number of Lorentzian widths from the centroid such as in Grimm and Heng (2015). However this does not take into account the full width of the profile after its convolution with the Gaussian component. I employ a cut off in multiples of Voigt widths, given by Eq 51 and implemented in Eq 52. The $\Delta\nu_c$ in this approach adapts with both the Lorentzian and Gaussian components, ensuring that the wings of the profile are accounted for in an adaptive manner depending on the broadening conditions.

⁶² Sharp and Burrows (2007); Grimm and Heng (2015)

Based on my investigation I find 500 Voigt widths to be sufficient for current applications, including JWST-like resolutions and VLT applications, with small uncertainties. $\Delta\nu_c$ is increased to 1000 Voigt widths at pressures of 1 atm and above as the pressure broadening increases. Several cut off values have been investigated to establish the optimal balance between accuracy and computational time. As discussed above, I use multiples of Voigt widths to establish a cut off that adapts to the specific profile. When using too few Voigt widths lower intensity lines are underestimated. This is due to the lack of additional intensity from the wings of high intensity neighbours. The underestimation in the profile wings is 10% for H_2O at the native spacing. However, this underestimation is confined to the lowest intensity transitions with high intensity neighbours, which are by their nature confined within high intensity features.

2.5 EFFECT OF PRESSURE BROADENING ON CROSS SECTIONS

In this section I systematically investigate the errors introduced in molecular cross sections by various parameters and assumptions involved in implementing pressure broadening. I focus on the H_2O molecule, which has the most complete line list and broadening data currently available for exoplanet atmospheres. I investigate the dependence of the cross sections on the following key factors: (a) pressure and temperature, (b) average versus line-by-line treatment of broadening parameters, (c) spectral resolution (i.e. binning) of the cross sections, and (d) broadening agent.

The effect of pressure broadening on cross sections as a function of pressure and temperature is shown in Figure 2.5. In general, an increase in temperature will mute the absorption features. This is due to the lower transitions becoming more populated. As pressure is increased, the broadening becomes much stronger due to the wide Lorentzian. This causes a smoothing of the whole curve. Figure 2.5 shows the cross sections at a resolution that is evenly spaced in frequency. By converting this into a resolution that is reflective of future instruments I can quantify the change we might expect to observe due to pressure broadening.

2.5.1 Definition of Change Due to Broadening

The cross sections for any molecule can span many orders of magnitude over a given spectral range and features vary drastically with wavelength. Because the cross section is so varied defining a robust metric to quantify the error is challenging. For example, a simple metric such as a 'mean difference' across the entire spectral range

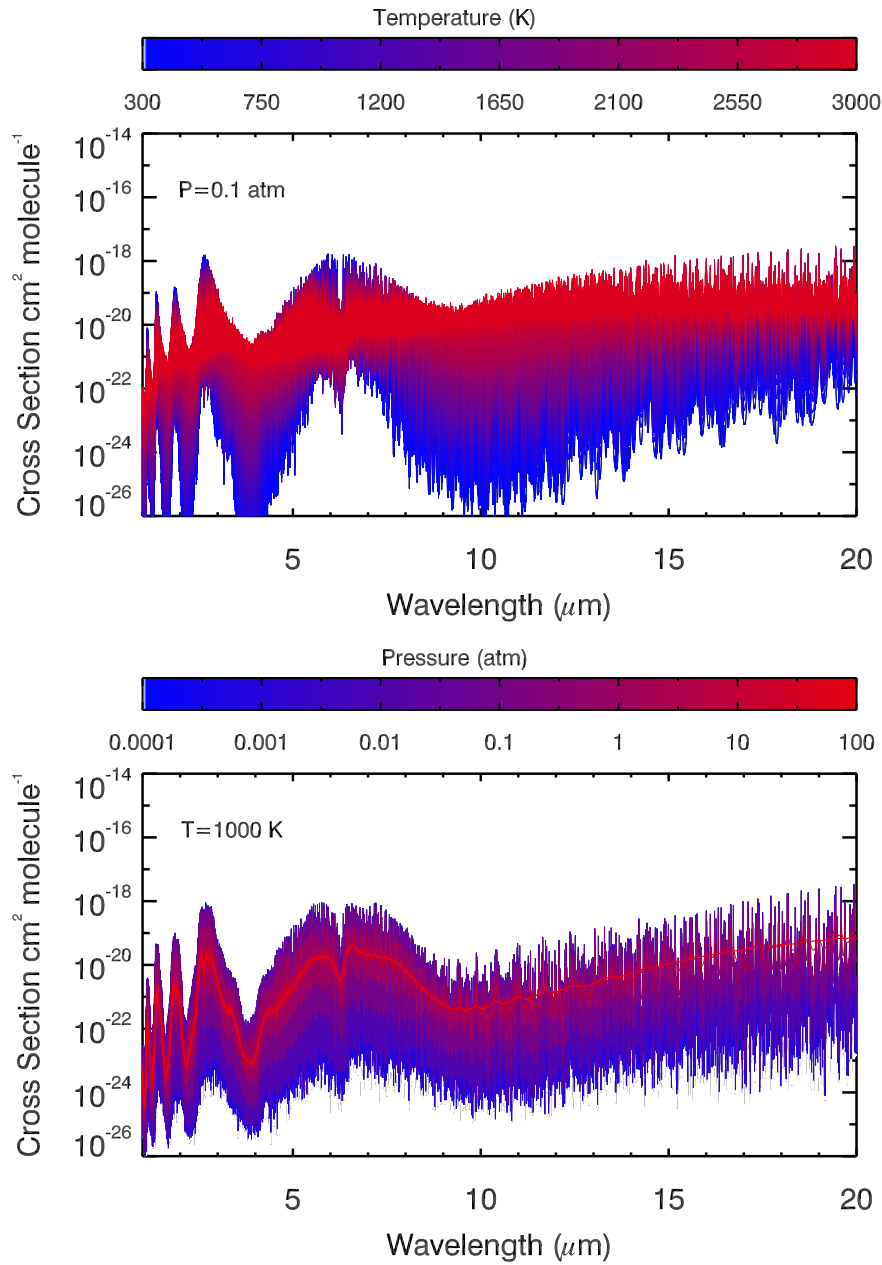


Figure 2.5: Cross sections for H₂O at various temperatures and pressures using air broadening at a grid spacing $\Delta\nu$ of 0.1 cm^{-1} wavenumbers.

available is often skewed by one or two errant lines. On the other hand, focusing on lines with maximum error places undue emphasis on the lowest intensity lines, which will see the highest fractional change. Conversely, focusing on the highest intensity lines is unreliable because they are not representative of the line population. I use the median percentage difference across the entire spectral range as my metric of choice to quantify the change in cross sections due to any aspect of broadening. The median percentage change in cross section for each line is defined as

$$\delta = \text{Median} \left\{ \frac{\sigma - \sigma_0}{\sigma_0} \right\}_\lambda \times 100 \quad (53)$$

where σ_0 and σ are the cross sections before and after incorporating the particular pressure broadening prescription, and the median is evaluated for cross sections computed over the entire wavelength range of interest, 0.5 - 20 μm .

2.5.2 *Line-by-line versus Mean Broadening Parameters*

As currently there is a lack of line-by-line broadening parameters for several molecules it is often unavoidable to rely on sparse broadening data when computing pressure broadened cross sections, as discussed in section 2.2.3. In such cases broadening parameters are available only for a few lines or only at certain temperatures. In this work values for the broadening parameters are based on the available data and the mean value is applied across all the lines. In this section I investigate the difference such an approach makes to the cross sections overall compared to cases where broadening parameters are available for all the lines.

For purposes of demonstration, I use the latest line list of H_2O from the HITEMP database which includes line-by-line broadening parameters with air broadening. In one case, I calculate H_2O cross sections over a wide range of temperatures and pressures using detailed line-by-line values for the air-broadening parameters. In another case, I adopt constant values for the broadening parameters averaged over the entire line list and apply those values for broadening every line. The median percentage difference in the cross sections derived from the two cases with a grid spacing of 0.01 cm^{-1} is shown in Figure 2.6. At this resolution I find that using mean broadening values can result in cross sections that are inaccurate by up to 20% for observable pressures (~ 0.1 bar) and low temperatures ($T \lesssim 500 \text{ K}$), where pressure broadening is strongest. For lower pressures and higher temperatures the effect is less pronounced. For lower resolutions, the differences reduce. Therefore, when numerous lines are available to calculate representative average values for the broadening parameters the mean treatment of pressure broadening is a reasonable approximation.

Figure 2.6 shows this difference to decrease as pressure increases. In high pressure cases the broadening becomes wide enough such that many profiles begin to overlap. This effectively smooths the information and causes the differences in profile shapes to be less distinguishable. From Figure 2.5 this effect is more clear. We see at high pressures much of the information from the individual transitions is lost. This effect occurs at pressures greater than 0.1 atmospheres implying that for high pressures of $P \gtrsim 1$ the detailed broadening parameters for each transition may not affect cross sections as much. However at high pressures there are other problems, such as the cut off width discussed above.

2.5.3 *Effect of Spectral Resolution*

One of the most important questions that can be answered in this work is how the difference created by pressure broadening to molecular cross sections is influenced by spectral resolution. I use H_2O as my case study and consider cross sections in the HST G141 bandpass (1.1-1.7 μm). This has a significant water feature (see Chapter 3 for more detail on HST and water absorption). Observations of exoplanetary

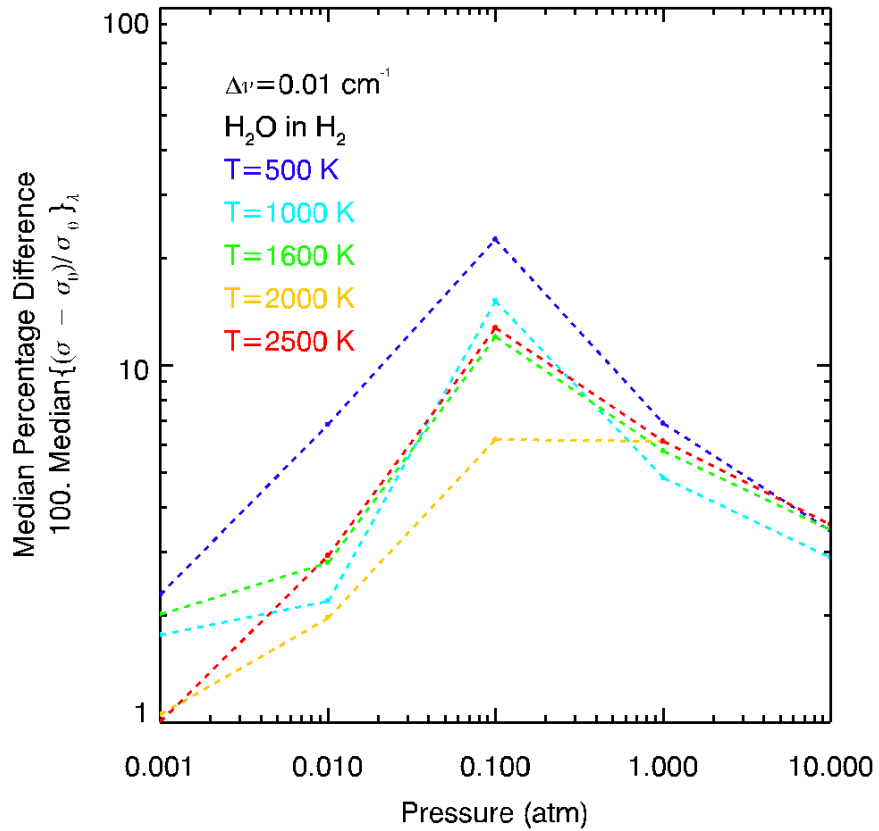


Figure 2.6: Effect of mean versus detailed pressure broadening. The curves show comparisons between cross sections obtained using mean values for all the line broadening parameters versus those obtained using detailed line-by-line broadening parameters. These results are for the highest-resolution spacing of 0.01 cm^{-1} , corresponding to a resolution of $10^5\text{-}10^6$ at $\lambda < 10 \text{ }\mu\text{m}$.

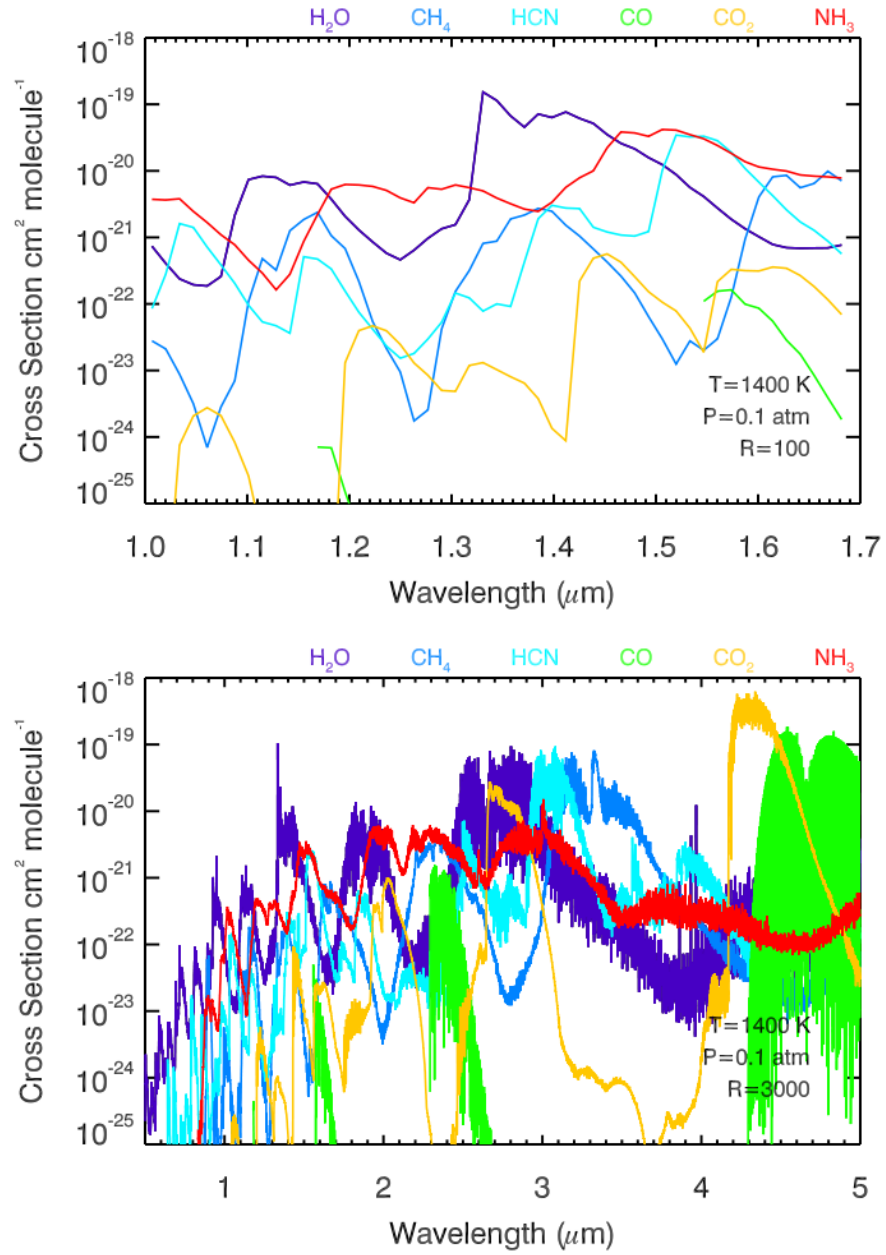


Figure 2.7: Comparison of molecular cross sections in the WFC3 G141 bandpass and the NIR-Spec bandpass at HST-like and JWST-like resolutions, respectively. The cross sections are generated using air broadening for all the molecules. Degeneracies between the specific molecule, the abundance of the molecule and the temperature can be harder to break at lower resolutions, however JWST's improved wavelength and resolution will help break these degeneracies in future.

spectra are conducted over a wide range of spectral resolution, ranging from broad-band photometric observations and low resolution spectra ($R \lesssim 100$). Resolution can greatly influence how an observed spectrum can be interpreted and can break the degeneracies between the presence of different molecules. For illustration, Fig. 2.7 shows molecular cross sections of several molecules binned to the spectral ranges and resolutions achievable with HST (WFC3 G102 and G141 grisms, $R \sim 100$) and JWST (NIRSpec, $R \sim 3000$). At the higher resolution of JWST it is much easier to break the degeneracies and identify molecules. The longer spectral range from JWST gives more potential to search for molecules.

In this section I discuss the effect resolution has on δ as a function of pressure and temperature. I find that at the highest resolutions and lowest temperatures ($R=10^5$ and $T=500\text{K}$) pressure broadening can introduce a difference to the final cross section of $\delta=1000\%$ for $P=0.1$ atm. For lower resolutions of $R=5000$, similar to those that will be attainable with JWST, the differences become much smaller. However at low temperatures ($T=500\text{K}$) and high pressures ($P=1$ atm) a δ of 40% is found for H_2 broadening at $R=5000$. For low resolution spectra ($R \lesssim 100$) of exoplanets, that are possible with current instruments, for representative exoplanetary temperatures ($T=500\text{K}-2500\text{K}$, $P \lesssim 1$ atm) and H_2 rich atmospheres, I find the median difference in cross sections to be $\lesssim 1\%$.

Figure 2.8 shows δ as a function of P and T . I find that δ increases with increasing resolution, reaching differences up to 100% or higher for $R \gtrsim 10^4$, $P \gtrsim 0.1$ atm, and $T \lesssim 500$ K. For example I find that at a nominal pressure of 1 atm δ can be as high as 100% for $R \approx 10^4$ or more, as shown in the upper panel of Figure 2.8. For the highest resolutions possible today of $R \sim 10^5$, $\delta \gtrsim 100\%$ even for pressures as low as 0.1 atm.

Similarly, the lower panel of Figure 2.8 shows the variation in δ with temperature for a nominal pressure of 1 atm, showing δ can be very high ($\gtrsim 100\%$) for $T < 1000$ K for $R > 10^4$. Consequently, I find that it is very important for atmospheric models to include pressure broadening when interpreting high-resolution spectra ($R \gtrsim 10^4$) of exoplanet atmospheres observable with current and upcoming facilities (e.g. VLT, Keck, and E-ELT). Otherwise, the derived molecular abundances will be limited by a minimum uncertainty of more than 100% due to inaccurate cross sections. For $R < 10^4$, δ is reduced reaching a maximum of $\sim 10\%$ for pressures of relevance to exoplanetary atmospheric observations of $P \lesssim 0.1$ atm. Figure 2.9 shows many slices across these plots with both H_2 broadening and self broadening. Self broadening has a larger effect on the cross sections than H_2 broadening, as discussed in section 2.5.4.

2.5.4 Effect of Broadening Agent

Another important factor in pressure broadening is the primary broadening agent in the planetary atmosphere. As shown in Eq.36, the broadening agent governs the Lorentzian HWHM of the broadening profile. Molecular line lists containing pressure broadening data, e.g. HITRAN or HITEMP, typically contain data for self and air as the broadening agents, motivated by the terrestrial applications which HITRAN was originally intended for. However, for giant planetary atmospheres H_2 is the dominant broadening agent and is of particular relevance for studying atmospheres at high spectral resolution and photometric precision. Accurate line-by-line H_2 broadening data for high temperatures are still elusive for most molecules of interest though a few molecules have data available, particularly for H_2O ⁶³ and more recently for CO ⁶⁴.

Here, I investigate the effect of broadening agent on the median accuracy of molecular cross sections for a representative case. I consider the case of H_2O for which I have line-by-line broadening parameters with H_2 , self, and air as broadening agents⁶⁵. To illustrate the differences made by changing the broadening agent I have used cases where the molecule is broadened only by a particular molecule self, air, or H_2 (i.e. the partial pressure is 1 in each case). Figure 2.10 shows the median percentage difference in cross sections caused by each of the three scenarios com-

⁶³ Partridge and Schwenke (1997)

⁶⁴ Li et al. (2015)

⁶⁵ Partridge and Schwenke (1997)

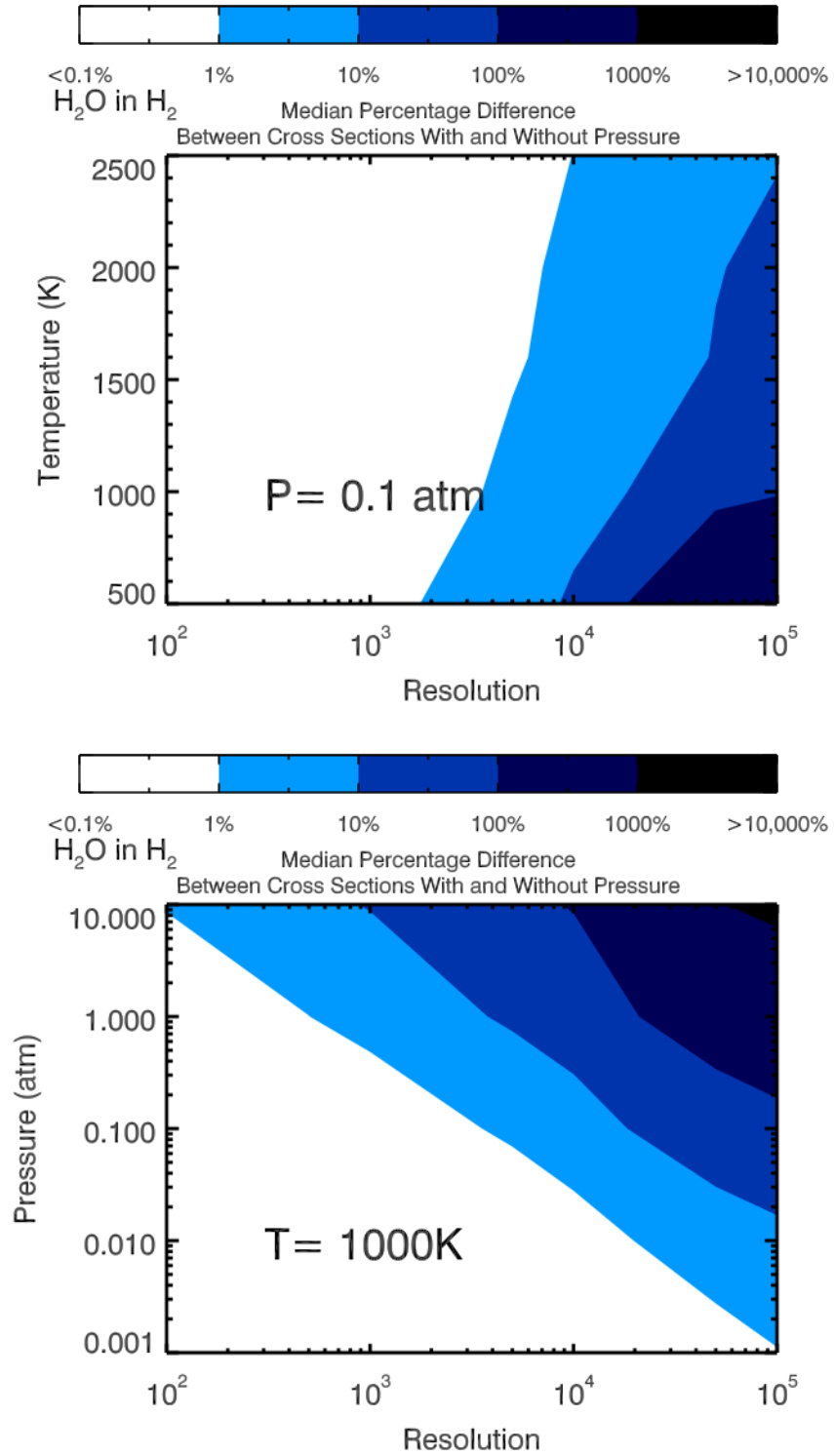


Figure 2.8: Effect of resolution on median difference between H_2O cross sections when pressure broadening is included compared with a Gaussian-only case across the WFC3 band pass range of 1-1.7 μm . Here I show H_2O broadened by H_2 though stronger broadening can be achieved using self broadening as discussed in section 2.5.4. (Note: Here the individual points of the T,P and R grid have been linearly interpolated over for plotting purposes. Hill, Yurchenko, and Tennyson (2013) discusses interpolation between temperature and pressure points.)

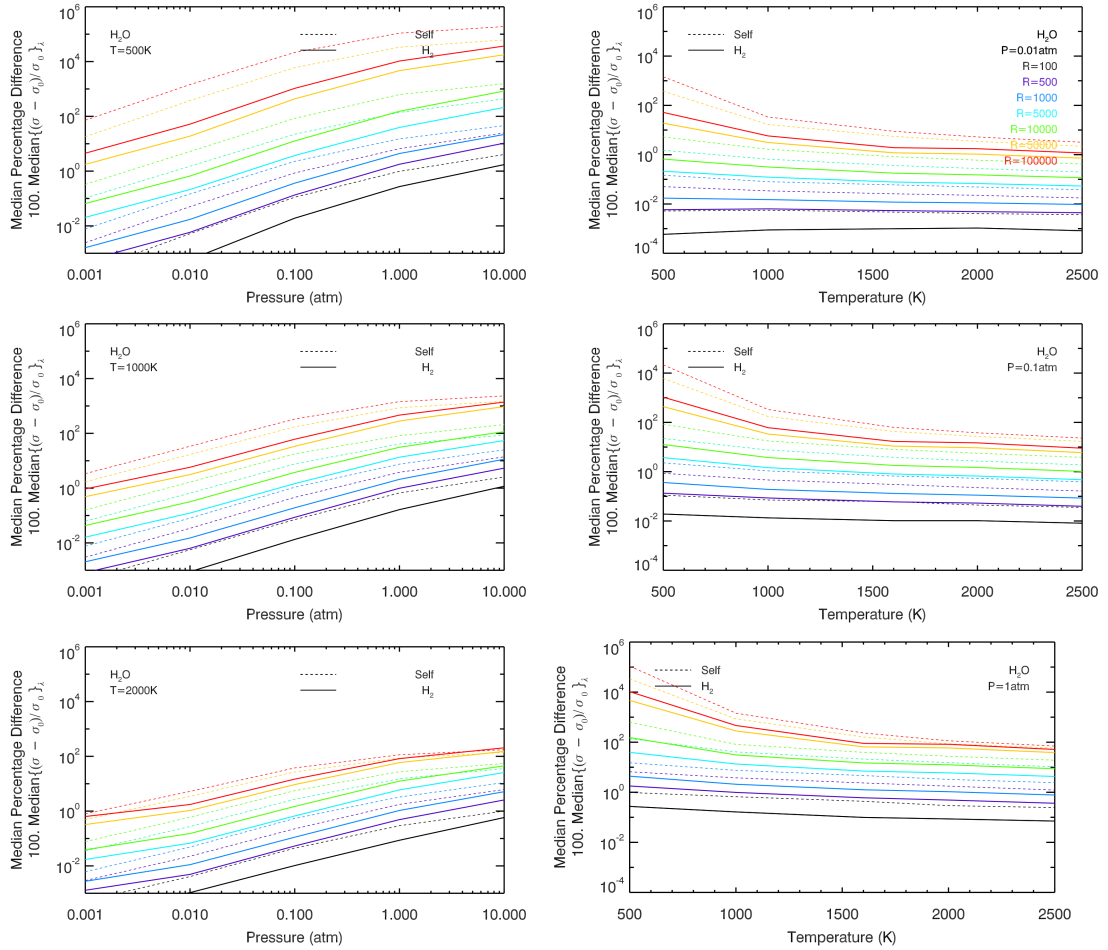


Figure 2.9: Effect of resolution at different temperatures and pressures on H₂O cross sections in the WFC₃ bandpass. Median percentage difference between cross sections evaluated including pressure and cross sections evaluated with a Gaussian-only, thermal broadening. At high resolutions, high pressures and low temperatures there is the largest change to cross section. At the highest resolution of R=100,000 the median difference can be more than 1000% for H₂ broadening. I see that H₂ broadening of H₂O is consistently weaker than self broadening. Resolutions of between R=100 and R=100,000 are shown in colours given by the top right panel.

pared to Gaussian-only broadening for an illustrative case with resolutions of 10^4 and 10^5 and $T = 500$ K.

Figure 2.10 shows that it is important to carefully choose broadening agents before generating cross sections for different planet types. Firstly, self-broadening can cause significantly higher δ values compared to air or H_2 broadening at observable pressures ($P \sim 0.1 - 1$ atm). Secondly, the differences between H_2 broadening and air broadening are relatively small in the H_2O case. Therefore, while modelling H_2 -rich atmospheres in the absence of any H_2 broadening data for H_2O molecules, though not ideal, it is more advisable to use air broadening than self broadening. When modelling atmospheres of low-mass exoplanets, e.g. super-Earths that can have volatile-rich atmospheres such as H_2O -rich or CO_2 -rich atmospheres, it is important to use cross sections that are generated with the appropriate broadening agent. For example, for H_2O -rich atmospheres self-broadening of H_2O should be considered in the cross sections rather than air broadening.

There are wide ranges of temperatures and pressures in exoplanet atmospheres that are accessible to current and upcoming observations. This will present a new challenge and line-by-line broadening parameters are required in molecular line lists for different broadening agents. In particular, there is a critical need for high-temperature ($\gtrsim 500$ K) H_2 broadening data. The most observable atmospheres are those of hot and giant exoplanets with H_2 -rich atmospheres, for which very high resolution spectra ($R \sim 10^5$) are also currently being reported. In the mean time, it is advisable to use air broadening where available for such atmospheres. While not ideal, air broadening provides closer cross section estimates to H_2 broadening for H_2O . It is also an improvement on incorporating no pressure broadening at all.

A realistic atmosphere will contain many different molecules, contributing broadening from many different species. For smaller planets I expect atmospheres that are more complex, containing more massive molecules with high abundance. This will effect the pressure broadening particularly as the partial pressure will no longer be 1 and there will be contributions from many species. In such cases I expect the contribution to vary depending on the abundance of more massive broadening molecules with greater pressure broadening parameters. My current work gives an estimate for the most extreme cases of H_2O or H_2 dominated atmospheres.

2.6 EFFECT OF PRESSURE BROADENING ON TRANSMITTANCE

A thorough investigation of the effect of pressure broadening on fully modelled exoplanetary spectra is non-trivial and beyond the scope of the present study. Many factors such as the inhomogeneous P-T structure and composition of the atmosphere will determine the final spectrum. Nevertheless, as a simpler exercise, here I asses the effect of pressure broadening on the transmittance through an atmosphere represented by a uniform column of gas. As in other parts of this study, I use H_2O as the only absorbing species and consider pressure broadening in a H_2 -rich atmosphere.

Cross sections are used in atmospheric codes to determine the resultant intensity transmitted through a column of gas. Usually, the column will undergo some changes in pressure, temperature, and number density over the length of the column. These factors combine to give an optical depth τ_λ where

$$\tau_\lambda = \int_{z_1}^{z_2} n \sigma_\lambda dz \quad (54)$$

where z is length through the column, n is the abundance (number density) of the molecule and σ_λ is the cross section which is a function of wavelength. The abundance of a molecule is determined by the temperature and pressure of the column by the simple gas law

$$P = nk_B T. \quad (55)$$

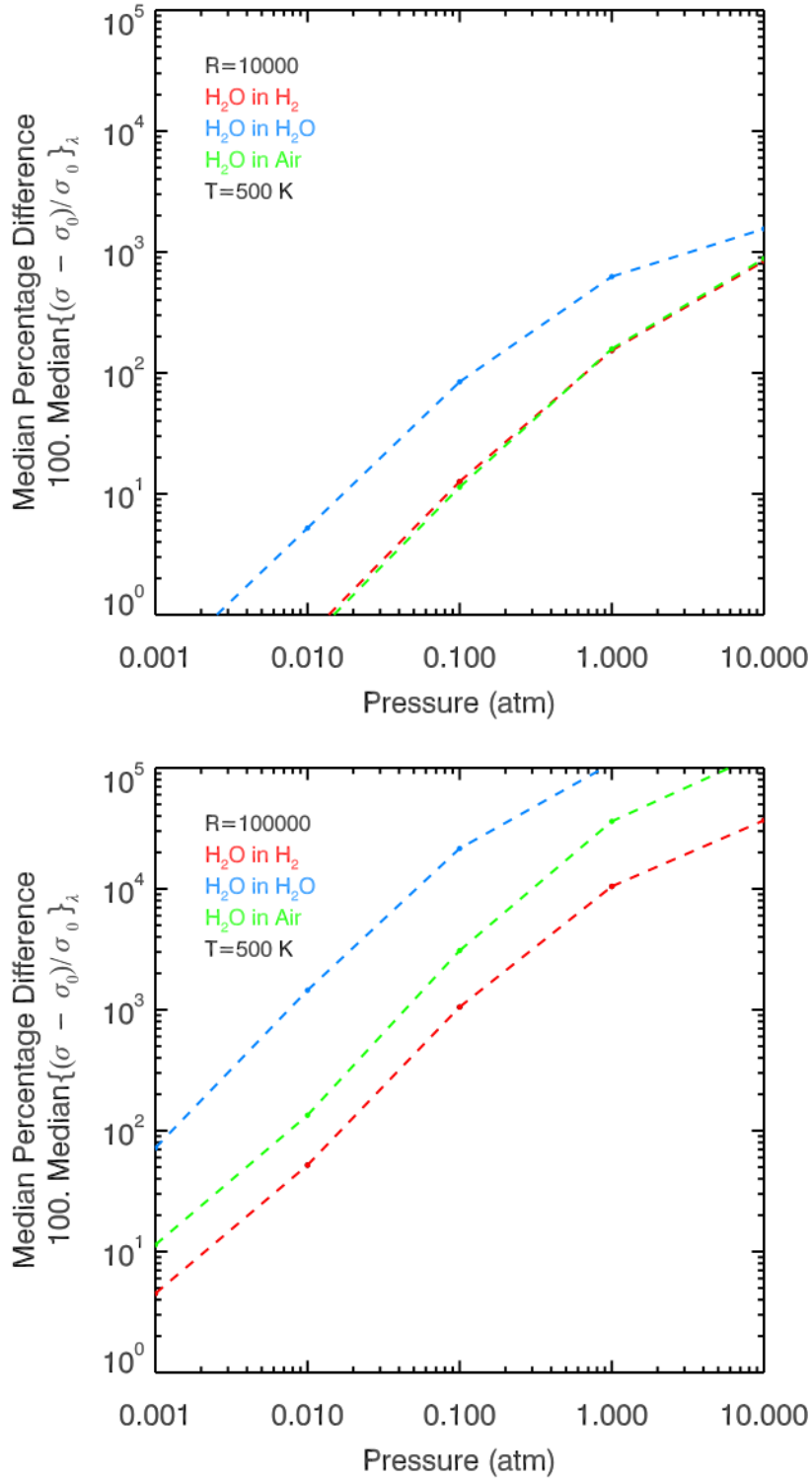


Figure 2.10: Effect of broadening agent on cross sections. The curves show median difference pressure broadening induces when compared with Gaussian-only cross sections when broadening agent is changed. Here the H_2O molecule is considered at $R=10,000$ and $R=100,000$ at a temperature of 500 K, chosen since lower temperatures provide the highest effect from pressure broadening. The figure illustrates that self broadening is 400% stronger on average than H_2 broadening and that air and H_2 broadening are comparable in magnitude.

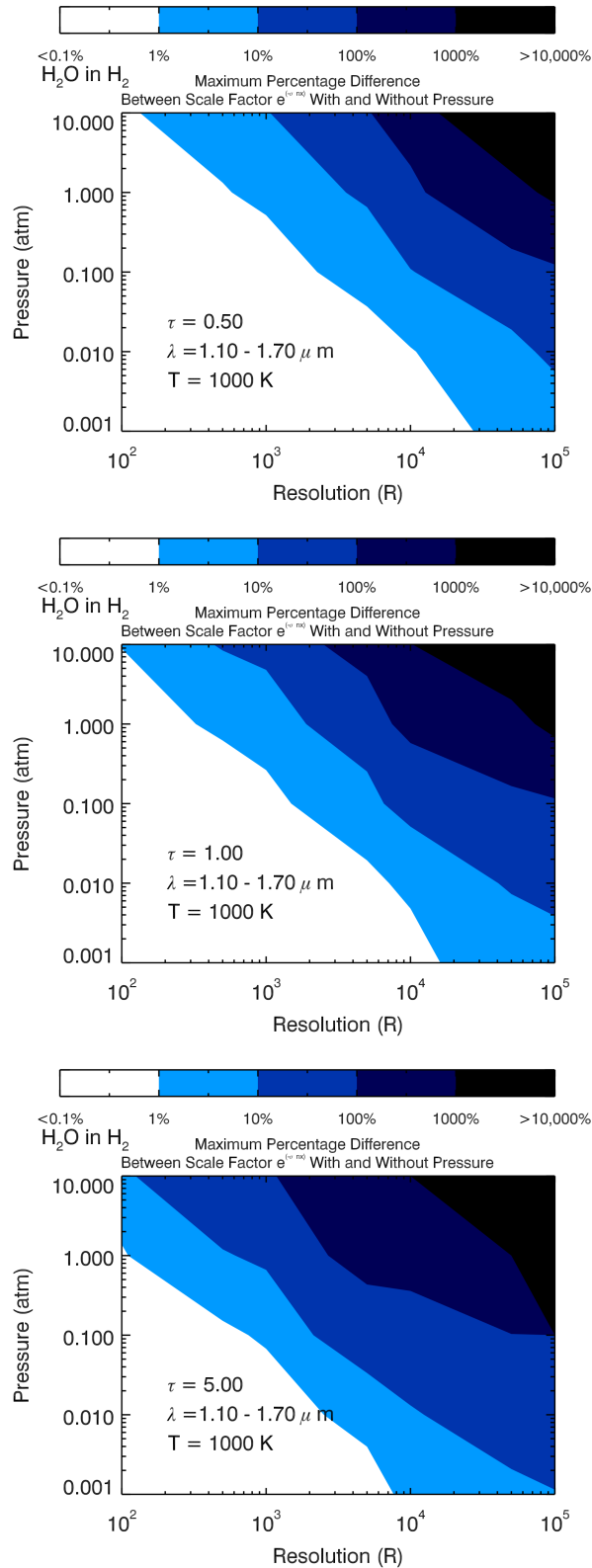


Figure 2.11: Effect of pressure broadening on the transmittance in an idealized atmosphere (see section 2.6). The contours show the maximum percentage difference in transmittance, i.e. the scale factor $e^{(-n\sigma x)}$, induced by considering cross sections with pressure broadening versus those with Gaussian-only thermal broadening in the HST WFC3 bandpass. The relative difference is shown for a wide range in key parameters: pressure (P), spectral resolution (R), and maximum optical depth in the WFC3 bandpass (τ); a nominal temperature of 1000 K is chosen for illustration but the general temperature-dependence is discussed in section 2.6. Here the individual points of the T,P and R grid have been linearly interpolated over for plotting purposes Hill, Yurchenko, and Tennyson (2013)

The optical depth gives a measure of how much intensity will be transmitted through a column of gas based on these properties. For a source intensity ($I_{0\lambda}$), the resultant intensity (I_λ) at the end of the column is given by

$$I_\lambda = I_{0\lambda} e^{-\tau_\lambda}, \quad (56)$$

where the scale factor $e^{-\tau_\lambda}$ is the transmittance.

In order to make a meaningful comparison between the effects of altering the cross section on emergent intensity as a function of pressure and temperature I choose to fix τ to a single value. Here, I assume the column of gas to be at a given constant pressure and temperature, and hence constant density. The length of the column is allowed to vary in order to contain the same τ regardless of pressure and temperature. As τ is also a function of wavelength its value alters depending on the particular molecular feature. To fix τ I take the value at the peak of the water feature near $1.4 \mu\text{m}$ in the WFC3 band. If only the cross section σ_λ is changed, between a pressure broadened case $\sigma_{1\lambda}$ and an unbroadened case $\sigma_{2\lambda}$ which will each have intensities $I_{1\lambda}$ and $I_{2\lambda}$, I can then find the effect pressure broadening has on the transmitted intensity. This is given as

$$\frac{I_{1\lambda} - I_{2\lambda}}{I_{2\lambda}} = \frac{e^{-\int_{z_1}^{z_2} n \sigma_{1\lambda} dz} - e^{-\int_{z_1}^{z_2} n \sigma_{2\lambda} dz}}{e^{-\int_{z_1}^{z_2} n \sigma_{2\lambda} dz}} \quad (57)$$

As I assume a gas of the same number density at each pressure and temperature point then I can assume

$$A = \int_{z_1}^{z_2} n dz = n x \quad (58)$$

where x is some distance scale. Substituting this I find

$$\Delta I_\lambda = \frac{I_{1\lambda} - I_{2\lambda}}{I_{2\lambda}} = (e^{-A(\sigma_{1\lambda} - \sigma_{2\lambda})} - 1). \quad (59)$$

Using the cross section across the WFC3 bandpass of $1-1.7\mu\text{m}$ and binning down to a given resolution I can find the difference to the transmittance of the column of gas as a function of wavelength. As discussed above, the length of the column is fixed such that the maximum optical depth of the column in the given bandpass equals a fixed parameter (τ), for a given density corresponding to a given temperature and pressure. I can then alter τ to investigate the optically thin and optically thick regimes as functions of pressure and temperature. I note that the change induced in transmittance (ΔI_λ) across a given bandpass is higher at wavelengths with higher absorption, which are also of the wavelengths of interest to observations. I therefore consider the $\max(\Delta I_\lambda)$ in the WFC3 bandpass as my metric of choice in evaluating the effect of pressure broadening on transmittance in that bandpass. This does not take into account how signal to noise might affect taking such observations as zero transmittance ($e^{-\tau}$) implies no signal; however, here I consider only values of $e^{-\tau}$ (which can have values between 0 and 1) that are greater than 0.01.

The effect of pressure broadening on the transmittance in my idealised column of gas is similar to the effect on cross sections discussed in previous sections. Figure 2.11 shows the fractional difference pressure broadening makes to the transmittance as a function of several key parameters: the optical depth (τ), pressure (P), and resolution (R). A temperature of 1000 K is chosen for illustration. For low resolutions ($R \lesssim 100$), ΔI_λ is $\lesssim 1\%$ across for almost the entire range of parameters of relevance to exoplanet atmospheres, particularly for $P < 1 \text{ atm}$, $T = 500 - 3000 \text{ K}$, and $\tau < 5$. This shows a very low impact of pressure broadening in these regions.

ΔI_λ is higher for higher resolutions. Considering $\tau < 1$, $P < 0.1 \text{ atm}$, and $T > 1000 \text{ K}$, I find a maximum ΔI_λ in the WFC3 band to be 6% for a JWST-like medium resolution of $R = 5000$, and 75% for a VLT-like very high resolution of $R = 10^5$.

This approach is simplistic as clearly it does not factor in the the changes that could happen within the column in temperature and pressure however this does give us a first approximation of the difference induced by changing cross sections

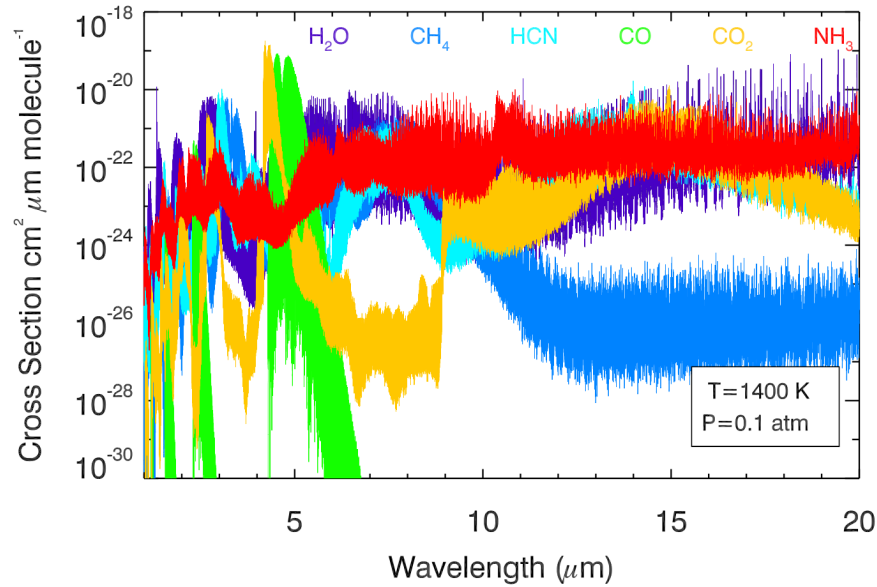


Figure 2.12: Absorption cross sections of molecules in my database for a representative $T=1400$ and $P=0.1$ at a resolution of 0.01 cm^{-1} wavenumbers, using air broadening, with the same relative abundances. Such cross sections have been generated for all the molecules over a wide range of P and T using different sources of line lists and broadening molecules. Sources are listed in Table 2.1.

on observations of transmission spectra of exoplanet atmospheres. In reality, light travels through many layers of an exoplanetary atmosphere, with different temperatures, pressures, and densities, before reaching the observer. The results above will hold for a specific pressure but full spectral models of exoplanet atmospheres, both for transmission spectra and emission spectra, are required for a comprehensive investigation of the effect of pressure broadening discussed in the present work.

2.7 CROSS-SECTION DATABASE

In this work I present a range of cross sections for H_2O , CO_2 , CO , CH_4 , NH_3 and HCN from a range of sources shown in Table 2.1. These have been investigated with detailed, line-by-line calculations of the Voigt profile with pressure and thermal broadening simultaneously included which no other database to date provides. The cross sections span a temperature range of 300K - 3500K and pressures of 10^{-4} to 10^2 atmospheres. Finally the cross sections have been created in a variety of resolutions.

The data in this work benefits not only from the addition of a further dimension of pressure with an accurate broadening profile, but also in being generated uniformly with the same code across molecules. This ensures low and consistent systematic errors across my data. The full database is represented in Figure 2.12. I intend to publish the cross sections used in this work on an online database for use by anyone, with pressure included. I have also developed a small web applet to view the data and pick out which molecules absorb strongly in certain regions, allowing optimal observation windows to be found.

2.8 DISCUSSION AND SUMMARY

In this work I present a systematic and quantitative investigation of the effects of various aspects of pressure broadening on molecular cross sections. These directly im-

pact modelling efforts of exoplanet atmospheres. I use H₂O as my primary molecule of choice for this investigation, as it has the most complete absorption line data. The factors I investigate include the resolution and evaluation width of Voigt profiles, pressure versus thermal broadening, broadening agent, spectral resolution, and completeness of broadening parameters. I investigate in detail the effect of pressure broadening, both on absorption cross sections under varied conditions and on the transmittance of a transmittance in a simple 1D gas cube. I use the optimal methods resulting from this investigation to systematically and homogeneously generate a library of pressure-broadened absorption cross sections. These span a wide range of temperature, pressure, and spectral resolution for a variety of molecules relevant for exoplanet atmospheres.

This study allows us to address the question of the inaccuracies introduced to molecular absorption cross sections from pressure broadening, both in the context of current and future observational capabilities. As new instruments come online with improved specifications we will have access to a wealth of high resolution data on exoplanet atmospheres. The interpretations of these data sets will be impacted by basic model inputs, such as cross sections. The comparisons presented here show in detail the magnitude of the errors I can expect in these fundamental inputs to atmospheric models across a range of parameters.

To generate cross sections I follow a prescription of mapping line intensities broadened by an appropriate function to a fine 'sub-grid' which finely samples the profile of the line. This is iterated over each transition from the source and binned to an output grid with a lower resolution, for further use. The lines are broadened by either a Gaussian-only model, (which uses only thermal broadening,) or a Voigt profile, (which combines the Gaussian thermal and Lorentzian pressure broadening,) evaluated using the Faddeeva package⁶⁶.

When evaluating the Voigt profile on a grid there are two clear sources of error. Firstly, the grid spacing may be too wide, leading to a poor normalisation and misrepresenting the line transition intensity. Secondly, the wings of the profile may be cut off prematurely, leading to small fractions of intensity from the wings being missed. This is aggravated by the range of intensity values, which span many orders of magnitude within a narrow wavenumber range. This leads to the wings of isolated high intensity profiles affecting the continuum level of low intensity neighbours greatly. This continuum can be underestimated when a cut off is too narrow.

I present a method of accurately evaluating the Voigt profile on a fine grid that produces minimal errors in the final cross section at resolutions of interest. This is achieved with a spacing that is adaptive based on temperature and pressure. The grid I adopt is found to be as accurate as the grid from Hill, Yurchenko, and Tenynson (2013) to within ~0.2% at pressures of 1 atm or less. This grid gives a vast saving on computational time, particularly for high pressures. I pair this grid with a cut off value, $\Delta\nu_c$, of 500 Voigt widths (raised to 1000 above pressures of 1 atm). $\Delta\nu_c$ describes the separation around the wavenumber centroid of the line transition up to which the Voigt profile is evaluated. Having investigated a range of values at different resolutions I find 500 Voigt widths to be sufficient both to provide good normalisation for the profile and to evaluate far into the extensive Lorentzian wings. When compared with other values of $\Delta\nu_c$ from literature I find my value to be more accurate (10-100%) at low pressures ($P=0.1 - 0.001$ atm) due to the Voigt width adapting with both temperature and pressure as the Gaussian and Lorentzian components change. This combination of $\Delta\nu_c$ and an adaptive grid provides low errors for all resolutions discussed in this work up to $R=100,000$. I find errors of less than 1% (averaging ~0.2%) in the final cross sections at the peaks of transition features. This increases to 10% within transition features at very low intensity, however I find such transitions to be less likely to significantly effect observations and modelling results. Beyond this resolution it may be wise to increase $\Delta\nu_c$ and use a finer sampling of the profile.

66

S. G. Johnson (2012)

In some cases broadening parameters for all lines are unavailable. A mean approach has been tested, where literature broadening parameters for a few lines are averaged and applied to each profile. I find that, when taken across a wide wavelength range, the differences between cross sections generated in a line-by-line manner and those with a mean broadening parameter applied is up to 20%.

I have investigated the influence of different broadening agents on the cross sections, using H₂O as a case study. The broadening agents are air, (N²), H₂ and self broadening, which is H₂O in this case. Generally, self broadening is significantly stronger than H₂ broadening by about a factor of 4 on average across the range of pressure, temperature, and resolution. For H₂ broadening I see a smaller effect on cross sections than that due to self broadening or air broadening.

H₂ is the dominant component for giant exoplanet atmospheres that are most amenable to spectroscopy. Information on this broadening agent is currently unavailable for many molecules. I find air broadening produces a closer result to H₂ broadening.

I find the effect of pressure broadening to be varied depending on the resolution, pressure and temperature. I choose to measure the change induced to H₂O cross sections due to pressure broadening using the median percentage difference. This provides a reasonable estimate of the characteristic difference, though it is possible to induce higher changes for specific lines. Generally, the differences are larger for higher resolutions, higher pressures, and lower temperatures. For low resolution spectra of exoplanets that are possible with current instruments ($R \lesssim 100$), I find this error to be small. For representative exoplanetary temperatures ($T = 500\text{K} - 2500\text{K}$, $P \lesssim 1$ atm) and H₂ rich atmospheres I find the median difference in cross sections introduced by various aspects of pressure broadening (δ) to be $\lesssim 1\%$. For higher resolutions ($R \lesssim 5000$), including those attainable with JWST, I find that δ can be up to 40%. For very high resolution spectra ($R \sim 10^5$) pressure broadening can introduce much larger errors. For low temperatures ($T \lesssim 500\text{K}$) $\delta \gtrsim 100\%$, reaching $\gtrsim 1000\%$. Such a case could be found with instruments such as CRIRES on the VLT (and in the future E-ELT) if cool H₂-dominated targets were observed. For hotter targets of $T = 2000\text{K}$ this reduces to 15%.

Even with very high resolutions current hot Jupiter targets with temperatures of 800K-2500K will not be greatly effected by differences induced from pressure broadening at pressures of $\lesssim 0.1$ atm. A more significant change is found at pressures of 1 atm or above, though current observations of exoplanet atmospheres typically probe pressures below 1 atm⁶⁷. Data on cool targets at high resolution is currently a distant future prospect and we are unlikely to be affected by this level of uncertainty in the near future. However, even with the lower temperature end of hot Jupiter targets ($T \sim 1000\text{K}$) and modern day instruments such as the VLT pressure broadening can cause discrepancies in the cross section of 30-200% for H₂ dominant atmospheres with $P = 0.1 - 1$ atm.

A great deal of work has already been done on obtaining spectra for exoplanet atmospheres using the VLT (for example Snellen et al. (2010); Brogi et al. (2012); Birkby et al. (2013); de Kok et al. (2013)) and in that work line profiles themselves can be resolved. This work would impact inferences made on exoplanet atmospheres with CRIRES. Additional work is needed to assess whether the data from the VLT is sufficient to observe pressure broadening in exoplanet atmospheres.

Molecular cross sections are degenerate with abundance in atmospheric models and any error in cross sections results in an uncertainty in abundance measurements. From this work I find that for cool targets ($T \sim 500\text{K}$) at high resolutions ($R \gtrsim 10^5$) I would expect uncertainties in the abundance measurements of at least 100%. This is purely from the cross section inputs to atmospheric models over those that do not include pressure broadening for H₂ dominated atmospheres. A true spectrum involves many cross sections from an atmosphere with many layers of temperature and pressure and an observation through many optical depths which will compound

67

Madhusudhan (2012)

this difference. For a true estimation of the difference pressure broadening will make to abundances full, rigorous atmospheric models are needed.

A final investigation has been undertaken to assess the difference including pressure broadening in cross sections makes to the transmitted intensity through a uniform column of gas, as a function of the pressure, temperature, spectral resolution, and optical depth. My investigation focused on an idealised column of H₂-dominated gas with H₂O as the only absorber in the HST WFC3 G141 bandpass (1.1-1.7 μm). For low resolutions ($R \lesssim 100$), I find the relative change in transmittance (ΔI_λ) to be $\lesssim 1\%$ across the HST WFC3 G141 bandpass (1.1-1.7 μm) for almost the entire range of parameters of relevance to exoplanet atmospheres. For representative parameters of $\tau < 1$, $P < 0.1$ atm, and $T > 1000\text{K}$, ΔI_λ can be up to 6% for a JWST-like medium resolution of $R = 5000$, and 75% for a VLT-like very high resolution of $R = 10^5$. ΔI_λ can be even higher for higher T, lower T, and larger τ . While for $R \lesssim 5000$ the ΔI_λ are still below $\sim 100\%$, for very high resolutions ($R \sim 10^5$) ΔI_λ can be as high as $\sim 2000\%$.

Ultimately, my work suggests that incorporating pressure broadening to compute molecular cross sections for atmospheric models will be necessary, depending on the desired accuracy in molecular abundance estimates retrieved from spectra. Across all the various factors considered in this work, for low resolution observations ($R \lesssim 100$) of exoplanetary spectra that are currently possible, e.g. with HST, the median differences in cross section induced due to accurate pressure broadening is found to be $\lesssim 1\%$. For medium resolutions ($R \sim 5000$), similar to those possible with JWST, the differences are expected to be at the $\lesssim 40\%$ level. For very high resolution spectra ($R \sim 10^5$), that are possible with current instruments such as CRIFRES on the VLT (and future large ground-based telescopes such as E-ELT), significantly higher differences are possible of 100% or larger, depending on other factors discussed above. In the case of CRIFRES observations in work such as Snellen et al. (2010) this is particularly important as line profiles are combined in that work to improve signal to noise.

With atmospheric characterisation becoming an ever more important part of exoplanet research we can see that pressure broadening will impact us in the future. With medium and high resolution spectra of exoplanets, both hot and cool, we can expect my abundance measurements to be affected in some way. Beyond that we may be able to detect and characterise the pressure in the atmospheres of other planets by finding regions of wavelength space particularly affected and using high resolution spectra. This goal would be difficult to achieve even with a wealth of molecular data at my disposal as signal to noise ratios for such data are likely to be low. The structure and dynamics of a full atmosphere leads to a convolution of many profiles making characterisation of pressure broadening exceedingly difficult. Other factors such as wind speed and Doppler broadening provide further barriers. These will be the ultimate challenges of the future when we will eventually be able to conduct very high resolution spectroscopy of cool low mass exoplanets.

Part III

EXOPLANET AND STELLAR SPECTRA FROM HST WFC₃

The study of exoplanets allows us to uncover the diversity of planets beyond our own. If we are to learn more about these worlds and their ability to host life, we must first understand what they are made from. This can include measuring their temperatures based on their distance from the star, analysing compositions based on their density, observing hot spots using phase curves and measuring the activity of their host star. Understanding the atmospheres of these planets gives astronomers insight into the surface conditions. This can range from analysing the level of haze in an atmosphere, observing a cloud deck or deriving abundances for molecular species⁶⁸. By observing exoplanet atmospheres astronomers can model the different conditions we might expect on planet surfaces, and how that might effect their habitability.

⁶⁸ see; *Sing et al. (2016)*

HST Wide Field Camera 3 has been utilised over the last several years to observe exoplanet atmospheres, with more than 1000 Hubble orbits spent on the endeavour. HST's Wide Field Camera 3 instrument offers coverage in the near-IR above the terrestrial atmosphere, allowing us to observe water without contamination. While its modest resolution ($R \sim 30$) is unable to resolve absorption lines, the long wavelength coverage (1.1 to 1.7 μm) enables a significant water feature to be observed. This window is also free from contamination from other molecules (see Chapter 2). These benefits have lead to over 30 unique exoplanets being observed with HST in transmission in order to assess their water content.

The hottest, largest exoplanets have been chosen as targets for HST, owing to their extended atmospheres. (See Tables 3.1 and 3.2 for lists of the most recent observations for exoplanet atmospheres.) These are planets with no solar system analogues. With the advent of instruments such as JWST, E-ELT and beyond we will push this boundary down to smaller, earth-like planets. To prepare for this new age of detailed exoplanet study we can use the wealth of data we already have at our disposal. We can also identify the best targets for further follow up observations.

In this work I develop a new pipeline to reduce HST WFC₃ observations and compare exoplanets as an ensemble. There are no accepted methods for the reduction of HST WFC₃ spatial scan data in the literature. By creating a pipeline I can 1) uniformly create transmission spectra for all targets, mitigating the same systematics, allowing meaningful comparison 2) investigate the level of systematics in each target to find the best observing strategy 3) create reproducible results with no decisions needed from the user. To do this I have created and improved several reduction steps, including an oversampling technique, removing subpixel shifts and stretches from the detector and improving the divide OOT technique from Berta et al. (2012) (see Section 3.2.2). I have implemented all stages in one code pipeline which can convert quickly any '_ima.fits' files from WFC₃ into transmission spectra with no user interaction.

I create transmission spectra for 30 unique exoplanet atmospheres using archival HST WFC₃ data. This set includes every publicly available WFC₃ IR spatial scan observation of exoplanets to date, with the exception of those that could not be reduced by my pipeline automatically due to multiple sources on the detector, data scanned off the edge of the detector or data without exoplanet transits.

Comparing these planets as an ensemble allows me to correlate exoplanet properties with observational properties and make empirical claims about the strength of water feature in a variety of exoplanet atmospheres. In this work I present a relation between the scale height of the planet, (a metric dependent on the mass and temperature of the planet,) and the observed water feature height. Using this relation I

find that there are 79 excellent candidates for spectroscopic follow up observations with HST with a high probability of a strong water signal ($\gtrsim 200\text{ppm}$). This includes 9 targets with radii smaller than 1 Jupiter radius.

The reduction process for the data is split into three stages. Firstly, the raw data are corrected for systematics on the detector, such as hot pixels, cosmic rays and different pixel areas. Secondly, the position of the source must be assessed in order to accurately stack the individual spectra and create a calibration solution. Finally, the individual light curves are cleaned and normalised. After the final cleaning stages a transmission spectrum can be produced.

In this chapter I will discuss my work in developing a pipeline to process exoplanet atmospheric spectra taken with HST WFC3. I have introduced the concept of exoplanet transmission spectroscopy in Chapter 1. I introduce the WFC3 instrument used for these observations in section 3.1. The corrections I apply to the raw data are discussed in section 4.3. In section 3.3 I propose two methods for correcting for sub-pixel shifts in the source position to produce more accurate stellar spectra. In section 3.4 I discuss the wavelength calibration procedure. I discuss light curve corrections in section 3.5. I introduce three methods to fit the transmission spectra and show the benefits of each in Section 3.6. In Section 3.7 I validate transmission spectra with comparisons to literature results. In Section 3.8 I show the sequence of transmission spectra created in this work and discuss the strength of the water feature.

3.0.1 *A Sequence of Exoplanet Atmosphere Spectra*

Sing et al. (2016) presents a sequence of transmission spectra of 10 hot Jupiter planets. These include full atmospheric retrieval, making a comparative study of their properties such as water abundance, clouds and hazes. Their sample includes data taken with WFC3, Spitzer IRAC and HST STIS covering $0.3\text{--}5\mu\text{m}$. It is their wide wavelength range study allows them to measure the Rayleigh slope from hazes. They show that strong water features are observed in clear atmospheres and weak water features are measured in cloudy and/or hazy atmospheres. They suggest that observing weaker water features in hot Jupiter planets is not due to any depletion or lack of water. It is only due to obscuration by opaque atmospheric clouds and hazes.

In this work I also aim to produce a sequence and compare a large sample of exoplanet atmospheres. However, I will take a different approach; I will use a narrow wavelength from one instrument (WFC3 $\lambda = 1.15 - 1.65\mu\text{m}$) and a large sample of 30 exoplanet transmission spectra to compare exoplanet atmosphere properties. This is a data driven approach, I will not use atmospheric models or infer any clouds or hazes in these atmospheres. Instead I will focus on characterising the strength of the water feature at $1.34\mu\text{m}$. This approach allows me to be free from assumptions of the atmospheric behaviour of exoplanets. I am able to use the WFC3 band pass to create a spectral sequence of exoplanets from water-poor to water-rich, shown in Figure 3.36. Finally, using this ensemble of planets I have shown a trend with the height of the observed water feature and the planetary scale height. This has led to a list of transiting targets with a high probability of a strong water detection for HST WFC3. These final targets are presented in Table 6.1.

3.1 HUBBLE SPACE TELESCOPE

The Hubble Space Telescope (HST) was launched in April 1990 and continues to function today. HST is in a close orbit to the Earth taking 96 minutes to complete one orbit. The near Earth orbit causes data to be missing during the Earth occultation. This can cause problems with observations having large gaps. Observers must be careful when scheduling observations of exoplanet transits to ensure that observations are taken during the ingress, egress and main transit event.

With the telescope being so close to the Earth it has been possible to send 4 service missions to HST. These have enabled the replacement of instruments as well as on-site repairs after electrical failures. The telescope orbits above the terrestrial atmosphere and so the observations are free from seeing, allowing exceptional quality of observations at the diffraction limit. (0.15" for WFC3 G141). Infra-red (IR) observations are also possible without the absorption of the atmosphere, which is particularly important when observing water. Water absorption in the terrestrial atmosphere causes it to be opaque in large fractions of the near IR. This particularly obscures observations of water on other planets when taken through the terrestrial atmosphere. Crucially for this work the terrestrial water signatures do not pollute the data, allowing us to measure water signatures from other planets with no confusion from terrestrial signals.

3.1.1 Hubble Programs and Treasury Data

In this work I use archival data from HST Wide Field Camera 3 (WFC3). There are several large treasury programs with many Hubble orbits on exoplanet host stars during transits. Notably there are proposals 12181 and 14260 from Drake Deming, proposal 13467 from Jacob Bean, proposal 13665 from Bjoern Benneke and proposals 12473 and 14767 from David Sing. These proposals have provided 1123 Hubble orbits on exoplanet observations using the IR detector. Several smaller programs with one off observations of particular planets of interest have also provided exoplanet spectra. This is one of the largest expenditures on a single science goal in the history of Hubble, with the famous Ultra-Deep Field image using only 400 orbits. A list of all of the observations of exoplanet host stars with WFC3 using the spatial scan mode (discussed below) is given in Tables 3.1 and 3.2.

Of all of the HST WFC3 IR spatial scan programs that observed exoplanets 30 exoplanets have been used to use in this work, given in Table 3.1. Any observations taken in stare mode, (see 3.1.3) and any observations where the guidance system failed have been omitted. In this work I have built a set of codes that automatically reduces the data with no input from the user. Because of this, any targets with further complications have been removed from this analysis. This includes targets multiple targets, multiple transits, eclipses or where the data has been scanned off the array. Those datasets that have not been used are given in Table 3.2 with the reason they have been excluded. All the data used in this work are publicly available through the STScI Mikulski Archive for Space Telescopes (MAST) service. The transmission spectra from each of these targets can be found in Section 3.8. The results are available in a spectral sequence based on the height of the water feature in Figure 3.36.

The final 30 planets make a diverse atmospheric properties, larger than any work to date including Barstow et al. (2017), who analysed 10 planets simultaneously. Table 3.1 shows the final list of exoplanet targets used in this work with their proposal numbers and the PI of that proposal. The planets are shown in a mass-radius diagram in Figure 3.1. Regions of Neptunian or Jovian planets have been included based on the regions established in Chen and Kipping (2017), which models a mass-radius relationship for bodies from moons through to stars. The planets in this work cover a range of masses and radii similar to Neptune and Jupiter, probing a range of possible atmospheres.

Table 3.1 shows that most of the newer planets observed in the 14260 treasury program have not yet been published with transmission spectra. This is most likely as the data has only been recently taken. Several of these targets show prominent features in the 1.34 μ m region, which may be from water, including HAT-P-32b, Wasp-52b and Wasp-76b, which are shown in the results section of this work in Figure 3.36.

The number of exposures are shown for each target in Table 3.1. There are a range of strategies from extreme detail with a single planet (such as GJ-436b⁶⁹) to relatively short observations covering more exoplanets (such as the planets in proposal 14260 where planets are observed with 50-80 exposures). GJ-436b is a particularly

⁶⁹ Knutson et al. (2014a)

Planet Name	Mass	Radius	Proposal ID	PI Name	Date	Array Size	Exposure Time (s)	Exposures	NSAMP	Publications Using Data
CJ436	0.073±0.003	0.377±0.009	11622	Knutson, H.	2015-04-14	256	7.6	480	3	Knutson et al. (2014a); Hu, Seager, and Yung (2015); Morley et al. (2017)
XO-1	0.918±0.079	1.184±0.04	12181	Deming, D.	2013-10-31	128	50.4	129	9	Deming et al. (2013a); Wakeford et al. (2016)
HD209458	0.69±0.024	1.38±0.018	12181	Deming, D.	2014-04-29	256	22.3	126	5	Madhusudhan et al. (2014b); Wakeford et al. (2016); Tsaras et al. (2016a); Sing et al. (2016); Barstow et al. (2017); Kataria et al. (2016); Line et al. (2016)
HAT-P-11	0.083±0.009	0.422±0.014	12449	Deming, D.	2014-06-16	256	44.4	114	8	Fraine et al. (2014); Line and Parmentier (2016)
WASP-31	0.479±0.033	1.537±0.06	12473	Sing, D.	2016-05-11	256	134.4	75	8	Wakeford et al. (2016); Sing et al. (2016); Barstow et al. (2017); Sing et al. (2015); Kataria et al. (2016)
HAT-P-17	0.53±0.02	1.01±0.029	12956	Huitson, C.	2015-04-14	256	66.4	100	11	
CJ-1214	0.02±0.003	0.238±0.012	13021	Bean, J.	2014-08-20	256	88.4	71	14	Kreidberg et al. (2014c)
WASP-18	10.201±0.336	1.165±0.077	13467	Bean, J.	2014-08-11	256	73.7	60	12	
HD-97658	0.025±0.002	0.2±0.009	13501	Knutson, H.	2014-07-17	256	15.0	103	4	Knutson et al. (2014b)
WASP 103	1.488±0.096	1.528±0.06	13660	Zhao, M.	2016-09-20	256	81.1	237	13	
CJ-3470	0.044±0.005	0.374±0.052	13665	Benneke, B.	2016-05-12	256	103.1	231	16	Wakeford et al. (2016)
55-CANCRI	0.026±0.001	0.177±0.007	13665	Benneke, B.	2016-05-12	512	8.8	268	3	Tsaras et al. (2016b)
K2-18	-	0.2±0.021	13665	Benneke, B.	2016-05-12	256	103.1	191	16	
WASP 103	1.488±0.096	1.528±0.06	14050	Kreidberg, L.	2016-08-09	256	103.1	593	16	
HAT-P-18	0.197±0.013	0.947±0.044	14099	Evans, T.	2016-09-21	256	89.7	99	6	
HAT-P-12	0.211±0.013	0.955±0.02	14260	Deming, D.	2015-12-12	256	112.0	75	7	Line et al. (2013); Barstow et al. (2017); Kataria et al. (2016)
WASP-52	0.457±0.022	1.27±0.03	14260	Deming, D.	2016-08-28	256	134.4	56	8	
WASP-29	0.243±0.02	0.841±0.046	14260	Deming, D.	2016-04-15	256	112.0	75	7	
HAT-P-18	0.197±0.013	0.947±0.044	14260	Deming, D.	2016-08-08	256	112.0	80	7	
HAT-P-32	0.862±0.165	2.037±0.099	14260	Deming, D.	2016-01-21	256	88.4	90	14	
WASP-67	0.419±0.033	1.4±0.2	14260	Deming, D.	2016-10-22	256	89.7	72	6	
HD-149026	0.361±0.016	0.718±0.065	14260	Deming, D.	2016-04-03	512	69.6	51	5	
HAT-P-38	0.268±0.02	0.825±0.078	14260	Deming, D.	2016-03-02	256	134.4	140	8	
WASP-69	0.26±0.018	1.057±0.017	14260	Deming, D.	2016-08-16	512	69.6	95	5	
WASP-39	0.284±0.031	1.27±0.04	14260	Deming, D.	2016-08-29	256	134.4	70	8	Sing et al. (2016); Kataria et al. (2016); Fischer et al. (2016); Nikolov et al. (2016); Barstow et al. (2017)
HAT-P-26	0.059±0.007	0.565±0.052	14260	Deming, D.	2016-05-02	256	112.0	150	7	
WASP-76	0.92±0.03	1.83±0.06	14260	Deming, D.	2015-11-26	256	103.1	93	16	
HAT-P-3	0.596±0.025	0.827±0.055	14260	Deming, D.	2016-02-25	256	89.7	178	6	
WASP-80	0.552±0.035	0.952±0.026	14260	Deming, D.	2016-06-21	256	103.1	75	16	
55-CNC	0.026±0.001	0.177±0.007	14453	Dragomir, D.	2016-03-31	512	8.8	467	3	
WASP-121	1.184±0.065	1.865±0.044	14468	Evans, T.	2016-08-08	256	103.1	85	16	Evans et al. (2016)
WASP-63	0.378±0.032	1.43±0.08	14642	Stevenson, K.	2016-09-19	256	103.1	183	16	

Table 3.1: All public exoplanet data for WFC3 of exoplanet hosts during transits that are used in this work. Targets where the data quality is in some way compromised or stare mode was used have been omitted, these are shown in Table 3.2. These are ordered by proposal number, with the earliest proposals first. Most of the data at the bottom of the table is fairly new, leading to fewer current publications. Exposures indicates the number of individual HST observations and NSAMP is the number of times each MULTITACCUM mode is read out.

Planet Name	Mass	Radius	Proposal ID	PI Name	Date	Array Size	Exposure Time (s)	Exposures	NSAMP	Publications Using Data	Notes
WASP-19	1.433 ± 0.039	1.395 ± 0.025	12181	Deming, D.	2015-04-14	128	21.7	101	5	Mandell et al. (2013); Hutson et al. (2013); Haynes et al. (2014); Sing et al. (2016); Barstow et al. (2017); Kataria et al. (2016)	Stare mode/Short Scan
HAT-P-1	0.525 ± 0.019	1.319 ± 0.019	12473	Sing, D.	2016-05-11	512	46.7	112	4	Wakford et al. (2016); Sing et al. (2016); Barstow et al. (2017); Wakford et al. (2013); Nikolov et al. (2014); Wilson et al. (2015); Kataria et al. (2016)	Multiple sources on the detector.
WASP-33	4.59 ± 4.0	1.603 ± 0.014	12195	Deming, D.	2016-05-11	256	51.7	240	9	Haynes et al. (2015)	Binary star.
HD-209458	0.69 ± 0.024	1.38 ± 0.018	13467	Bean, J.	2013-12-10	256	15.0		16		Only eclipses taken.
WASP-12	1.361 ± 0.051	1.736 ± 0.092	13467	Bean, J.	2016-09-19	256	103.1	400	16	Mandell et al. (2013); Swain et al. (2013); Madhusudan et al. (2014b); Haynes et al. (2014); Sing et al. (2016); Barstow et al. (2017); Sing et al. (2013); Stevenson et al. (2014b); Kreidberg et al. (2015)	
WASP-43	1.776 ± 0.103	0.93 ± 0.08	13467	Bean, J.	2016-09-19	256	103.1	1503	16	Kreidberg et al. (2014b); Stevenson et al. (2014b); Kataria et al. (2015b); Stevenson et al. (2017)	Narrow transit; requires many stacked visits for good SNR.
XO-2	0.567 ± 0.057	0.983 ± 0.028	13653	Griffith, C.	2016-09-20	512	321.8	87	16		Binary star. Multiple sources on detector.
HD-97658	0.025 ± 0.002	0.2 ± 0.009	13665	Benneke, B.	2016-04-12	512	23.8	193	3		Zeroth order on detector.
HATS-7	0.12 ± 0.012	0.563 ± 0.034	14260	Deming, D.	2016-03-17	256	313.1	80	16		Multiple exposure times used.
TRAPPIST-1	-	-	14500	de Wit, J.	2016-05-04	256	112.0	75	7	deWit2016	Observed during a double transit.
K2-3	0.012 ± 0.003	0.139 ± 0.019	14682	Benneke, B.	2017-01-08	256	103.1	337	16		No ephemeris data.
WASP-101	0.5 ± 0.04	1.41 ± 0.05	14767	Sing, D.	2016-10-02	512	138.4	65	8		Background Star contaminates spectrum.
GJ-3053	-	-	14888	Dittmann, J.	2017-01-28	512	2.6	69	4		No ephemeris data.

Table 3.2: Targets excluded from this work. Most of these are due to problems or complications in the light curve that make it difficult to reduce uniformly with the pipeline. These could all be reduced using the scripts and methods presented here, but would need to be individually treated. Exposures indicates the number of individual HST observations and NSAMP is the number of times each MULTACCUM mode is read out.

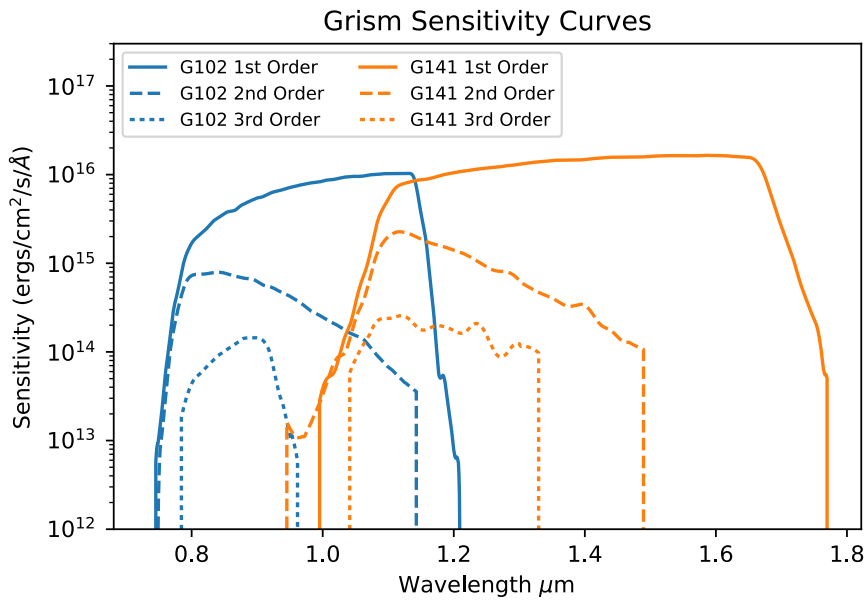


Figure 3.2: The sensitivity curves of the blue G102 and red G141 grisms. Note that water has a prominent spectral feature at approximately 1.34 μm, making the red grism most useful for observing water. The sensitivity curve converts the count rate, (counts per second), into flux. See Section 3.4 for more details.

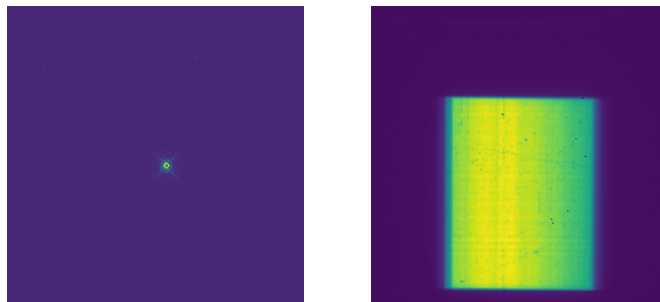


Figure 3.3: Example of the two types of images from WFC₃. Left: Direct image of HD209458b. Right: Grism image of HD209458b. Note the grism image has been spatially scanned as discussed in Section 3.1.3. In this case there is an offset between the source observation and the spectrum. The spacecraft is moved between observations to allow both to be central on the detector.

The first order can be read out using the smallest subarray on the IR detector (128x128 pixels). However, the edges of the dispersion will be missed making absolute calibration of the source position difficult. The 256x256 subarray is most commonly used and easily covers the first order dispersion. Finally the 512x512 subarray can cover the first and second orders. It also has the largest spatial extent, allowing a longer spatial scan and more light to be collected. An example of the different read outs from the detector is given in Figure 3.5.

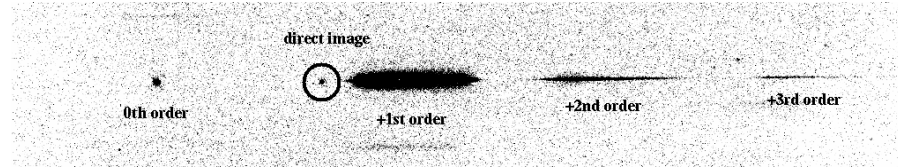


Figure 3.4: G141 grism response as a function of wavelength, where a direct image of standard star GD153 (circled) is overlaid on a grism dispersion with G141. The three spectral orders can be seen on the right of the circle. The image shows the full 1014 pixels of the detector in the x dimension and 200 pixels in the y dimension. Dressel (2014)

⁷¹ Dressel (2014)

The G141 grism also introduces a tilt with respect to the dispersion (x) axis of the detector. This tilt has been measured to be 0.5° ⁷¹. The G102 Grism is also slightly tilted at 0.7° . These tilts cause the spectrum not to lie perpendicular to the dispersion axis. In section 3.3 I discuss how I mitigate the effect of this small tilt and other geometric distortions of the image.

3.1.3 Spatial Scan

⁷² McCullough and MacKenty (2012)

There are two observation modes in WFC3: stare mode and spatial scan mode (introduced in April 2011.⁷²). Stare mode is simply a fixed pointing at the source. In scan mode sources are dispersed in place on the detector and read out. Spatial scan mode was developed to distribute flux across multiple detector rows, ensuring high count rates could be registered without saturation. This allows the measurement of bright stars for long exposures, benefiting from an increased signal to noise ratio. For example 55 Cancri, one of the most studied exoplanet hosts to date with 5 confirmed planets, is a magnitude 6 star. It will easily saturate the detector in less than a tenth of a second in stare mode. The transits for these planets are shallow, requiring as many photons as possible to remain above the photon noise. To avoid saturation while collecting as many photons as possible, the spectrum is scanned over 340 rows of the detector for 8.5 seconds.

Spatial scan mode can be more difficult to process, the calwfc3 pipelines are not applicable to scan data and observers must reduce the data themselves. The scan mode causes a larger fraction of the detector to be illuminated, amplifying the ef-

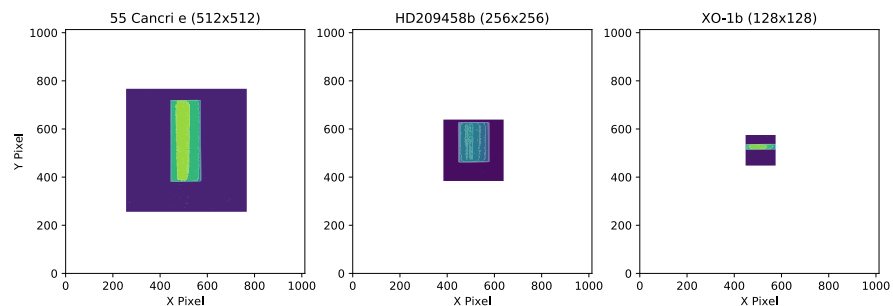


Figure 3.5: Examples of the different subarray sizes. From left to right the sources are 55 Cancri, HD209458 and XO-1. In the case of 55 Cancri a large subarray was chosen as the source is bright and the extent of the spatial scan would be large.

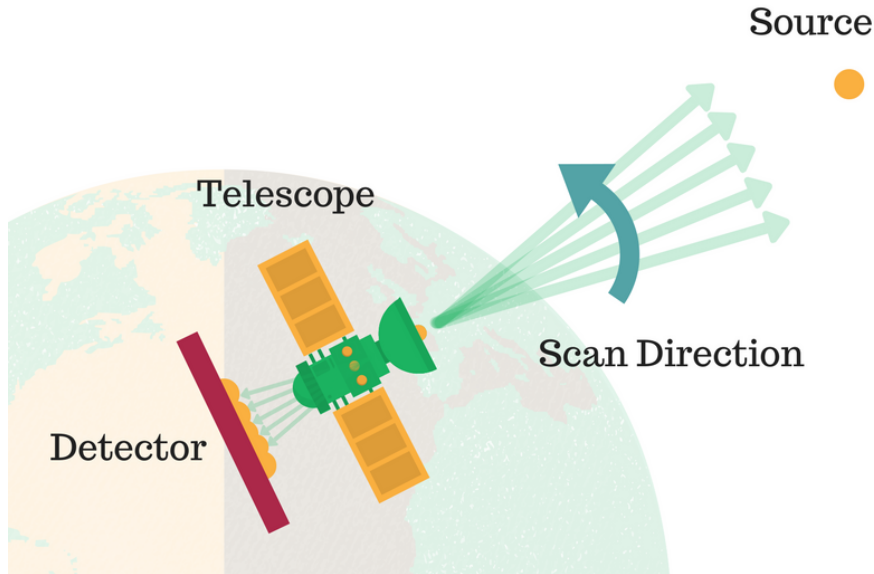


Figure 3.6: Diagram of spatial scan mode. The pitch of the spacecraft is altered in order to spread the light of the source over multiple detector rows. The pitch can be altered to scan up the detector or down the detector, resulting in different readout lengths as discussed in section 3.2.1.4.

fects of both source drifting and geometric distortions. The flux from the star is distributed over many rows of the detector with different pixel properties, including bad portions of the detector.

A diagram of how spatial scan mode operates is shown in Figure 3.6. To scan the data the telescope alters its pitch to move the target vertically. This pitch change is not entirely perpendicular to the wavelength axis and the spectrum becomes slightly shifted as it is moved up the array. Further to this shift, the spectrum is also displaced from exposure to exposure. This requires careful wavelength calibration to mitigate systematics and smearing over multiple pixel, as discussed in Section 3.3.

3.2 DATA

In this section I discuss the initial reduction process that takes the original data and creates light curves. Before these corrections are applied the fits files are separated into individual visits. Visits describe a single set of Hubble orbits and usually encompass a single transit or eclipse. If the observations were taken in 'round-trip' mode (section 3.2.1.4) the forward scans and backward scans are first separated into two different groups to be reduced separately. Figure 3.7 shows a light curve with each of these different sections of the light curve highlighted.

3.2.1 Data Description

In this section I will describe and summarise the properties of the data, including its structure and observation strategies that users have taken. The pixel level corrections applied are discussed in Section 3.2.4.

3.2.1.1 Subarray Size

The 1024×1024 array can be read out in smaller subarrays which allow detectors to be read out more quickly. Choosing smaller subarrays also allows observers to limit their exposure, since there is no shutter on the IR detector to limit exposure. The

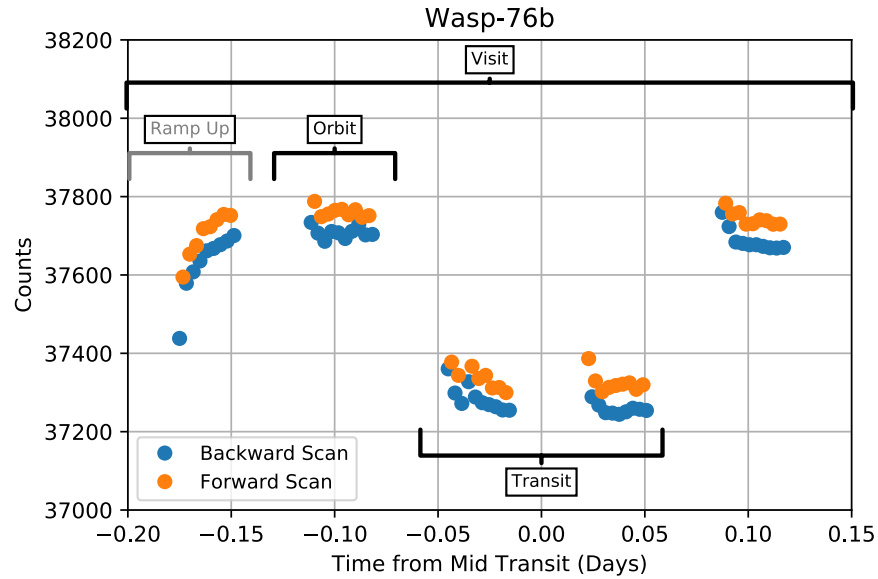


Figure 3.7: White light curve for target Wasp-76b which was taken in round-trip mode. In this mode the data are alternately scanned up the array and down the array. This produces slight differences in the readout times, creating an offset in flux. These two sets are reduced separately in the pipeline.

256x256 is the most commonly used subarray (see Table 3.1) as it balances short read out times and overheads with the exposure of the detector. 512x512 is used for extremely bright stars such as 55 Cancri where a large spatial scan is needed to avoid saturation.

3.2.1.2 Ramps

The `_ima.fits` files are multi extension fits files which contain several reads from the MULTIACCUM read out mode of the IR detector. This mode dumps the exposure level on the detector to a buffer multiple times during a single exposure, set by the NSAMP keyword. (The number of samples for each observation is given in Table 3.1). This allows the detector to be read out before the saturation of any pixels, effectively increasing the dynamic range of any final image. However, for spatial scan data this creates a set of distinct rows of spectra which slowly increase in counts. When these are assembled they are known as the 'ramp' as they increase in counts due to increased exposure. Figure 3.8 shows the ramp over the detector for HD209458. The array is read out at different times depending on those chosen by the observer.

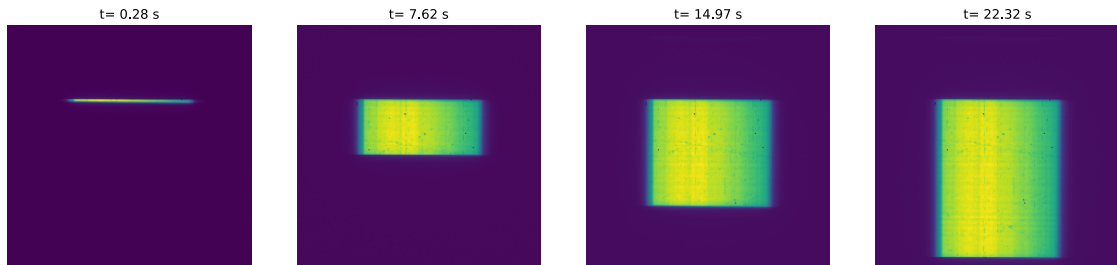


Figure 3.8: Example of each individual read out in the MULTIACCUM mode from one exposure of HD209458 with the G141 grism.

3.2.1.3 Overhead Times

When taking observations there are overheads in time which cannot be avoided. These include the time taken to move filter wheels, read out the detector and transfer and store data. To read a single image from the IR detector there is a 3 second overhead. Each exposure is read out multiple times, which is indicated by the number of samples (NSAMP). For a 16 sample read the read out time will be 48 seconds. Reducing the sub array size reduces this read out time proportionally to the area of the subarray.

The WFC₃ buffer stores images temporarily before they can be dumped to Science Data Formatter. This buffer dump will happen either when the WFC₃ buffer is full or 304 image headers are stored. The buffer can hold 2 full frame images with 16 samples before needing to be dumped, which will take 646 seconds. Using a sub array reduces the amount of data stored so more observations can be taken before needing to dump the buffer. The number of observations that can be stored is given by

$$n = 2 \frac{1024^2}{A_{SA}} \quad (60)$$

where A_{SA} is the area of the subarray in pixels. For the 512x256 subarray 8 exposures with 16 samples could be stored before a buffer dump was required, for the 256x256 subarray 64 could be stored. However, the buffer can hold at maximum 304 image headers before a dump is required. This limits the observer to

$$n = 304 / (\text{Number of Samples}) \quad (61)$$

Balancing the subarray choice and the number of samples enables the highest observation efficiency and high 'orbit packing' (number of observations per orbit). Minimising the need to dump the buffer reduces wasted time. Dumping can occur 'in parallel' (during an exposure of the detector), 'in series' (between two exposures), or during earth occultation. The later is the most useful, since no observations can be taken with HST is behind the earth relative to the source. For the proposals in this work the buffer dumps occur in occultation. Observations take between 9 and 48 seconds to read out, depending on the number of MULTIACCUM samples.

3.2.1.4 Read out directions

During an exposure the target can be scanned either 'forward' relative to the read out direction, 'backward' or alternate directions in a 'round-trip' read out. There slightly different read out times depending on whether the data was scanned in the same direction as the detector read out or against it. Each of these directions produces slightly different flux measurements.⁷³ When observed in round-trip mode one set of scans has a consistently lower flux than the other, this is seen in Figure 3.7 for target Wasp-76b where forward scans are slightly brighter.

To account for this effect in my pipeline the two read directions are split into two groups. Direct images are copied to each group. The two groups are reduced entirely separately and each produce a transmission spectrum. These are then compared in the final results of this work.

3.2.1.5 Transit Observations

The data given in Table 3.1 covers only those targets that were observed during at least one transit. In the beginning of my pipeline I establish which observations were taken during the planet transit and which were taken out-of-transit. The out-of-transit observations establish a base line for the star and the in transit observations contains the exoplanet atmosphere signal. Using transit data from the NASA Exoplanet Archive⁷⁴, exoplanets.eu⁷⁵, exoplanets.org⁷⁶ I find the transit centre time (T_{14}), transit duration and orbital period for each planet. When using the 'median' method (see Section 3.6.0.1) observations taken during ingress or egress are not used

⁷³ McCullough and MacKenty (2012)

⁷⁴ Akeson et al. (2013b)

⁷⁵ Schneider et al. (2011)

⁷⁶ Wright et al. (2011)

to create the transmission spectrum as the atmosphere is partially obscured. (In other methods a full transit model fit is used, accounting for these points.)

3.2.1.6 Initial Ramp Up

In each visit the first 5 to 10 exposures are affected by a sharp ramp up in flux. An example of this is shown in Figure 3.7 which shows the final white light curve for HD209458b after all corrections. This sharp increase in flux is due to the heating of the spacecraft as the telescope changes orientation to the Sun in order to take new observations.⁷⁷ The first 30 minutes of the exposures are removed from any analysis of the white light curve as they can cause transit model fitting to fail. However, they are still used to create the spectral template of the host star, as described in Section 3.3.

⁷⁷ Zhou et al. (2017)

3.2.1.7 Geometric Distortions

There are geometric distortions in the final image on the detector due to imperfections in the optics of the telescope, filters and grisms. These add an element of stretching and skewing to the data as discussed by Kozhurina-Platais et al. (2012). According to that work the sub-pixel distortions can be modelled with a fourth order polynomial. Further STScI software such as the *drizzle* package does account for this distortion, however this cannot handle spatial scan data. I employ my own correction using a least squares fit of a template spectrum that is allowed to stretch, as discussed in Section 3.3. This largely corrects for the effect. It would be possible to utilise the geometric distortion files from STScI to develop a routine to correct for this in a more rigorous way.

3.2.1.8 Other Neighbouring Sources

One potential source of inaccuracy that is not addressed in this work is contamination from nearby sources on the detector. In stare mode two spatial resolved sources will easily remain distinct. However, the scanning of the telescope in spatial scan mode may cause two sources to overlap. In the targets chosen for this work there are no neighbouring sources to contaminate the observation. However, there are some targets with nearby sources such as HAT-P-1b. Such targets have been vetted by eye and omitted from this work as they are difficult to account for in a uniform pipeline. These sources would require careful attention to reduce.

3.2.1.9 Persistence

The combination of filters and subarrays play an important role in ensuring the detector doesn't saturate. Saturation of the detector can cause charge bleed and persistence leading to artefacts in the data. Persistence is defined as an image of a previous exposure persisting on the detector through to the next observation. This is only problematic if an exposure is particularly bright and the detector is not given adequate time for the charge to dissipate. The amount of time needed for the persistence to dissipate is not well understood.⁷⁸ When a pixel is saturated to the level of 100,000 e⁻ it will contribute 2e⁻/s after 200s and 0.3e⁻/s after 1000 seconds. Between most of the read outs in the observations listed in Table 3.1 there are at least 2 minutes. We might naively expect persistence to contribute approximately 2e⁻/s in the case of saturated pixels.

⁷⁸ Dressel (2014)

It is almost impossible to guard against persistence from a previous observation. However, persistence within one cycle of observations of the same object is the observers responsibility. None of the observations used here are close to the saturation point for the IR detector (78000e⁻) and so I do not anticipate persistence becoming a serious problem. There are no procedures in place to correct for it in my reduction pipeline.

3.2.1.10 Crosstalk

The WFC₃ detector is made up of four 512x512 pixel quadrants. If a source is illuminated in one quadrant, due to them being coupled, a negative mirror image of the source appears in the neighbouring quadrant. This is known as crosstalk. This effect is not removed in any of the calwfc₃ pipelines for the IR detector. The effect has been measured to be approximately 1ppm of the original source flux. Here we are measuring signals of the order of 100 ppm. As the effect of cross talk is much smaller there are no measures in place to address it.

3.2.2 How to Reduce HST Data

In the literature there are several works discussing the reductions of individual transmission spectra⁷⁹. However there are no reduction routines available for public use or standard practices for data reduction. As such I have chosen to create a bespoke pipeline, investigate systematics that present across the targets and apply corrections uniformly and automatically to each light curve. By writing a pipeline the reduction process is general and does not require user input, ensuring reproducibility of results.

As discussed in Chapter 1, the signals for exoplanet atmospheres are of the order of 100ppm. This requires that we clean large order effects from the data in order to be precise to this level. The stages for correcting WFC₃ spectra are 1) pixel level corrections for background, flat fields, cosmic rays etc. 2) wavelength calibration 3) stacking spectra that have been scanned spatially 4) cleaning each light curve in the channel by removing out-of-transit variability 5) measuring the transit depth as a function of wavelength to produce the transmission spectrum. Below I list the corrections that are standard in the literature for creating clean HST WFC₃ transmission spectra. I discuss how I apply them and their effects in the following sections. I also list the corrections that are unique to this work. Each of these are discussed in greater detail in the sections below.

STANDARD CORRECTIONS These corrections are standard in the literature and I largely follow procedure described by the works listed. I have created routines which uniformly implement these corrections across all targets.

- Pixel Level Corrections
 - Flat fielding: Standard correction discussed in Tsiaras et al. (2015) and Wilkins et al. (2014). Requires calibration files from STScI.
 - Background corrections: Following procedure from Deming et al. (2013a) any background sources are masked out of ramp reads.
 - Cosmic ray rejection: Following procedure from Deming et al. (2013a) any 6 sigma outliers in pixels as a function of time.
 - Data Quality Masking: Using a similar procedure to Berta et al. (2012) and other works I mask out pixels based on their data quality flags.
- Flux and Wavelength Calibration: Discussed in detail in Tsiaras et al. (2015). I employ an altered version of this correction using subpixel shifts of the source, see Section 3.4.
- Variable Scan Rate: Deming et al. (2013a) uses a simple removal of the variable scan rate (see Section 3.3.5). I present an improved correction, see below.
- Divide OOT Method: Berta et al. (2012) proposes a divide OOT method (see Section 3.5.4) which is employed by many works (e.g. Kreidberg et al. (2014c); Knutson et al. (2014a)). I discuss this correction however do not apply it as standard. I present two other corrections and improve on this method.

⁷⁹ Berta et al. (2012); Deming et al. (2013a); Wilkins et al. (2014); Knutson et al. (2014a); Kreidberg et al. (2014c); Tsiaras et al. (2015)

UNIQUE CORRECTIONS APPLIED IN THIS WORK

- Pixel Level Corrections
 - Pixel area map: I employ the pixel area correction suggested by STScI using their area mask. See Dressel (2014). This is a 4% effect, however as transmission spectra uses relative photometry this correction only serves to help in template fitting later in the analysis.
 - Masking array: I use a masking array throughout my correction process which carries information on bad pixels and the edges of the source-illuminated part of the array. These edges are detected using a simple algorithm I've included to avoid user choices in the pipeline and allow reproducibility.
- Shift and stretch corrections/stellar template oversampling: In Deming et al. (2013a) the shifting of the stellar spectrum across the array during a spatial scan was noted and shown to produce discrepancies between results. In this work I correct for shifts in the source position in 2D and geometrical distortions using stretches. This is discussed at length in Section 3.3. These shift and stretch corrections are applied to the wavelength calibration in order to create an oversampled stellar template. This template can then be removed from each spectral row, correcting for shifts and distortions. This approach is unique. The effect of removing these shifts is shown in Section 3.3.4.
- Improved Variable Scan Rate Removal: Using a similar process as above the variable scan rate is corrected for allowing for tilts and geometric distortions. The variable scan rate is a 2-4% effect across the array and so its careful removal is essential for clean transmission spectra.
- Improved shift/background removal: In Section 3.5.1 I discuss the corrections I apply at the light curve level. I use the background, source shift and out of transit information to correct the light curve and improve transit fitting. These effects can be at the $\sim 0.5\%$ level (see Figure 3.20). I have written a procedure to fold the information in each orbit and increase the signal to noise before each trend is removed, as discussed in Section 3.5.1.

3.2.3 Calibrations from STScI

In this work I use the '_ima.fits' extension files from MAST. These have undergone initial calibration processes from the STScI *calwfc3* pipeline but are an intermediate stage in their calibration pipeline. The corrections already applied to the data are

- Non Linearity: Where the pixel response is not linear with the amount of flux it is exposed to. Highly exposed pixels are not as responsive as less exposed pixels, the counts measured from each pixel is not exactly linear with the flux it was exposed to. A correction is applied to linearise this. Non-linearity is used to define the saturation point for the IR detector. Where the non-linearity level is 5% the pixel is considered to be saturated and flagged in the data quality file. Additionally, any pixels that are saturated in any of the reads from the MULITACCUM mode are flagged in subsequent reads, regardless of whether they have fallen back below the saturation limit.
- Dark current subtraction: There is still an amount of charge in each pixel when the array is un-illuminated, known as dark current. This current is measured pre-flight by taking exposures with an opaque aluminium plate instead of a filter. Each pixel has a slightly different amount of charge. The dark current is measured and each pixel is weighted to remove the effects. Hot pixels, where the dark current is higher than $\sim 0.1e^-/s/pixel$, are flagged in the data quality.

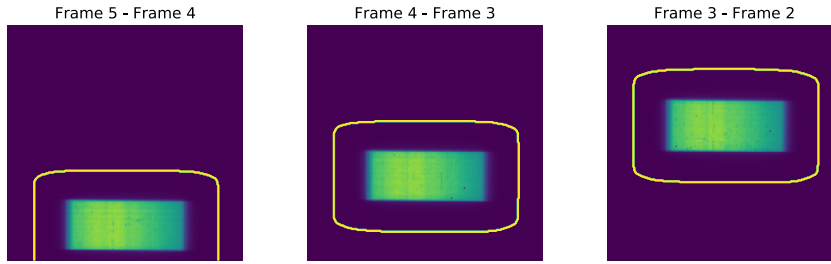


Figure 3.9: Example of how removal of sky background and neighbouring sources works. Each of the MULTIACCUM frames from Figure 3.8 is subtracted from the subsequent frames in order to produce one sky-subtracted frame. The sources are then masked, any pixels that were not exposure to the source are zero'd. (Outline shows mask.) These frames are then summed to create one sky-subtracted frame. This does not account for neighbouring sources that are scanned over between MULTIACCUM readouts. Note: The final frame is added without sky-subtraction.

- Gain calibration: The correct conversion between counts and number of photons received is put in the header file for later use.
- Reference Pixel Subtraction: While the whole detector is made of 1024×1024 pixels the outer edge of 5 pixels are not used in the detector for collecting light from the source. These are reference pixels which are designed to be unilluminated. They allow an accurate read of the bias of the detector. As here I employ the intermediate stage '*ima.fits*' file type this 5 pixel border is still present but has served its purpose during the reduction. It is clipped out at the start of my pipeline.

3.2.4 Pixel Level Corrections

In this section I discuss the first level of correction I apply to the data at the pixel level. These follow procedures suggested by Deming et al. (2013a). I have developed routines to perform both of these corrections to the '*_ima.fits*' files from STScI with no input from the user. I will briefly explain how each stage works and the effect of each.

3.2.4.1 Pixel Area Map

The IR detector does not have uniformly sized pixels. Pixels decrease in physical size by approximately 8% across the full 1014×1014 array, with pixels being smaller at the top. This is corrected for in my pipeline with the pixel area map from STScI. Smaller pixels have their flux weighted against larger ones to balance out their response.

3.2.4.2 Background Correction

In each observation there is a level of background noise. I can estimate the background value in each frame using portions of the detector where no light from the source fell. This measures the level of exposure experienced by pixels due to residual sky background and readout noise. I employ the method proposed by Deming et al. (2013a) to correct for sky background. This method relies on the nature of scanned data; the area of the detector that the spectrum has been scanned over increases in each MULTIACCUM readout, see Figure 3.8. The illuminated part of the array contains both the star and any sky background. To correct for this I do the following: 1) each MULTIACCUM read is converted to counts using the exposure time. 2) Each read is then subtracted from the previous read to give one "sky-subtracted" frame containing the star. (See Figure 3.9) 3) All of these new frames are masked

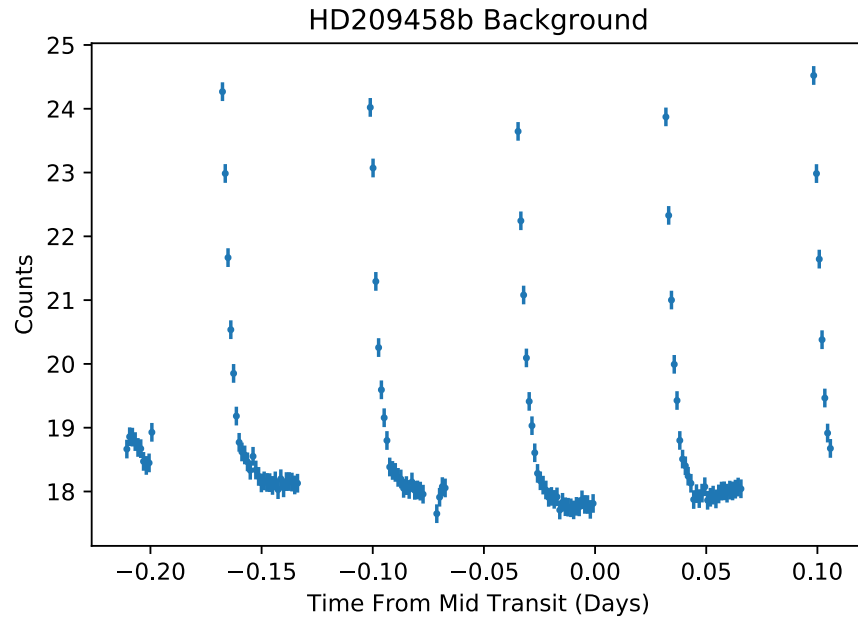


Figure 3.10: Measurement of the average background counts for HD209458b. The background is assumed to be uniform across all wavelengths and parts of the detector. This trend is removed later in the reduction (see Section 3.5.2). The background trend is least squares fit to each channel light curve using the out-of-transit data in order to remove it. This occurs after the stellar information has been fit and removed.

with a ~ 15 pixel border around the star signal, all parts of the detector that are unilluminated are zero'd. 4) These sky-subtracted frames are then summed to create one frame spanning the full exposure. The last frame is added without this procedure for sky-subtraction. This is given as

$$S_t = \sum_{i=0}^{n-1} M_t(R_{t,i+1} - R_{t,i}) \quad (62)$$

where S_t is the summed frame at each time stamp t , $R_{t,i}$ is the i th read out at that time stamp and n is the number of reads. M_t is a mask that zeros all parts of the detector that are not illuminated by the source. This procedure removes the effects of having neighbouring sources on the detector, assuming that the scans are short enough that the two sources do not overlap. A higher MULTIACCUM sample rate alleviates this overlapping problem, as there are fewer pixels scanned in each MULTIACCUM frame. This procedure does leave some residual sky background very near to the source, but this is usually small.⁸⁰ This is performed for each read except the last, which has the minimum possible time exposure. The last frame is simply included with no sky background correction.

While this method can remove sky background and readout noise, it does not address any charge that accumulates during the exposure (for example from detector heating). To correct for this I use the same procedure as above but mask and zero all pixels containing the star, leaving only the pixels with no direct starlight. These allow me to measure the residual response in the detector as a function of time. Each of the MULTIACCUM frames is then summed as above to create a background frame for every time stamp. An example of this background measurement as a function of time is shown in Figure 3.10. I have found this trend to be multiplicative in all of the observed spectra. To account for this background trend I perform a least squares fit of this trend to all the out-of-transit data and divide it out. This largely removes the effects. This is performed after the shift corrections described below.

⁸⁰ Deming et al. (2013a)

3.2.4.3 Cosmic Ray Rejection

Cosmic rays are high energy particles of unknown origin. They hit the detector causing charge to be recorded that is unrelated to the source. For cosmic ray rejection I use a procedure similar to that adopted by Deming et al. (2013a) where each pixel is inspected as a function of time. Assuming that each pixel is illuminated by approximately the same amount of light during each subsequent scan, any significant outliers will be due to spurious signals such as cosmic ray hits. Pixels that are 5 sigma outliers for each frame are added to the masking array and zero'd, removing them from further analysis.

3.2.4.4 Flat Field Correction

The flat field for the WFC₃ detector can now be built from the coefficients given in the WFC₃ calibration files from STScI, following the prescription from Kuntschner et al. (2009). The file contains four 1014x1014 frames of coefficients for creating a flat field based on the wavelength solution, as shown below

$$F = \sum_{i=0}^{i=4} x_i^i f_i \quad (63)$$

where x is the relative pixel position in the detector and f is the flat field coefficient from the STScI calibration file. The flat field is then a value between 0 and 1 which weights each pixel to correct for small inhomogeneities on the detector. The data are divided through by the flat field before any further corrections are applied. The flat field can alter individual pixels by ~1% and contains structure (particularly 'blobs'), which can effect the final transmission spectrum if not masked.

3.2.4.5 Data Quality

The fits files used here contain the data, errors and a third extension for data quality. Data quality is assessed by *calwfc3* which flags each pixel with a sum of binary values denoting its quality. A list of the quality flags possible are given in Table 3.3. Some flags, such as the cosmic rays detected during up the ramp fitting, are designed to work in stare mode. These are often raised in spatial scan mode though the data quality is actually acceptable. Those flags that were used in my analysis have been highlighted in bold. Pixels with a poor data quality are masked from the beginning of the analysis by weighting them to zero. Bad pixels and hot pixels, where a particular pixel in the detector is known to malfunction, make up only a small fraction of the detector but can provide unreliable results. Full well saturation is where due to some source in the exposure, such as a cosmic ray hit. Too many counts are registered in a pixel. This is rare but can affect results. Finally, unstable-zero read signifies that the response of the pixel may be variable and unreliable.

3.3 SPECTRAL AND SPATIAL DRIFT IN HST WFC

Spatial scan mode has provided an excellent resource for observing the brightest exoplanet host stars, with the best signal to noise ratio possible while not saturating the detector. However, this method comes with a draw back in the loss of some precision when the spacecraft moves. The guidance and pointing systems for HST were designed to work when pointing at a fixed location. Scanning the spectrum leads to small imprecisions when the spacecraft pitches to drag the light over the spatial dimension of the detector. These shifts in position cause light to be smeared over several pixels, causing a small blurring effect. This causes uncertainty in the positioning of some spectral features. As the stellar spectrum is 4 orders of magnitude brighter than the signal from the planet atmosphere, any star light that is not removed causes discrepancies. Sub-pixel shifts cause stellar features to pollute neighbouring pixels.

Table 3.3: Data quality with corresponding binary values from STScI. Those flags that I mask out of the data are highlighted.

FLAG Value	Data Quality Condition
0	OK
1	Reed-Solomon decoding error
2	Data replaced by fill value
4	Bad detector pixel
8	Unstable in zero-read
16	Hot pixel
32	Unstable photometric response
64	(Obsolete: Warm pixel)
128	Bad reference pixel
256	Full-well saturation
512	Bad or uncertain flat value
1024	(unused)
2048	Signal in zero-read
4096	Cosmic ray detected by AstroDrizzle
8192	Cosmic ray detected during up-the-ramp fitting
16384	Pixel affected by crosstalk (not used)

⁸¹ e.g.; Tsiaras et al. (2015); Deming et al. (2013a)

This has been noted in the literature⁸¹ as causing issues in transmission spectra from WFC3. In this section I will discuss my procedure for measuring the shifts and geometric distortions from the exposure and how I mitigate the shift. After finding the shifts I have also designed a routine to use them to my advantage, creating an oversampled stellar spectrum as discussed below. When the spacecraft moves the target would ideally be dragged up the detector exactly perpendicular to the dispersion axis. However, in reality the source is dragged at some angle relative to the dispersion. This is shown in Figure 3.11 for a single exposure, where red lines indicate a (slightly exaggerated) slant in each dimension of the spatial scan. There is also a smaller shift with respect to the spatial axis due to geometric distortions from imperfections in the telescope optics and the small 0.5° angle of the grism.

The drift in the spectrum over time causes spectral features to move from one pixel to another during the course of one exposure. This causes more or less light to be read as a function of time, proportional to the shifting function. This is particularly apparent with spectral features of high contrast such as the Paschen β line. Figure 3.12 shows this in greater detail, where we see around the Paschen β line there is a slope and additional trend similar to that shown in Figure 3.17 from the shift in wavelength. To account for this effect I build an accurate stellar spectrum template, shift it in the same way as the original source shift and then bin it to the same pixel resolution. The data are then divided by the stellar template, normalising all of the channels.

In this section I will define two different types of shift:

- The shift in position of the spectrum during a single exposure, as shown in Figure 3.11. I will refer to this as **Exposure Shift**.
- The shift in position of the spectrum from one exposure to the next. I will refer to this as **Orbit Shift**.

The shift is an important factor in both dimensions of the detector. Firstly the dispersion axis (x pixel) which will cause errors in the calibration of the data, making it the most crucial. Secondly the spatial axis (y pixel) which is the direction of the drag. Shifts in this axis become important when attempting to correct for the variable

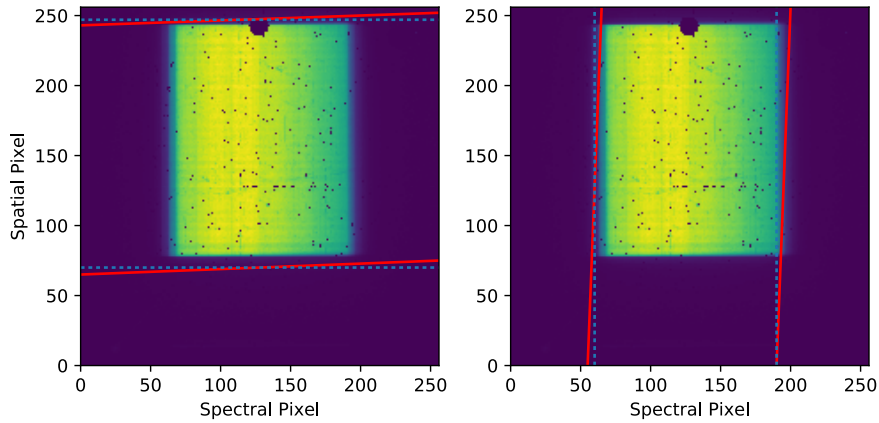


Figure 3.11: Example of the shifts on the detector as a function of both spectral and spatial pixel. The shifts cause the data to be sloped in each dimension, as shown by the red lines (this has been exaggerated in the above image.) Right: Spectral shift, where each spectrum is slightly offset from the next by a fraction of a pixel. Left: Spatial shift. The detector is also subject to stretches and geometric distortions from the telescope optics.

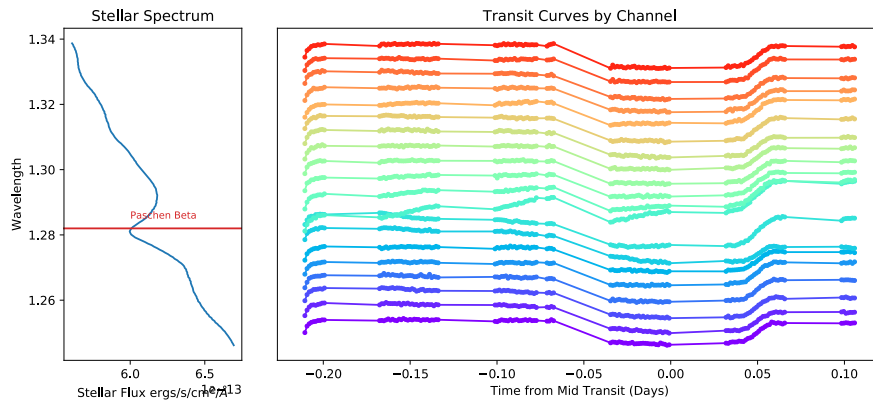


Figure 3.12: The effect of the Paschen β spectral line on the transit curves in each channel due to the drifting of the spectrum over multiple pixels. The drift slight slope which is amplified around strong spectral features. This is removed firstly with a stellar spectral template which is perturbed by the same shift. Any residual effects are removed with a fit to the out-of-transit data in each channel light curve.

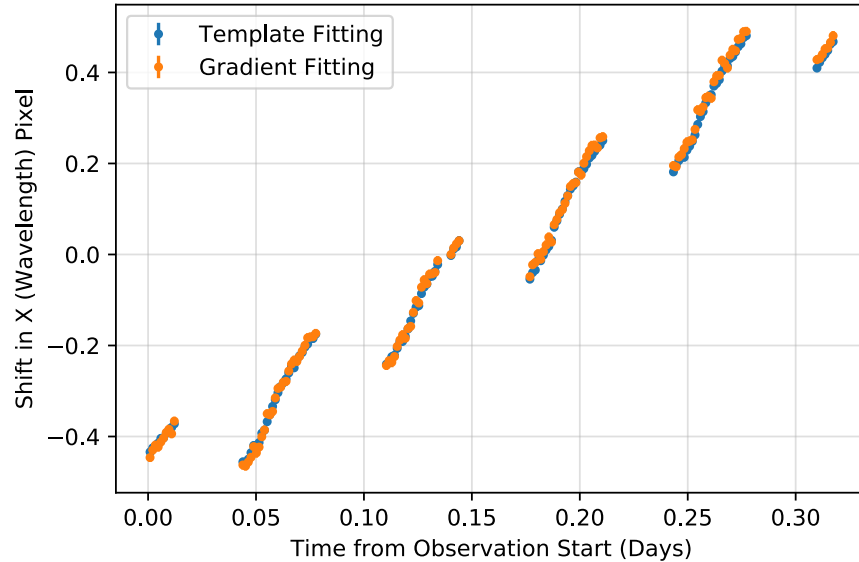


Figure 3.13: Orbit Shift in wavelength for HD209458b as measured by two different methods, discussed in Sections 3.3.0.1 and 3.3.0.2. Both methods produce similar results with small errors. The template fitting method is used in this work as more points are used and it is less susceptible to errors in fitting from bad pixels.

scan rate, as discussed in section 3.3.5. I will refer to these as **Wavelength Shift** and **Spatial Shift** respectively.

Correctly assessing each of these shifts should result in the correct wavelength calibration for all pixels. To create an accurate wavelength calibration solution the position of the source is needed. The shift in the source is assessed in each of the grism images before calibration. This shift is then passed to the calibration code to create a final wavelength solution and flat field.

There are several ways to find the shifts in source position. I have created two methods which both perform well, the first being more speedy at the cost of accuracy and the second being more accurate at the cost of time. Both of these methods utilise the sensitivity curve, which produces a steep slope at the edge of the spectrum. This provides a high gradient value and an easy point to anchor any template fitting. Both methods are discussed below. I employ the second method in this work as it is less susceptible to errors in fitting from masked 'bad' pixels. The two methods produce very similar results, as shown in Figure 3.13.

3.3.0.1 Estimating Shifts Using The Gradient

To estimate the path the source took as the telescope moved we can use the position of the spectrum as a function of time, both as a function of y pixel on the detector and from exposure to exposure. To estimate the position of the spectrum we can use the steep sides of the sensitivity curve. At the edges the sensitivity curve any astrophysical signal is reduced quickly to zero. The shape of a spectrum after it has been convolved with the instrument sensitivity curve is shown in Figure 3.14, which illustrates the steep edges of the spectrum. By taking the gradient of this spectrum and finding the maxima we can accurately locate the steepest parts of the spectrum, the edges of the sensitivity curve. This produces two peaks, one for each side of the curve, (see lower panel in Figure 3.14). These peaks can be approximated as Gaussian in shape and have a FWHM of ~ 8 pixels. By fitting an optimal Gaussian to each of these peaks we retrieve a position estimate for these turning points. As the slope is much greater than the astrophysical signal this is largely informed by the

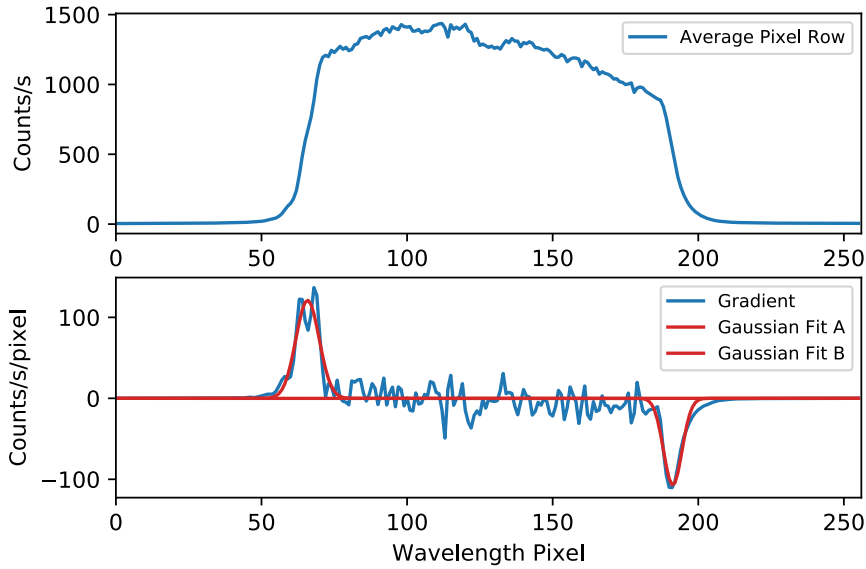


Figure 3.14: Example of how to use the gradient in order to find the position of the spectrum in each detector row. Turning points in the gradient of the spectrum are fit with Gaussian to track their movement as a function of time.

motion of the detector. The locations of these peaks are then measured as a function of time.

In the gradient fitting method any masked pixels in the ~ 8 pixel Gaussian will cause either the shift to be misreported or the Gaussian fit not to converge. This causes a problem with this method as it relies on data from only a few pixels. The method discussed below uses more of the data and so is less susceptible to errors from bad pixels.

3.3.0.2 Estimating the Shift Using a Template and Least Squares Fit

A second approach to find the position of the spectrum on the detector is to use a template spectrum. In this case we find the position of the template that minimises the reduced χ^2 . I firstly create a template spectrum. This is initially the average of all of the frames, weighting each pixel by the data quality and having removed any cosmic rays. This produces a first estimation of the true stellar spectrum. To ensure the best signal to noise ratio all of the observations are used, including those that were taken in transit. We assume that any contribution from the planet is negligible compared to both the detector sensitivity curve and the stellar spectrum. An example of a template spectrum is shown in Figure 3.15. The template is then shifted as a function of dispersion axis (x) pixel to find the optimal fit.

Using the whole spectrum to find the optimal fit provides more information than using just the two turning points. However fitting each spectrum requires more time than using only the edges.

3.3.1 Stretch as a Function of Row

Beyond the shift in position there are also geometrical distortions in the image. Imperfections in the telescope optics, filters and grisms cause small distortions in the image before it illuminates the detector. This can result in a sub-pixel stretch or skew. A fourth order polynomial is used to describe the distortion in Kozhurina-Platais et al. (2012). In this work I do not employ the full correction. I utilise a very similar process to the shift finding with a template spectrum. The template spectrum is re-interpolated onto a stretched grid and reduced χ^2 is used to find the optimum

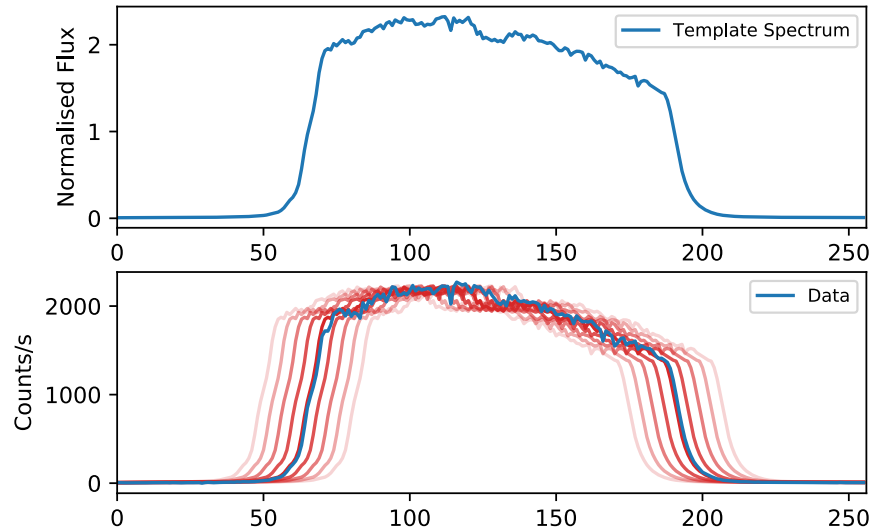


Figure 3.15: Example of how to use a template spectrum and a least squares fit in order to find the position of the spectrum in each detector row. Upper Panel: Data to be fit. Lower Panel: The template spectrum (red line) is shifted in dispersion axis pixel to find the optimum fit based on least squares fitting.

stretch. This information is then used to inform the wavelength calibration solution. When using the largest subarray, (512x512) this stretch will not exceed 3.2 pixels and when using the 256x256, (the most common used in all the proposals investigated here,) the stretch will not exceed 1.1 pixels. Where the spatial scan covers a large extent of the detector the stretch will increase up to these values. While the effects of stretches and geometric distortions on the detector are small I find removing them has only a minor affect in most cases. In HD209458b the effects of stretching alter the wavelength calibration by at most 3nm. Wakeford et al. (2016) also includes a stretching term to account for this distortion.

3.3.2 Oversampling And Removing The Stellar Spectrum

Targets with the largest shifts are affected most by the blurring of stellar spectral information into more than one spectral bin. To reiterate; the stellar spectrum is 4 orders of magnitude brighter than the exoplanet transmission spectrum. Any small amount of light from a stellar spectral line moving into a neighbouring bin can affect our final results. It is important to accurately find and correct for shifts. The shifts found here are then used in the calibration codes to accurately map the counts from each pixel back to the correct wavelength solution. This new calibration is then used to create an oversampled stellar spectrum to update the stellar spectral template.

Oversampling in this case refers to placing the spectral information on a finer, sub-pixel grid with the sub-pixel shifts. Oversampling allows information from narrow features that span a few pixels or less to be reconstructed. For example the Paschen β hydrogen line at $1.28\mu\text{m}$ spans approximately 2 pixels. Using oversampling these features are reconstructed into a more accurate template which uses the shifts in the spectrum position to our advantage. If the pixel shifts cover a full pixel this can increase resolution by a factor of ten. This reconstructed stellar spectrum template is then shifted in the same way the original source was shifted. This is then re-binned back to the resolution of the detector. This creates an accurate reconstruction of the stellar information, preserving the counts in each pixel. This reconstructed stellar spectrum can then be removed. This corrects for the errors introduced from narrow features crossing pixel boundaries.

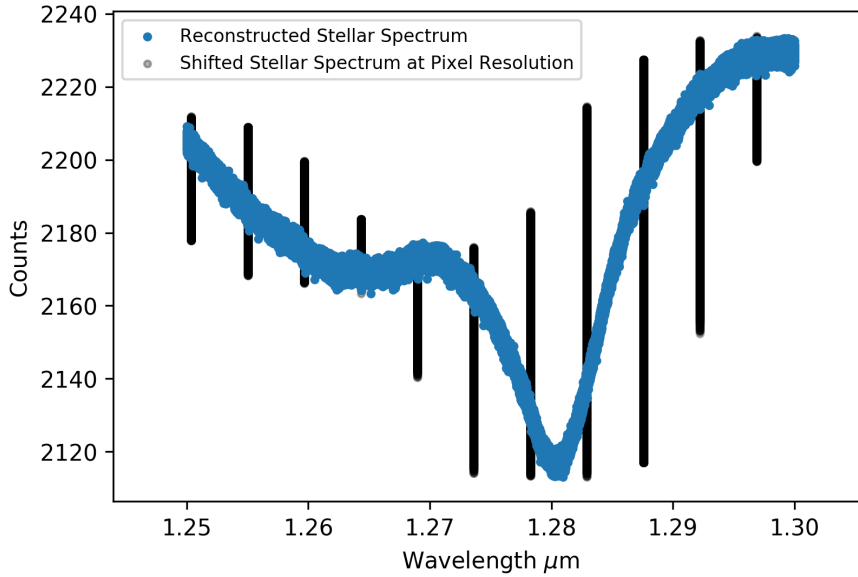


Figure 3.16: Reconstructed template after shifts have been removed. Here only the Paschen β line is shown to clarify the effect. Blue data points show the reconstructed spectrum oversampled to a tenth of a pixel. Black points show the reconstructed template shifted in the same way as the source and binned to the pixel level. The shift of the spectral line causes a wide range of flux to be read in each bin. All data in the visit has been used to reconstruct this spectrum.

Figure 3.16 shows the reconstructed stellar spectrum for HD209458b after source shifts and geometric distortions have been taken into account. The Paschen β line has been chosen to show the effect more clearly. Here black points show this reconstructed template having undergone the same shift as the source and binning back to the original pixel level. As the spectral line moves over a pixel during the course of multiple exposures the deep line causes a large variance in the recorded pixel level. Pixels where the spectrum is more flat undergo a smaller change.

3.3.3 Shifts for All Exoplanet Targets

Both the exposure shift and orbit shift vary greatly depending on the target brightness. Brighter targets are usually scanned over larger areas of the detector than dimmer stars to avoid saturation. This causes any shifts in the source position as a function of time and position to be exacerbated. This leads to the brightest targets having the largest Exposure Shift. Targets with more exposures have more opportunities for the pointing to drift. Because of this targets with many observations tend to have a greater Orbit Shift. Figure 3.17 shows the Orbit Shifts for the first visits of each of the targets given in Table 3.1. We see some targets such as XO-1b, Wasp-29b and GJ3470b have fairly good tracking and shift only $\sim 5\%$ of a pixel during a single visit due to short scans. Some targets however such as Wasp-33b, GJ436b and HAT-P-11b have much larger shifts moving \sim one pixel during the visit. The exposure shift is measured during one exposure of the detector and then approximated with a linear fit.

The amount of exposures and length of exposure is not the only factor. I have not investigated further into the causes of this shift. Further work could potentially correlate the magnitude of the shift with other behaviour detectors, such as the angle that the data was scanned at.

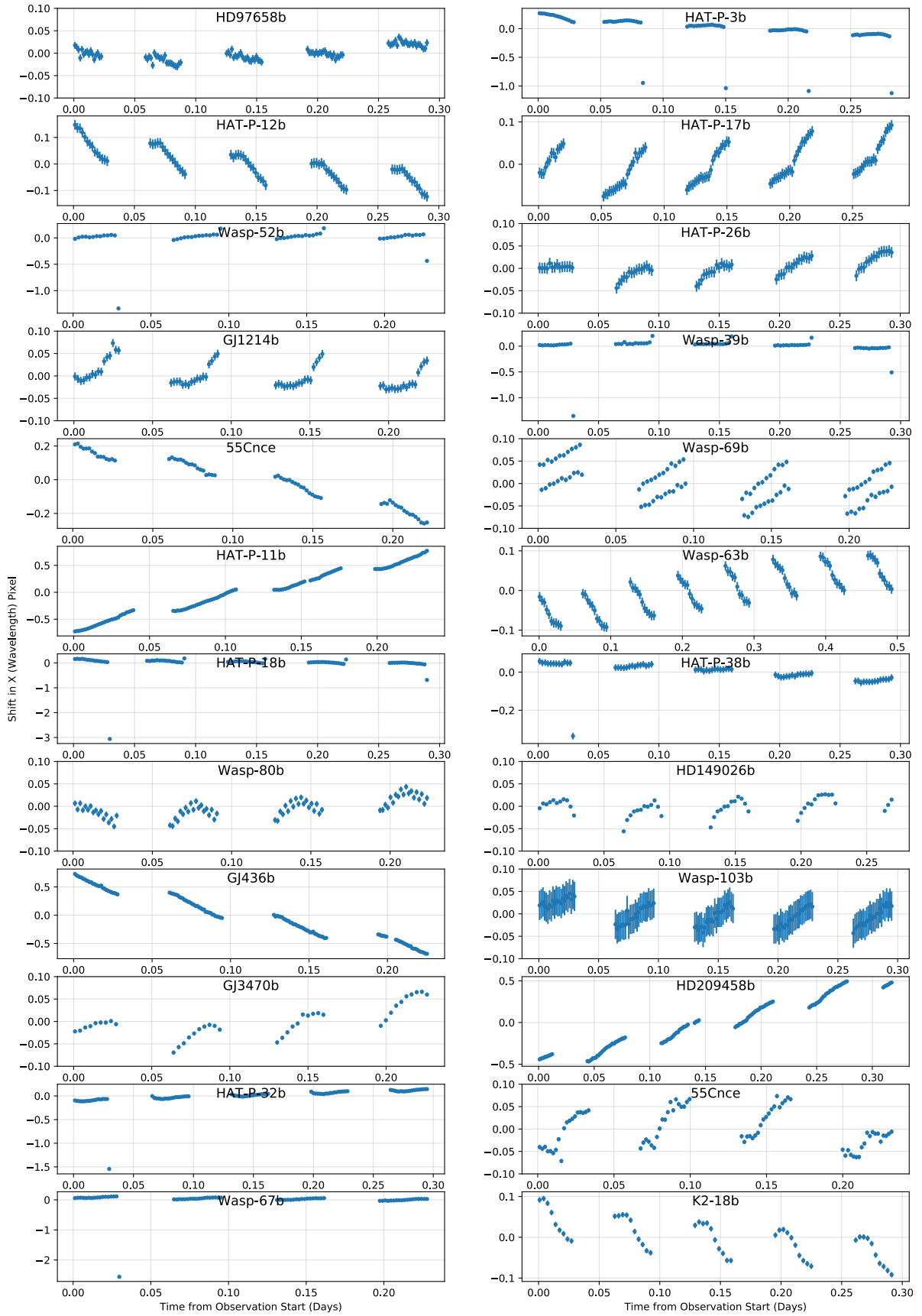


Figure 3.17: All shifts in dispersion axis (x) pixel from every exoplanet host target used in this work. Those with the widest shifts produce the best stellar spectra using the oversampling method.

3.3.4 Effects of Shift Corrections

The shifts and stretches discussed in section 3.3 can have a small but noticeable effect on the derived transmission spectra, particularly for those that have been spatially scanned across a large portion of the detector. Figure 3.18 shows the correction for shifts and stretches for a few different transmission spectra that show signs of water absorption. Brighter targets, that are in more danger of saturation, are scanned up a larger amount of the detector usually increasing the shift, and so some targets are more affected than others. We see that for some targets the effect is small such as with HD209458b. However for some targets such as Wasp-76b and HAT-P-26b the effect is at the $1\text{-}2\sigma$ level.

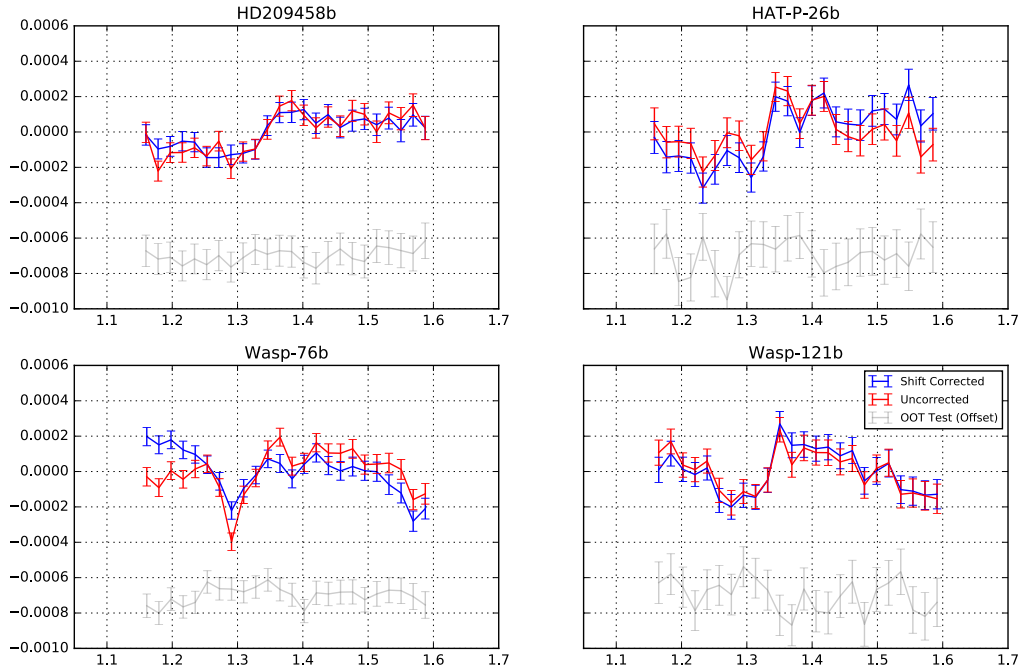


Figure 3.18: Four exoplanet targets with prominent features in their light curves with flat out of transit tests. Here the shift corrected and shift uncorrected versions are shown in blue and red respectively. The out of transit test is shown in grey, slightly offset for clarity. For Wasp-76b the shifts in source position cause a $\sim 2\sigma$ discrepancy between the corrected and uncorrected transmission spectra. For targets with smaller shifts the effect is $\lesssim 1\sigma$ in most channels.

3.3.5 Variable Scan Rate

During a spatial scan the telescope tracks the star up or down the array using the fine guidance system. Small variances in the speed of the motion cause the telescope to spend longer on some rows than others. This causes some rows to receive more exposure. This results in a wave like pattern on the detector as shown in Figure 3.19. I will refer to this variance as the Variable Scan Rate (VSR). The VSR causes a change in flux on the order of 2% in most exposures in a horizontal striping patterning. The VSR pattern varies significantly from each exposure.

The VSR would provide no problems in the reduction if it were perfectly perpendicular to the dispersion axis. However, due to the slight tilt in the dispersion of 0.5° and geometric distortions, this is not the case. As the effect of the VSR on the flux is

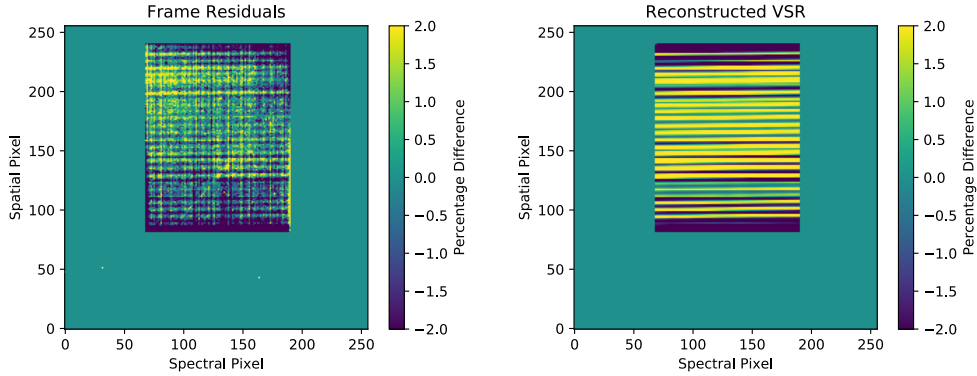


Figure 3.19: Variable scan rate for HD209458b. Left: Data from the first grism exposure of the visit, flat fielded and divided by the average spectrum to remove the astrophysical variability and highlight the VSR. Right: The reconstructed VSR including the shift in the y direction as the star is scanned up the detector. Note both images have been masked to only include the illuminated portion of the detector.

quite large I fit the VSR using the template shifting method discussed in section 3.3. The procedure is identical but performed in the spatial dimension (y pixel) rather than the dispersion axis (x pixel). Firstly, I construct a template of the variable scan rate as follows. 1) The shift and stretch of the spectrum is found in the x dimension using the methods discussed above. 2) The VSR template oversampled by using these shifts and stretches in the same way as above. 3) This oversampled template is then shifted back to find the best approximation of the VSR without the shifts and distortions. This is done for each frame individually as the VSR changes significantly from exposure to exposure. This reconstructs in 2D the VSR. An example of the reconstructed VSR is shown in Figure 3.19.

Once the VSR has been reconstructed it is then divided out of each frame. This removes the effect of the variable scan rate.

FINAL DATA CUBE Each frame has been divided through by a 2D reconstruction of the VSR and a 2D reconstruction of the stellar spectrum, accounting for shifts in source position and geometric distortions. Only the illuminated portion of the array is used in this summation. The final corrected frames are then summed up over the spatial direction. This creates the final 2D dataset with dimensions of dispersion axis (x) pixel in microns and time.

3.4 FLUX CALIBRATION AND WAVELENGTH SOLUTION

While there are calibration routines available through STScI and IRAF, I create my own calibration code. The difficulties of spatial scan mode are not addressed in the calibration pipelines from STScI. Creating a bespoke calibration routine allows me to use spatial scan data. It also allows me to use the shifts and geometric distortions to oversample the stellar spectra to create a highly detailed spectral template. I follow the prescription from Kuntschner et al. (2009) to calibrate the data as below, however I also utilise the scan direction to create a calibration as a function of detector row and source position.

3.4.1 Flux Calibration

The data must be converted from detector counts to flux in $\text{ergs/s/cm}^2/\text{\AA}$. Firstly any sources where given in units of counts/s are converted to counts by multiplying by exposure time. The counts are then converted using the PHOTFLAM keyword from the header file.

3.4.2 Wavelength Calibration

To produce the wavelength solution I employ the calibration files from STScI. These provide the flat field, wavelength solution and sensitivity curve as a function of source position.

To create the wavelength solution the direct image, (taken in a 128, 256 or 512 pixel subarray) is placed in the reference frame of the entire 1024x1024 detector. This is done using the CRPIX and LTV keywords from the header (the position of the reference pixel and the subarray starting pixel respectively) This is repeated for the grism image which is offset from the direct image slightly to encompass the first order dispersion.

Using a 2D Gaussian fitting routine I find the location of the source in the direct image in x and y pixel. Some observing strategies take multiple direct images to update the source position on the detector. In those cases I update the position of the source with each direct image.

The filter in which the direct image is taken with also adds a small, subpixel shift. This can be found in Kuntschner et al. (2009) for each filter.

With each of these shift components the x position of the source can be mapped in the reference frame of the full detector, accounting for all source shifts. The x position of the star for each grism image is given by

$$x'_{j,f} = x_0 + (507 - 0.5 * L) + \Delta F_x + d_{sub} + s_{j,f} \quad (64)$$

where $x'_{j,f}$ is the position of the source in x for a given row j and a given frame f. x_0 is the position of the source in the most recent direct image, L is the size of the sub array used, ΔF_x is the shift introduced by the filter, d_{sub} is the offset in pixels between the direct image and the grism image and $s_{j,f}$ is the shift as a function of the row and the frame.

This x position can be calculated for every row of the sub-array (j) and every frame of the observation (f). We can then calculate the wavelength solution at this x position using

$$a_\lambda = a_0 + a_1 x' + a_2 y + a_3 x'^2 + a_4 x' y + a_5 y^2 \quad (65)$$

$$b_\lambda = b_0 + b_1 x' \quad (66)$$

$$\lambda = a_\lambda d + b_\lambda \quad (67)$$

where x' is the x position of the star after undergoing the shifts from Equation 64 and y is position in the y axis. In this case, we are creating a solution for each row of the detector and so y is simply each row number. d is the position of each pixel in the row, (i.e. an array of 1014 values centred around x'). The coefficients for this conversion are given in Table 3.4. λ can now be corrected in accordance with the stretch values found in Section 3.3.1 for each row. This removes the geometric distortions from the telescope optics. Equation 67 is used for converting pixel to wavelength based on the coefficients from Kuntschner et al. (2009). Wilkins et al. (2014) proposed alterations to these coefficients. However, I find that if the shifts and geometric distortions in the data are removed there is no need to correct the calibration coefficients. Tsiaras et al. (2015) also finds the corrections are unnecessary.

3.5 CORRECTIONS APPLIED TO LIGHT CURVES

Once the calibration has been found and the images have been flat fielded the data can undergo a second stage of correction. The data is divided through by the VSR and the stellar spectral template. The illuminated portions of the array are averaged over the spatial dimension. This results in a 2D data frame of flux with dimensions

Table 3.4: Wavelength calibration coefficients taken from Kuntschner et al. (2009).

Coefficient	Value	Error
a_0	4.51423E1	6.26774E-2
a_1	3.17239E-4	3.98039E-04
a_2	2.17055E-3	2.31850E-4
a_3	-7.42504E-7	4.45730E-7
a_4	3.48639E-7	3.20519E-7
a_5	3.09213E-7	2.1638E-07
b_0	8.95431E3	8.14876E0
b_1	9.35925E-2	1.09748E-02

of wavelength in microns and time in days. There is a transit light curve for each wavelength channels on the WFC3 detector, (107 channels total). By dividing out the stellar spectrum I have normalised the light curves. This section details the further corrections I have designed and applied to each light curve. An example of the effect of these correction steps is shown in Figure 3.20.

3.5.1 White Light Curves

Once the 2D dataset has been generated we are left with a set of light curves, with one light curve per wavelength channel. A “white light” curve is generated for the target by averaging over all channels where the sensitivity curve was highly responsive (>50% flux). Here the term white light is used to mean a summation over all channels. This removes the wavelength dependency but is still centred around 1.41 μm rather than in the visual white light as the name suggests. An example of a white light curve for HD209458b is shown in Figure 3.21.

The white light curves for all targets used in this work are given in Figure 3.22. Most proposals use 4-5 Hubble orbits per target to encompass in and out-of-transit observations. The ingress and egress portions of the light curve are often sampled where possible as this aides in transit model fitting.

3.5.2 Residual Shift Trends

The Orbit Shift discussed above introduces a slope and multiplicative trend to each channel, as shown in Figure 3.12. The slope is largely removed with the stellar template, as it is shifted for each row in response to the source shift. However, there can be a slight residual trend left in the channels, particularly around high contrast features such as the Paschen Beta line. To correct for any further effects of the shift I have designed the following routine. I least squares fit the Orbit Shift trend to each channel (an example of Orbit Shift is given in Figure 3.13). This procedure is as follows:

- **RENORMALISE** The Orbit Shift is renormalised, removing the long term variation from orbit to orbit.
- **FOLD** The trend is folded on the orbital phase.
- **AVERAGE ORBIT** The folded trend is then averaged and smoothed by a boxcar (where the width is 2 observations).
- **UNFOLD** The smoothed trend is re-interpolated back to the original time points.

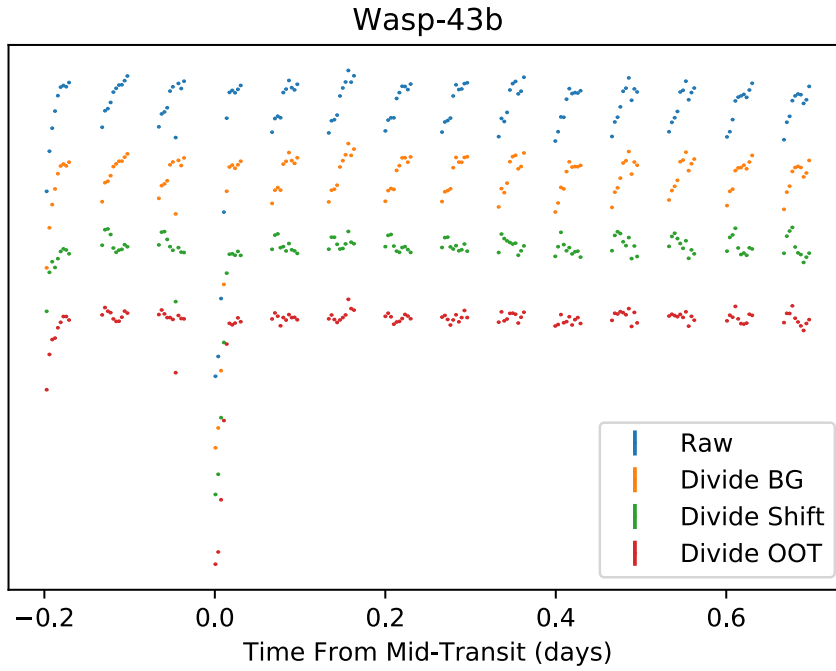


Figure 3.20: Example of the effect of the light curve corrections on Wasp-43b. This target presents particularly strong systematics due to the shifting of the target on the detector. Wasp-43b has a very narrow transit and so is not used in this work. Numerous orbits were taken to encompass the full phase curve. Each of the three corrections applied here are discussed below, offset for clarity. The systematics in the raw light curve are $\sim 0.5\%$. The final light curve (red) has systematics greatly reduced over the raw case.

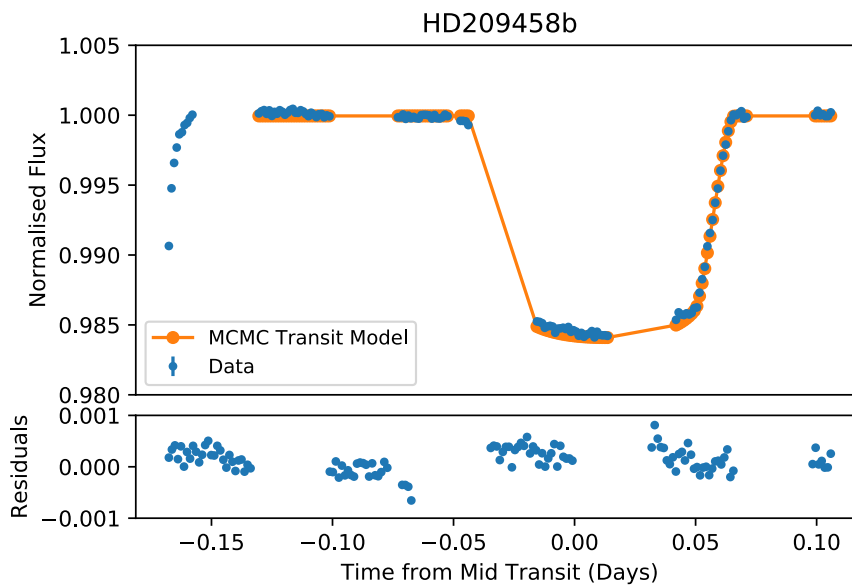


Figure 3.21: White light curve for HD209458b with the best fit transit model as derived by MCMC fitting routine EXOFAST. Note the initial 8 points have been omitted from the transit model fit due to the ramp up experienced by the first few points of all exposures. (See section 3.2.1.6)

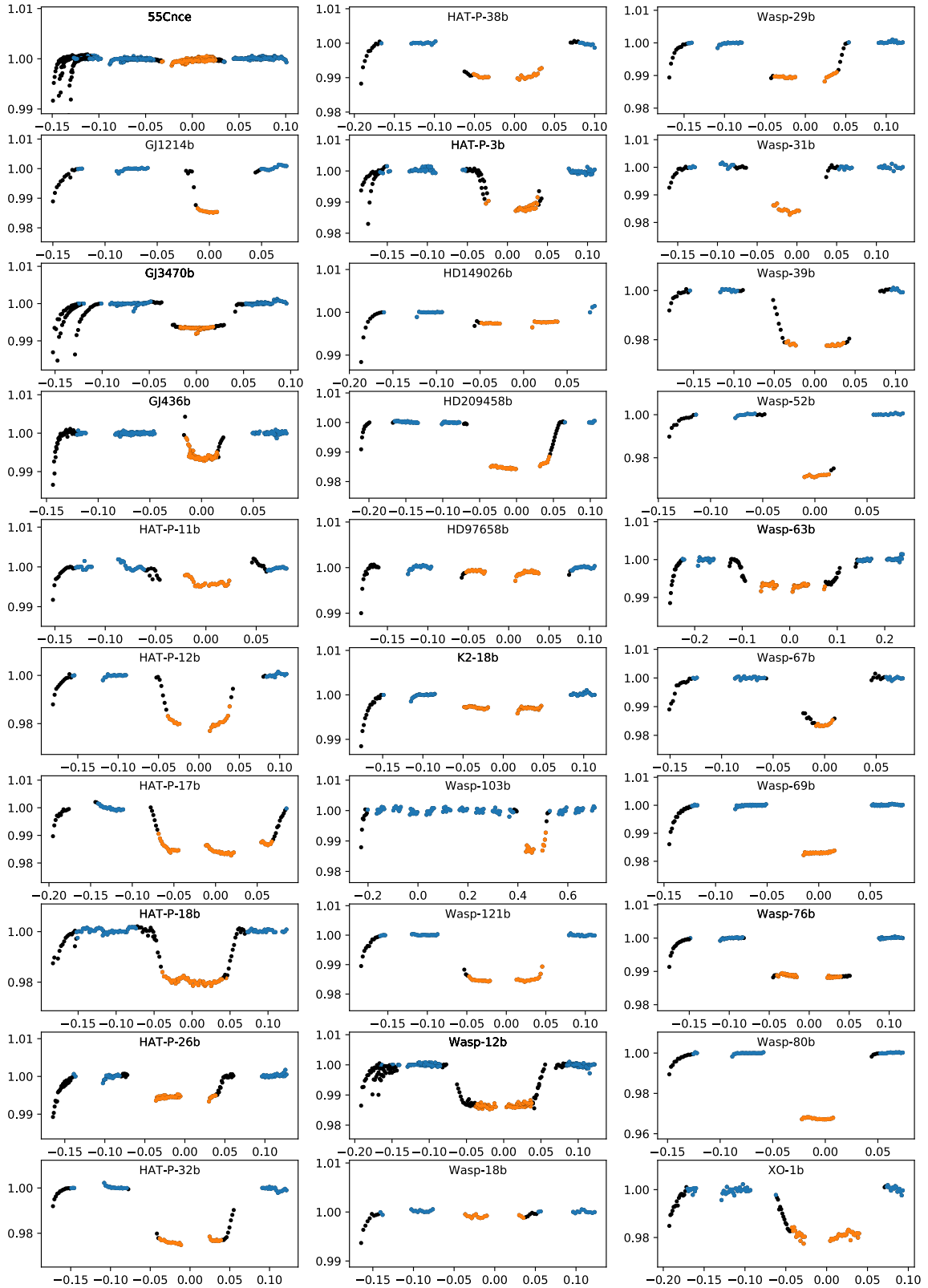


Figure 3.22: Examples of the white light curves derived by my pipeline. In cases where multiple visits of data have been taken I reduce each visit separately. The light curves from each reduction are over-plotted. Here orange points indicate what my pipeline uses as 'in-transit' observations and blue points are 'out-of-transit' observations.

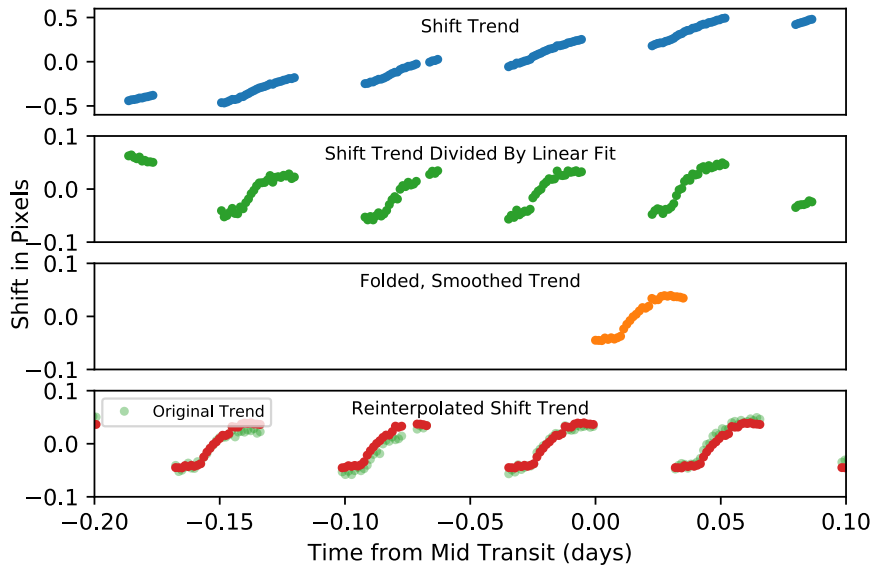


Figure 3.23: Example of how orbit folding works to create a smoothed residual shift trend for HD209458b. The original shift is first divided by a linear fit, folded based on the orbital phase and then averaged and smooth. The new trend is then re-interpolated onto the original time grid. This process is also followed to create a uniform background trend for each orbit.

- **LEAST SQUARES FIT** The trend is varied in amplitude and least-squares fit to the out-of-transit data only, this ensures the transit and ingress/egress points do not affect the fit.
- **DIVIDE** The final trend is divided out of each channel.

The reduced χ^2 is calculated for each channel individually as channels close to sharp spectral features are most affected, as seen in Figure 3.12. This procedure is also shown for clarity in Figure 3.23.

3.5.3 Residual Background Trends

The background found in Section 3.2.4.2 is a multiplicative trend that is found in each channel. An example of the trend is shown in Figure 3.9. This trend is fit to each channel in exactly the same way as above. The background is folded, averaged, unfolded and least squares fit to the out of transit data. Each channel is divided through by the best fitting background trend.

3.5.4 Divide Out Of Transit (OOT) Method

The Divide OOT method was first shown by Berta et al. (2012) and used in many other works.⁸² The method consists of using the average orbit trends in the out-of-transit (OOT) light curve data to create a trend to divide out of the in-transit data. It is assumed that the out-of-transit data samples a periodic trend that is identical in each orbit. Each orbit has this “OOT” trend divided through. This trend is created with the white light curve, as this has the best signal to noise ratio. I use the same method as presented in Section 3.5.2 to construct the average, phase-folded trend for the out of transit data, smooth and re-interpolate onto the time grid of the observations. This allows me to include partial information from incomplete orbits or orbits where some observations are missing.

⁸² etc; Deming et al. (2013a); Mandell et al. (2013); Kreidberg et al. (2014c)

The Divide OOT method is used in Deming et al. (2013a) to remove the systematic they label ‘the hook’. The hook receives its name from its distinctive curved shape, with an increase in the first few exposures then flattening. (Note this is different to the initial ramp-up from the space craft heating and occurs in every orbit regardless of the position within the visit.) In my work I find that the combination of dividing through by the shift trends and the background trend (discussed above) accounts for this hook in most targets. In most cases the divide OOT methods provides only a small correction.

3.5.4.1 *White Light Residuals*

Having corrected for the three trends above there may still be a residual trend. Mandell et al. (2013) uses this method to further clean the data. Using the EXOFAST code from Eastman, Gaudi, and Agol (2013) I fit a transit model to the white light curve with a Monte Carlo Markov Chain (MCMC). The model is then subtracted from the white light curve to create “white light residuals”. These residuals can then be fit to each channel using the same procedure as above and removed. However, there is a criticism of this method; instead of comparing the channel light curves to the average white light curve you are instead tuning it to the theoretical model flux. Because of this I do not employ this method as standard in my pipeline.

3.6 TRANSMISSION SPECTRA

Once the light curves has been cleaned and normalised I create the transmission spectrum. This is simply the change in transit depth δ as a function of wavelength, δ_λ . Having cleaned the data any remaining change in transit depth should be due to the exoplanet atmosphere. We assume that features such as star spots, which might also cause changes in transit depth, do not vary greatly with wavelength. I test this using the out-of-transit data as discussed in Section 3.7.3.

There are three ways to find δ_λ : the median of in transit data, least squares fitting the white light curve and fitting a transit model to each channel light curve. These are discussed below, and compared in Figure 3.25.

Binning and Smoothing Channels

Knutson et al. (2008) and Deming et al. (2013a) employ a Gaussian smoothing kernel and binning of 4 channels (wavelength pixels) in order to mitigate the effects of the shifting of the star as a function of time. In this work I follow this procedure and smooth and bin, increasing the signal to noise ratio for each light curve. This is performed after all corrections, before analysing the transmission spectrum. Binning also increases signal to noise in the final transmission spectrum at the cost of lowering resolution.

An example of the effect of smoothing and binning is show in Figure 3.24 where we see the peak from the Paschen β line being poorly approximated is smoothed over. This would theoretically allow atmospheric models to be fit more easily, although inflating the error bars based on the shifts and relevant stellar features would be more robust.

3.6.0.1 *Median Level*

The first way to find the change in transit depth as a function of wavelength is to simply average all the in-transit data and compare with the out-of-transit data. This is the most simple of the available options. It relies on there being a significant portion of the data in-transit, as well as the lack of stellar activity such as star spots. Any ingress and egress points are omitted, as they will only contain a fractional contribution from the atmosphere and may have contributions from stellar limb-darkening. The out-of-transit portion of the light curve is assumed to be completely

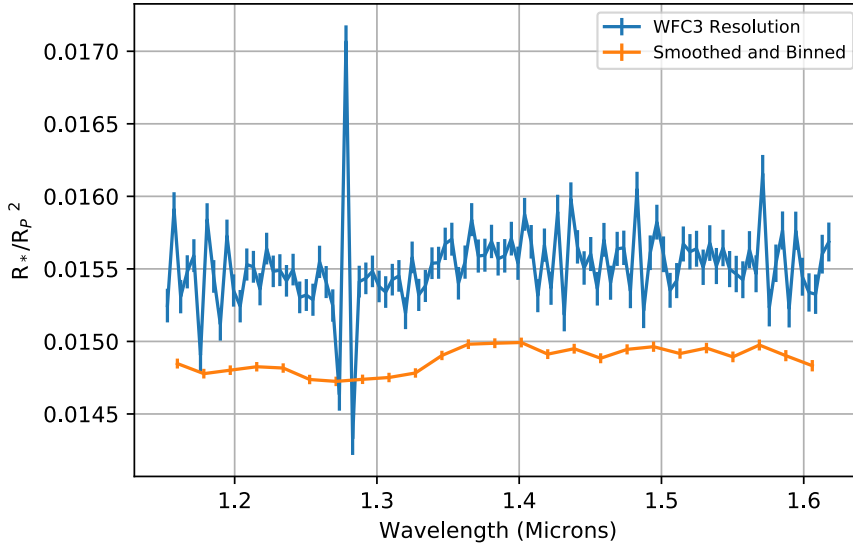


Figure 3.24: Example of the HD209458b transmission spectrum in the native WFC3 resolution (blue) and after binning and smoothing by 4 pixels (red). Note the Paschen β line at 1.28 μm is a high contrast feature where shifts during the course of the observation cause large errors.

flat, with a normalised stellar flux of 1. This is enforced in the code with linear fit on the out-of-transit data in each channel to remove any slopes induced by source shifting (see Section 3.5.2). The in-transit data is averaged, using only data in the ‘base’ of the transit. The in transit data is averaged for each channel, creating one value as shown below

$$\delta_\lambda = 1 - \sum_{t=a}^b \frac{f_\lambda}{(b-a)} \quad (68)$$

where δ_λ is the value of the transmission spectrum in each wavelength (R_p/R_p^2 as shown in Section 3.2.4.2) and $t = a, b$ are the times at the start of the transit (a) until the end of the transit (b). f_λ is the normalised flux as a function of wavelength.

This approach is simplistic. The drawback for fitting in this way is that the ingress and egress points cannot be used, reducing the number of observations that can be used to construct the average.

3.6.0.2 Least Squares Fitting

In order to use all of the observations we must fit a transit curve to the data. One simple way to do this is to fit the white light curve to every channel, allowing only the transit depth to vary. Deming et al. (2013a) employs this method and I adopt it in this work. This approach has an added benefit of using more information than taking the median transit level, as the ingress and egress slopes are used to aid with the fit. However, there is a drawback that the effects of limb darkening are not taken into account. Limb-darkening is wavelength dependent and will cause changes to the ingress and egress shape. Using an average white light transit fixes the shape of the limb-darkening contribution and may reduce the quality of the fit. In this work I assume that the effect of limb-darkening is small and can be ignored.

3.6.0.3 Full Transit Model Fitting

A final approach is to fit a transit model to every channel. I do this using the EXOFAST code⁸³ which employs an MCMC to fit a transit model. The MCMC will fit

⁸³ Eastman, Gaudi, and Agol (2013)

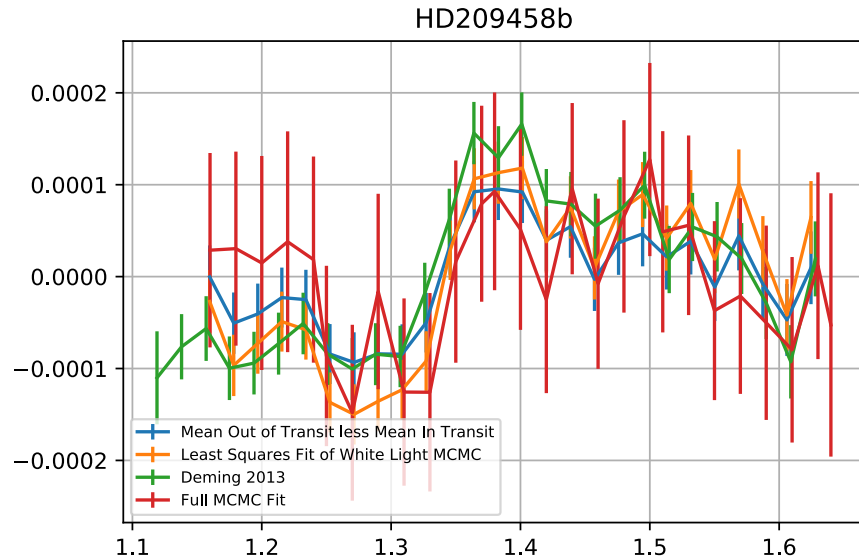


Figure 3.25: Comparison between the results from (Deming et al. (2013a)) and the results of each different type of fit discussed in Section 3.6.

many more parameters than the transit depth including the transit centre, R_p/R_* (relative planet radius), a/R_* (orbital distance/stellar radius), limb darkening coefficients and orbital inclination. The benefit of fully fitting each light curve is that more information can be used to constrain the fit. This would include fitting parameters such as the wavelength dependent limb-darkening. I find fitting a transit model in this manner leaves too many open parameters, inflating the errors in the retrieved transit depth unnecessarily. Full model fitting has one final drawback; for some targets there is not enough in-transit data which causes the fit to produce large errors or not to converge. In such cases it is not possible to estimate the transmission spectrum using an MCMC transit model fit.

On balance, the cost of fitting more parameters on the errors outweighs the benefit of fitting limb-darkening parameters in this case. Further work could be undertaken to fit a transit model with only limb-darkening and transit depth as free parameters.

3.6.0.4 Comparison of Methods

Examples of all three types of fitting are shown in Figure 3.25 with the literature data on HD20958b from Deming et al. (2013a). All methods return similar results. The errors are large in the MCMC fit as too many parameters have remained open to fitting. Based on the three methods I find the least squares fitting to be optimal as it has the smallest errors. The median method is more susceptible to errors from variance in the base of the transit from stellar spots and does not use all of the ingress and egress data.

3.7 DATA VALIDATION

In the section above I have attributed the wavelength variability to the exoplanet atmosphere. However, we have made an assumption that we have appropriately corrected for all systematics. There may be other systematics in the observation that haven't been addressed in my pipeline, or other astrophysical sources of variability. In this section I present four tests to assess the quality of the data and validate it. The tests performed here show the data are internally and externally consistent, lending weight to further assessment of the data.

Firstly, I test different observations of the same planet to find if the data are internally consistent. I also compare my results with literature results to find if the transmission spectra produced in this work are externally consistent.

Finally I test the repeatability of the water abundance measurements using atmosphere models on my results and the accepted literature result for HD209458b. This tests the repeatability of abundance measurements between independent analysis of the data. I find that the water abundance retrieved is identical within errors between my reduction and the literature result. This lends weight to further assessment of the water feature in this work despite small differences in reduction methods and systematic corrections.

In this section I present a new test for transmission spectra that I will refer to as the “out-of-transit test”. This tests the variability in wavelength in all of the out of transit data and compares it with the transmission spectrum. This is used to discount targets with high variability from further analysis.

3.7.1 *Internal Consistency*

I am able to check for internal consistency in my results using multiple observations of the same target. Allowing for any small changes in systematics or astrophysical variability I expect observations of the same target to produce the same result. Below I discuss two such tests, one using the round-trip mode of WFC3 and one using multiple visits.

3.7.1.1 *Round trip Observations*

Observations made in round trip mode alternate two different scan directions, (see section 3.2.1.4). The two sets are split into separate groups at the beginning of the reduction. This creates two transmission spectra for each target which I can compare. These two spectra should in theory be identical, since they are both observations of the same transit with the same observing strategy.

Figure 3.26 shows the different reductions of the transmission spectra of Wasp-76b. The two scan directions produce identical results within errors. This lends weight to the reduction process producing consistent results. Figure 3.36 shows all of the final transmission spectra produced in this work. Each of the

3.7.1.2 *Consistency Between Visits*

Some targets have benefited from multiple visits by HST. I treat each visit individually in my reduction and combine them after transmission spectra have been produced. Unlike the round trip case, multiple visits observe different transits. These different transits potentially cross star spots or contain different systematics. Additionally, the exoplanet atmospheric signal itself could be changing, though we would expect any effects to be small. However, allowing for these factors we would expect the transmission spectra to be similar from visit to visit.

The exoplanet GJ3470b has been observed in 3 visits, each in roundtrip mode. Based on the above section each scan direction is consistent. Figure 3.27 shows the final transmission spectra for each visit of GJ3470b after the round-trip observations have been averaged. Each of the spectra have been compared with the average of the three after smoothing by a 6 point boxcar. The spectra are consistent within errors. Based on these three visits the reduction process appears to be stable from visit to visit.

3.7.2 *Consistency with Literature Results*

Having validated that the data produced by my pipeline are consistent I can now compare them with independently produced reductions from literature. I expect independent reductions to align with my results within errors. Figure 3.28 shows a

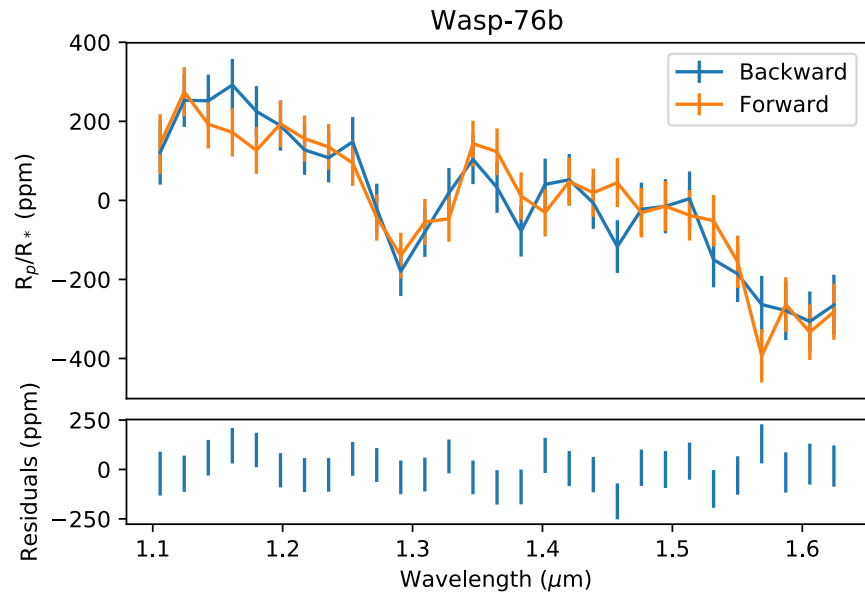


Figure 3.26: Retrieved transmission spectra for Wasp-76b. The two scan directions are broken up into two separate groups and reduced entirely separately. (Note there is an offset between these two transmission spectra which has been removed, due to slightly different transit depths.)

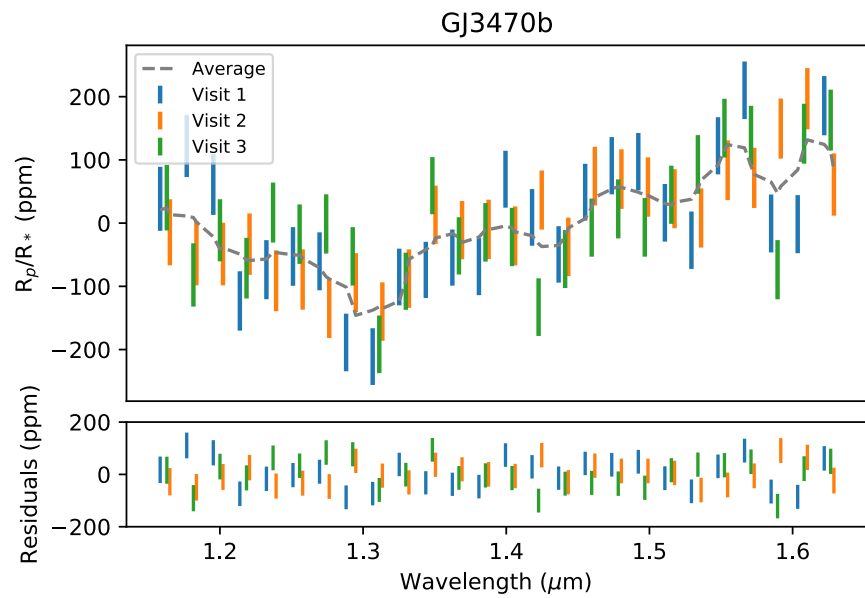


Figure 3.27: The transmission spectra for three visits of GJ3470b with the two scan directions added. We see the spectra are largely within errors and there is only a small discrepancy at the blue end of the spectrum.

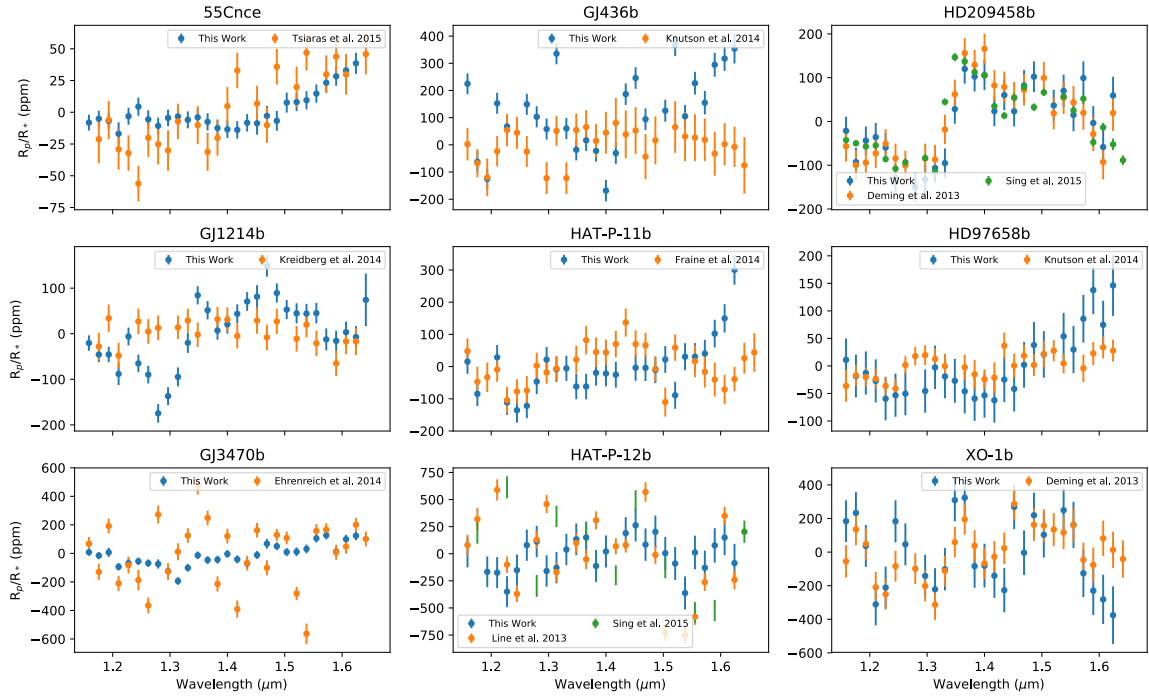


Figure 3.28: Examples of transmission spectra with this data from literature as accessed through the NASA exoplanet archive. Many of the transmission spectra derived in this work have not yet been published and have no literature values to compare to.

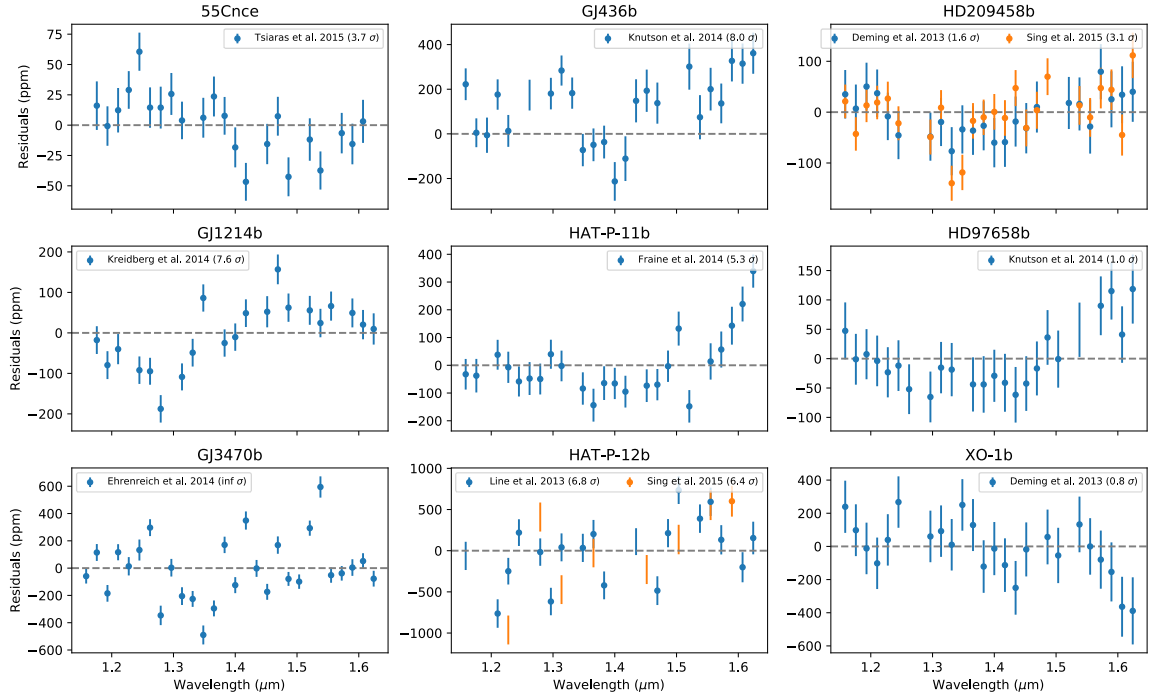


Figure 3.29: Residuals between the transmission spectra produced in this work and literature results accessed through the NASA exoplanet archive. Note that because the literature spectra are quoted at a range of resolutions I have binned down both spectra. In many targets there is a slight slope towards the red end of the spectrum.

Planet	Ref
55Cnce	Tsiaras et al. 2015
GJ1214b	Kreidberg et al. 2014
GJ3470b	Ehrenreich et al. 2014
GJ436b	Knutson et al. 2014
HAT-P-11b	Fraine et al. 2014
HAT-P-12b	Line et al. 2013
HAT-P-12b	Sing et al. 2015
HD209458b	Deming et al. 2013
HD209458b	Sing et al. 2015
HD97658b	Knutson et al. 2014
XO-1b	Deming et al. 2013

Table 3.5: List of literature results for exoplanets used in this work reported by the NASA Exoplanet Archive.

comparison between my work and literature results for the 9 targets where literature transmission spectra are available. Transmission spectra are retrieved from the NASA Exoplanet Archive, a table showing all of the planets and each of their references is given in Table 3.5. All of the transmission spectra have been renormalised to account for slight differences in the retrieved transit depth. Different sources use different wavelength grids for their transmission spectra. To compare each source all the transmission spectra binned to a lower resolution. I average transmission spectra from this work with multiple sources, either from multiple scan directions in roundtrip mode or multiple visits.

Figure 3.28 shows the retrieved transmission spectra are largely within errors of the literature results. Figure 3.29 shows the residuals between the my transmission spectra and literature results. Note in this work 55 Cancr e and GJ3470b both use more visits than the literature transmission spectrum, due to more data having been taken since their publication. This results in smaller errors in my reduction than in the literature spectra. HAT-P-12b is a smaller planet (see Figure 3.1) and so has a noisy transmission spectrum. This is shown by both two literature transmission spectra producing very noisy results.

Based on comparisons with literature results I find that my analysis produces transmission spectra consistent with other independent reductions. Small differences are expected due different assumptions in systematic removal. Particularly, HD209458b is consistent with reductions both from Deming et al. (2013a) (within 1σ) and Sing et al. (2015) (within 2σ). Similarly 55Cnce, XO-1b, HD97658b and GJ1214b are all consistent within 2σ . This lends weight to the consistency of my reduction and I am confident in the results of my pipeline.

In HD97658b, HAT-P-11b and GJ346b there is a slope at the redder edge of the spectrum, (clearly seen in the residuals). This suggests there may be a further systematic in my data that I have not corrected for. In further work I will use the water feature at $1.34\mu\text{m}$ to analyse these transmission spectra, which I expect not to be affected by this systematic. This is discussed further in Section 3.8.

3.7.2.1 Stability of the Water Feature

In the Section 3.8 I investigate the water feature in each of the transmission spectra. To use this feature in further assessment I must first be confident that the measurement of the water feature is repeatable between different independent reductions of the data. I do this in the simplest terms by fitting an atmospheric model to the water

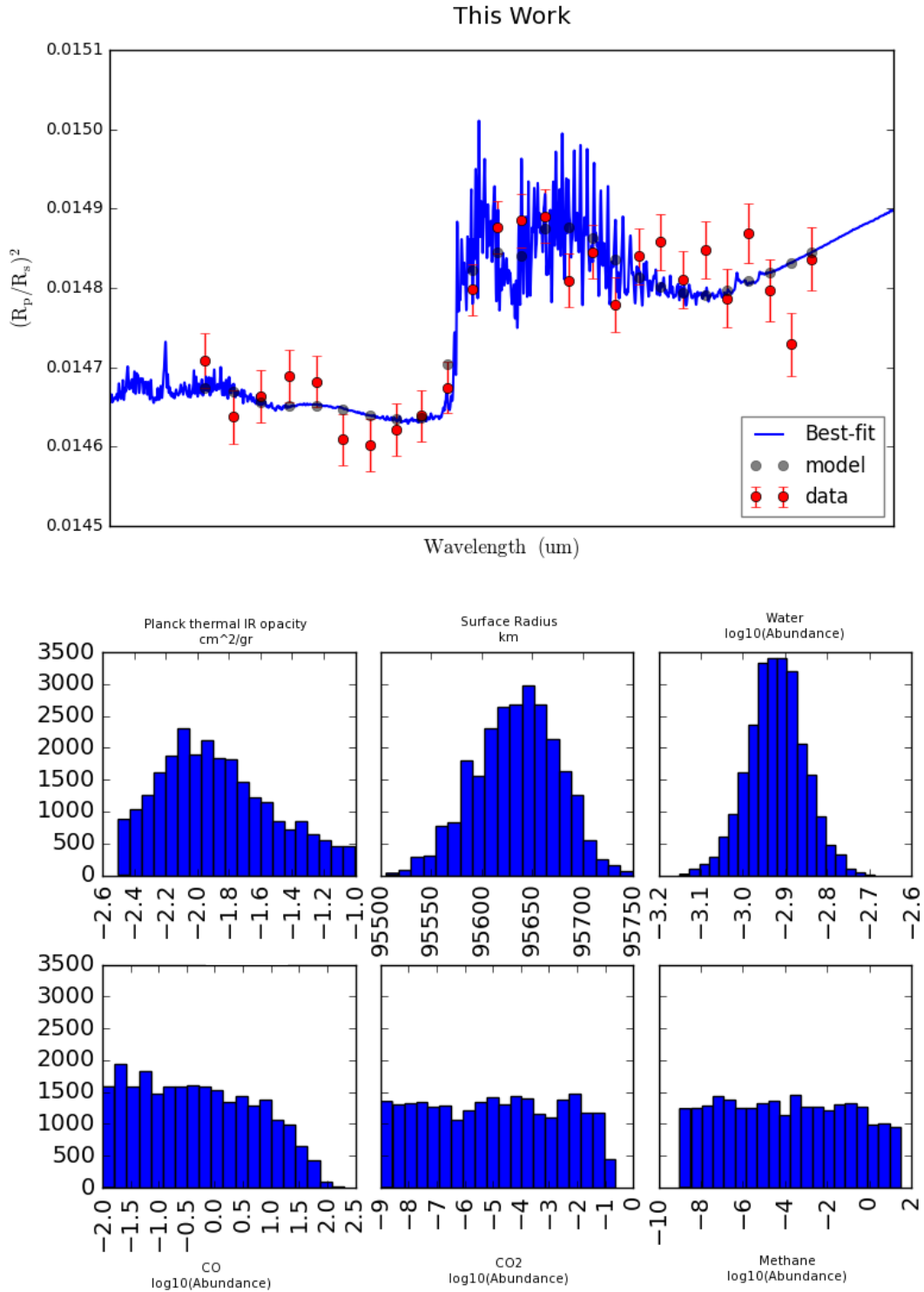


Figure 3.30: Fit to the transmission spectrum of HD209458b derived by this work. The derived atmosphere fits well across the transmission spectrum. CO and CO₂ are unable to be constrained in this portion of the spectrum however methane does peak in the near IR, though here it is also unconstrained. The water abundance is $\log_{10}(n) = -2.93 \pm 0.065$.

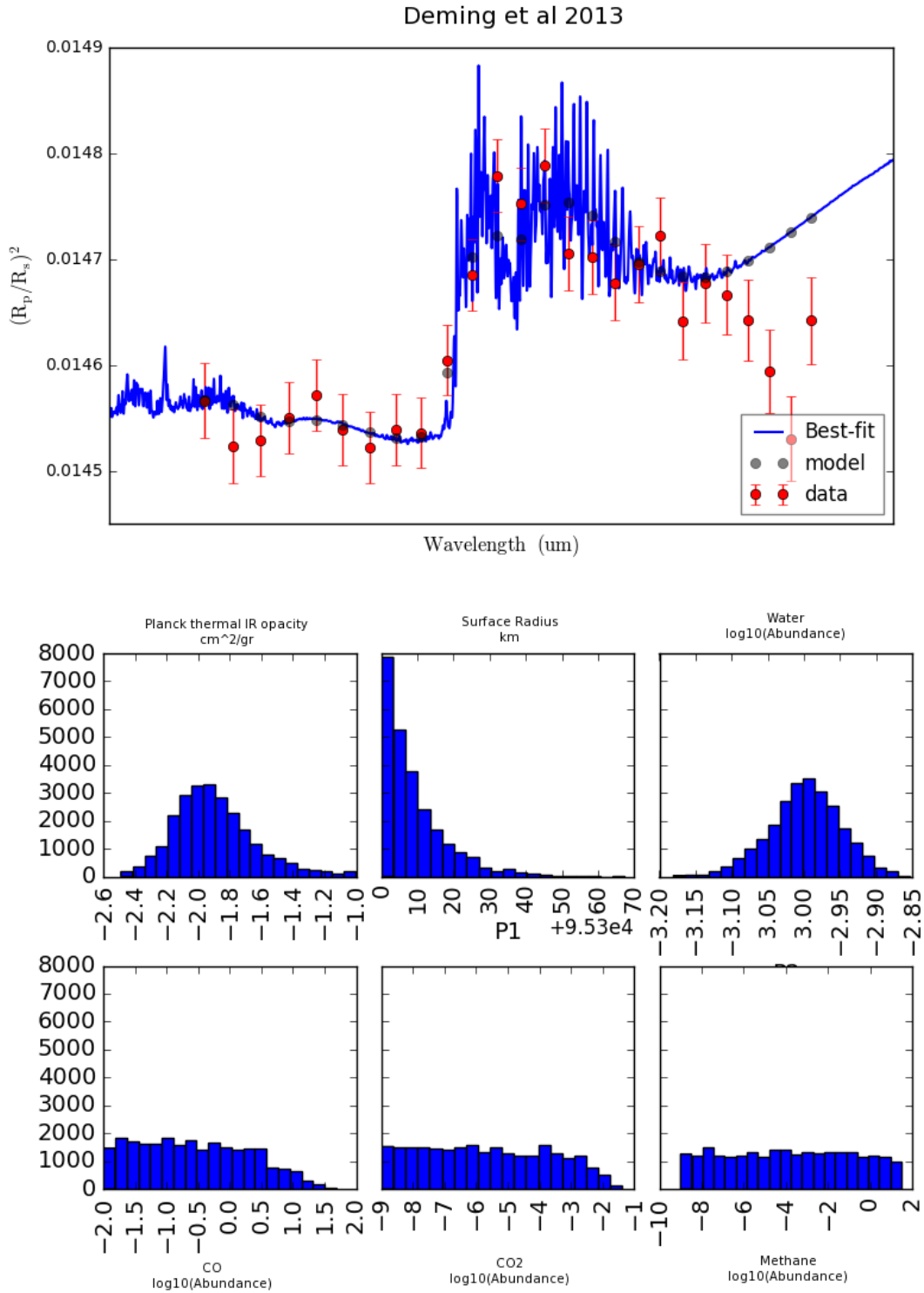


Figure 3.30: Fit to the transmission spectrum of HD209458b derived by Deming et al. (2013a). All the priors and fixed parameters have the same value as for the model fit above. The derived abundance parameters are very similar, with a water abundance of $\log_{10}(n) = -3.00 \pm 0.046$. While this produces a fairly good fit the redder end of the spectrum is not well described. A more sophisticated atmospheric model may be needed to conclusively find the difference between the two cases.

Reduction	Water Abundance
This Work	$\log_{10}(\eta) = -2.93 \pm 0.065$
Deming et al. (2013a)	$\log_{10}(\eta) = -3.00 \pm 0.046$

Table 3.6: Derived water abundances for HD209458b using atmospheric retrieval code BART. Both the transmission spectrum from this work and from Deming et al. (2013a) agree well on the abundance measurement.

feature for HD209458b and measuring the theoretical water abundance. If this abundance measurement is the same between the two reductions the water feature must be fairly stable, regardless of different assumptions between different reduction procedures. This is shown for the exoplanet HD209458b, compared with the accepted literature result from Deming et al. (2013a).

In Figure 3.30 I show the final transmission spectrum of HD209458b from this reduction. In the second panel I show the literature result from Deming et al. (2013a). Each spectrum has been fit using the atmospheric retrieval code ‘Bayesian Atmospheric Retrieval Code’ (BART), which is publicly available Cubillos et al. (2014); Cubillos (2016). BART combines atmospheric models from Blečić, Harrington, and Bowman (2016) with models of transit geometry and MCMC fitting. It finds the optimal abundances for molecules in exoplanet atmospheres based on transmission spectra. BART fits for the abundance of H₂O, CH₄, CO₂ and CO. It also fits for the surface radius of the planet and the atmosphere opacity. We see from both panels in Figure 3.30 CH₄, CO₂ and CO are not constrained in this fit. This is expected, as they do not exhibit strong features in this wavelength regime (see Chapter 2).

Both transmission spectra are well fit by a water rich model. The model performs slightly worse at the red end of the spectrum with the literature data, though it would be possible to achieve a good fit if less strict priors were set on the surface radius parameter. The surface level of the planet is a few percent smaller than the one found using my reduction, but is poorly constrained by the same prior. Water is fairly well constrained in both cases. The water abundance derived in each case is shown in Table 3.6. I find that the two reductions produce the same water abundance within errors, suggesting that the water feature itself is fairly similar regardless of the reduction used. This supports further analysis of the water feature in the sections below.

3.7.2.2 Evidence for Systematic in Transmission Spectra

In this analysis some transmission spectra show evidence of molecular features in the same region as the water feature. I have attempted to fit two of these planets with atmospheric models using BART. Transmission spectra and model fits for Wasp-76b and HAT-P-32b are shown in Figure 3.31. I have been unable to fit a physical model accurately to the transmission spectra due to an apparent excess at wavelengths shorter than the 1.34 μ m water feature. It is tempting to suggest that there is some feature in the model that is not being fit, either some haze component or some molecule beyond H₂O and CH₄. However, there are no common molecules that peak in this region, as shown in Chapter 2. I believe this may be evidence of a further systematic problem that has not been mitigated in my pipeline.

Both the above model fits and comparisons with literature have shown that there may be additional systematics in the transmission spectra produced in this work. This includes the slope at bluer wavelengths seen in HAT-P-32b and Wasp-76b and the slope at redder wavelengths seen in HD97658b, HAT-P-11 and Wasp-18b, (see Figures 3.28 and 3.36).

One cause of these systematics may be other sources on the detector. In this work I do not attempt to correct for any background sources contaminating the spectrum. This is particularly problematic in spatial scan mode where the traces can overlap between MULTIACCUM readouts. This additional source will cause discrepancies

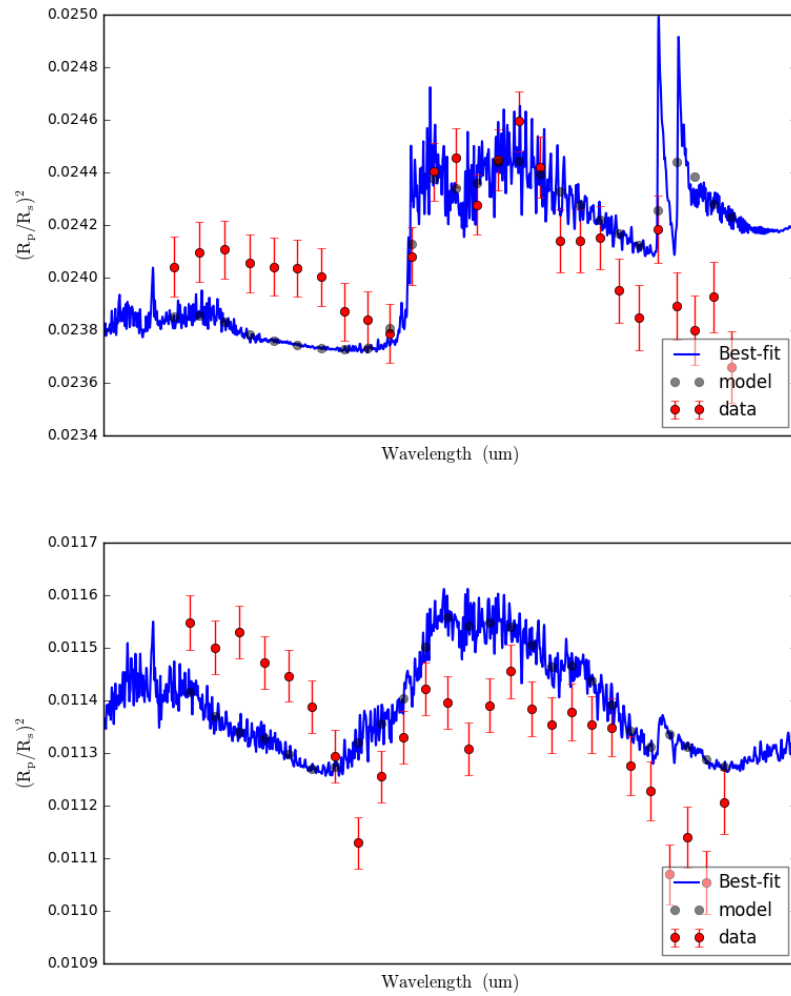


Figure 3.31: Best fit BART atmospheric spectrum to HAT-P-32b (top) and Wasp-76b (bottom). Here only water and methane have been used. Neither fit converges well and the best fits fail at the blue edge of the spectrum.

in the measured stellar template and exoplanet transmission spectrum. It is hard to mitigate such a problem and a detailed investigation into each target would be needed to find any contaminating nearby sources.

A further cause for any discrepancies or slopes in the final spectra may be from limb darkening. While the effects of limb darkening are small, there is a wavelength dependence which will reduce the transit depth towards longer wavelengths. Based on preliminary investigations, the magnitude of this effect may be large in some cases and limb darkening may explain the persistent slopes in some targets. Figure 3.32 shows the observed data for targets Wasp-76b and Wasp-80b with synthetic HST data I have generated. The synthetic data contains only water absorption, (using data from Chapter 2), scaled to a physical level based on the scale height of the planet (see Section 3.8). The synthetic data has been generated both with and without limb darkening (using the LDTK code⁸⁴ and PyTransit code⁸⁵) to gain a qualitative understanding of the effect. Both targets show an additional slope, with the hotter Wasp-80b showing a significant slope at the redder end. Based on this, it is clear that limb-darkening must be accounted for and more work on the pipeline is warranted.

⁸⁴ Parviainen and Aigrain (2015);
Husser et al. (2013)

⁸⁵ Parviainen (2015)

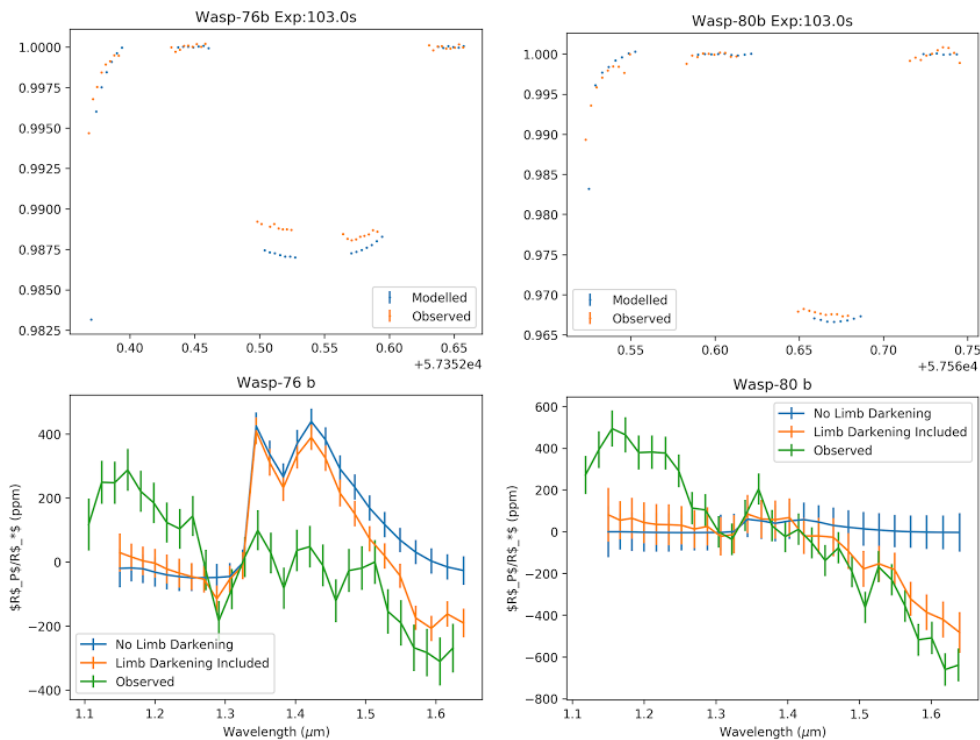


Figure 3.32: Preliminary test of the effect of limb-darkening. I developed a synthetic model of HST data using my own routines and the codes LDTK and PyTransit. The top panels show synthetic transits and the lower panels show synthetic spectra. These spectra are based on simple water absorption and the scale height of each planet. The synthetic model was run on two targets, both with and without limb-darkening. It is clear that limb-darkening does play a role, particularly in the case of the hotter star Wasp-80b.

3.7.3 Out-of-Transit Testing

One of our assumptions is that the variability between channels occurs only during transit. However, there may be variability also in the channels before or after the exoplanet crosses. For example, there may be stellar activity that causes a channel dependent variability. There may also be systematics which causes the channels to be noisy. Any signal from the transmission spectrum must be stronger than this channel variability.

To test the base level of channel by channel variability we can use the out-of-transit data. We can perform a simple test by taking the average of the first half of the out-of-transit data from the average of the second half. This is equivalent to the Median Level fitting method, see Equation 68. However, in this case we are comparing the star to itself rather than the star to the transit. This test is given as

$$\delta'_\lambda = \sum_{t=a_1}^{b_1} \frac{f_\lambda}{(b_1 - a_1)} - \sum_{t=a_2}^{b_2} \frac{f_\lambda}{(b_2 - a_2)} \quad (69)$$

where $t = a_1 \dots b_1$ are the time stamps for the first half of the out-of-transit data and $t = a_2 \dots b_2$ are the time stamps for the second half. I refer to this as the OOT test. An example of the transmission spectrum for HD209458b compared with the OOT test is given in Figure 3.33. The OOT test is flat within errors and the transmission spectrum deviates significantly from it, suggesting there is true astrophysical variability.

The resultant OOT test spectrum should be flat. If the variance in the OOT test is similar to the variance in the transmission spectrum this suggests there is no significant astrophysical signal beyond that of the star and the systematics. If the out of transit test is correlated with the transmission spectrum this suggests that the variability is consistent across all channels, regardless of the planet presence. Finally if the out of transit test is not flat with respect to wavelength we would expect the same trend in transmission spectrum.

Two examples of the OOT test are given in Figure 3.34. For HD209458b the test is flat, uncorrelated with the transmission spectrum and has a smaller variance than the transmission spectrum. For 55 Cancri e the transmission spectrum is sloped, non-flat to a 2σ level and has a much larger variance than the transmission spectrum. Based on visual inspection of the transmission spectra and OOT tests I present a scheme for rejecting badly reduced transmission spectra based on the OOT test. The criteria are the following: 1) The OOT Test variance must be less than twice the transmission spectrum variance. 2) The transmission spectrum must be flat with respect to wavelength based on a reduced chi-squared fit. Any targets that are not flat to the 2σ level are discounted. 3) The OOT Test and the transmission spectrum must have a correlation coefficient less than 0.6 based on a Pearson correlation test (implemented by numpy's *corrcoef* function). These cuts are conservative and exclude only the most extreme cases. Harsher cuts could be applied to get a cleaner sample. Figure 3.35 shows these thresholds against the population of planets. Those targets that were rejected are given in Table 3.7. In further analysis in the sections below these targets have been excluded.

3.8 RESULTS

Having validated the data and rejected based on the OOT test I can be confident in the ensemble of transmission spectra. In this section I will analyse the spectra as a group to establish trends in the strength of the water feature across a range of planet types.

While estimating the abundance of water would be a useful way to track the strength of the water feature, this would require full atmospheric retrieval. There are many assumptions in modelling an exoplanet atmosphere based on chemistry and the interior conditions. In this work I rely only on the data to make claims about the strength of the water feature in each target. This is a data driven approach and has fewer assumptions. This also makes my work easily reproducible.

To measure the water feature height I follow a similar procedure to that in Sing et al. (2016). I subtract the average of the transmission spectrum from $1.22\mu\text{m}$ to $1.33\mu\text{m}$ from the average cross section from $1.34\mu\text{m}$ to $1.49\mu\text{m}$, where the water feature peaks. The water feature height h_w is given as

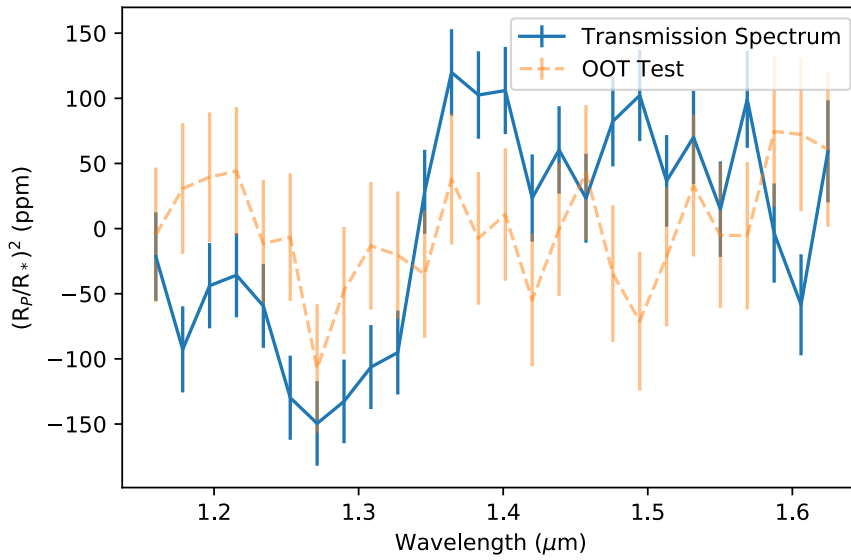


Figure 3.33: Example of an OOT test for HD209458b compared with the retrieved transmission spectrum. The OOT test shows whether there was similar variance in the channels before and after the planet was transiting. In this case we see a significant signal above the out of transit test.

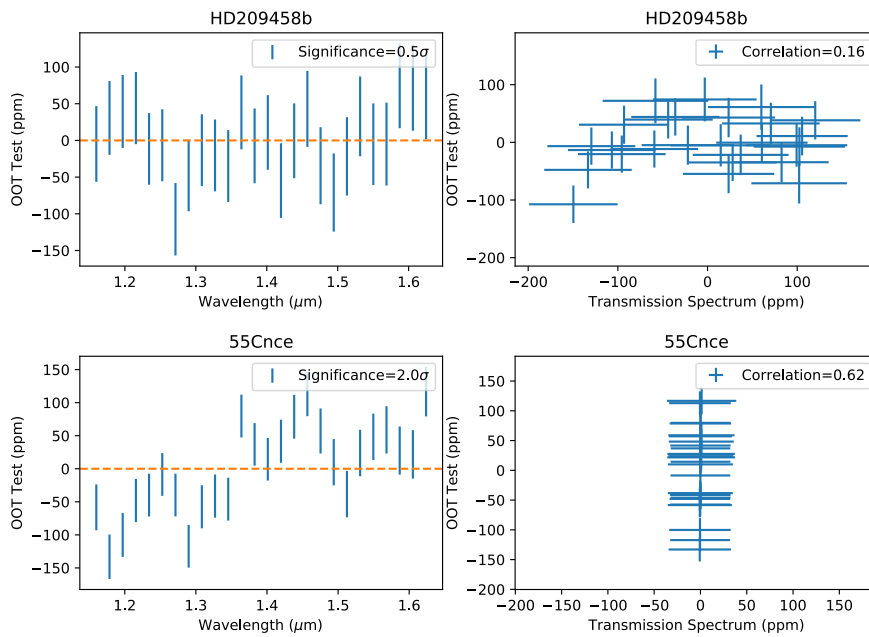


Figure 3.34: Two examples of the out-of-transit test from my pipeline. We see HD209458b has an uncorrelated, low variability out-of-transit test. However, XO-1b has a correlated, highly variable out-of-transit test, suggesting that the signal is not due to variability in the exoplanet atmosphere.

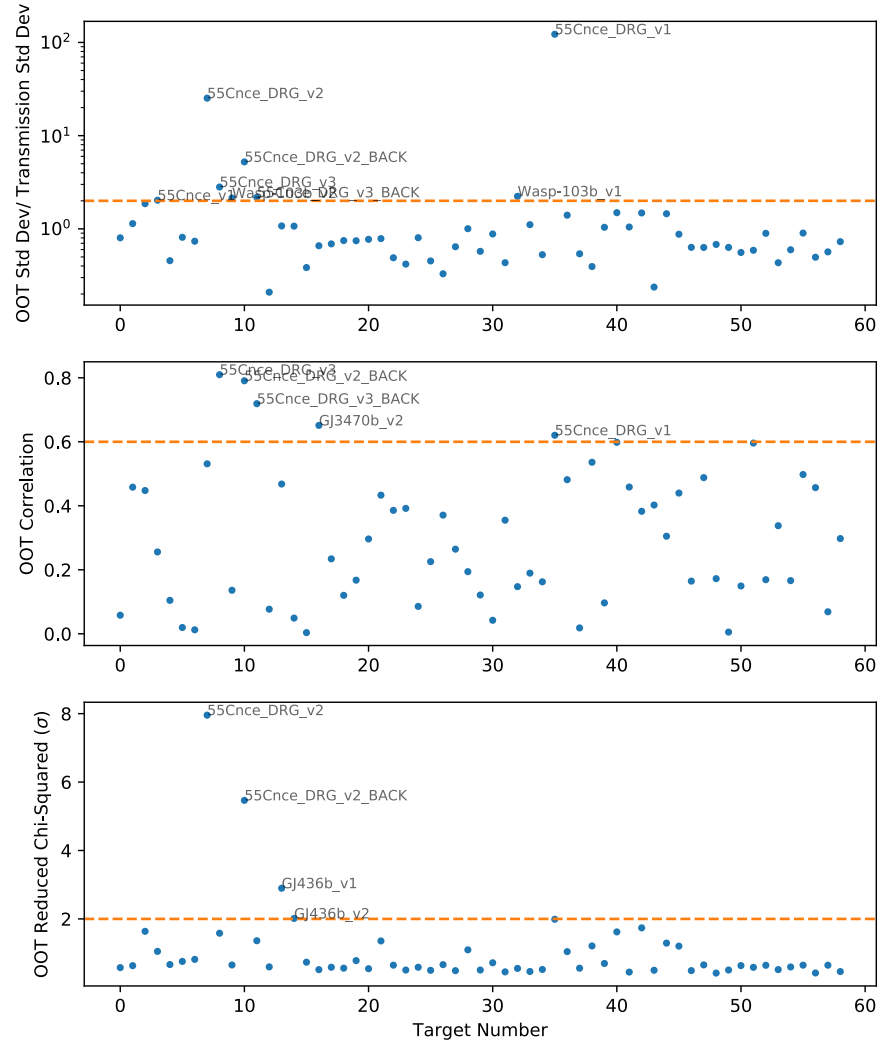


Figure 3.35: Thresholds for three different oot test parameters. Top: Ratio of standard deviation of the OOT test to the standard deviation of the transmission spectrum. Middle: Correlation between the OOT of transit test and the transmission spectrum as measured by a Pearson test implemented by numpy's *corrcoef* function. Bottom: significance of reduced chi-squared of the OOT test. All thresholds have been chosen by eye based on inspection of the transmission spectra and OOT tests.

Planet	Visit	Scan Direction	Variance	Correlation	Reduced Chi
55Cnce	1	Forward			Failed
55Cnce	2	Forward		Failed	Failed
55Cnce	3	Forward	Failed		Failed
Wasp-103b	2	Forward			Failed
55Cnce	2	Backward	Failed	Failed	Failed
55Cnce	3	Backward	Failed		Failed
GJ436b	1	Backward		Failed	
GJ436b	2	Backward		Failed	
GJ3470b	2	Backward	Failed		
Wasp-103b	1	Backward			Failed
55Cnce	4	Backward	Failed		Failed

Table 3.7: Targets disqualified by the OOT testing procedure with the tests that were failed.

$$h_w = \overline{\delta(\lambda)}_{\lambda=1.33\dots 1.49} - \overline{\delta(\lambda)}_{\lambda=1.22\dots 1.32} \quad (70)$$

where δ_λ is the transmission spectrum. In this section I will use the height of transmission spectrum in this region h_w as a measure of the strength of the water feature. This comes with the caveat that other molecules such as methane may be polluting the region, and that there may be residual systematics which could affect this measurement.

Based on the analysis of HAT-P-32b and Wasp-76b in Section 3.7 it seems there may be an excess in some targets blueward of the water feature. This would disrupt the height of the water feature as analysed by Equation 70. This is expected to give a lower estimate for water content in targets that exhibit this excess. In such cases h_w would be an underestimate.

3.8.1 A spectral sequence of Exoplanet Transmission Spectra

In a similar way to work from Sing et al. (2016) I am able to produce a sequence of transmission spectra based on the strength of the water feature, given in Figure 3.36. There are only five targets in common between these two works: HD209458b, HAT-P-12b, Wasp-31b, Wasp-39b and Wasp-12b. The sequence presented here is more limited in wavelength range, covering only the WFC3 G141 bandpass, but covers 30 unique exoplanets. My sequence has been ordered using the height of the water feature (h_w) to create a sequence of water rich targets to water poor targets. Figure 3.36 shows a wide variety of exoplanet transmission spectra, with clear water signals in several unpublished targets. (e.g. Wasp-39b, HAT-P-32b and Wasp-52b)

In the sequence we see HD209458b is not the most water rich planet. However, HD209458b is one of the best approximated transmission spectra with small errors. This is due to a combination of factors which amount to a high number of photons through the atmosphere: HD209458 is a bright star, the planet has a large scale height and the transit is long enough for several observations to be made at the base of the transit. These combine to make it one of the best measured transmission spectra.

Planets such as HAT-P-32b, Wasp-121b, Wasp-39b and Wasp-52b all appear to have strong peaks in their transmission spectra, leading them to be at the top of the sequence. They are much noisier than HD209458b and have larger errors owing to dimmer stars and the reduced number of in-transit points. Full atmospheric retrieval would enable further assessment of these features and an estimate of the water abundance in their atmospheres.

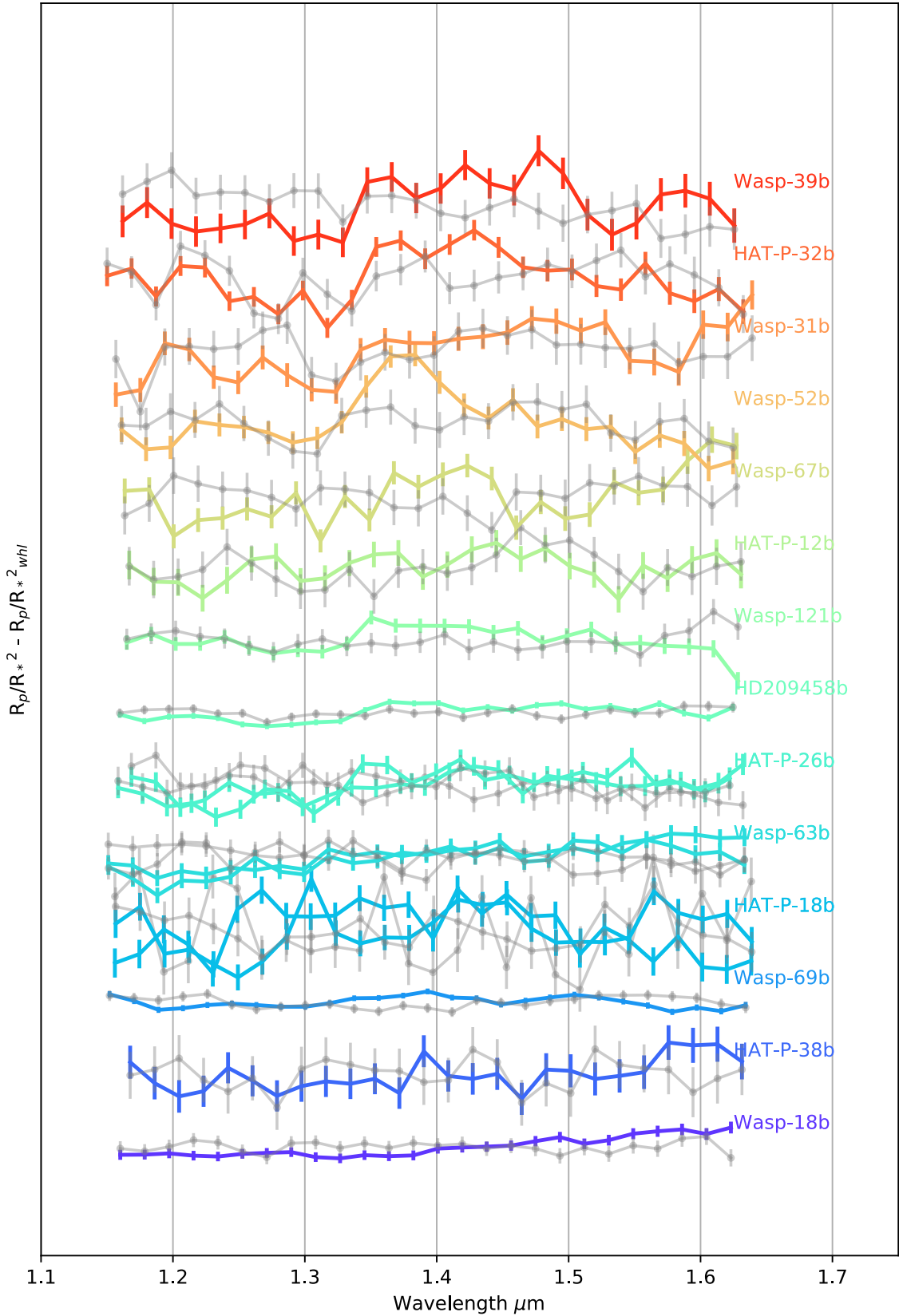


Figure 3.36: Spectral sequence of exoplanet transmission spectra based on water feature height given in Equation 70. The spectra are then ordered with the largest water feature to the lowest. The methane feature also peaks in a similar region making this an imperfect solution. Poor reductions such as XO-1b, where the OOT test is completely correlated with the transmission spectrum have been omitted.

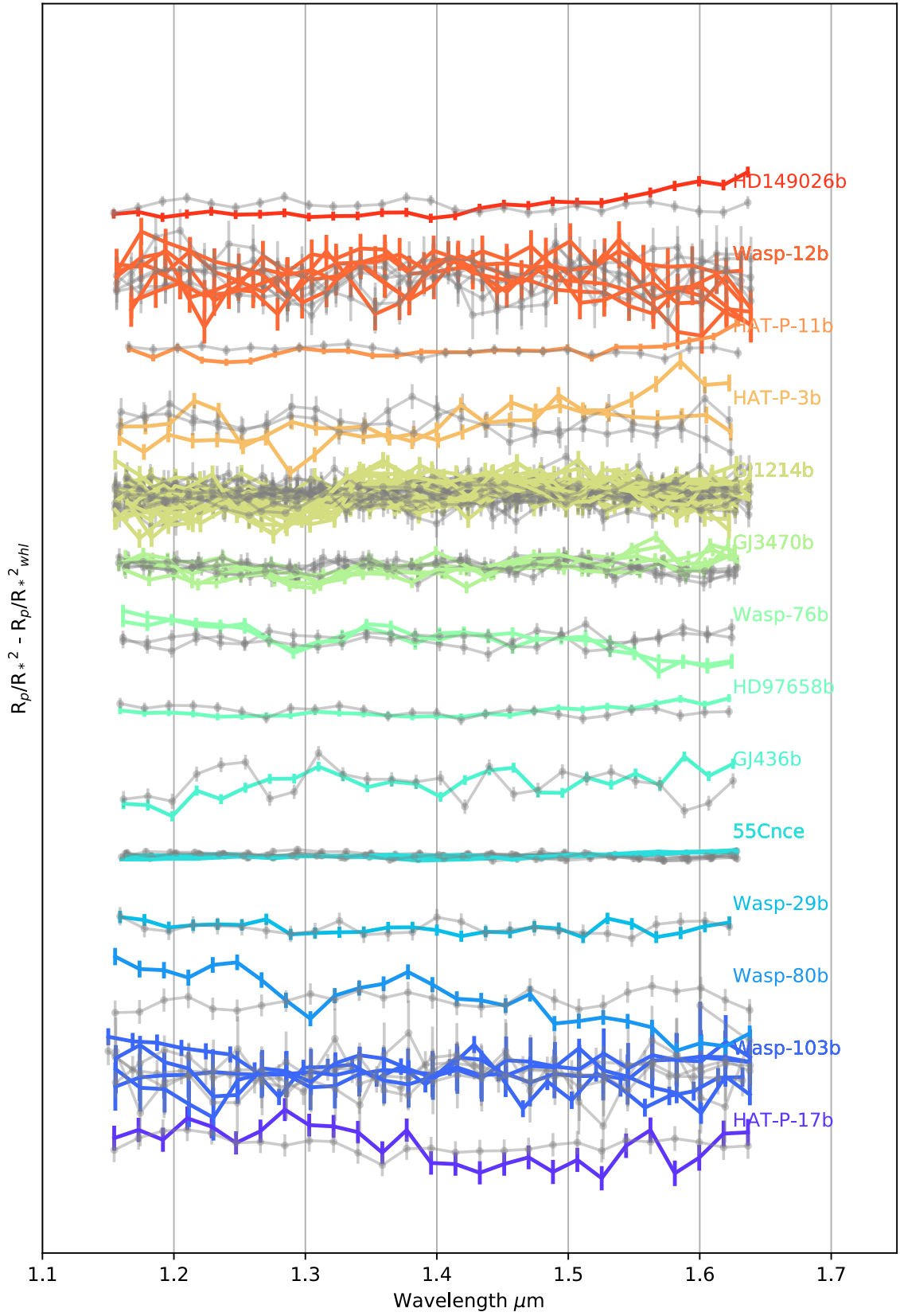


Figure 3.36: Figure 3.36 continued.

Wasp-39b also features in the spectral sequence in Sing et al. (2016). In that work the observations of Wasp-39b had not been completed with HST WFC3. The target was modelled using data from Spitzer and STIS only. However, the planet ranked very highly in their sequence, suggesting that there would be a significant water feature in the WFC3 G141 bandpass. That data has now been taken and is included in my sequence. We can see that Wasp-39b is one of the highest ranking watery planets in my sequence, ratifying what Sing et al. (2016) predicted.

The sequence of planets shows there are clear trends that may be due to systematics. Wasp-76b, HAT-P-32b and Wasp-80b show a significant blue-edge excess. Wasp-80b also shows a steep, negative slope that is not shown by any other target and is not seen in the OOT test. This may be a systematic that has not been addressed in this work, or an astrophysical slope from a haze. Without full atmospheric fitting it is difficult to distinguish these two possibilities or find the cause of this blue feature.

Conversely, I find planets HD149026b, Wasp-18b, HD97658b and HAT-P-11b are sloped in at the redder end of the spectrum. If the atmosphere were hazy we would expect a negative slope based on Rayleigh scattering. A positive slope is harder to fit with an physical atmospheric model. This suggests either a molecular feature at the red end or an error in reduction.

Based on this sequence I believe there may be final systematics that have yet to be considered in this work. These issues may be addressed by using a more sophisticated fit to geometric distortions or by a full transit model fit to each coloured light curve including limb darkening.

3.8.2 Comparative Exoplanetology

Using the large sample of 30 unique exoplanet transmission spectra I can investigate observability of water across and range of planet types. To do this I can first estimate the expected water feature height under the simplest conditions. I do this by using an analytic model for the height of the atmosphere that would be measured by the transit depth.⁸⁶

The analytic relation for the transit-measured altitude of an atmosphere (in hydrostatic equilibrium) is given by

$$z(\lambda) = H \ln \left(\frac{\epsilon P \sigma(\lambda, P, T)}{\tau} \sqrt{\frac{2\pi R_P}{k_B T \mu g}} \right) \quad (71)$$

where $z(\lambda)$ is the altitude as a function of wavelength. H is the scale height, which I have discussed in Chapter 1 and is given as $H = k_B T / \mu g$. ϵ is the abundance of the absorbing species (in this case water), $\sigma(\lambda, P, T)$ is the wavelength dependent absorption cross section (see Chapter 2), P is the pressure at a reference altitude, τ is the optical thickness at the transit-measured altitude, R_P is the planet radius, k_B is Boltzmann's constant, T is the temperature of the gas at the measured altitude, μ is the mean mass of the gas particles and g is the surface gravity of the planet.

We see from this relation that the scale height is an important scaling factor to the transit-measured altitude, as we anticipate (see Chapter 1). The absorption from particular molecules will alter this transit-measured altitude as a function of wavelength. By increasing the abundance ϵ the transit-measured altitude is increased as there are more molecules present to absorb (or scatter) the star light. Observing in wavelengths where the cross section $\sigma(\lambda, P, T)$ is high will also increase $z(\lambda)$. In practice we do this by observing in the G141 waveband, which covers the strong water absorption feature at $1.34\mu\text{m}$ (see Figure 3.37).

Sing et al. (2016) uses metrics based on Equation 71 to analyse their transmission spectra at different wavelengths. By comparing the transit-measured altitude in one waveband to another many of the factors in Equation 71 will cancel.

$$z(\lambda) - z(\lambda') = \Delta z_{\lambda-\lambda'} = H \ln \left(\frac{\alpha}{\alpha'} \right) \quad (72)$$

⁸⁶ Lecavelier Des Etangs et al. (2008)

$$\alpha = \epsilon\sigma(\lambda) \quad (73)$$

where α is the absorption-plus-scattering extinction coefficient. The quantity $\Delta Z_{\lambda-\lambda'}/H$ gives a metric to compare the extinction between different wavelength regions. If $\Delta Z_{\lambda-\lambda'}/H$ deviates significantly from theoretical values this would indicate cloud layers or hazes altering the transit-measured altitude from Equation 71. For this to be effective, measurements are ideally taken from different wavelength regimes where $\sigma(\lambda, P, T)$ is significantly different.

Sing et al. (2016) uses a full radiative transfer model including chemistry and clouds to compare their measured values of $\Delta Z_{\lambda-\lambda'}/H$. They also use optical and mid-infrared data from HST STIS and Spitzer IRAC respectively. In this work the wavelength coverage is much more limited. The WFC3 band is much too narrow to perform the above comparison. No measurements of the haze or cloud level can be made with this data with a limited wavelength range and a simple analytic model. However, the absorption cross section for water does vary significantly in this band. I can begin to measure the strength of the water feature and compare it to a theoretical value using a very simple analytical model.

To measure the theoretical height of the water feature (h_w) in the most simplistic terms I use the analytical model given in Equation 71 and 72, using the same wavelength regions as given in Equation 70 ($\lambda=1.22-1.32$ and $\lambda'=1.33-1.49$). I assume that in these two regions T, P, τ and ϵ do not vary. I also assume no scattering and use only the absorption cross-sections $\sigma(\lambda, T)$ from Chapter 2. (Here I will assume pressure makes a negligible difference in the HST WFC3 band pass, which is very reasonable given the conclusions of that chapter.) Based on these assumptions we find that the theoretical height of the water feature h_w is given as

$$h_w = \delta_\lambda - \delta_{\lambda'} \quad (74)$$

where δ_λ and $\delta_{\lambda'}$ are the average transmission spectra in the two regions λ and λ' . The transit depth is simply $(R_p/R_*)^2$ + an additional atmosphere layer. The height of this layer as a function of wavelength is $z(\lambda)$ giving

$$h_w = \left(\frac{(R_p + z(\lambda)) - (R_p + z(\lambda'))}{R_*} \right)^2 = \left(\frac{\Delta z_{\lambda-\lambda'}}{R_*} \right)^2 \quad (75)$$

$$\Delta Z_{\lambda-\lambda'} = H \ln \left(\frac{\sigma(\lambda, T)}{\sigma(\lambda', T)} \right) \quad (76)$$

$$h_w = \left(\frac{H \ln \left(\frac{\sigma(\lambda, T)}{\sigma(\lambda', T)} \right)}{R_*} \right)^2 \quad (77)$$

I make the most basic assumption that the atmosphere contains only absorption from water. Using the water absorption cross section from Chapter 2 and interpolating to the equilibrium temperature of the planet, (assuming all energy from the star is absorbed and none is reflected) we can approximate h_w for these planets. This is shown in Figure 3.38.

Equation 77 shows us how we would increase the detectability of water in our targets. Based on the equation there are two ways we can do this: increase the signal size or increase the contrast. Increasing the scale height of the atmosphere increases the amount of material in the atmosphere for light to pass through. Because the atmosphere is thicker, there is more water to absorb the stellar light. This increases the signal from the absorption feature. A low temperature creates a narrow absorption feature in the cross section (see Figure 3.37). This causes the contrast between the two wavelength regions to become more pronounced. Finally, by lowering the stellar radius the transit depth is increased, also increasing the contrast between the two regions.

Figure 3.38 shows the theoretical water feature height (h_w) as a function of scale height. Hotter targets have much lower theoretical h_w values due to the cross section $\sigma(\lambda, T)$. As temperature increases the absorption feature becomes much broader and

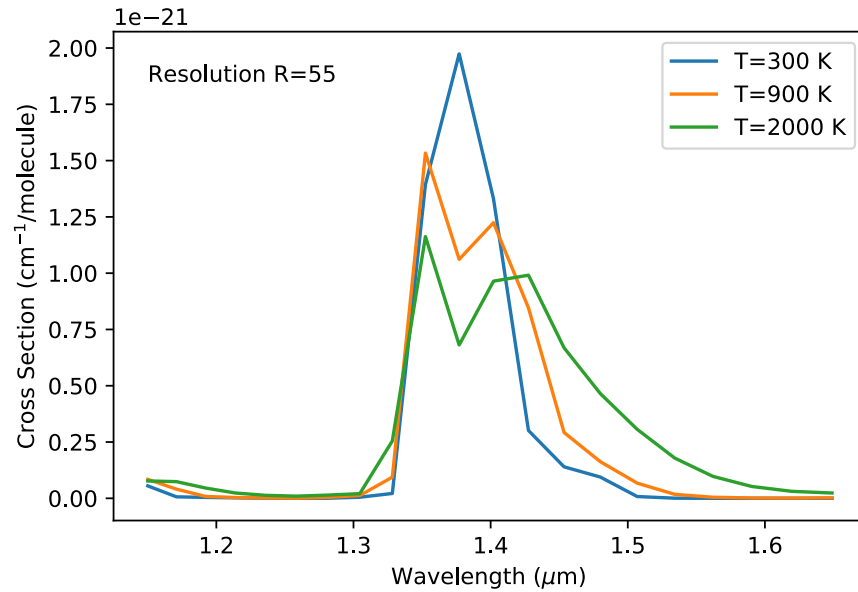


Figure 3.37: Example of the cross section of water at a resolution similar to transmission spectra reported by literature and this work. (Choices in binning for each individual target cause different R values.) At low temperatures the cross section is narrow, as temperature increases it becomes more broad.

shallow, causing h_w to decrease. Targets of similar temperatures have a stronger water feature as a function of scale height, as predicted in Chapter 1.

In Equation 77 there is a third factor which affects h_w : the star radius. A small stellar radius massively increases the transit depth making the relative contribution of the atmosphere much more pronounced. The smallest host star in this sample (GJ1214) has a stellar radius of only 0.2 solar radii making the height of the water feature much stronger. This causes the theoretical height of the water feature to be more than 50ppm. It has been excluded from Figure 3.38 as an outlier.

Based on this model we would expect high scale height, low temperature planets to have the strongest water features. Using literature values for the planet and host parameters I can estimate the scale height for each of my targets and directly compare the predicted water feature height to the measured one.

Figure 3.39 shows the height of the water feature for each planet used in this work as a function of scale height. (Note some targets have been removed based on the OOT Test, see Section 3.7.3). I find a significant correlation between scale height and the observed water feature in the observed exoplanet sample. Exoplanets with scale heights of more than $670\text{km} \pm 110\text{km}$ show a significant water feature of more than 200 parts per million.

When Figures 3.38 and 3.39 are compared they clearly show the same trends; there is a general correlation between scale height and the height of the water feature in the WFC3 band in both the theoretical and observed value of h_w . Hotter targets also show much weaker water features, due to the water absorption cross section being broader at high temperatures. Figure 3.40 shows the two values are highly correlated. A Pearson correlation test returns a correlation of 0.65 with a p-value of 1.5×10^{-4} suggesting the model is highly predictive of the data. If the h_w values were due to systematics we would expect no correlation between the model and the data at this level.

There is a high degree of scatter in the relation, suggesting that there are other factors affecting the results. The measured values are much larger than the predicted values by a factor of ~ 15 . This is likely due to the over simplification of the model; in this case we are using a simple analytic model for a 1D atmosphere containing

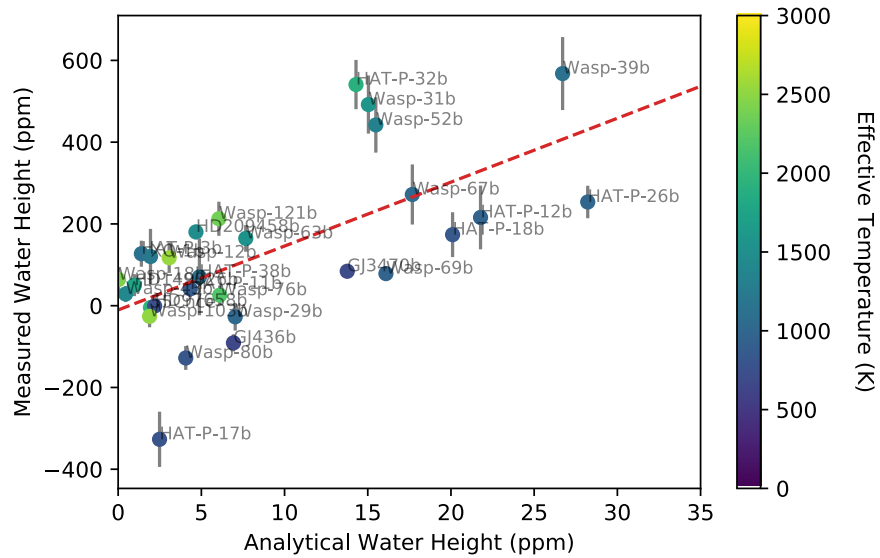


Figure 3.40: The theoretical height of the water feature for each target based on a simplistic analytic model compared with the true measured height. The correlation between the two as measured by a Pearson test is 0.65 with a p -value of 1.5×10^{-4} , suggesting that the water feature height being measured in the transmission spectra are related. Note GJ1214b has been removed from this correlation as an outlier.

only water and molecular hydrogen. A full radiative transfer model will provide a much more accurate estimate. Crucially we have ignored the following factors beyond radiative transfer. 1) Temperature-Pressure profiles. The actual temperature at the transit-measured altitude is likely different from the equilibrium temperature. 2) Albedo. Similarly, we have not included any reflection from the atmosphere which would reduce the heating in the upper layers. 3) Scattering, hazes and clouds. These features will affect the measurement of h_w and will reduce the observable contrast between absorption features in this region. 4) No chemistry and uniform abundances. The addition of more molecules and chemistry may drastically alter the results. Together these could combine to explain the scatter in h_w . Full atmospheric model fitting and better wavelength coverage would allow us to establish whether the variance in h_w is due to any of these atmospheric features and begin to constrain them, as done in Sing et al. (2016).

Many of the targets in this work also show a negative h_w value. This is not allowed for in our simplistic model; there is only one molecular cross section included and it cannot become negative. By including more molecules in this region, (such as methane) and particularly by including hazes this negative h_w value could be achieved. Full atmospheric modelling would help understand targets such as HAT-P-17b with such a low h_w value.

Ultimately the correlation between model and data shows that the retrieved transmission spectra are truly informing us about the strength of the water feature in these atmospheres. The increase in h_w as a function of scale height is not simply due to an unresolved systematic, but is truly astrophysical.

This is a new result which has not been discussed in literature. The benefit of this work was to use the largest exoplanet sample to date. With only a small sample of exoplanet transmission spectra it would be difficult to make this assessment. The strength of having such a large ensemble of planets is being able to see a correlation in their overall behaviour, based on the simplest models. Using this sample I have shown water absorption is clearly a dominant factor in the behaviour of exoplanet atmospheres in the $1.34 \mu\text{m}$ region.

Using this large ensemble and trend it is possible to forecast which planets will have the strongest water features. It would have been possible to do this using only the analytic model. However, by using the data we are also including the variance caused by HST systematics in our prediction and making no assumptions about the behaviour of these atmospheres. We instead assume that this sample is large enough to predict general behaviour for all similar exoplanet atmospheres.

3.8.2.1 Future Target Lists

There are many exoplanets which a) have known mass, radius and orbital periods with which to calculate the scale height and b) are known to transit their host stars. Using the relation between scale height and h_w we can build an optimal target list of known exoplanets that, if observed with WFC3, would have a strong water signal. In this Section I will use the correlation discussed above to predict the height of the water feature h_w for these planets. I do this with a linear fit to the planet sample above for planets with equilibrium temperatures less than 1500K. Temperatures higher than this cause a broad cross section and a much lower h_w value to be measured, as shown in Figures 3.38 and 3.39.

For the purpose of designing a target list we will make a number of assumptions about our observational needs. In order to find a large enough signal for water to be identified and model we will assume we require at least $h_w=200$ ppm. I will assume that observations of 100 seconds are optimal based on the observational strategies in Table 6.1. 100 seconds is a short enough duration to use the 256x256 subarray for most targets, maintaining high observation efficiency without requiring data dumps in the middle of the observations. Lastly we will assume that a signal to noise ratio of at least 5 is required to confirm any observation.

Using the NASA Exoplanet Archive I have built a list of all the transiting exoplanets that have mass, radius and period estimates. An effective temperature and a scale height is calculated for each planet, assuming a μ of 2. The scale height in this case is dominated by the surface gravity of the planet g . This leads to less dense planets having a much larger scale height. This is shown in Figure 3.41. The most amenable targets for water observations are in the top left of the radius/mass diagram for exoplanets.

To estimate the signal to noise ratio of the observation for HST WFC3 we first estimate the transit depth. This is based on the stellar and planet parameters from the NASA exoplanet archive. The transit depth in absolute flux units is

$$\delta = F_* R_p^2 / R_*^2 \quad (78)$$

where F_* is the flux from the star. Using the stellar luminosity and modifying it by a blackbody curve I obtain the projected stellar flux in the WFC3 waveband. The final signal to noise ratio of the observation is then the signal in counts due to the additional layer of the atmosphere. Using the equations from Chapter 1 we can calculate the counts recorded by HST WFC3 as

$$\text{counts} = t P F_*' \left(\frac{(R_p + NH)^2}{R_*^2} - \frac{R_p^2}{R_*^2} \right) \quad (79)$$

where t is the exposure time in seconds, P is the conversion between $\text{ergs/s/cm}^2/\text{\AA}$ and detector counts/s and F_*' is the flux of the star in the WFC3 bandpass. As discussed in Chapter 1 N is the number of scale heights of a uniform density gas that approximates a full atmosphere where density varies under gravity⁸⁷ ($N=5$). The signal to noise ratio is then $\sqrt{\text{counts}}$.

Figure 3.42 shows the projected signal to noise ratio of each exoplanet atmosphere as a function of mass and radius. Only planets with equilibrium temperatures less than 1500K have been included, as I assume that the correlation breaks down for hot planets. In Figure 3.42 we see that most of the ideal candidates are not large, hot Jupiter planets but instead 'hot Neptunes' with masses less than 0.5 Jupiter Masses. Hotter, higher mass planets have broader cross sections. Small planets, particularly

⁸⁷ Seager and Sasselov (2000)

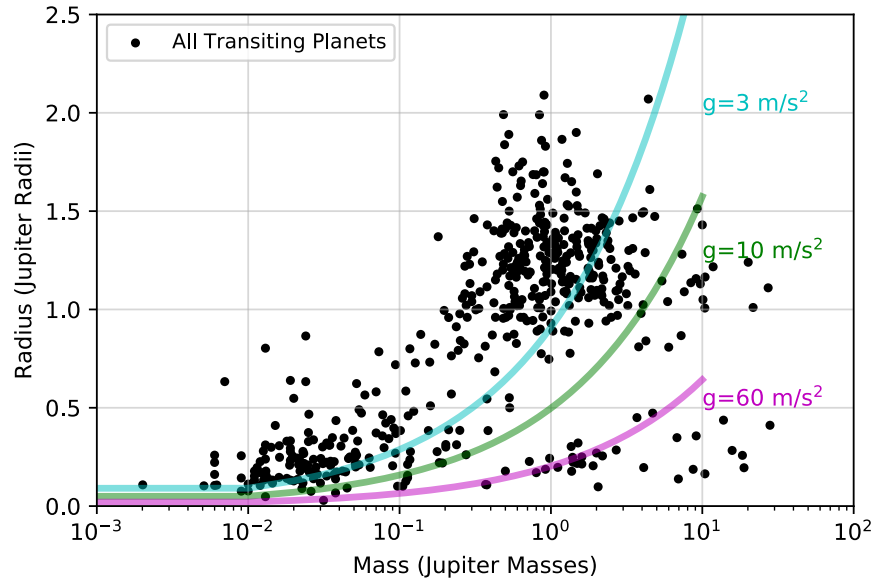


Figure 3.41: Mass/radius diagram for all known transiting exoplanets with mass and radius measurements. Different values for surface gravity have been over plotted to show where planets most amenable to water observation are likely to lie.

with very low masses such as hot Neptunes provide high scale heights and low temperatures making them perfect targets for observations of water with HST WFC3. Beyond HST these would be ideal targets to observe with JWST's IR instruments in the future. This is a paradigm shift from what is currently done in the field. As shown in Figure 3.1 high mass, very hot planets are often chosen for exoplanet atmosphere observation.

A full list of the known transiting exoplanet targets with conditions ideal for a detection of $h_w \gtrsim 200\text{ppm}$ is given in Table 6.1 in the Appendix of this chapter. These are ordered by the predicted HST signal to noise ratio. Several of the targets in this list have already been observed with HST, notably Wasp-69b, Wasp-67b and HAT-P-26b rank highly on the list of candidates and in the spectral sequence given in Figure 3.36.

There is a shorter version of this table given in Table 3.8. Here only the smallest exoplanets are shown, with radii less than one Jupiter. I find there are several unobserved small planets with high predicted h_w values. These candidates would provide excellent opportunities to constrain the water abundance on smaller exoplanets. Several of these small planets are also part of multiple systems. Notably, Kepler-18c and Kepler-18d both appear on the list of optimal targets. Studies of atmospheres in multiple-planet systems may allow us to investigate how water abundance varies as a function of distance from the host star and better constrain formation models.

3.9 CONCLUSIONS

In this work transmission spectra for 30 unique¹ exoplanets have been derived uniformly, mitigating systematics from the shift in source location on the detector and geometric distortions. Due to the nature of observations of exoplanet atmospheres, signals from transmission spectra are small. It proves important to remove these

¹Note added in Proof: While this work was in the final stages of proofing a similar publication was added to the arxiv. Tsiaras et al. (2017) presented a set of 30 exoplanet spectra take with WFC3 and fits each with a full atmospheric model. They note similar features, such as the absorption feature in Wasp-76b which they attribute to TiO. The analysis of the water feature height presented in this work remains unique.

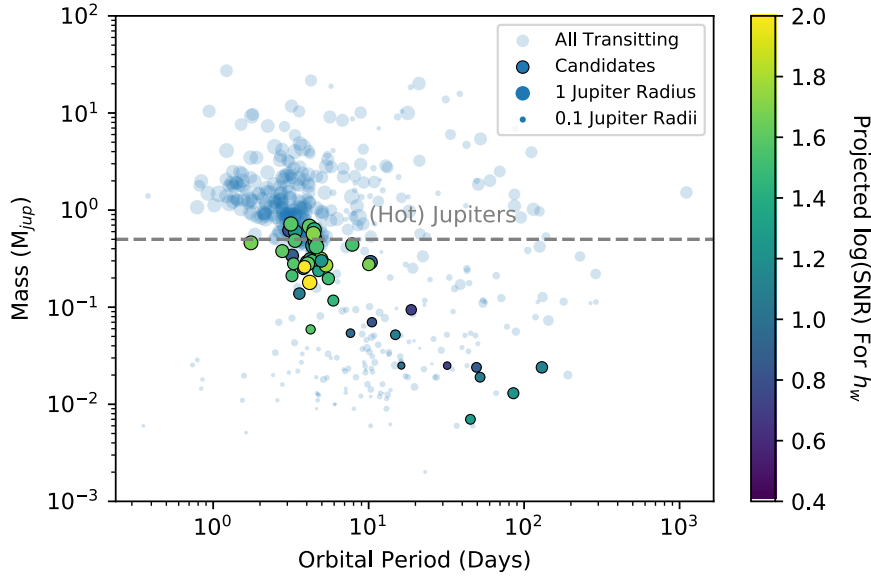


Figure 3.42: Mass/period/radius diagram for all known transiting exoplanets. Coloured points indicate exoplanets with a scale height large enough to expect $h_w \gtrsim 200$ ppm. The colour scale gives the projected signal to noise if observed with WFC₃ for either 100 seconds or until the saturation limit of the detector is reached, (whichever is shorter).

Name	Scale Height	Temperature	Radius (R_{Jup})	Mass (M_{Jup})	Magnitude (V)	Projected HST SNR
Kepler-78b	678.0 ± 45.2	2217.0 ± 42.0	0.105 ± 0.014	0.006 ± 0.001	11.551	12.5825
Kepler-36c	728.0 ± 25.5	1016.0 ± 11.0	0.328 ± 0.005	0.025 ± 0.002	11.866	6.96643
Kepler-18c	733.0 ± 15.0	990.0 ± 34.0	0.49 ± 0.023	0.054 ± 0.006	13.549	6.45995
HAT-P-26b	895.0 ± 37.2	994.0 ± 73.0	0.565 ± 0.072	0.059 ± 0.007	11.744	26.5179
Kepler-18d	986.0 ± 17.1	793.0 ± 27.0	0.623 ± 0.029	0.052 ± 0.004	13.549	8.45964
K2-39b	1046.0 ± 21.7	1855.0 ± 93.0	0.732 ± 0.098	0.158 ± 0.031	10.832	10.6641
WASP-139b	835.0 ± 8.0	917.0 ± 22.0	0.8 ± 0.05	0.117 ± 0.017	12.4	20.7725
Kepler-51c	3747.0 ± 373.0	454.0 ± 108.0	0.803 ± 0.25	0.013 ± 0.001	14.669	12.0111
HATS-8b	1216.0 ± 61.1	1322.0 ± 92.0	0.873 ± 0.123	0.138 ± 0.019	14.03	8.38614
HAT-P-12b	695.0 ± 12.7	958.0 ± 22.0	0.959 ± 0.029	0.211 ± 0.012	12.84	23.2324
WASP-126b	814.0 ± 11.7	1486.0 ± 70.0	0.96 ± 0.1	0.28 ± 0.04	10.8	26.4225
Kepler-425b	683.0 ± 133.1	1072.0 ± 18.0	0.978 ± 0.022	0.25 ± 0.08	14.97	6.09235
HAT-P-18b	709.0 ± 0.3	848.0 ± 31.0	0.995 ± 0.052	0.197 ± 0.013	12.759	22.0615

Table 3.8: Projected best candidates for HST WFC₃ observations of water features. Here scale height is derived from the mass of the planet, temperature of the star and orbital period of the planet as given by NASA Exoplanet Archive with a μ value of 2. HST signal-to-noise ratio is based on an observation with WFC₃ G141 grism with an integration time of 50 seconds. Targets that have also been observed with HST spatial scan mode have been highlighted, though some have been removed from the reduction.

small systematics carefully to correctly analyse the transmission spectrum and remove all signals from the host star.

In this work I employ several stages of correction. I use only spatially scanned, `ima.fits` files from STScI MAST in this work. These have undergone preliminary corrections in the `calwfc3` pipeline. Initially this raw data is corrected for systematics such as the background and cosmic rays at the pixel level.

In the second stage of correction I use a least squares fitting routine and template spectrum to find the source position as a function of time. The subpixel shifts in source position are used to create a high resolution, oversampled stellar spectrum. This enables accurate removal of the stellar signal despite shifts in the source over time. The same least squares fitting approach is used to remove small, geometric distortions due to imperfections in the telescope optics, which result in a stretch in the spectrum. The variable scan rate is removed using the same template fitting method.

The final stage of corrections clean the individual light curves from each wavelength channel. I employ the divide OOT method developed by Berta et al. (2012). I remove the hook systematic noted by Deming et al. (2013a) using background reads from the un-illuminated portions of the array and a least squares fit.

The transmission spectrum is generated using the white light curve which is least squares fit to each channel light curve to find the change in transit depth.

I take several approaches to validating the transmission spectra. Targets that have been observed in round-trip mode are split into two different groups before reduction. I analyse the precision of the reduction through comparison of the transmission spectra from the forward scan group and the backwards scan group. Similarly, different observations of the same target should produce similar transmission spectra, assuming no additional astrophysical variability. I find that both of these internal validations show that my transmission spectra are consistent.

9 of the transmission spectra produced in this work have been externally validated by comparing with literature results. I find that the transmission spectra produced here are very similar to those from literature. There is also evidence for a small increase in flux at the red end of the spectra, suggesting there are further systematics in the data. Targets such as HD209458b, XO-1b and HD97658b are consistent with literature.

Some targets show a feature blueward of the water absorption that is not well approximated by an atmospheric model. This is shown particularly for Wasp-76b and HAT-P-32b where a full atmospheric retrieval fails to converge. This may be due to further instrument systematics that have not been addressed in this work.

In this work I propose a new test for assessing the quality of the data: the Out-of-Transit Test. In this test the average of the first half of the out-of-transit data is subtracted from the last half for every channel. This produces the equivalent of the transmission spectrum for when the planet is not transiting. Any remaining channel variance must either be due to the star or due to systematics. For the transmission spectrum to truly contain astrophysical variability, it must be detected above the variance of the OOT test. In this work, any instances where the OOT Test is found to be significantly correlated with the transmission spectrum, noisier than the transmission spectrum or significantly sloped have been removed from further analysis.

In this work I present a spectral sequence of exoplanet atmosphere transmission spectra from water-poor to water-rich atmospheres. This is similar to the sequence presented in Sing et al. (2016). By using all spatial scan mode data from HST I am able to increase the sample size significantly compared to that work (though Sing et al. (2016) covers a much wider wavelength range enabling modelling of clouds and hazes). Only 5 targets overlap in the two works, and due to the difference in wavelength coverage the two cannot be compared. However, in Sing et al. (2016) the planet Wasp-39b was missing from the analysis as data had yet to be taken with WFC3. They predicted based on their models and their sequence that Wasp-39b would have a strong WFC3 water signal. I have since produced a transmission

spectrum for this planet and find that to be correct; Wasp-39b has one of the strongest water features as measured by h_w in my sample.

In this work I use the averages in two regions of the spectrum ($\lambda=1.22-1.32$ and $\lambda'=1.33-1.49$) to measure h_w . This measures the strength of the water feature. Using an analytical expression for the transit-measured altitude⁸⁸ I have estimated the value of h_w for each target. This theoretical value correlates significantly with the measured value from the transmission spectra of the 30 exoplanets used in this work. This suggests that the transmission spectra are showing truly astrophysical variation related to the water absorption in the exoplanet atmosphere.

I find a new, empirical relationship between the scale height of an atmosphere and h_w for planets $T \lesssim 1500\text{K}$. Using this relationship it is possible to find the list of exoplanets that are most likely to have an observable water signal with HST. I have produced a list of the transiting exoplanets that are most likely to have a strong water signal. Of this list I have highlighted the smallest planets with radii less than 1 Jupiter radius. These planets have large scale heights due to their extremely low density. They are the best candidates for water observation in a super-Earth/Neptune type planets.

Based on this relationship I find that the ideal candidates are not hot Jupiters, which are often chosen for atmospheric retrieval. Instead I find 'hot Neptunes' have properties that create a high h_w value. These targets can have large scale heights due to their low densities, but are cooler than hot Jupiters with temperatures $\lesssim 1500\text{K}$. I suggest that the candidates in this list will provide the best opportunities for characterising water around small exoplanets either with HST or future instruments such as NIRSpec on JWST.

Particularly, I suggest the planets Kepler-18c and Kepler-18d would make excellent targets for observation with HST WFC3. They are small with a high probability of water observation, making them astrophysically interesting. They orbit a G-type star and have orbital periods of 7 and 14 days respectively. This make their transit durations long ($\gtrsim 1$ hour), providing the opportunity for plenty of in-transit observations. Finally, by observing both as members of the same system it may be possible to constrain water abundance as a function of orbital distance in a single system.

The collection of exoplanet spectra used here span a wide range of morphologies as shown in Figure 3.36 with some displaying clear and strong water signals. In particular HAT-P-32b, Wasp-76b and Wasp-52b show very strong signals and have not been discussed to date in literature. With access to a more sophisticated set of models it may also be possible to compare the exact abundances of water across the spectrum and begin a census of exoplanet atmosphere composition in the near IR.

Before any transmission spectra for these planets are investigated further all evidence of systematics should be removed. In particular there is the blue-edge feature that is not well described by models. There would be many approaches in finding whether this feature was physical but under-represented in the models or systematic. One approach would be to use the synthetic exoplanet transit data from BART and create synthetic observations. Varley, Tsiaras, and Karpouzas (2015) have created a code for producing synthetic observations based on HST's behaviour and noise profile. Testing my pipeline in conjunction with synthetic observations would be the first step in finding any residual systematics.

In this work I have used the collection of public, archival exoplanet atmosphere observations for a data driven comparison of exoplanet atmospheres. I have shown with the simplest analytic model that these transmission spectra are consistent with atmospheric absorption. Using this dataset it is possible to look forward to what we might achieve with JWST. The increased collecting area of JWST will require less exposure time to achieve the same signal to noise of HST. The longer wavelength coverage of NIRSpec and MIRI will allow degeneracies in molecular abundance to be broken. The targets shown here with high h_w values will be excellent candidates for follow up with prominent molecular absorption features in the IR, where Rayleigh scattering is less pronounced. High contrast molecular features allow the

⁸⁸ Lecavelier Des Etangs et al. (2008)

best constraints of abundances from atmospheric models. By learning more about atmospheric composition we can inform our knowledge of planet composition and begin to build a picture of the conditions on these planets.

3.10 ACKNOWLEDGEMENTS

All of the data presented in this paper were obtained from the Mikulski Archive for Space Telescopes (MAST). This work is based on observations made with the NASA/ESA Hubble Space Telescope, obtained from the data archive at the Space Telescope Science Institute. STScI is operated by the Association of Universities for Research in Astronomy, Inc. under NASA contract NAS 5-26555.

4.1 INTRODUCTION

In the previous chapter I have presented an ensemble of 30 unique exoplanet transmission spectra. I have compared them in order to study the range of water content in exoplanet atmospheres. That work required that the spectra be **precise**, in order to make the inter-comparison possible. In this chapter I will focus the stellar spectrum that was taken in the same data. The stellar spectrum had been actively corrected for and removed in the reduction process to find these small exoplanet signals. However, stellar spectra can be used to retrieve stellar parameters, such as temperature. These in turn are used to find exoplanet parameters such as mass and radius (see Chapter 1 for more details on this). To study exoplanets further we require that these parameters are **accurate**.

Accurate mass and radius parameters allow us to unlock further characterisation (such as the mean density) and have implications for the composition and formation. Characteristics such as the effective temperature of the planet are built from the stellar temperature. These stellar parameters are usually found through models based on the stellar temperatures and metallicities, and in rare cases measured using interferometry (see Section 4.2). Inaccuracies in stellar parameters directly impact our ability to investigate and characterise exoplanets. Before we can learn more about exoplanets we must first understand their hosts.

In this chapter, I use space-based, IR spectra to test the accuracy of retrieved exoplanet parameters. I use state-of-the-art stellar atmosphere models to find mass and radius estimates using only the near-IR. I compare these values with those obtained in literature from other methods in the visual. The IR wavelength range has not been tested in literature, where models are known to be less accurate (see Decin et al. (2004) for a comparison of ATLAS and MARCS models in the IR). The retrieved uncertainties in the host star temperatures are then used to project uncertainties in their planet parameters, were only the IR region used to estimate stellar parameters.

The sample of 32 stellar spectra used in this work present an excellent opportunity to obtain the stellar properties of some of the most interesting exoplanet host stars. Their planets are some of the best characterised to date (see Chapter 3). These stars span a wide range of masses from M to F type, making them also excellent templates for the majority of exoplanet host stars. Uniquely, this data set has been taken by HST WFC3 covering a wavelength range of 1.15-1.65 μ m. This allows a wavelength regime to be observed that would otherwise be impossible from the ground due to strong atmospheric water absorption. The stellar spectra also have excellent signal to noise (SNR~30000). Thanks to the spatial scan mode of HST, spectra can be taken of even the brightest stars without saturation. This includes stars such as 55 Cancri e (6th magnitude) and would otherwise be difficult to observe in the IR without saturation. One weakness of this data set is the very limited spectral resolution of $R\approx 100$. However, in this work I will focus on deriving the temperature, which can be constrained using only the blackbody slope of the spectra and does not require high resolution.

Full stellar spectral modelling relies on having distances to the stars, usually through parallax (see Section 4.2). With Gaia able to provide these parallaxes in the near future, stellar parameters are likely to be known much more accurately. Further, with PLATO being launched in 2025⁸⁹ we will have access to asteroseismically measured mass and radius estimates for stars, though these will depend on modelled stellar temperatures. In this work I normalise the spectra rather than fitting for distance. This allows a tight fit to the black body slope.

⁸⁹ Rauer et al. (2014)

Surveys such as TRAPPIST have validated that cool M stars are useful for finding nearby, small exoplanets with deep transits, (see Gillon et al. (2017)). These small stars provide the largest transit signal and, due to their low luminosity, have close in Habitable Zones. This makes their planets excellent targets for follow up with missions such as JWST to measure their atmospheres. However, the temperatures, masses and radii of these stars are hard to measure. These cool stars often peak in luminosity in the near-infrared (TRAPPIST-1 peaks at $1.13\mu\text{m}$) and so obtaining spectra in the visual can be more difficult. By testing the accuracy of stellar parameter retrieval only in the near IR we can be better prepared for the coming data on these cool, small stars.

The spectrum of TRAPPIST-1 has already been observed by HST WFC3. It was produced in this work using the methods discussed in the previous chapter. However, the stellar spectral models used here are not currently valid at the temperature of this star ($T=2600\text{K}$) due to molecular absorption. This already highlights a potential shortfall for the accurate characterisation of these star types.

I will discuss the methods of measuring stellar temperatures in Section 4.2. I introduce the data in Section 4.3 and discuss the models in Section 4.4. I present stellar temperature estimates and show a discrepancy in the accuracy of WFC3 in Sections 4.5 and 4.6.

4.1.1 Importance of Accurate Stellar Parameters

Inaccuracies in the surface temperature of a star relate directly to inaccuracies in the estimated planet mass, radius and surface temperature. To show the importance of accurate stellar properties we can use a quick example. From the Stephan-Boltzmann law

$$L_* = R_*^2 \propto 1/T_*^4 \quad (80)$$

where L_* is the luminosity of the star, R_* is it's radius and T_* is it's temperature. The radius of the planet is derived through the transit depth

$$\delta = (R_p/R_*)^2 \quad (81)$$

where δ is the transit depth and R_p is the planet radius. Large errors in T_* directly impact the measured planet radius. A 1% error in the temperature of the star will result in a 2% error in the measured radius of the planet. For the sun a discrepancy of 200K in temperature would cause an uncertainty of 7% in the radius of the star and 14% uncertainty in the radius of the planet. Stellar parameters used in this work currently have uncertainties of $\gtrsim 50\text{K}$, though up to 300K for the coolest stars (see Table 4.1).

4.2 METHODS OF STELLAR PARAMETER RETRIEVAL

There are several methods used in the field for deriving stellar temperatures. I will briefly discuss the most common methods here, which are split into three families of detection methods: photometric, spectroscopic and interferometric. These methods are used to measure the effective temperature of the star, the surface gravity ($\log g$) and metallicity. The different methods are known to provide slightly different results (see Section 4.2.1).

4.2.0.1 Photometric

In photometric methods a model stellar spectrum is fit to an SED of a star. For many stars this SED is sparsely sampled and only a few photometric colours are available. To counter this, models are used to create a calibration for well known bright stars where a full SED is available. These calibrations can then be applied to more sparsely

sampled stars based on colour-magnitude diagrams. See Casagrande, Portinari, and Flynn (2006) for a detailed application of this method to main sequence stars.

This method relies heavily on the assumptions made in the specific atmospheric models. The calibrations will change slightly depending on the set of models used. Choosing a different set of models can cause the temperatures retrieved to be offset, though they will be internally consistent. Casagrande, Portinari, and Flynn (2006) suggests that these inaccuracies will be small, with their work being 50K – 100K too hot when all systematics are included (see that work for the sources of error in detail). This method is also susceptible to errors from reddening, where dust between the star and the observer will cause stars to become more red in the colour-magnitude diagram. This in turn causes errors in temperature estimation.

4.2.0.2 Spectroscopic

In this method, high resolution spectra of stars are needed. The line profiles of strong absorbers such as the wings of hydrogen lines and iron lines can be used to measure the temperature of the star (for example see Tsantaki et al. (2013)). The equivalent widths of iron lines are strong indicators of temperature. Iron provides many lines in a single spectrum due to its complex absorption cross section, which allows us to measure line widths. However, issues with multiple neighbouring lines blending and inaccurate line-lists can cause errors in this method. This causes issues in cooler stars particularly ($T \lesssim 5000\text{K}$) where molecules can persist in the atmosphere, further complicating the spectrum and crowding the absorption lines⁹⁰.

This method still relies heavily on atmospheric modelling in order to relate the equivalent widths back to a temperature, as discussed in Tsantaki et al. (2013). As with the photometric method, different assumptions between models can cause discrepancies in this calibration. This can cause offsets in the temperatures retrieved between different works (see Section 4.2.1).

⁹⁰ Bonifacio et al. (2011); Gustafsson et al. (2008)

4.2.0.3 Interferometric

The final method for obtaining stellar information is through interferometry (for example Heiter et al. (2015) and Boyajian et al. (2008)). In this method the radius of the star is measured with no assumptions based on a stellar atmospheric model. The temperature can then be derived using the measured bolometric luminosity and the distance to the star. Since this method does not require any atmospheric modelling it is considered to be the least biased. However, it is only possible for the closest and brightest stars. In such cases it can be used to compare the accuracy of the other two methods.

4.2.1 Comparison of methods

Heiter et al. (2015) shows a comparison for bright FGK stars in GAIA between interferometric, spectroscopic and photometric methods of assessing effective temperature. Figure 4.1 shows their comparison. They show there is scatter between the results with errors of up to $\sim 100\text{K}$ for bright stars, effecting cool stars slightly more. The results are accurate, despite some scatter for individual targets.

We can also compare the results of different methods of temperature estimation using literature. There are many literature temperature values available for some stars used in this work. Particularly, bright stars such as HD209458 and 55 Cancri have many values estimated using all of the different methods discussed above. The PASTEL database provides an excellent resource for searching for literature values of stellar parameters.⁹¹ Using that database, I find a large degree of scatter in literature values for HD209458 and 55 Cancri, shown in Figure 4.2. HD209458 shows a spread of 70K in retrieved temperature values over the last 15 years. 55 Cancri has an error of 100K, however shows much more consistent temperature retrieval in more recent works.

⁹¹ Soubiran et al. (2016)

Based on these sources we can expect some degree of scatter in stellar temperatures from different retrieval methods. However, we would not expect a discrepancy of more than $\sim 100\text{K}$ based on these literature values and Heiter et al. (2015) (see Figure 4.1) for bright stars. Different methods produce accurate results, though they have a precision limited to $\sim 100\text{K}$.

4.2.1.1 Other Methods

There are other methods for obtaining stellar parameters that can also produce accurate parameters. For example, asteroseismology can produce mass and radius estimates independent of the spectrum or photometry of the star. However, asteroseismology does require temperatures of the stars before hand to make these parameters and is based on models of stellar density and heavy element abundances⁹². Eclipsing binaries can also be used to inform stellar evolution models and obtain mass estimates (see López-Morales (2007)) though there are some limitations for smaller and more active stars, as discussed in that work.

⁹² Gilliland et al. (2010)

4.3 DATA: STELLAR SPECTRA

In order to derive the correct stellar temperature T_* , I will analyse spectra of exoplanet host stars in the near IR. The stellar spectra used here have been derived in Chapter 3 using HST WFC3 spatial scan data and span a wavelength range of $1.15\mu\text{m}$ - $1.65\mu\text{m}$. To form the spectra all observations of the system are normalised and stacked, regardless of whether the planet transited. The addition of the planetary atmosphere is considered to be negligible ($\lesssim 200\text{ppm}$). The transit and any other light curve variations have been normalised.

To create the spectra I use the sub-pixel shifts of the source to oversample and increase the resolution. To recap, the data are taken in spatial scan mode, where the spectrum is dragged up the y axis of the detector. This is to avoid saturation while maximising the number of photons collected. The source experiences some shift in position during a single exposure. This spreads the light over neighbouring pixels. These shifts are fractions of a pixel. By measuring the shift using a template spectrum the shift can be calculated and each spectral row can be related back to the original incident light. The data is placed on an oversampled grid, taking these shifts into account. Geometric distortions caused by the optics (which causes a “stretching” of the spectrum) are also used in the same way to oversample. The result of the oversampling is shown in Figure 4.3. The Paschen β spectral feature from absorption from molecular hydrogen is reconstructed in this approach. The spectra themselves are high signal to noise (SNR=29300 for HD209458) and so do not suffer greatly by dividing the flux into smaller wavelength bins.

Some targets in Chapter 3 do not undergo large shifts on the detector. This minimises the gains that can be made in oversampling. Such stars are still valuable and included in the reduction. The wide wavelength range allows for the slope to be accurately estimated, even in the lower resolution case. The oversampled spectra allow a tighter fit with models than the lower resolution spectra around features such as the Paschen β line.

When the spectra are oversampled, the spectrum of the star is essentially smoothed by a moving boxcar of the same width as the pixel. This effect can be seen in Figure 4.3, where spectral features such from absorption are smooth. While this does degrade some of the information of the individual absorption lines, the slope of the spectrum is preserved. It is this slope that enables temperature fitting.

The errors in Figure 4.3 are derived from the original error array given by the STScI *calwfc3* pipeline. These errors are derived from shot noise having been propagated through the *calwfc3* pipeline from the raw data. I propagate these through my corrections and inflate the errors proportionally during oversampling.

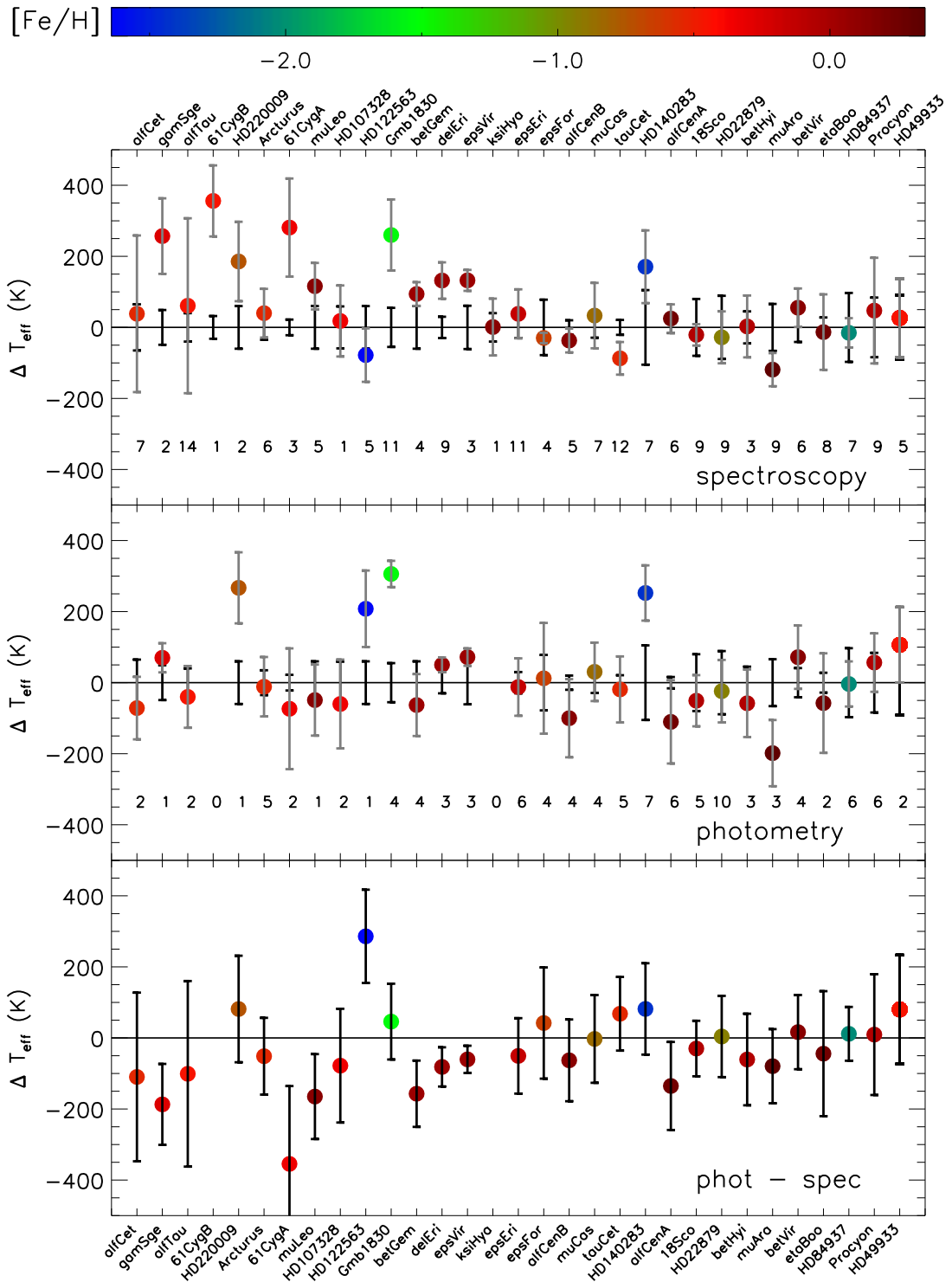


Figure 4.1: Comparison between photometric and spectroscopic methods for stellar temperature retrieval for GAIA benchmark stars, taken from Heiter et al. (2015). Stars are ordered from coolest to hottest. In the first two panels the methods are compared to ‘fundamental T_{eff} ’ values using interferometric measurements of the bolometric flux of the stars and limb darkening parameters. See Heiter et al. (2015) for more details. The lower panel compares the methods showing that the temperatures that are retrieved by each method are generally accurate but can be imprecise, especially at low temperatures.

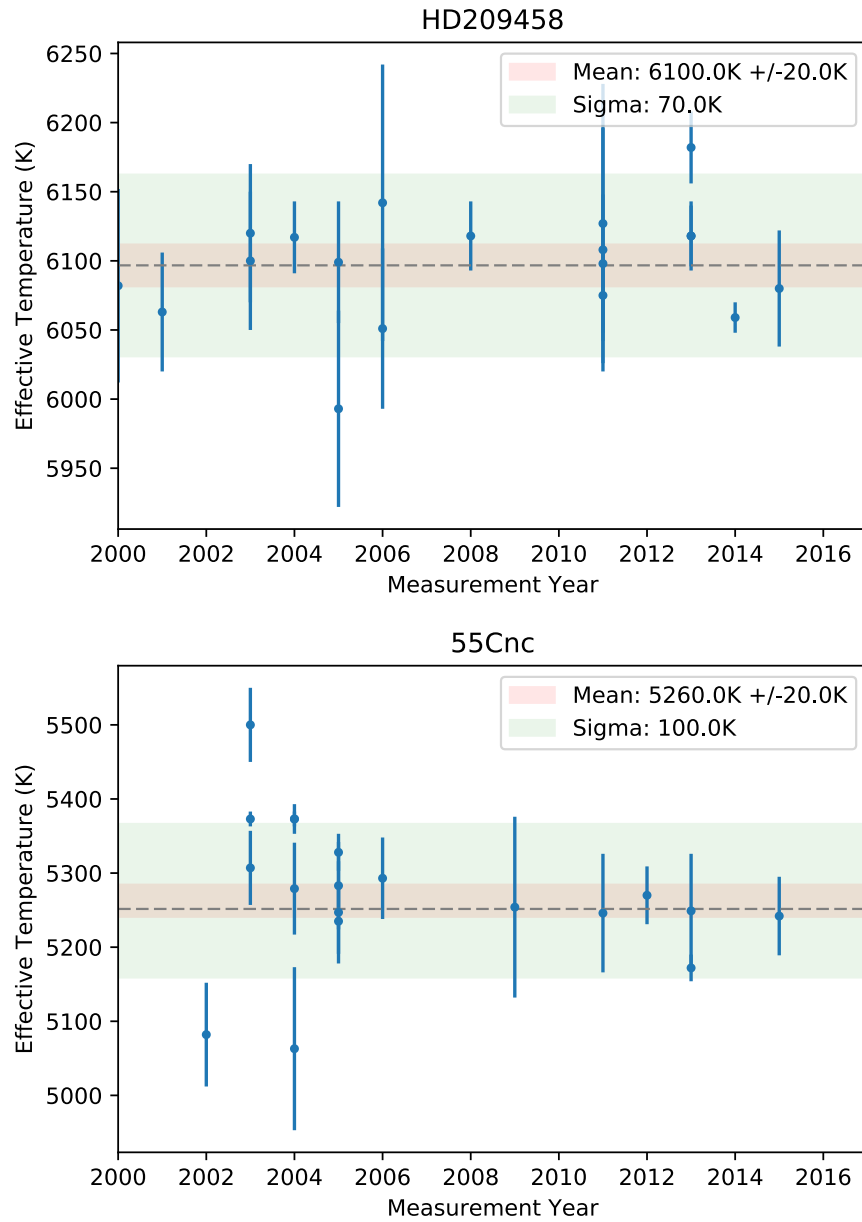


Figure 4.2: Temperature estimates for HD209458 and 55 Cancri from literature retrieved using the PASTEL database (Soubiran et al., 2016). There is a high degree of scatter between the methods, though temperature estimates for 55 Cancri have become more consistent in recent years. Based on this and work from Heiter et al. (2015) we would expect a scatter between different methods of $\sim 100\text{K}$. for bright stars.

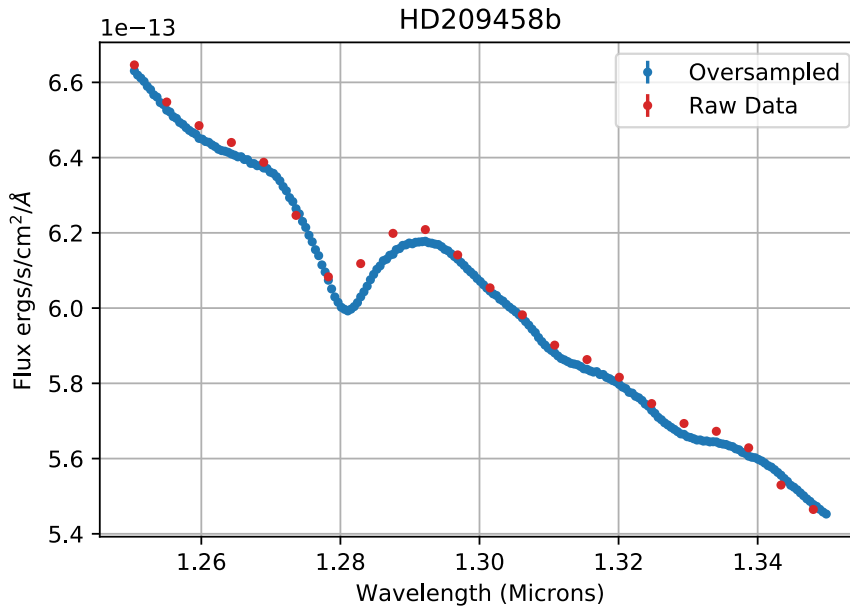


Figure 4.3: Comparison between the stellar spectrum for the raw data for HD209458 and the full corrected and oversampled spectrum. Here the spectrum is averaged over all observations, including those when the planet was transiting, as the effect of the planet atmosphere is a few hundred parts per million.

The exoplanets discussed in the previous chapter all have a matching, oversampled stellar spectrum output from my reduction pipeline. There are some targets that have been removed from the reduction for the previous chapter. (This is based on difficulties such as correlated out of transit tests, multiple or neighbouring sources on the detector or scanning over the edge of the detector.) For some of these targets stellar spectra are still derived and are presented here. This leads to a sample of 32 distinct exoplanet host stars, with some having multiple spectra from multiple visits and scan directions. These are stacked to produce one, average stellar spectrum.

Figure 4.4 shows the spectral sequence of stellar spectra as a function of temperature. In cooler targets (such as GJ1214b, GJ436b and K2-18b) there is an absorption feature from molecular water at $1.34\mu\text{m}$. This feature is similar to that seen in the previous chapter in exoplanet spectra. In targets such as these, where the stellar surface temperature is less than 3500K , molecular water can persist in the stellar atmosphere (see Jørgensen et al. (2001) and the references therein).

Molecular absorption can be problematic, particularly with low resolution data and photometry. The additional water absorption causes an increased slope in the spectrum, which mimics the slope of a hotter target. With low resolution spectra or IR photometry (e.g. 2MASS) this can cause some degeneracy; cool stars with significant molecular absorption mimic hotter stars with a steeper slope.

Towards the redder end of the spectrum at $1.5\mu\text{m}$ there are prominent lines that appear in the warmer stars with temperatures of 3500K - 5000K . From Lancon and Rocca-Volmerange (1992) these lines are due to Mg (peaking at 1.5029 - $1.5052\mu\text{m}$) and Fe (peaking at $1.5774\mu\text{m}$ and $1.5817\mu\text{m}$).

As temperature increases we see an increase in the depth of the Paschen β line at $1.282\mu\text{m}$ as a function of temperature. In the hottest stars with temperatures of 6000K - 6500K spectral features from metals have reduced, with absorption hydrogen becoming the dominant feature.

The star sample used here spans a range of 3000K - 6500K in temperature space. This allows a thorough comparison of stellar models from cool cases containing molecular features through to hot, molecule-free atmospheres.

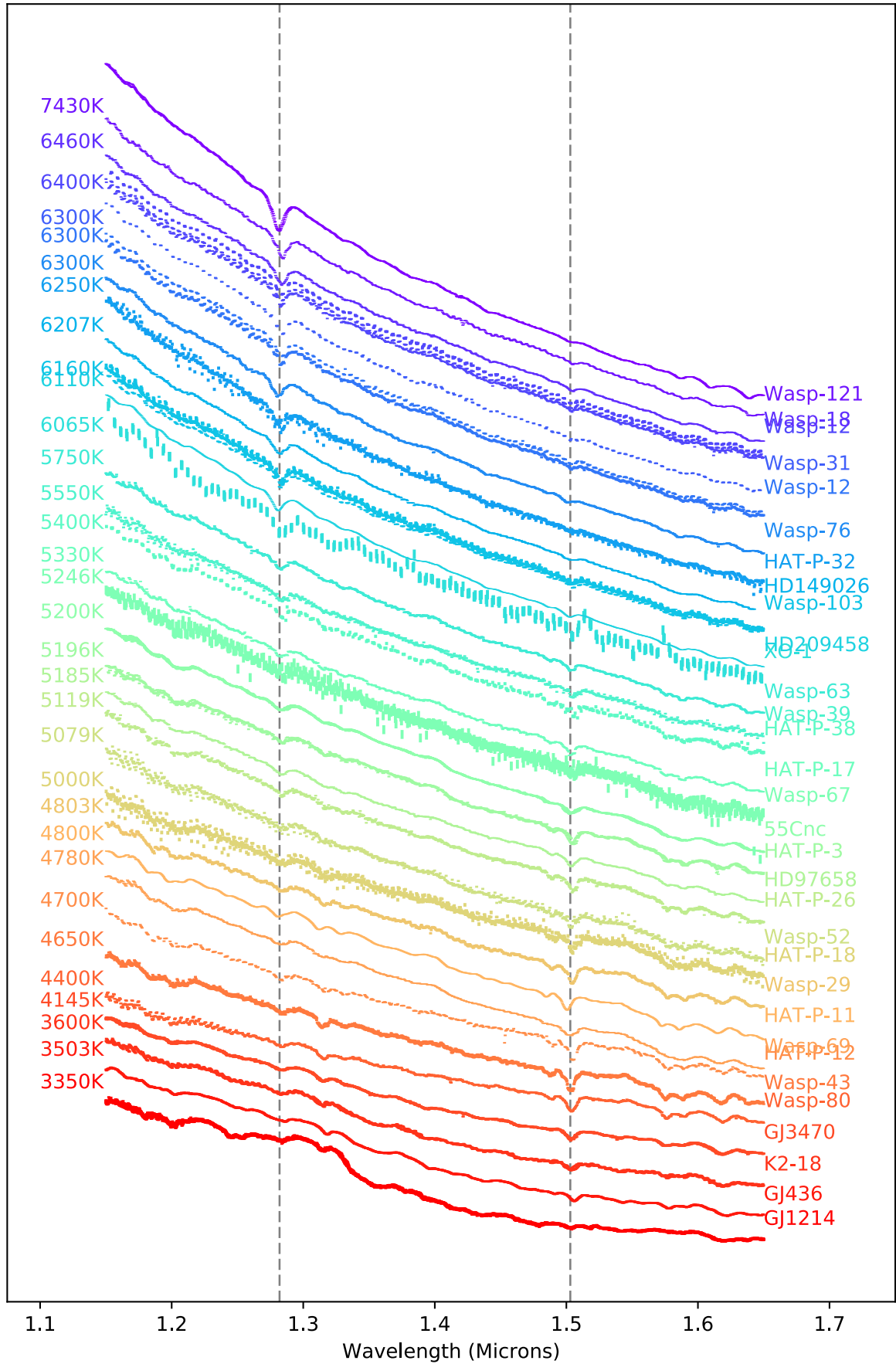


Figure 4.4: Spectral sequence of all the stellar spectra used in this work. All spectra employ some level of oversampling up to a tenth of a pixel depending on the amount of shift the source underwent on the detector. This reduction method for these spectra is discussed in the previous chapter. Spectra are ordered in temperature from top to bottom with temperatures ranging from 3500K to 6500K. Two lines have been added to show the Paschen β feature at $1.28\mu\text{m}$ and Mg lines at $1.50\mu\text{m}$.

Star	Temperature (K)	Citation	Method
WASP-18	6400 ± 100	Hellier et al. (2009)	Spectroscopic (H α Fitting)
HAT-P-17	5246 ± 80	Howard et al. (2010a)	Spectroscopic (SME Tool (Valenti and Piskunov, 1996))
HAT-P-32	6207 ± 88	Hartman et al. (2011)	Spectroscopic (SME Tool (Valenti and Piskunov, 1996))
HAT-P-11	4780 ± 50	Bakos et al. (2010)	Photometric (SED fitting)
HAT-P-26	5079 ± 88	Hartman et al. (2010)	Photometric (SED fitting)
GJ 436	3350 ± 300	Torres (2007)	Photometric (SED fitting)
HAT-P-18	4803 ± 80	Esposito et al. (2014)	Spectroscopic (Iron Line EW Fitting)
WASP-43	4400 ± 200	Hellier et al. (2011)	Spectroscopic (H α Fitting)
HAT-P-38	5330 ± 100	Sato et al. (2012)	Photometric (SED fitting)
GJ 1214	3026 ± 130	Charbonneau et al. (2009)	Photometric (SED fitting)
HD 149026	6160 ± 50	Sato et al. (2005)	Spectroscopic
HD 97658	5119 ± 80	Howard et al. (2010b)	Spectroscopic (SME)
55 Cancri	5196 ± 24	Braun et al. (2011)	Photometric (SED fitting)
HD 209458	6065 ± 50	Schuler et al. (2011)	Spectroscopic (EW Fitting)
WASP-31	6302 ± 102	Anderson et al. (2010)	Spectroscopic (H α Fitting)
XO-1	5750 ± 75	Tinetti et al. (2010)	
WASP-39	5400 ± 150	Faedi et al. (2011)	Spectroscopic (H α Fitting)
WASP-80	4145 ± 100	Triaud et al. (2013)	Spectroscopic (H α Fitting)
WASP-52	5000 ± 100	Hebrard et al. (2012)	Spectroscopic (H α Fitting)
GJ 3470	3600 ± 200	Bonfils et al. (2012)	Photometric
WASP-67	5200 ± 100	Mancini et al. (2014)	Photometric
WASP-29	4800 ± 150	Hellier et al. (2010)	MCMC Transit Fitting with Spectroscopic Priors
HAT-P-3	5185 ± 80	Chan et al. (2011)	Spectroscopic + Isochrones

Table 4.1: Literature values for stellar temperatures based on exoplanet discovery papers. Original sources for each value are given along with the method used to obtain the effective temperature where possible.

4.3.1 Literature Temperature Values

In this work, literature values of temperature are used to compare my derived temperature estimates. A summary of these literature temperature values is given in Table 4.1 with their sources and the method with which they were derived. These values are taken from the original exoplanet discovery papers. I have chosen these values as they are the ones used in deriving exoplanet parameters. They are also the most likely values to be quoted in any further work using these exoplanets, including Chapter 3. If these are substantially different to the temperature estimates retrieved in this work there would be a proportional knock on effect to retrieved exoplanet parameters.

4.3.2 Checking WFC3 Calibration with 2MASS

To check the calibration and consistency of my stellar spectra I can compare the data used here to data from other surveys. Many of these stars have 2MASS photometry. Some of these stars are bright, such as 55 Cancri e, which causes saturation and larger errors in the retrieved j magnitudes. I have used 2MASS photometry to check my calibrations for WFC3 are correct.

Using the zero-points from the SVO Filter Service⁹³ I convert the 2MASS magnitudes for each star into j band fluxes. I compare this with the average value from WFC3 at $1.235\mu\text{m}$, the midpoint of the 2MASS j band. The percentage error between the two is shown in Figure 4.5. Almost all candidates in this work match within a $\sim 5\%$ of their 2MASS values. 55 Cancri has the largest errors, likely due to saturation in 2MASS. Some fainter stars are discrepant by 10% or more. Based on testing

⁹³

Carlos Rodrigo (2012)

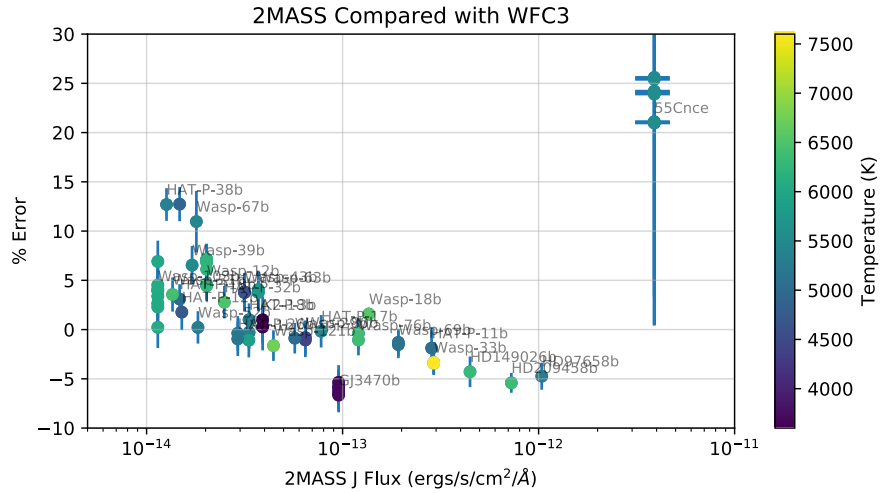


Figure 4.5: Comparison of 2MASS j magnitude values for all the stars used in this work and the equivalent j magnitude derived from WFC₃ spectra. 55 Cancri is the most discrepant as it is bright and most likely saturates 2MASS. Most values are within $\sim 5\%$, suggesting that my WFC₃ data are well calibrated.

against literature spectra and photometry, I am confident in the absolute flux and wavelength calibration of the spectra produced in this work. This allows meaningful and accurate comparisons with stellar models, which are discussed below.

4.4 SPECTRAL MODELS

In this chapter I employ 1D stellar atmosphere models to create synthetic spectra across a wide temperature grid. These have kindly been produced by Thomas Masseron and make use of the 1D LTE MARCS model atmospheres of Gustafsson et al. (2008). The synthetic grid was created using the TURBOSPECTRUM synthesis code from Plez (2012). The atomic and molecular data are compiled from the VALD database from Ryabchikova et al. (2015). The models cover a temperature range between 3000K and 8000K and $0.3\mu\text{m}$ - $2\mu\text{m}$. There are three possible free parameters to this model; the surface temperature (T), the metallicity (m) and the surface gravity of the star ($\log(g)$). The models are given in flux as a function of wavelength in units of $\text{ergs/s/cm}^2/\text{\AA}$ per unit surface area of the star. I have fixed the metallicity and $\log g$ parameters in the models to solar values. Due to the low spectral resolution of the data in this work, these parameters cannot be constrained.

To assess the spectra from WFC₃ I have built a grid of models across temperature in 25K increments. The literature values of temperature for all of the stars in this work have errors of $\gtrsim 25\text{K}$, making this fine grid appropriate. The models are between temperatures of 3000K and 8000K, with the lower limit being due to uncertainties in molecular chemistry and convection in the star.⁹⁴

It would be possible to have a second free parameter in this work for the distance to the star. The distance to the star effectively creates the normalisation in flux. This normalisation is instead allowed to vary to optimise the fit to the slope.

There are several other models available including ATLAS⁹⁵ (another 1D LTE model) and more sophisticated 3D models such as CO₅BOLD models⁹⁶. As discussed in Bonifacio et al. (2011), these models do produce different results due to their differences in assumptions and geometry. They each have strengths and weaknesses (for example, ATLAS goes to higher temperatures where MARCS is capped at 8000K, while MARCS is able to hand both plane parallel and spherical geometry). Most models assume local thermodynamic equilibrium (LTE), which is not the

⁹⁴ Bonifacio et al. (2011)

⁹⁵ Kurucz (1992)

⁹⁶ Freytag et al. (2012)

case due to escaping radiation. It is up to the user to choose the models that meet their needs. In this case we choose the MARCS models as they are considered to be slightly more reliable and they include a more complete set of molecular opacities, which are crucial for cool stars ($T < 3750\text{K}$)⁹⁷. However, as these spectra cover a wide range of temperatures they would be an excellent test case to compare the reliability of major stellar atmosphere models in the IR.

⁹⁷ Bonifacio et al. (2011)

4.4.1 Known Problem with Stellar Models and Cool Stars

Stellar spectral models perform poorly for cool stars such as M and K dwarfs. As discussed in Bonifacio et al. (2011), their low temperatures ($\lesssim 3750\text{K}$) allow molecules to persist in their atmosphere. This can cause absorption in the spectrum and create more complex chemistry. Cool stars are also largely convective in deeper layers, and 1D models (such as the MARCS models used here) make assumptions based on mixing length to approximate this⁹⁸. These two factors cause larger errors in the reported temperatures for these stars than for the FGK stars.

⁹⁸ Bonifacio et al. (2011)

Cool, small stars present excellent opportunities to classify transiting planets⁹⁹. Their small sizes create a larger transit depth. The transit depth for a planet around a small M star is almost double that of a planet around a sun-like, G type star. A further benefit of cooler stars is that their habitable zone is much closer in, leading to shorter orbital periods and more frequent transits for habitable zone targets. This gives a higher observation probability. For these reasons, several missions have targeted smaller stars including the TRAPPIST, MEarth and SPECULOOS instruments. NGTS will also be able to observe nearby, bright K and M stars. It is imperative to be able to accurately estimate stellar parameters of cool, small stars for these missions to produce accurate exoplanet parameters.

⁹⁹ Gillon et al. (2017)

4.5 TEMPERATURE ESTIMATES USING WFC3

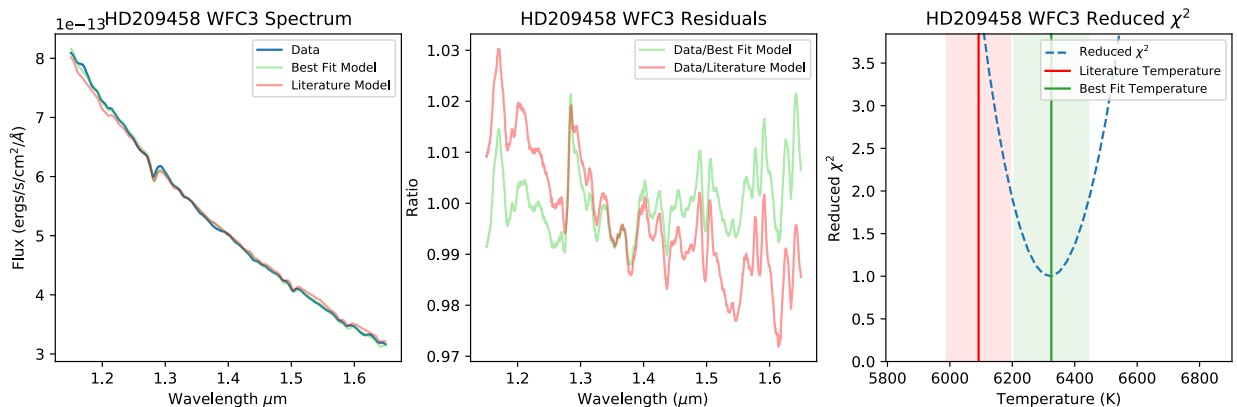


Figure 4.6: Model fit to HD209458 WFC3 data. Here there are two models plotted. The model with the temperature closest to the literature value and the model that is the best fit to the data. Left: Original spectrum and two model fits. Middle: Residuals between the data and the two models. The literature model shows a strong slope. Right: Reduced χ^2 for the model grid with literature best fit value plotted. Here shaded regions indicate 1σ errors.

To fit WFC3 spectra with the model I employ a reduced χ^2 fit across the model grid. For literature temperatures above 4250K the entire temperature grid is used. However, for cooler stars I employ a flat prior. This prior limits the temperature of the star to between 3000K and 4250K . This prior ensures that the degeneracy between cool stars with molecular absorption and warmer stars with a steeper blackbody slope is avoided.

An example of this fit process is given in Figure 4.6 for HD209458. There are two models, the literature model (which is atmospheric model at the closest grid point to the literature value) and the best fit model (which is the model at the grid point that produces the lowest reduced χ^2). Note that the χ^2 here has been normalised to find the best fit possible given this set of models. The original χ^2 values range from $\gtrsim 1.5$ to ~ 30 , with HD209458 having a minimum reduced χ^2 of 19. This suggests either the errors on the data are too small (which could be the case as they do not take into account the correlated errors of neighbouring pixels) or that the model is not a particularly good fit. The reduced χ^2 improves to 16 if the Paschen Beta line is removed from the fit, suggesting that the model is not fitting well around absorption features and that the inclusion of model errors would improve the fit.

We see from the residuals in the middle panel of Figure 4.6 there is a slope in the literature model. The best fit model is a slightly steeper model, creating a higher temperature.

All of the stellar spectra from the sequence in Figure 4.4 have been fit for temperature using the model grid. The results are shown in Figure 4.8. Model fits to IR WFC₃ data are consistently $160\text{K} \pm 30\text{K}$ hotter than literature values given in Table 4.1. Figure 4.8 shows this offset is consistent across all spectral types used in this work. There is a large spread in this individual values of this discrepancy of $\sim 200\text{K}$. This is larger than the discrepancy expected from literature values due to different temperature estimation methods (see Section 4.2).

This temperature offset should equate to a steeper spectral slope in the WFC₃ band pass. The ratio of the data to the model given at the **literature** temperature is shown in the upper panel of Figure 4.7. Across all stars the blue end of the model spectrum has consistently higher flux than the data. There is consistently lower flux at the red end. This equates to a steeper slope in the data than in the model at the temperatures given by literature. The model flux for this region is found to be consistently too flat to adequately explain HST observations. This offset is $\lesssim 4\%$ for targets hotter than 4000K .

In the lower panel of Figure 4.7 the residuals between the data and the model at the **best fit** temperature are shown. The slope in the residuals has been removed and the cooler stars are fit more accurately with average discrepancies of $\lesssim 5\%$. In the best fit residuals we see overall the fit is good. There are no discrepancies due to the Paschen Beta line at $1.28\mu\text{m}$ or other elemental absorption lines. However, there are some remaining discrepancies in cool stars. These are likely due to poor approximations by the model around individual features and absorption due to water.

The $160\text{K} \pm 30\text{K}$ offset is not temperature dependant. However, on top of this offset cool stars are fit much worse in the IR than their hot counterparts, as shown in Figure 4.7. The molecular water feature in stars less than 3500K at $1.3\mu\text{m}$ is overestimated by the model by up to 15% causing large errors, shown in the residuals. I discuss potential sources for these errors below.

4.5.1 Inaccuracy in WFC₃ Data

The data presented here have been generated using the calibration files from STSci, which may be inaccurate. Errors in the detector sensitivity curve may cause a slope in the final data product. This curve is generated using a combination of pre-launch, ground-based observations supplemented with further in-flight corrections, see Kuntschner et al. (2011). These allow for small changes in the spacecraft after a turbulent launch and settling into a cold vacuum. It is possible that this instrument sensitivity curve is incorrect and there is an inaccuracy contributing to the slope I detect. Kuntschner et al. (2011) show their corrected sensitivity curve is accurate to $< 5\%$ across the detector and expect accuracy of $\sim 2\%$. The effect of the slope in the data is 4% from each edge of the spectrum (see Figure 4.6). This level of discrepancy could be caused by an inaccurate sensitivity curve.

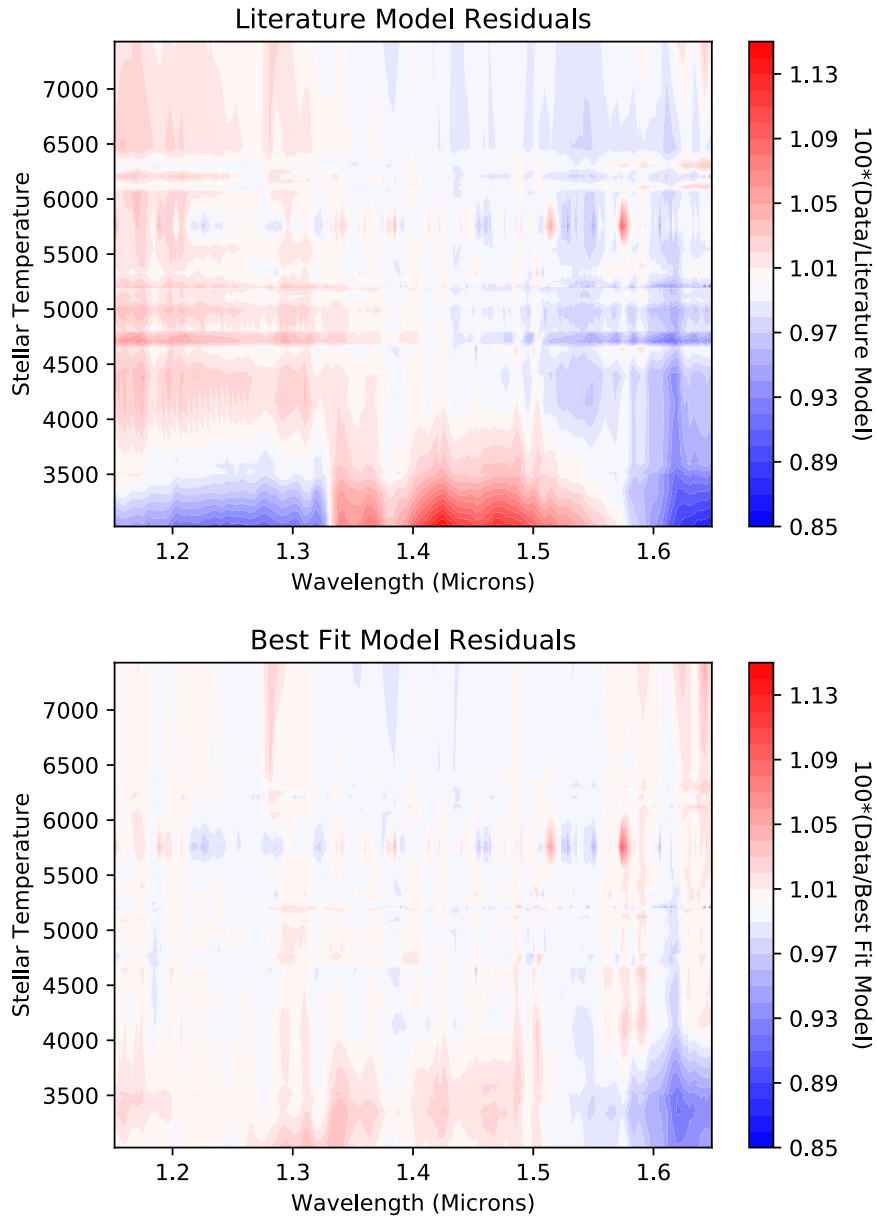


Figure 4.7: Residuals of the best fit model compare to the data for all of the stellar spectra used in this work. The general increase in flux on the blue end of the spectrum and general decrease in flux on the red side indicates a consistent slope in all the residuals across all temperatures. Cooler stars are also poorly approximated.

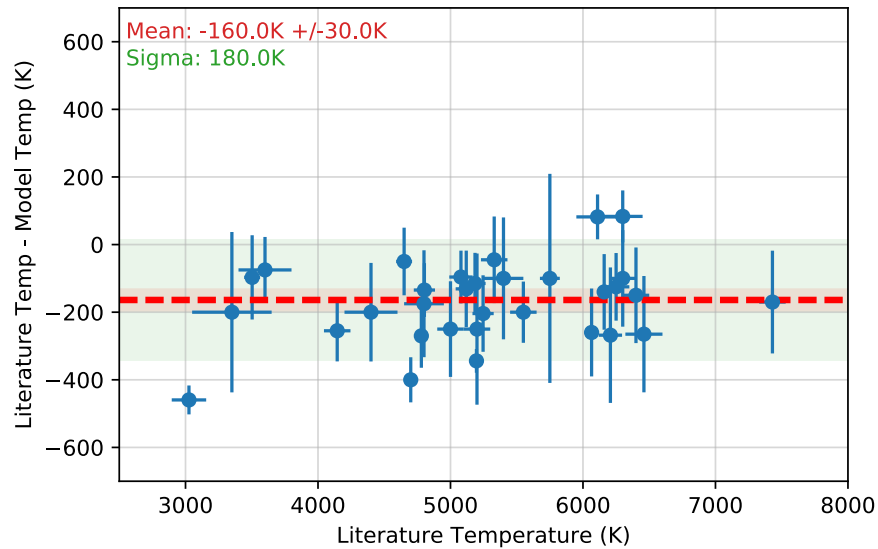


Figure 4.8: Distribution of discrepancy between literature values and best fit temperature values as a function of stellar temperature. There is a consistent offset between all stars and their literature value when measured only in the IR and renormalised to the optimum fit. Here the red line is the weighted average of all stars. There is a mean offset of $160\text{K} \pm 30\text{K}$ towards hotter stars. There is also a spread in these values of 200K .

4.5.2 Testing WFC₃ Calibration with NICMOS

The accuracy of the sensitivity curve is difficult to test. One method would be to compare to other IR stellar spectra. There is only one star in this sample with an available IR spectrum to test against: HD209458. Its stellar spectrum is provided in calspec, a repository of standard stars from HST as measured by STIS and NICMOS¹⁰⁰. The full spectrum is shown in Figure 4.9 with literature photometric values adapted from Boyajian et al. (2015). These include 2MASS points covering the same near-IR region as the WFC₃ data from this work. Blue points show the oversampled WFC₃ spectra from this work. The stellar spectra from calspec and WFC₃ match well and the IR 2MASS photometry agrees. The Paschen β feature also lines up in both spectra, lending weight to both the wavelength calibration and the photometric calibration used in this work.

The calspec database provides a spectrum of HD209458 covering a wavelength range of $0.3\mu\text{m}$ - $3\mu\text{m}$. This spectrum uses STIS and NICMOS data. I can compare the temperature retrieved from this independently produced IR spectrum with the temperature retrieval for HD209458 for WFC₃ using the same method. It can be divided into different sections; a full spectrum and one only in the IR. Each of these fit with a model in order to derive a temperature estimate as the wavelength range is changed. Figure 4.10 shows these two cases with best model fits and the model point closest to the literature value. The literature value here is taken from Boyajian et al. (2015), which provides a temperature measurement based on interferometry. (As discussed in Section 4.2 this is considered to be the most accurate method for temperature measurements.) Table 4.2 shows the results of the two fits, compared with literature and WFC₃. Both calspec cases are consistent with the literature value of temperature, though the IR only cases has larger errors due to the reduced number of points. Only WFC₃ is significantly hotter.

Based on this test, WFC₃ and NICMOS spectra produce different results. This suggests there is a problem with WFC₃ calibration. The slope in WFC₃ spectra may be introduced by a poorly approximated sensitivity curve. This would cause all spectra to have a slight ($\sim 4\%$) slope, explaining the offset in temperature values.

¹⁰⁰ Bohlin and Landolt (2015)

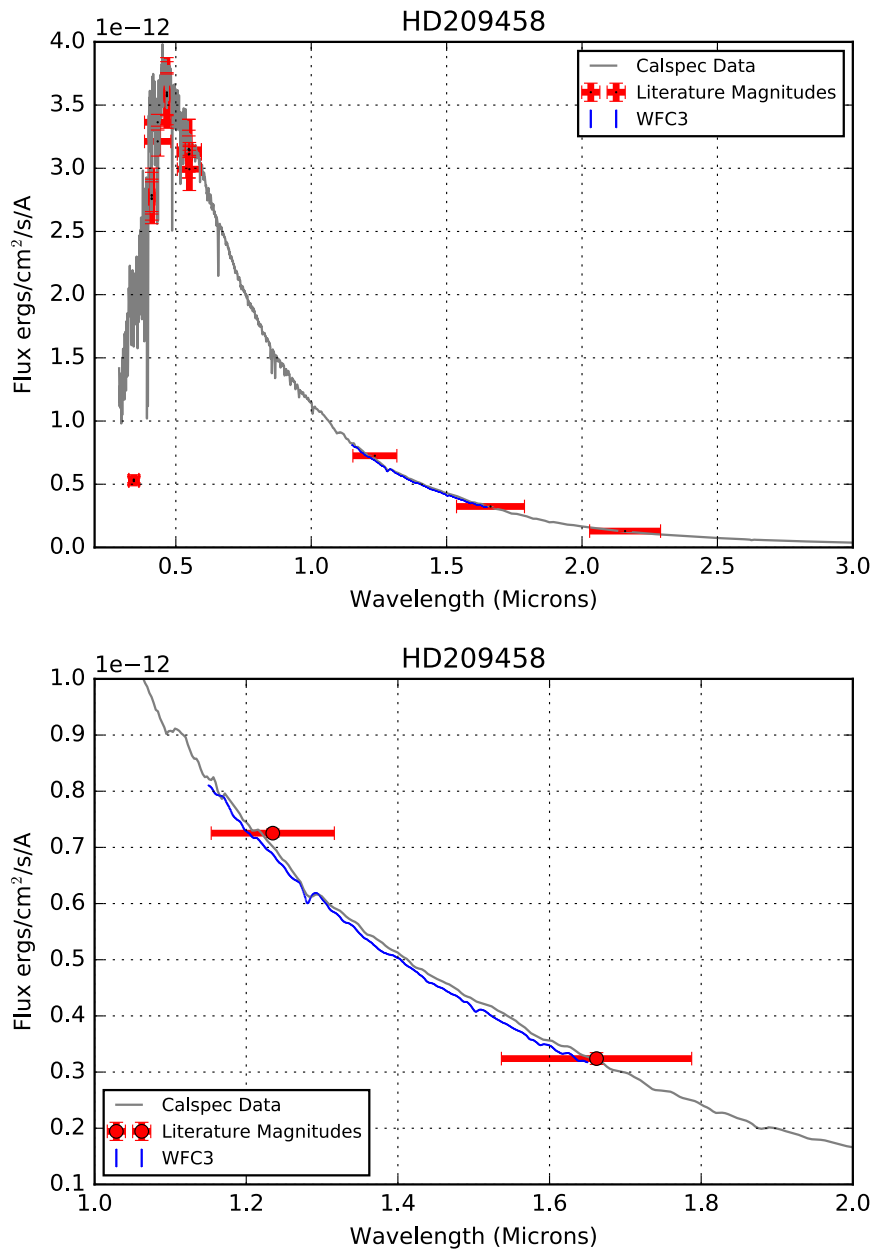


Figure 4.9: Standard star HD209458 calspec spectrum generated from HST STIS and compared with the spectrum produced in this work. Error bars in x indicate the width of the filter. Top: Calspec spectrum including literature values for photometric points adapted from Boyajian et al. (2015). Bottom: As before, zoomed in to the WFC₃ region. Here we see that the red points from 2MASS, grey points from calspec and blue points from this work agree well.

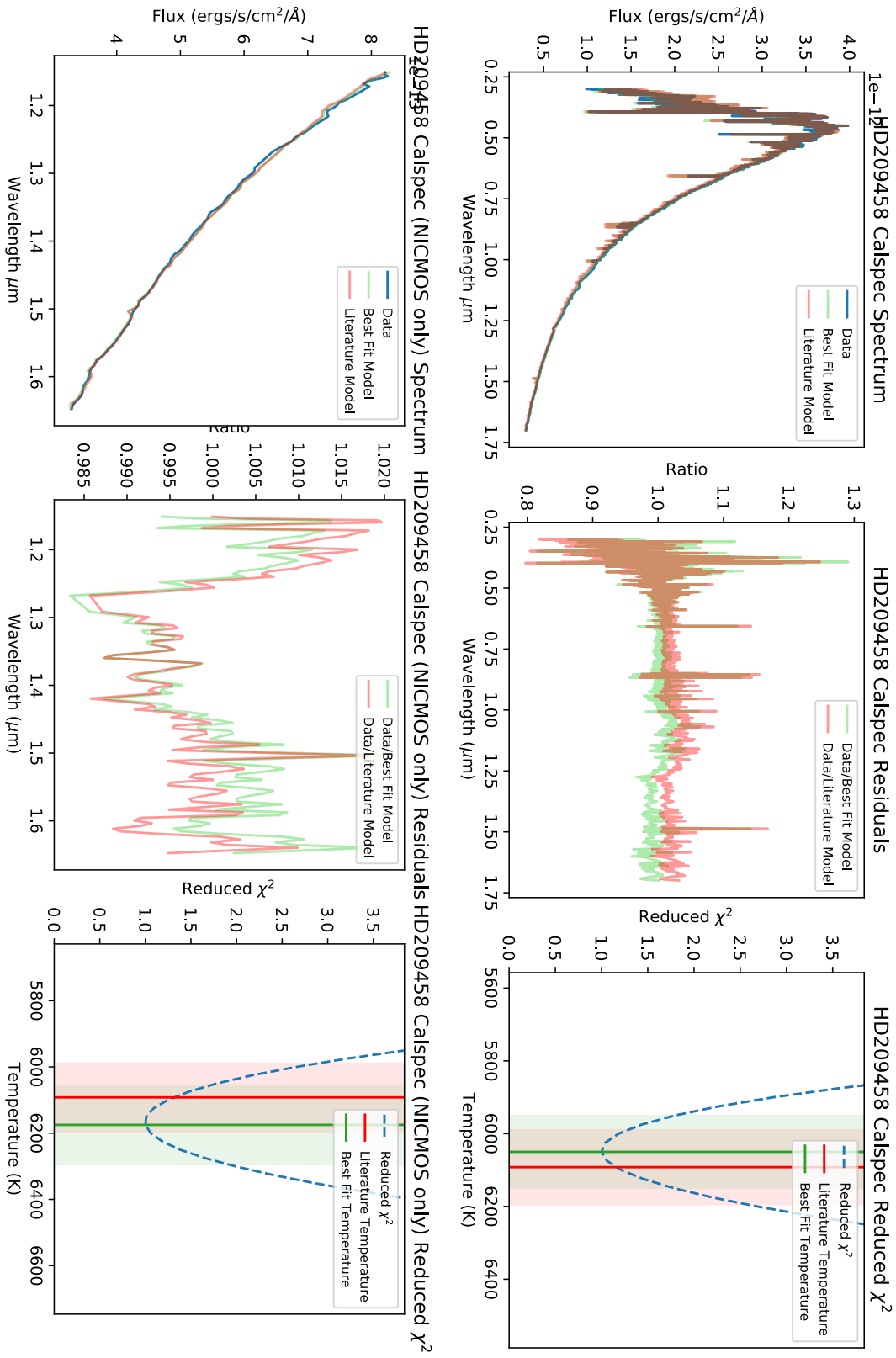


Figure 4.10: Stellar spectrum from calspec for HD209458 in full and in the IR. Top: Stellar spectra. Bottom: Reduced χ^2 fit to spectral models. Left: Full IR and Optical calspec spectrum. Right: IR only calspec spectrum. Using the entire calspec spectrum the literature value is easily found, however in the WFC3 band (centre) the temperature and distance is overestimated. The addition of visual data in the APASS bands creates recents the best-fit value through errors are still large.

Case	Temperature (K)
Literature (Interferometry)	6092 ± 103
Calspec (Full)	6050 ± 100
Calspec (IR)	6175 ± 120
WFC3	6325 ± 100

Table 4.2: Retrieved best fit temperature values for HD209458 using calspec spectrum from HST STIS and WFC3. Here the literature values for temperature and distance have been used from Boyajian et al. (2015). The literature results are consistent to 1σ , however the WFC3 measured temperature is hotter.

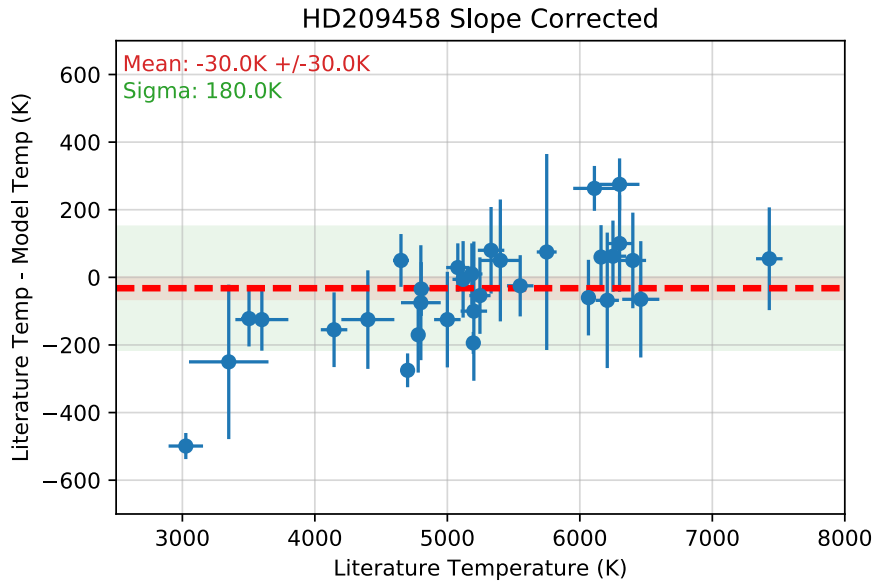


Figure 4.11: Distribution of discrepancy between literature values and best fit temperature values as a function of stellar temperature after the removal of the common mode slope. This slope is to correct the sensitivity curve and is estimated using HD209458. The offset from Figure 4.8 has been removed by correcting this slope. However, there is still a large spread in values suggesting the models do not fit accurately, particularly for cool stars.

4.5.3 Dividing Through by Common Slope

Based on the calspec data for HD209458 and the offset between literature values and retrieved values it is clear there is a persistent slope in HST WFC3 spectra. HD209458 is the only target with an interferometric measurement of temperature. Using the residuals between the literature model (based on interferometrically measured temperature) and the WFC3 data for HD209458 I can estimate this slope. These differences are shown in the middle panel of Figure 4.6. I perform a simple linear fit to the literature fit residuals (red line in Figure 4.6) and divide all stellar spectra by this slope, assuming it to be common mode through out all spectra. The results of this correction are shown in Figure 4.11.

Figure 4.11 shows that the $160\text{K} \pm 30\text{K}$ discrepancy has been removed, on average the data accurately reproduce the literature results. However, the scatter in the retrieved temperature values is 180K and cooler stars are over estimated in temperature. (Particularly GJ1214b, which is the coolest star.) This is larger than the discrepancies we would expect based either on the errors from literature or the scatter recorded in Heiter et al. (2015) (see Section 4.2.1). This suggests there are additional

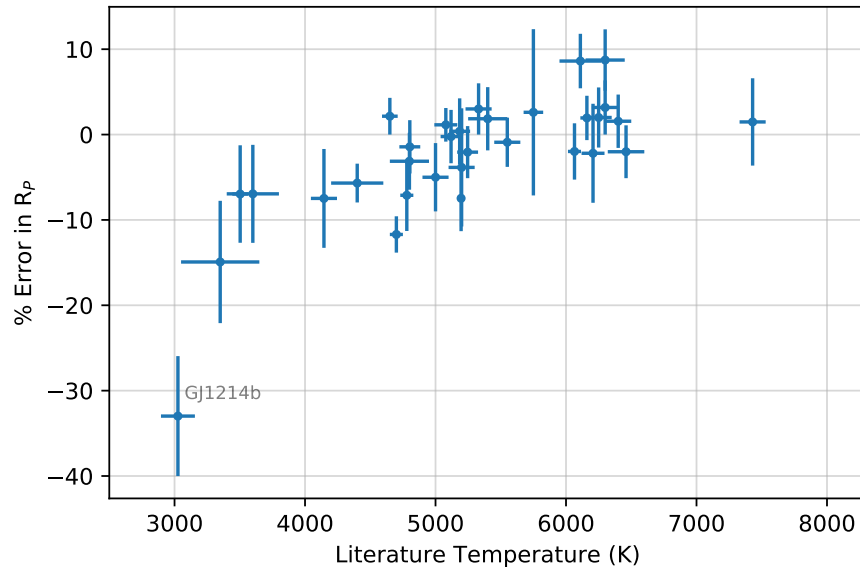


Figure 4.12: Projected change in planet radius measurements under the assumption of stellar temperatures from Figure 4.8. A increase in temperature of $160\text{K} \pm 30\text{K}$ causes stellar radii to increase, reducing the measured planet radius. This is particularly apparent for cool stars such as GJ1214.

errors in the temperature measurement. This scatter is likely due to inaccuracies in the models in the IR. In particular, based on the residuals in Figure 4.7 between literature models and WFC3 data, absorption from molecules causes significant discrepancies. This is due to the molecular absorption features being poorly approximated by cooler models (shown in the lower panel of Figure 4.7 at temperatures below 4000K).

The large discrepancy might instead suggest that the literature value for GJ1214 is simply too cool. The original literature value from Charbonneau et al. (2009) measures the stellar effective temperature to be 3026K. Anglada-Escudé et al. (2012) find a hotter temperature for GJ1214 of 3250K based on HARPS spectra and WISE photometry. Similarly Rojas-Ayala et al. (2011) finds a temperature of 3245K based on K-band water absorption. If these temperatures were accepted, GJ1214 would not be a significant outlier in this work, with a 250K discrepancy.

If we were to accept the measured temperature of these stars using WFC3 there would be large uncertainties in the inferred properties of their exoplanets. Figure 4.12 shows the projected change in exoplanet parameters with the retrieved values of stellar temperature from Figure 4.11 (after the removal of a common mode slope). Many planet radii would be under or overestimated by 10% or more compared to literature values. Planets around cooler (and therefore smaller) stars such as GJ1214b are reduced in size by 30%. Such large changes in radius could easily cause changes in the modelled density of the planets. For GJ1214b this would change the composition from 100% water to a rocky composition, based on the models from Zeng, Sasselov, and Jacobsen (2016).

4.6 DISCUSSION

From the sample of 32 stellar spectra from HST WFC3 spatial scan observations I have made a robust test of temperature retrieval using stellar spectra and a grid of stellar atmosphere models. I find that stellar spectra are consistently modelled $160\text{K} \pm 30\text{K}$ hotter in data retrieved from HST WFC3 than predicted by literature. WFC3

data does not match stellar spectral models in the IR at the 2 – 4% level. There are three possible causes for this discrepancy: 1) The reduction of the data from the previous chapter introduces an error. 2) The calibration files from STScI are not accurate. 3) The stellar atmosphere models are incorrect.

In this work I have not tested the accuracy of my reduction process. It would be possible to do this either by comparing to results from other works or by applying the same procedure to raw data. There are no libraries currently of WFC3 stellar spectra and these spectra often go unreported by those hunting for exoplanet atmospheres. Applying the same methods discussed above to raw data would be possible, however raw data would require a wavelength calibration which may also be a source of error. It would be possible using the Paschen Beta line and other absorption features to apply a simple wavelength calibration to the data and compare it to models. This would allow me to test the accuracy of my reduction compared to raw data, but has not been attempted here. It would be prudent to compare the accuracy of the spatial scan mode data used here to the accuracy from stare mode data.

The second source of a discrepancy would be the sensitivity curve applied to the data. Based on this work, the sensitivity curve appears to be discrepant by 2-4%, introducing a slope across the data. The sensitivity curve is discussed in Kuntzschner et al. (2011) and discrepancies at this level are expected. This slope is common mode across all data used here. When the sensitivity curve is corrected there is no offset between literature temperature values and stellar model fits in the IR. Pirzkal, Ryan, and Brammer (2016) also shows a correction is needed to the sensitivity curve using archival science and calibration data for WFC3. They present improved calibration files compare with those provided by STScI. As further work it would be useful to compare their updated sensitivity curve to the one currently provided by STScI to see if this alleviates the problem. By combining their work and the 32 stellar spectra presented here it may be possible to improve the accuracy of the WFC3 calibration without the need for more observations of calibration stars.

The final source of error is the stellar atmosphere models themselves. Once the sensitivity curve has been corrected, there is a large degree of scatter of $\sigma = 180\text{K}$ between literature and model fit temperatures. This scatter is larger than would be predicted from the works of Heiter et al. (2015), which compared three methods of stellar temperature retrieval. It is also larger than what would be expected based on literature values of temperature for HD209458 and 55 Cancri from the PASTEL database. This scatter may be due to inaccuracies in models in the near IR. By including a wider range of wavelengths it may be possible to estimate the shape of the black body curve better and remove this large scatter in retrieved temperature values. Further data on these exoplanet targets in the optical, near IR and mid IR region would allow the limits of the stellar atmospheric models to be tested. Some targets already have high resolution optical spectra from HARPS. Combining HARPS spectra and WFC3 spectra will likely produce a more accurate temperature fit, if the issues with the calibration of WFC3 could be overcome.

Finally, in this work I have shown that cool stars are modelled to be much hotter using only IR data. This is due to the water absorption feature being poorly approximated. There is some evidence that this may also be due to literature underestimating the true temperature of these cool targets such as GJ1214.¹⁰¹

Stellar atmospheric models contain chemistry which uses inputs of molecular and atomic transitions (see Gustafsson et al. (2008) for more details of the stellar models used in this work and the molecules included). The molecular and atomic databases used in these stellar models are based on room temperature observations. Models of stars are also informed by observations which are largely taken on the ground as the opaque atmosphere prevents infrared observations. The use of room temperature, optical information to inform models makes them more accurate under those conditions than in the IR. This leads to a set of models that are better approximated in the visual than in the infrared. Models are naturally limited and less reliable in

¹⁰¹ Anglada-Escudé et al. (2012); Rojas-Ayala et al. (2011)

the WFC3 wavelength region, potentially contributing to the large scatter I find in retrieved temperatures. There are also few points being used to constrain the fit in the IR. With the addition of more points the fit will improve.

This sample of stars covers a wide range of spectral types and a temperature range of 2600K-6500K (if TRAPPIST-1 is included). This would be a good test case to compare the performance of stellar spectral models in the IR. It would be possible to use the ATLAS models and compare with MARCS in this region to find which 1D model is more reliable in the IR. Models such as CO5BOLD could also be tested to find whether more sophisticated 3D geometry perform better in the IR. This set could also be used to calibrate these models.

Here and in many literature works, the measured temperature values rely on stellar atmosphere models (see Table 4.1). These models come with various assumptions about composition and chemistry. Measurements of temperature from interferometry are much more reliable, but difficult and only viable for the closest and brightest stars. In the future we will have access to highly accurate distance measurements from Gaia. By combining these accurate distances with photometry from GALEX, 2MASS and WISE we will be able to improve calibrations for measuring stellar temperatures via the photometric method. This will create more accurate temperature measurements for stars that are too dim or distant to measure with interferometry.

As we push the boundaries of what can be achieved with observation, these cool stars present excellent opportunities for exoplanet astronomers. Brown dwarfs can be used for the easiest observations of atmospheres and weather. Cool M and K stars can be used for the highest SNR observations of small, Earth-like planets. But to capitalise on these gains the host stars must be well understood. Obtaining accurate stellar information is important as the majority of planet properties are derived from stellar properties, these are difficult to obtain and model for cool stars. To truly understand exoplanets we must first model stars well.

Beyond understanding stars in general, small stars such as TRAPPIST-1 are cool and peak in the infrared. This may mean that for some cool and distant stars the best way to analyse their temperature will be with IR spectra. Limits in models will prevent accurate measurements of exoplanet mass and radius values and limit the possibility to model compositions of planets such as those around TRAPPIST-1.

Part IV

FINDING YOUNG DIPPER STARS IN K₂ DATA WITH
MACHINE LEARNING

5.1 INTRODUCTION

Young stars are known to exhibit a wide range of variability based on many astrophysical processes, such as stellar spots, accretion bursts, hot spots and occultations by circumstellar disks. Variability can be both aperiodic and periodic, ranging in periods of many years to periods of a few hours.

For example, the eruptive variable FU Orionis stars can increase in brightness by 6 magnitudes, lasting years.¹⁰² UX Orionis stars are observed to undergo aperiodic occultation-like events on the order of days to weeks, reducing their brightness by a magnitude or more. This is attributed to extinction from circumstellar material.¹⁰³

Herbig Ae/Be stars, which are characterised as having intermediate masses between $2M_{\odot}$ and $10M_{\odot}$, are early type stars with circumstellar disks.¹⁰⁴ Many are known to vary in their light curves and spectra as material occults the star. These are distinguished from their smaller, cooler counterpart, known as T Tauri stars. T Tauri stars also host young protoplanetary disks and are divided into Classical T Tauri Stars (CTTS) and Weak-line T Tauri Stars (WTTS) based on the equivalent width of their H α absorption feature, though their absorption is known to vary. WTTS stars host tenuous disks whereas CTTS stars host optically thick, gas-rich disks.

The variations seen in young stars are often attributed to either features on the stellar surface or interactions with the stellar environment.¹⁰⁵ Due to the young age of the stars they have large dust fractions, causing optically thick material close to the host star. This in turn leads to variability. This is attributed to one of two processes; either occultations of the star by dust in the local environment or by interactions between the disk and the star causing accretion bursts/hot spots. These can vary from highly regular and periodic to aperiodic and stochastic, particularly in the case of dipper stars.

In recent years a new class of CTTS's has been discussed known as a "dipper" star.¹⁰⁶ These are characterised as CTTS with a relatively flat light curve and sharp, short duration dips. An example of a dipper star is shown in Figure 5.1. These dipper stars have particularly interesting variability where reductions in flux of more than 50% have been observed. This variability can range in time scales down to that of a few days or less. Such large dips can not be explained by star spots alone and are attributed to occulting material at the inner edge of the circumstellar disk. The observed extinction between the optical and IR during dips adds weight to this theory.¹⁰⁷

Dipper stars are young, disk bearing stars that undergo rapid occultation events due to circumstellar dust. The dipper phenomenon is characterised by the depth of the occultations, the re-occurrence of similar events on short time scales, irregularity in dip depth and changes in dip shape as a function of time. The dip depth must be large enough to be distinct from star spots, blocking at least 10% of the stellar flux. Dips must also reoccur during an observation. The dip depth can vary greatly within the light curves of individual objects. This suggests the material blocking the stellar light is depleted and replenished regularly during the orbits of the host star. An example of a dipper light curve is given in Figure 5.1.

Young dipper stars have been observed photometrically with Spitzer, CoRoT and K2 which have provided light curves of more than 40 days of continuous monitoring. Monitoring of an individual target by a single instrument has not exceeded 80 days. In work from Cody et al. (2014) the NGC 2264 region was studied using CoRoT and Spitzer, observing both the optical and infrared simultaneously. Out of the 162 disk

¹⁰² Hartmann and Kenyon (1996)

¹⁰³ Herbst et al. (1994)

¹⁰⁴ Herbig and H. (1960); Waters and Waelkens (1998)

¹⁰⁵ Herbst (2012)

¹⁰⁶ Morales-Calderón et al. (2011); Cody et al. (2014)

¹⁰⁷ Bouvier et al. (2003); Alencar et al. (2010); McGinnis et al. (2015); Bodman et al. (2016)

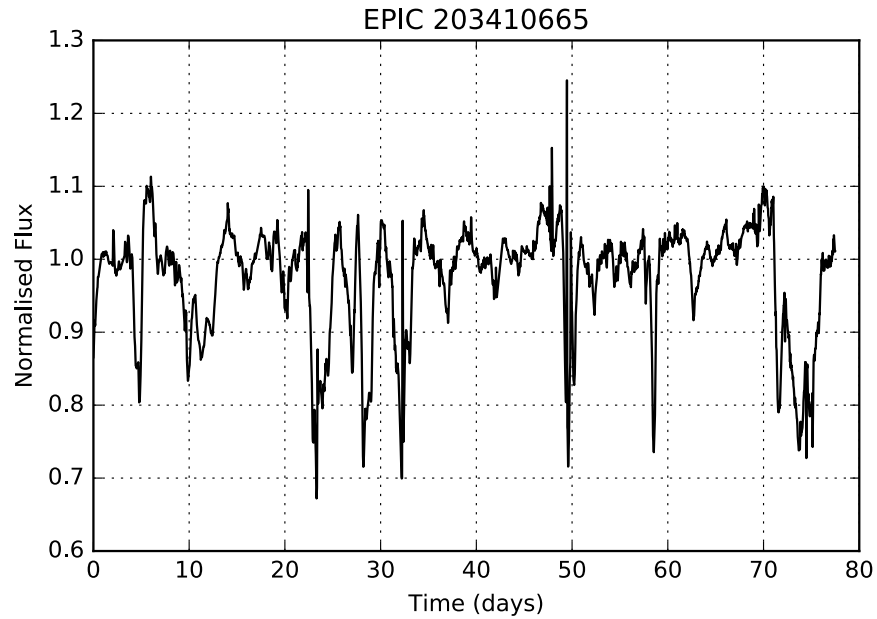


Figure 5.1: An example of a star in K2 Co2 exhibiting the dipper phenomenon. Notable features include the depth of each dip, the repeatability of the events and the changing dip depth over time. While the dips do repeat and reappear, the dipper is not regular and periodic.

bearing stars in the survey, 35 were found to be dipper stars. This leads to a dipper fraction quoted in their work of $21.6\% \pm 3.7\%$.

A separate burster class of stars was also discussed in the accompanying paper Stauffer et al. (2014). Bursts are defined as distinct from stellar flares due to their symmetric shape, their long duration (up to several days), their frequency and their periodicity. The bursts in such targets are attributed to accretion instabilities.

¹⁰⁸ Ansdell et al. (2015)

Dippers exhibit occultations with periods of $\lesssim 10$ days¹⁰⁸. Though many dipper light curves are not periodic, they exhibit recurring events which are attributed to multiple occultations of the same material. This short period corresponds to an orbital distance, if Keplerian rotation is assumed, of $\lesssim 20R_{\odot}$.

Work from Bouvier et al. (2003), Alencar et al. (2010), McGinnis et al. (2015) and Bodman et al. (2016) suggests that the photometric variability of young T Tauri stars such as those shown in NGC 2264 by Cody et al. (2014) and Stauffer et al. (2015) can be attributed to warps in the disk at the inner edge and accretion streams. This warp would be caused by interactions between the stellar magnetic field and an inclined disk. McGinnis et al. (2015) show also that when observing dips in both optical and IR the extinction is large and consistent with some amount of growth of dust grains in the disk. The occurrence rate of dippers ($\sim 20\%$) is therefore attributed to an inclination effect where by the occultations are only observable at inclinations of $\sim 70^{\circ}$. Ansdell et al. (2015) also suggests vortices introduced by Rossby Wave instabilities or inhomogeneities in the disk as mechanisms for creating the dipper phenomenon. In Ansdell et al. (2016) it is noted that three of the young dipper sample in Upper Sco and ρ Oph that have resolvable disks in archival sub-mm data are not edge-on, and suggest that the mechanism to cause dips is not due to a viewing angle observational bias. However it is possible that these cases have inner disks which are inclined to the observer at a preferential angle for viewing the dipper phenomenon.

Ansdell et al. (2015) presented 10 new dipper targets discovered in the ρ Oph and Upper Sco region with a range of periods and occultation depths. These objects were found by eye using the 13399 K2 Co2 light curves, searching for targets with semi-periodic or aperiodic dipping events. This reduced the sample to 100 candidates. The light curves of this sample were then put through a high pass filter to remove stellar

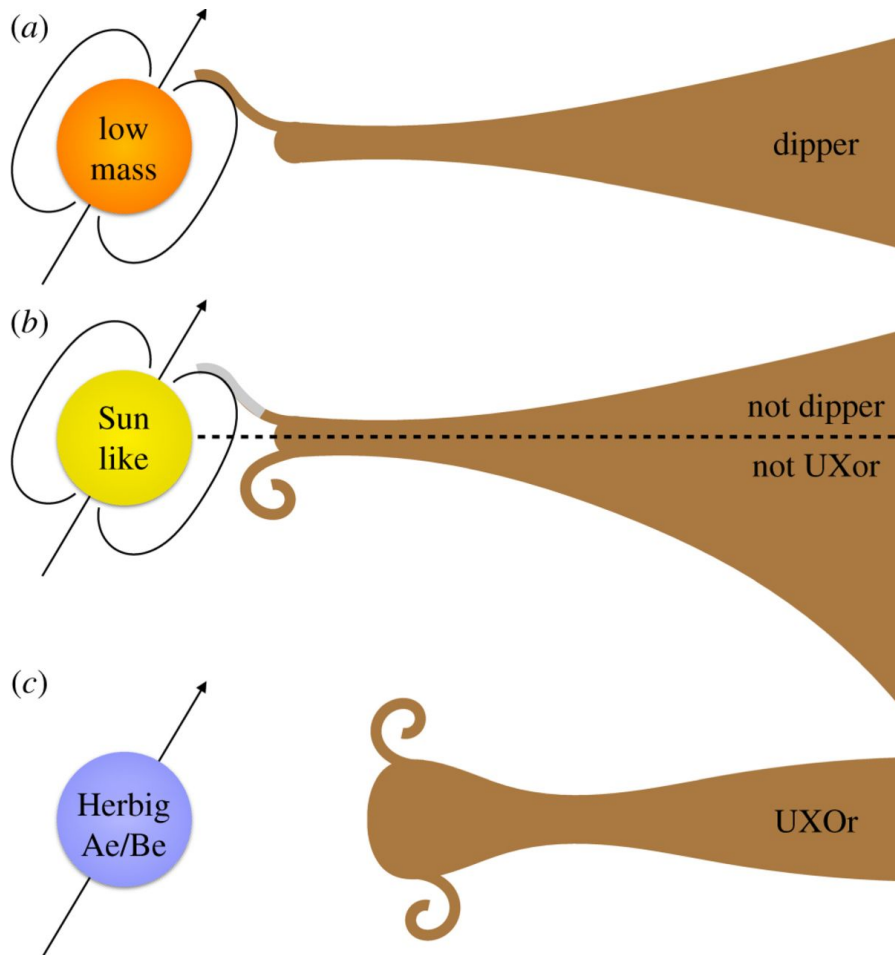


Figure 5.2: Cartoon from Kennedy et al. (2017) showing the origins of dippers and UXOrs. In the first case of the low mass star material is accreted onto the star surface because the dust sublimation radius is inside the co-rotation radius. For larger stars dust sublimates outside of the co-rotation radius (shown in grey) and any material that is not accreting but is lifted out of the disk due to turbulence is obscured by the outer disk. For very large stars the turbulence is large enough to be viewed above the disk and occult the star, causing UXOrs.

variability. Each light curve was then compared with several metrics to determine whether they would be classified as dippers. This metric based on having several dips which are deep, narrow and distinguishable from other modes of variability. This metric is discussed further in Section 5.7.1. The sample was reduced to 25 targets flagged as dipper candidates with 10 of them being firmly classified as dippers.

Figure 5.2 shows a diagram of the current theory for the dipper phenomenon, taken from Kennedy et al. (2017). Dippers have only been observed in low mass M and K stars, with high mass Herbig A/B stars showing UXOr behaviour. In dipper stars the occultations are attributed to dust from the circumstellar disk accreting onto the surface of the star. In larger stars the sublimation radius is also larger, and so the dust sublimates before it can be accreted. Any small warps in the disk where turbulence causes material to be lifted out of the disk are blocked by the outer edges of the disk. In UXOrs the turbulence can cause large outflows out of the disk plane which can occult the star without the outer disk shadowing it. In the dipper case the material is funnelled down magnetic field lines onto the surface of the star. Bodman et al. (2016) discusses how the tilt of the magnetic axis relates to the observability of dippers and suggests highly tilted systems may show larger amplitude dips. Based

on this theory of dipper stars we would expect to find 1) dippers are reddened due to their dusty disks 2) dippers are only seen in M and K type stars.

In this work I present a Machine Learning (ML) approach to finding dipper stars in the same K2 Co2 dataset as used by Ansdell et al. (2015). This approach is preferable to other methods such as searching by eye, where biases may be introduced that define the final sample, or colour cuts designed to find IR excesses indicative of a disk, which may clip out valid and interesting candidates with other disk properties. A machine learning approach will build a list of features that describe the behaviour of training candidates which can then inform my selection criteria for dippers. Our approach is to use the light curves alone to discover and classify dipper stars.

Bloom et al. (2011) have argued that machines can have a number of advantages over simple classification by eye. Firstly, the speed of a machine learning algorithm becomes much faster when several thousand light curves are used. Though there is some time investment needed to build and train the machine there are significant speed gains when using large datasets compared to human effort. Secondly, the exercise can be repeated accurately, whereas if using only classification by eye people quickly become fatigued. Finally the machine is reproducible between different groups, regardless of the biases of human opinion. These advantages combine together very well to enable possible biases in the ML approach to be tested, and mitigated against.

¹⁰⁹ Richards
et al. (2012)

One of the goals of this work is to define a (reasonably) unbiased sample. ML approaches have been shown to be powerful tools for classification¹⁰⁹. A further advantage of ML approaches is the classification is probabilistic, enabling statistical analyses of the sample.

By building an unbiased model I anticipate being able to form a more complete sample of dippers. If I can build a larger sample of dipper stars, that the ML algorithm classifies as being self-similar, I will be able to investigate population statistics for dippers in this region. A larger sample will also help to define the shared properties and characteristics of these objects, leading to insights into the physical mechanism causing the behaviour.

In this work I use K2 Co2 observations of the Upper Sco and ρ Oph clusters which are known to contain dipper stars. In Section 5.2 I discuss these observations. In Section 5.3 I summarise the two young clusters observed in K2 Co2. In Section 5.4 I discuss the building of the machine learning algorithm and the features used for training, designed specifically to highlight features of dipper stars. In Sections 5.5 and 5.7 the sample of dipper stars found by the machine learning algorithm and their characteristics are discussed. In Section 5.8 I discuss the burster stars found by this work. I summarise my findings and inferences from this dipper sample in Section 5.9.

5.2 K2 OBSERVATIONS

¹¹⁰ Aigrain
et al. (2015)

The K2 mission is a follow-up to the original *Kepler* mission launched by NASA in 2009 which failed in 2013 due to the loss of a second reaction wheel. K2 now uses thrusters to alter the roll angle of the satellite, which fire every few hours. This process causes a significant systematic in the data which has proven difficult to correct¹¹⁰. K2 must now observe on a plane close to the ecliptic and observes for 80 days in four campaigns each year, with a long cadence sampling of 29.4 minutes.

Figure 5.3 shows the K2 Co2 field centred at an RA of 246.12° and Dec of -22.44° with 13,399 stars observed in long cadence mode beginning on the 23rd of August 2014. Note that two modules (3 and 7) are no longer functional and appear as gaps in the field.

Unlike the majority of other large scale missions, K2 has not benefited from a single reduction team. Instead, the data have been processed by many separate teams. This results in several light curves per target for the user to choose from, as well

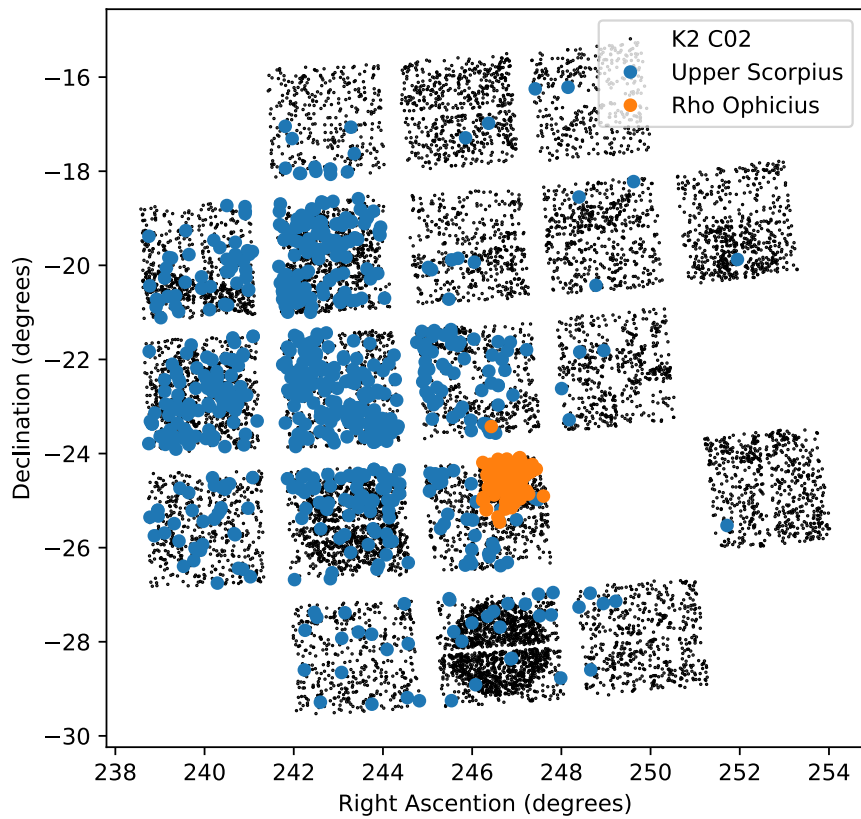


Figure 5.3: K2 Campaign 2 field. ρ Ophiuchus members have been highlighted in red and are much more localised than the Upper Scorpius members, highlighted in blue. Here only members that are also observed in K2 Co2 are shown. The two large gaps in the field are from modules that have failed and no longer produce data.

as the option to reduce the data themselves. While this approach has led to the data becoming available quickly and many complex problems in correcting for the roll angle of the spacecraft being overcome, it does leave us with light curves with varying assumptions and systematics.

There are several reductions publicly available through the STScI MAST service. Vanderburg and Johnson (2014) employs a Self-Flat-Fielding technique to remove the noise from the roll of the space craft. Aigrain, Parviainen, and Pope (2016) uses Gaussian Process regression using the 2D position of each star to model the instrumental systematics and astrophysical variability in each light curve. Luger et al. (2016) utilises a pixel level decorrelation to remove systematics as well as Gaussian processes to find the astrophysical variability for each source. All of these reductions improve the raw K2 aperture photometry, known to be up to a factor of 3-4 times less precise than the *Kepler* mission. These reductions achieve an improvement in precision to within a factor of two of the original mission. Another approach is to use the software PyKE to reduce both *Kepler* and K2 light curves with a variety of techniques based on the user requirements, including Principle Component Analysis. This approach is taken in Ansdell et al. (2015) to produce their dipper sample.

Dippers are very unusual targets. Their strong astrophysical variability may be misclassified as systematic error by many reduction pipelines. Notably some pipelines sigma clip their final data product, which could potentially remove dipper trends. I find that the reduction from Vanderburg and Johnson (2014) (hereafter referred to as VJ2014) does not heavily penalise dippers by sigma clipping and I employ this reduction in my work. As the dipper phenomenon causes extreme variance in flux it would be possible to find evidence for it even in the raw data in some cases, though I do not explore this possibility in this work.

There are still notable systematics which heavily affect dippers. Particularly step functions, where at approximately 40-60 days the light curve will increase by some nominal factor, and long term low order polynomial trends are prevalent in the data. In order to correct for this I apply a 30-day smoothing kernel to the data and divide this trend out of the light curve. Since dippers are known to vary on the order of a few days this 30-day kernel leaves the dipper phenomenon unchanged. I also clip out any 6 sigma outliers. The data were also converted from normalised flux to magnitude using a g photometry from APASS.

As K2 pixels are approximately 5 arcseconds across I also remove any sources that are within 20 arcseconds of another source, assuming they are duplicates or will contaminate each other. In such cases I take the brightest source and remove the dimmer source from the search.

5.3 UPPER SCORPIUS AND ρ OPHIUCHUS

¹¹¹ Wilking, Gagné, and Allen (2008); Lodieu (2013); Luhman and Mamajek (2012); Parks et al. (2014); Rizzuto, Ireland, and Kraus (2015); Ratzka, Köhler, and Leinert (2005); de Zeeuw et al. (1999); Slesnick, Hillenbrand, and Carpenter (2008)

Membership lists for ρ Oph and Upper Sco can be created from the literature¹¹¹. Using a cross match radius of 1 arcsecond I am able to differentiate which K2 targets are likely members of each cluster, though some members have not been identified in the literature to date. In the K2 Co2 sample I find 708 stars to be members of Upper Sco and 199 to be members of ρ Oph. These are shown in Figure 5.3. From colour diagrams such as Figure 5.19 it is clear that this membership list is incomplete and there are young stars with IR excesses consistent with being a member of one or both of the clusters. With the release of measurements of parallax for these targets in April 2018 from the GAIA mission the two clusters will be much easier to distinguish. I recommend revisiting the cluster memberships used in this work after GAIA DR2 data is available to better estimate the dipper fraction in these clusters.

Both of these clusters are young star forming regions. ρ Ophiuchus is a smaller cloud complex which is highly extincted causing many stars to be extremely reddened. Upper Scorpius was found to have an age of 11 ± 2 Myrs by Pecaat, Mamajek, and Bubar (2011) while ρ Oph is a younger cluster with an age of 0.1-1 Myrs as

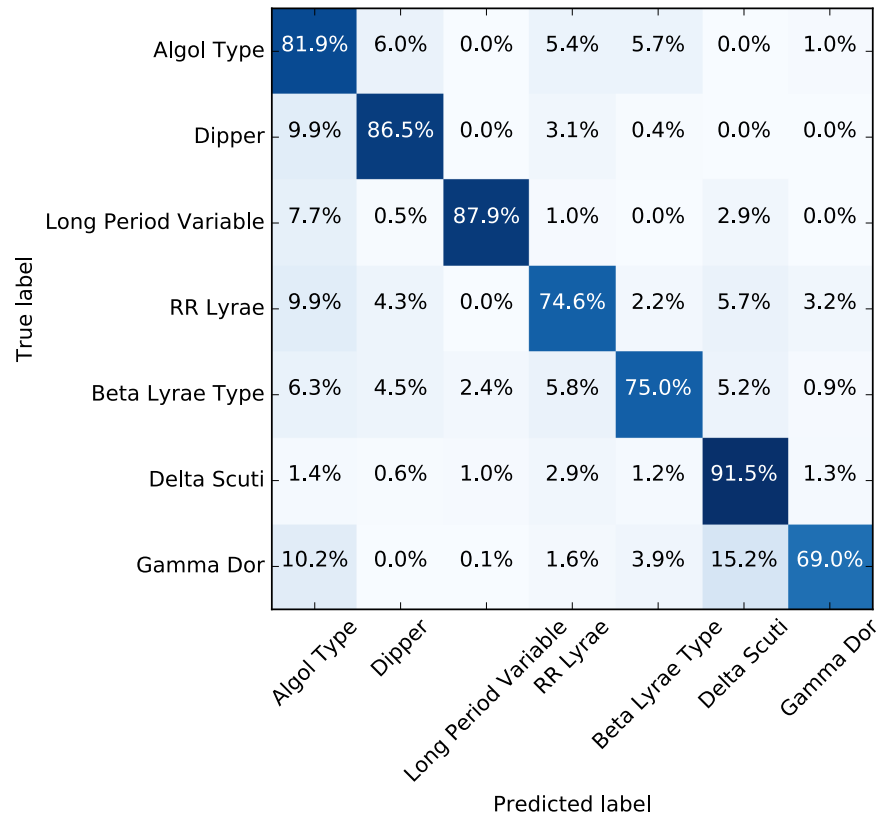


Figure 5.5: Confusion matrix for the final classifier after 200 iterations using an 80-20 train-test split. I see for dippers that $\sim 86\%$ of dipper stars were correctly classified with most of the incorrect classifications lying in Beta Persei or Algol type binaries. The matrix is well diagonalised showing that the method works well for classifying variables.

tures measured directly from the light curves have been used, (see Section 5.4.3). I use the implementation of RF classifiers from python’s scikit-learn¹¹³ which gives a classification for each target with a weighted probability.

¹¹³ Pedregosa et al. (2011)

5.4.1 Training Sample

As with all supervised machine learning, RF requires a training set. In this set the true classification of the data is known. The training set was built from four primary references, which provided us with classification labels for stars observed in K2 Co2. The first was the K2 Variability Catalogue II¹¹⁴ (A2016), based on K2 data from campaigns 0–4. A2016 include 7 distinct classes in their final results table: RRab, DSCUT, GDOR, EA, EB, OTHPER and Noise (see A2016 for more details on these classes). The second catalogue is the Machine-learned ASAS Classification Catalog¹¹⁵. Here I chose targets that had a classification probability of more than 60% and cross matched them with targets in the K2 Co2 sample. I also use stars classified in the Simbad database that have been classified in the literature. Finally we select a sample of 22 (out of 25) dippers in Ansdell et al. (2015) and Bodman et al. (2016), 3 being rejected as having low signal-to-noise light curves on inspection. Table 5.1 shows the final number of training targets that are in Kepler Co2 and were used to train the machine.

¹¹⁴ Armstrong et al. (2016)

¹¹⁵ Richards et al. (2012)

As mentioned previously I am concerned only with classifying dippers well, rather than comprehensively classifying variable stars. However, as discussed in Section 5.4.2.1, I find that having additional classifications does improve the dipper classification. The classifications used in this work are Eclipsing Binary (Beta Lyrae type

Table 5.1: Number of objects in each training class, built from BIGMACC, K2 VarCat and the literature objects. Includes one iteration as discussed in Section 5.4.2.1

Classification	Number
Dipper	40
Beta Persei Type Binaries	69
Beta Lyrae Type Binaries	55
Long Period Variable	45
RR Lyrae	74
Delta Scuti	121
Gamma Doradus	32

and Beta Persei type), Long Period Variable, Gamma Doradus, RR Lyrae, Delta Scuti and Dipper.

5.4.2 ML Performance

In order to test the efficiency of the RF classifier a portion of the training sample is kept to one side (20% in this case). The RF classifier is then trained on the remaining data (80% in this case). The classifications of both sets are known. Once the RF classifier is built this can then be run on the remaining 20% set to find the “predicted” classifications. I then compare the known classifications to the predicted classifications. This produces a confusion matrix which is shown in Figure 5.5, run on an 80/20 test-train split. The matrix is well diagonalised, showing the classifier correctly classifies each variable type the majority of the time.

There are only a small number of targets in each classification, shown in Table 5.1, which can produce some scatter in results. To avoid errors from the small training sample I run the classifier 200 times and record the result for each iteration. Figure 5.5 is produced by running the classifier 200 times and taking the average number of targets in each class.

5.4.2.1 Iterations

Once the RF classifier has been built it is then possible to use metrics such as the confusion matrix, (see Figure 5.5), to evaluate the quality of the machine. After the first iteration of the machine it was noted that the classifier did not perform adequately with a small sample of dipper stars. Using only the literature sample of 22 dipper stars in K2 Co2 provided a correct classification of the training set 68% of the time. This small sample caused approximately 32% of candidates to be misclassified, mostly as Beta Persei or Algol type eclipsing binaries. To avoid this I manually vetted the results of the machine learning algorithm for dippers in this first iteration (with the 22 literature dipper stars as a training sample). After running the classifier once, a further 18 targets that clearly met the classification boundaries were chosen and added them to the training sample. After retraining, this increased my correct classification percentage from 68% to 86%. This was then applied again to the K2 Co2 data to find my final sample. The final sample of dippers used to train the machine is shown in the Appendix in Chapter 6.6.

I find the approach of classifying many types of variable produces better results than classifying dippers and ‘non-dippers’ only, improving our correct classification probability by 18%.

5.4.2.2 Limitations of RF Classifier

RF classifiers are limited in several ways but notably in this application it is not possible to classify an object as multiple classifications e.g. An eclipsing binary with

dipper characteristics. This can partly be addressed by running the RF algorithm many times, as it is using a random method. An object with two potential classifications will then be classified as each one multiple times over multiple iterations. I am not concerned with this in my work, as I expect the signature of dipping to overcome most other modes of variability, e.g. Eclipsing binaries, stellar variation, LPVs etc, due to the depths of the dips and my designing of a feature list specifically tuned to highlight the dipper phenomenon.

5.4.3 Features

RF classifiers use a distinct set of features that describe the behaviour of the target. I use a set of features that I have specifically designed to distinguish dippers from other variable stars. These features are based solely on the Kepler light curve with all being easily derivable from the time series based on periodicity, symmetry in the light curve and “groups” of points that are distinct from the average population. The 25 features used in this work are reduced from an initial 60 features, based on those that were the most relevant and useful to dipper classification. The final 25 used here have been shown to have high importance scores using the scikit-learn package ‘extra-tree-classifier’ function as shown in Figure 5.6. These are shown in Table 5.3.

Based on the works of Cody et al. (2014) and Richards et al. (2011) I have included some features that are common in literature works with ML algorithms (see below). I have uniquely added Gaussian Mixture Models and Wavelet Analysis to measure asymmetries in the light curve and changes in periodicity. These are also discussed in the sections below. These features have high importance as shown in Figure 5.6. I have also developed routines to find features based on ‘groups’ of points, that are three or more points continuously above a threshold. This allows me to find true astrophysical dips above any spikes due to errors in reduction.

5.4.3.1 Literature Features

I have included several features that the literature works have shown to be important in the classification of dippers and variables in general. Cody et al. (2014) uses a statistic to quantify the asymmetry in flux that I will refer to as the M statistic defined as

$$M = (\langle d_{10\%} \rangle - d_{med}) / \sigma_d \quad (82)$$

where $\langle d_{10\%} \rangle$ is the mean of all the data at the top and bottom decile of the light curve, d_{med} is the median of all the data and σ_d is the RMS of the light curve. I use this statistic as one of my features in my machine learning as discussed in Section 5.4.3.

Two of the features I use have been chosen based on the work of Richards et al. (2011) which are shown in Table 5.2. *flux_mid20* is very similar to the M statistic and is a ratio of the lower 40% of the data to the upper 40% of the data, normalised to the flux in the top 95th percentile. The percentage amplitude was also used, which gives the maximum flux as a ratio to the median flux. These were found to be particularly useful in distinguishing variable stars. Richards et al. (2011) also included several features designed to analyse the periodicity in the data. I have chosen to include some measures of periodicity, however as dipper stars are often irregular I do not put a great deal of emphasis on periodic features. I instead include features that are designed to show whether there is sporadic periodicity in the data, as discussed in Section 5.4.3.3.

It would be possible in this work to also utilise colour information from surveys such as WISE, 2MASS, APASS and GAIA DR1. When infrared colours are included the classification efficiency is increased to 95%, an improvement over my current 86%. Colour information was rejected for two reasons; firstly there are many stars in the K2 Co2 field with incomplete colour information which I would then be unable

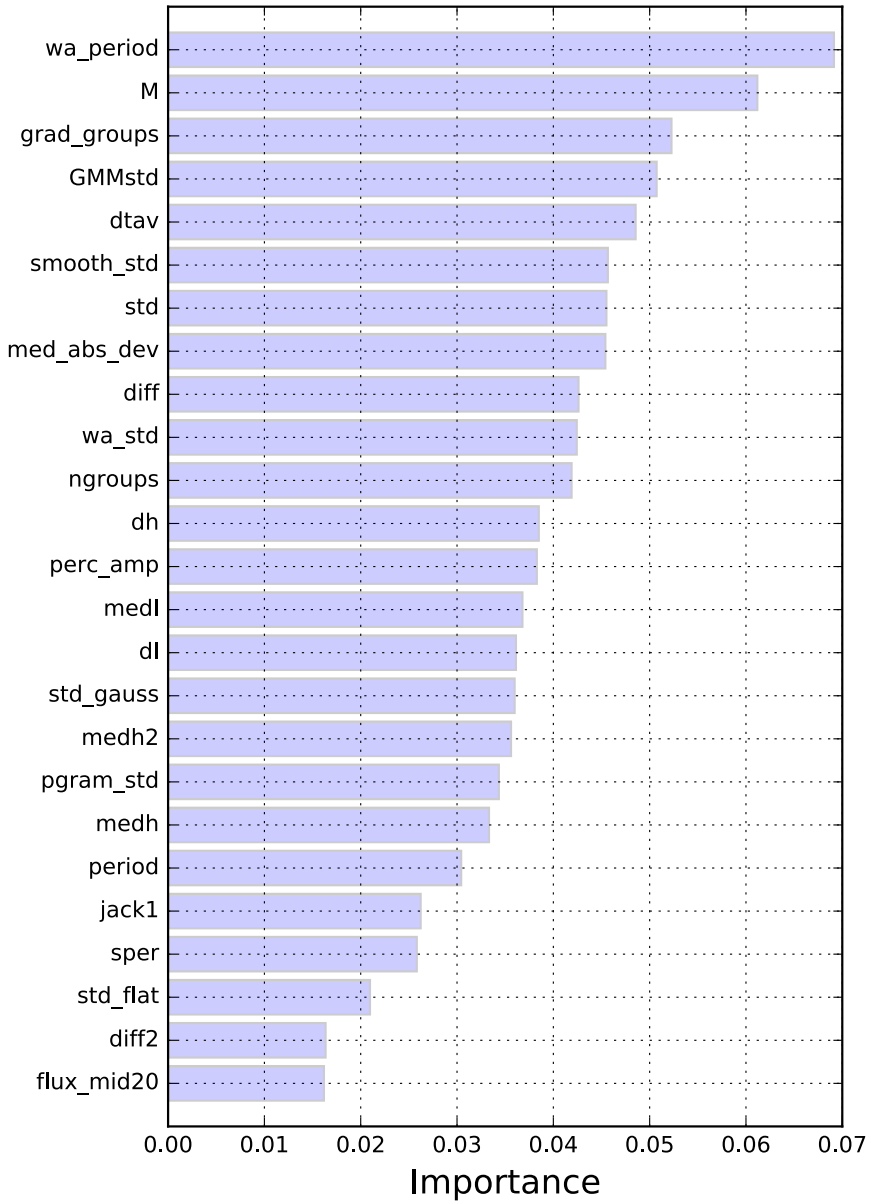


Figure 5.6: Importance score for the classifier when using only two classifications, ('Dipper' and 'Non-Dipper'). I see that the most important features for this class of object are period, M stat, the number of groups of turning points and the standard deviation. Note that this is the relative importance of each feature, summing to one.

Table 5.2: Features from the literature used in the random forest algorithm. Here features are used from works from Richards 2011 and Cody 2014

Feature	Description
flux_mid20	The difference between the median of the lower 40th percentile and the median of the upper 40th percentile divided by flux_95.
perc_amp	The maximum flux value divided by the median magnitude value.
M	The M statistic as defined in Cody 2014

to analyse and secondly adding colour information greatly weights targets with obvious disks. In order to ensure this classifier works for any star of any age and will still perform well for any stars with little to no IR excess, colour has been omitted as a feature. This ensures we are not preferentially selecting young stars to test. As the machine is not trained on colour information it would be possible to find any stars that are dippers with a smaller IR excess (i.e. no dust disk).

By omitting colour information I can also check the performance of the ML algorithm. As dippers are expected to host dust disks I would expect the dippers classified by the machine to show an IR excess and be distinguished in colour space from the background population.

Table 5.3 shows the light curve based features used in this work that were found to have high importance. These include tests of how the data varies in the first half of the light curve compared with the last half and the variance of the data.

5.4.3.2 Gaussian Mixture Models

I have included the use of 1D Gaussian Mixture Models (GMM) to split the light curve into different Gaussian populations. A GMM is a model that assumes all data points are drawn from underlying, finite, unknown Gaussian populations. Using the python package scikit-learn's Gaussian Mixture Model package¹¹⁶ I calculate the optimal number of Gaussians to describe the distributions in the light curve. This ideally splits the light curve into a stellar activity population and a number of Gaussians relating to other populations, e.g. dips, bursts, transits, eclipses etc.

In the dipper case this allows us to accurately compare the median level of the star to the average level of the dips. An example of this diagnostic is given in Figure 5.7. I use the GMM to establish a background population and then track several features given in Table 5.4.

I can use the standard deviation of the highest weighted Gaussian as a standard deviation of the stellar variability itself, assuming that other populations describe different behaviour (such as dipping, flaring or eclipses). I then use an algorithm for finding clusters of points 3 sigma away from this distribution which would describe bursts or dips. I define that clusters must contain at least three consecutive points, all of which are 3 sigma away from the stellar background population. This ensures I am not sensitive to the small spikes due to issues in the reduction of the K2 data. This also limits my sensitivity to those dippers that vary on time scales of longer than 1.5 hours (as K2's cadence is approximately 30 minutes). This creates a new set of features based on groups of points. These features are given in Table 5.5. This group finding method is simplistic and does have limitations, especially where two dips might overlap, however I find that this method is sufficient to find the majority of dips and estimate their behaviour including the depth, duration and number of dips.

¹¹⁶ Pedregosa et al. (2011)

Table 5.3: Additional light curve features used in the random forest algorithm designed to highlight dipper stars.

Feature	Description
smooth_std	The standard deviation of the smoothed data with a kernel size of 20 days. (Smoothed to the wa_period)
std	The standard deviation of the highest weighted Gaussian from GMM
med_abs_dev	The median of the absolute magnitude values less the median of the absolute magnitude values. $\text{median}(X_i - \text{median}(X_i))$
jack1	The ratio of the standard deviation of the first half of the data to the standard deviation of the second half of the data.
diff	The maximum of the magnitude less the minimum of the magnitude. (After clipping)
dtav	The difference between the mean of the magnitudes and the median of the magnitudes.

Table 5.4: Gaussian Mixture Model based features used in the random forest algorithm.

Feature	Description
GMMdiff	The difference between the median of the highest weighted Gaussian from GMM to the median of the second highest weighted Gaussian from GMM.
GMMstd	The standard deviation of the highest weighted Gaussian from GMM
GMMstd2	The standard deviation of the entire set of Gaussian Mixture Models
dGMM	The standard deviation of the residuals from the data less the GMM model

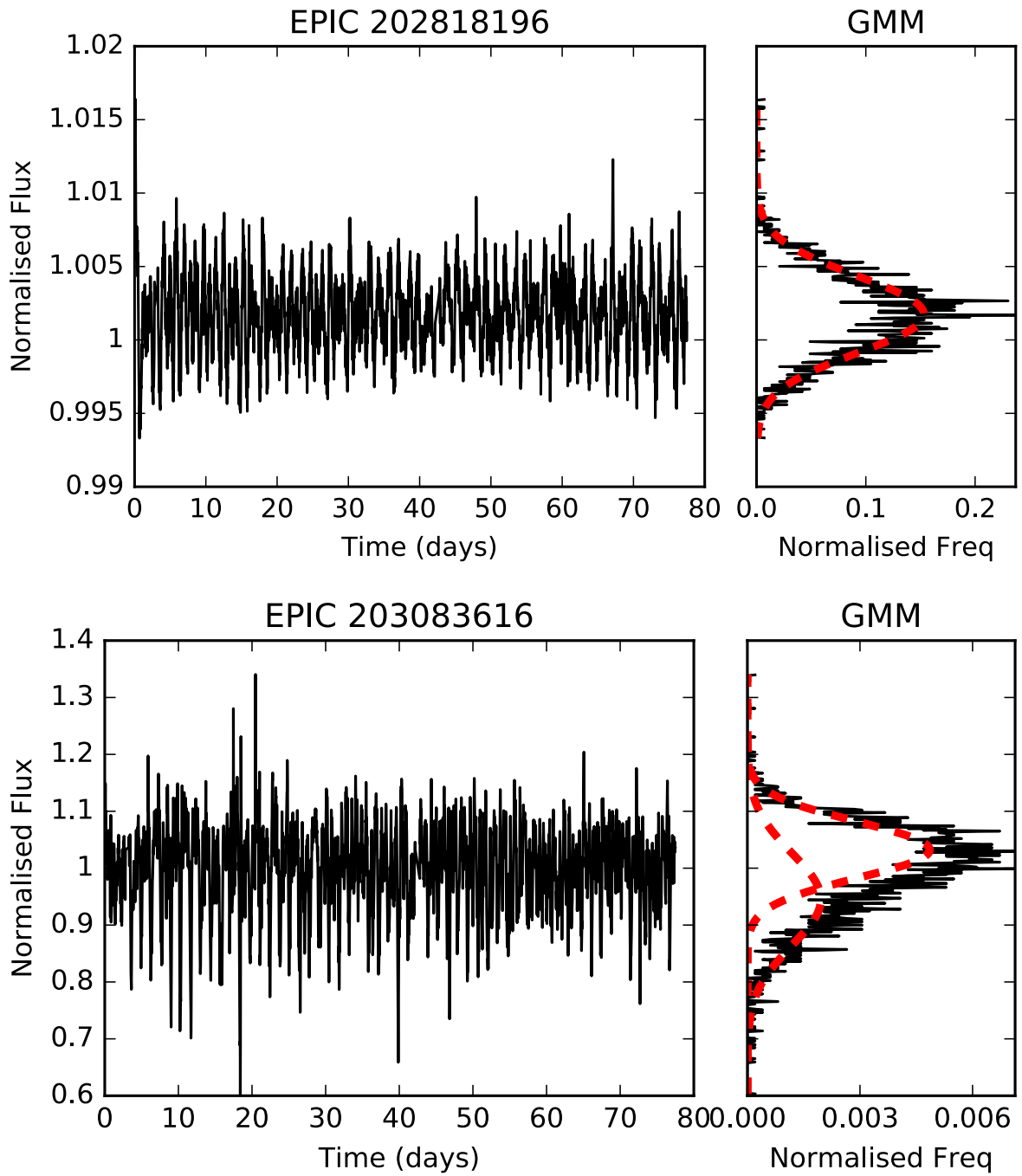


Figure 5.7: Example of Gaussian Mixture Models in 1D for a single light curve of a quiet star (top) and a dipper star (bottom). Both light curves have been corrected with a 30-day Gaussian smooth. I see a main population in the dipper star and a second, broad population due to the dips.

Table 5.5: Features based on groups of points used in the random forest algorithm.

Feature	Description
ngroups	Number of groups, defined as a cluster of at least three consecutive points below a 3 sigma clip.
medh	Median value of the height of the groups.
medh2	Median value of the height of the 5 deepest groups.
medl	Median duration of these groups.
dh	Maximum height of these groups less the minimum height.
dl	Maximum duration of these groups less the minimum duration.
grad_groups	The number of groups in the gradient of the light curve.

5.4.3.3 Wavelet Analysis

Wavelet analysis is a method of describing periodicity in a time series while preserving information about the localisation of the periodicity.¹¹⁷ The procedure is similar to applying a windowed Fourier Transform, though by using wavelets adverse effects such as ringing can be avoided. In wavelet analysis a small wavelet (in this case a Morlet function which is a sine wave modified by a Gaussian) is passed along the light curve. The correlation between the light curve at each point and the wavelet is measured. The wavelet can be scaled as a function of time and the analysis repeated. This creates a power as a function of wavelet scale and position in time along the light curve. An example of a wavelet power spectrum is given in Figure 5.8. The high power features correspond to the deepest dips in the light curve. In the case of this target, although the dips change and almost disappear they are always on the same time scale of 2.3 days.

¹¹⁷ Torrence and Compo (1998)

Wavelets are often used where the variability of a source is changing. For dippers this is particularly relevant. An object with one mode of variability (such as a pulsating star or an eclipsing binary) has a simple wavelet power spectrum that does not vary significantly across this diagram in power. However a dipper will have several modes of variability, changing power wherever there are changes in dip depth. The use of wavelet analysis allows an important feature to be attained; the change in aperiodic features over time. This can either be by changes in depth or by the time scale of the feature changing. For this feature I use the standard deviation of the wavelet power spectrum as a function of time in the region where the object was most periodic. This region is highlighted in Figure 5.8 and corresponds to one sigma around the period with the highest power. This feature is referred to as *wa_std* in Table 5.6. This feature is one of the top 10 most important features. It helps to distinguish dippers from beta Lyrae type variables, (see Figure 6.3 in the appendix of this chapter).

Periodic features found using this method are given in Table 5.6. I additionally compute the standard deviation in the Lomb-Scargle periodogram as a further feature based on the periodicity of the data. Unlike Lomb-Scargle periodograms, Wavelet Analysis requires evenly spaced data and that all time stamps have a corresponding flux value. For any gaps in my data I fill in points with a linear interpolation. This is an oversimplification at small time scales but allows us to establish my features given in Table 5.6 across the whole 80 day light curve.

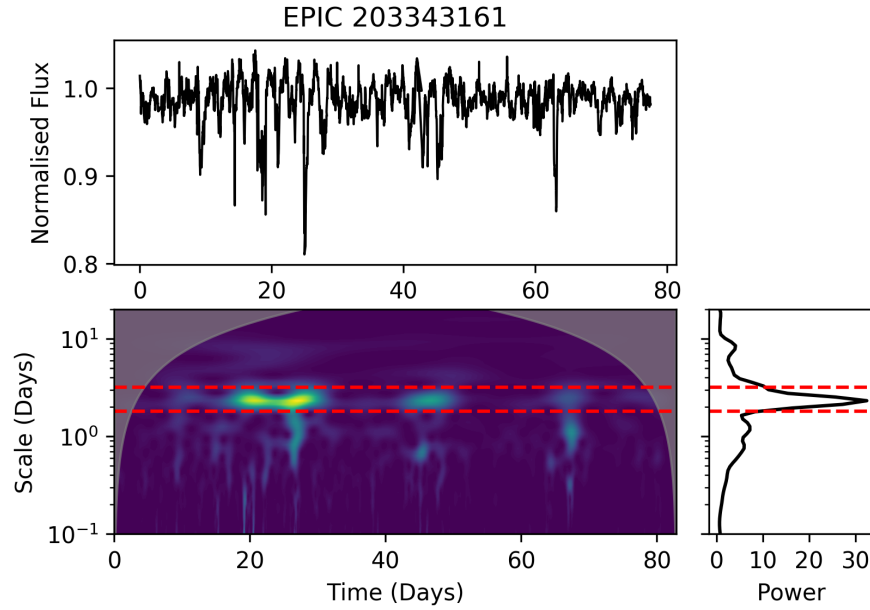


Figure 5.8: Wavelet power spectrum of dipper target. Here scale refers to the width of the wavelet packet in days, I see the scale of the dips is 2.3 days. Although the periodicity changes in power as the dips decrease in depth they reappear at the same scale in days. The red line drawn over the power spectrum indicates the region selected for determining the wa_period , s_per and std_flat features in Table 5.6.

Table 5.6: Features based on wavelet analysis and the Lomb-Scargle periodogram used in the random forest algorithm.

Feature	Description
wa_period	Period from wavelet analysis
s_per	Width of the Gaussian fit to the period peak in wavelet analysis.
std_flat	Standard deviation of the flattened wavelet analysis
wa_std	Standard deviation of the power spectrum from wavelet analysis
$pgram_std$	Standard deviation of the Lomb-Scargle periodogram

5.5 DIPPER CANDIDATES

Once the classifier has been trained on the targets found in Section 5.4.1 the same algorithm can be used on unclassified data. This gives us a classification probability for each target between zero and one. The full target list can then be reduced to my final list of candidates based on this probability.

Firstly, all candidates with a median magnitude greater than 18 are removed. These targets are faint and, on inspection, have too low a signal to noise to classify clearly as a dipper phenomenon. From this list I then take all the objects that were classified as dipper in the majority of the 200 iterations. Of these I take those that have a dipper probability of 40% or more. This reduces to a list of 229 candidates with a high probability of being a dipper. From this list targets are verified by eye to remove any cases where strong systematics may have caused a misclassification. (This is usually due to strong systematics in a periodic variable, where there is a step function introduced by VJ2014 or where the target is very dim and has a low SNR.) The set was further cleaned to remove any low order dippers that could reasonably be explained with spots on the surface of the star (which are able to reduce the flux from a star by up to 20%) or eclipsing binaries.

Finally, I also verified by eye any targets that had a dipper probability of more than 20% but were classified as another object. Of these 120 objects, 4 candidates were found to be dippers. This resulted 95 dipper stars, including the 40 objects used to train the machine. My final sample is given in the Appendix of this chapter in Chapter 6.6, where all 95 dippers are shown (training objects are highlighted in orange). Note, as discussed above, the reduction from Vanderburg and Johnson (2014) in some cases introduces an offset or step function in the light curves close to the midpoint of the K2 campaign. (This can be seen clearly in examples such as EPIC 204811478). The final list of dipper candidates was then cross matched with lists of cluster memberships for Upper Sco and ρ Oph.

In this search there were also several stars that I have classified as “burster” stars. These stars are visually distinct from dipper stars and are discussed in more detail in Section 5.8. Any burster stars presented in this work have been classified as dippers by the machine and later distinguished by eye. As the machine was not trained on this particular class, we can not be certain of completeness. I expect there to be other burster examples in this data set that have not been found.

Figure 5.9 shows the dipper sample as a function of IR excess and M statistic. Despite not training on colour information, the dipper population is clearly biased towards a high infrared excess. This suggests the object really does occur only in young stars with disks. I find no dipper stars that are inconsistent with this theory. Similarly, burst stars are consistent with having disks.

5.5.1 Top 10 Features

Figure 5.10 shows how the top 10 high importance features correlate with each other, with the final dipper sample used in this work highlighted in orange. We see that the dipper sample is not clear or unique in any of these features, showing the need for a ML algorithm to distinguish between dippers and other classifications taking into account multiple features. The dippers themselves occupy broad ranges of each parameter space, making them harder to identify.

Figure 5.11 shows the frequency of each classification across the value of the M statistic. (This is calculated after the machine has been run on the data and classified each light curve.) We see for M stat that, while dippers show different behaviour, the behaviour is mimicked in Beta Lyrae type eclipsing binaries (BL*). This is expected, as M statistic measures the asymmetry of the light curve and eclipsing binaries will show frequent, deep eclipses. In the Appendix of this chapter I show similar plots for the top 10 features, ranked by importance. The dipper sample is not uniquely identifiable in any one feature, showing the need for multiple features to be taken

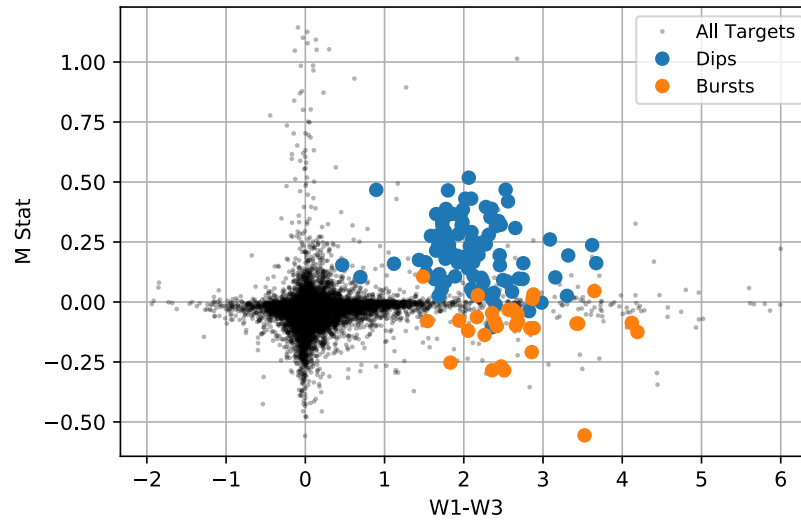


Figure 5.9: M statistic, defined in Eq 82, as a function of $W1-W3$ IR excess for Kepler Campaign 2 found using a random forest algorithm. The algorithm was trained only on light curve parameters and shows dipper stars in K2 Co2 occur in systems with an infrared excess indicative of hosting a disk. Note: the smoothing and clipping used to clean the light curves creates a slightly different M value than from Cody et al. (2014).

into account. Together, these features allow me to distinguish dippers from eclipsing binaries and other variable types.

5.5.2 $F1$ Score

The $F1$ score gives a weighted average of the precision and recall where

$$F1 = 2 \frac{pr}{p+r}$$

where p and r are precision and recall, defined as

$$p = \frac{\text{True Positives}}{\text{True Positives} + \text{False Positives}}$$

$$r = \frac{\text{True Positives}}{\text{True Positives} + \text{False Negatives}}$$

Here a value of 1 would indicate perfect precision and recall. When using multiple classifications we find an $F1$ score for dippers of ~ 0.8 , as shown in Figure 5.12. This could be improved by including colour information as a feature. However, as discussed above, by discounting colour we are more sensitive to dustless dippers (were any to exist). We are also able to test our final sample of dippers in colour space (see Figure 5.9). We find an $F1$ score of 0.8 to be sufficient for our purposes, and further clean the sample by eye as discussed in Section 5.5.

5.6 MEASURING DIP PARAMETERS

In the following sections I will refer to the periodicity, the dip depths and the dip durations for each dipper target. Below I define how these parameters are measured. I also use the M statistic from Cody et al. (2014), however in this work I clip 6 sigma outliers and remove a 30 day smoothing kernel before assessing the M value. This makes the M value used in the machine learning slightly reduced compared with the ones shown in that work.

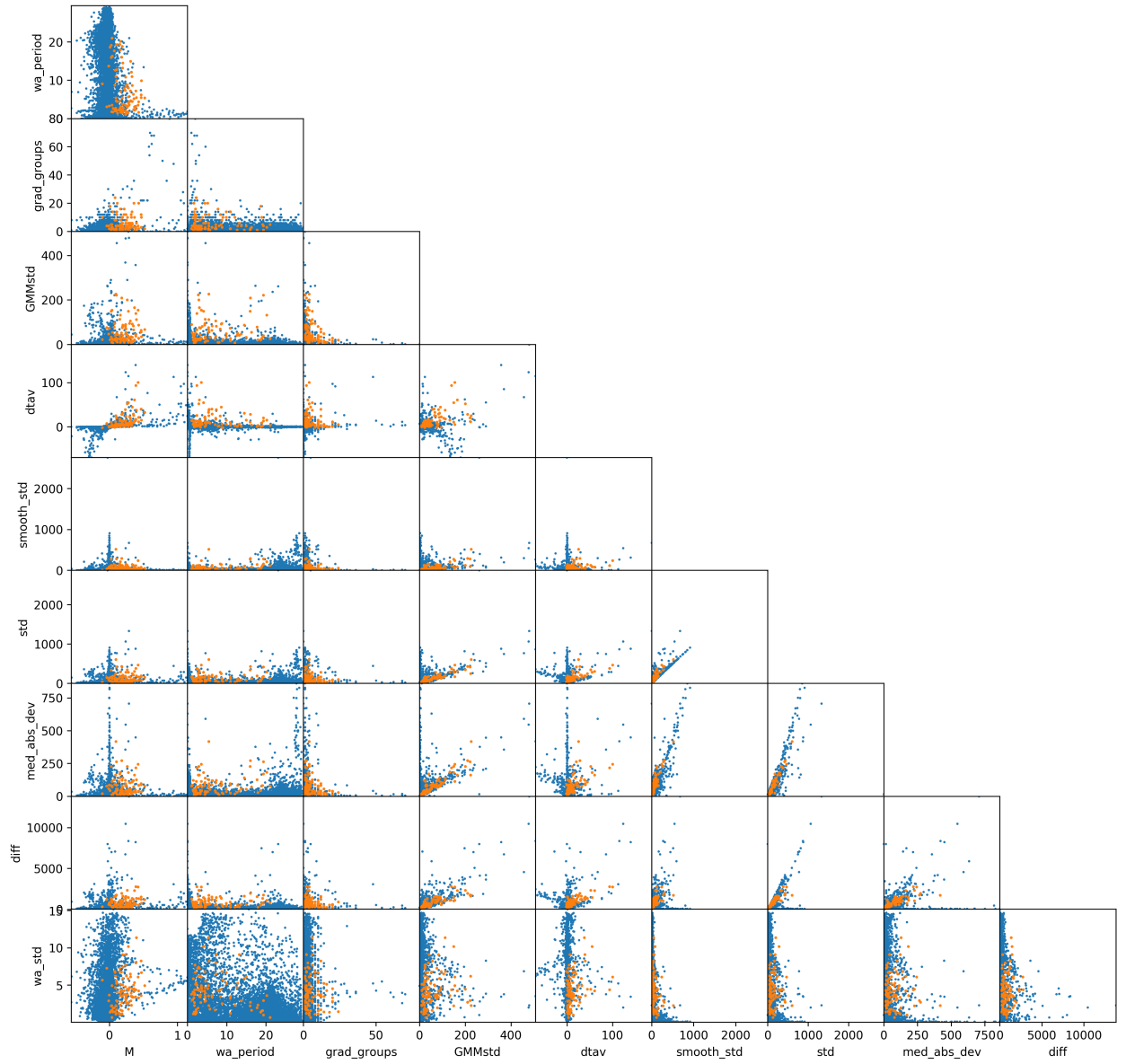


Figure 5.10: Correlation between the top 10 features of the ML algorithm as ranked by importance. Blue points show all 13000 light curves used in this work, orange points show the 95 dipper candidates that were confirmed by eye as discussed in Section 5.5. Dippers are mixed with the population in most features and are not uniquely identifiable in any one feature. This supports the need for a ML approach.

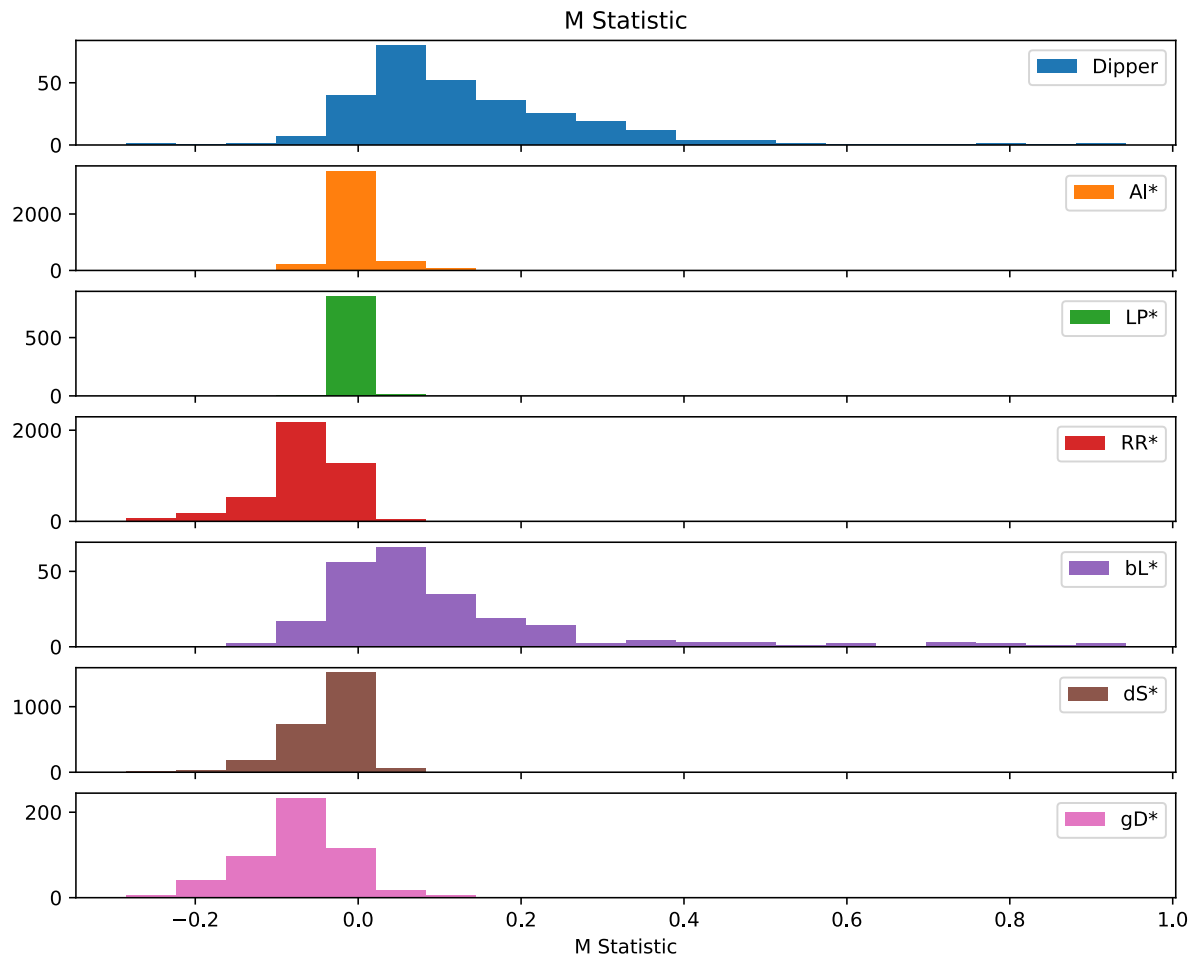


Figure 5.11: Distribution of each class of object in M statistic, having run the ML algorithm. The classes are (from top to bottom) Algol Type EB, Long Period Variable, RR Lyrae, Beta Lyrae Type EB, Delta Scuti and Gamma Doradus. While there is some contamination in each classification this gives a broad idea of where each classification clusters. Beta Lyrae type EBs mimic dippers in M statistic. The top 10 features ranked by importance are plotted in this way in the appendix of this chapter.

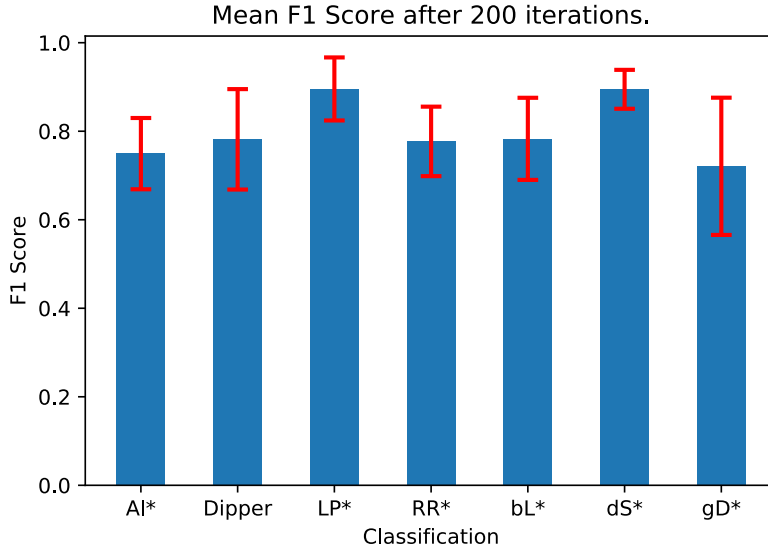


Figure 5.12: F1 score as a function of classification having run the ML algorithm 200 times. We see that all classifications have high F1 scores and that dippers score ~ 0.8 which suggests we have fairly good precision and recall. Long period variables are much easier to retrieve due to their uncomplicated light curves. Precision and recall can be improved by including colour information in the machine.

5.6.1 Periodicity

To find the period of each dipper I employ a Lomb Scargle periodogram, as discussed above. The periodicity can then be measured using a Q value from Cody et al. (2014). I use a slightly different formulation of the Q value to that in Cody et al. (2014), under the assumption that the noise profile for K2 targets is small compared to the dips and similar across targets. Q is assessed by firstly phase folding the light curve and smoothing with a boxcar at 25% of the period of the dipper. This light curve is then ‘unfolded’, such that it creates the same smoothed, repeating pattern for the whole light curve. Q is given as

$$Q = \frac{\text{RMS}(y - m)^2}{\text{RMS}(y - \text{med}(y))^2} \quad (83)$$

where y is the light curve, $\text{med}(y)$ is the median value of the light curve and m is the smoothed and unfolded model. The Q value compares the residuals of the light curve to the residuals when this model is removed. This tests whether it is well described by a repeating pattern at all points across the light curve. For low values of Q the model fits well and the dipper is considered to be periodic. For high Q values the dipper is assumed to be aperiodic, with either a changing period or changing dip depths in each event. From Cody et al. (2014) I adopt a Q value of 0.6 to distinguish between dippers that are mostly periodic or mostly aperiodic.

Figure 5.13 shows the value of the M statistic (see Equation 82) and Q statistic for each dipper and burster found in this work. (Dippers and bursters have been distinguished by eye.) In order to approximate this we can naively place a cut at $M=0$; above this stars are classed as bursters and below this stars are classed as dippers. At $Q=0.6$ the stars are split into periodic or aperiodic behaviour. Examples of dippers from each section of this cut are shown in Figure 5.14. The metric performs qualitatively well, separating out mostly stochastically behaving dippers from those that are more regular, as shown in Figure 5.14.

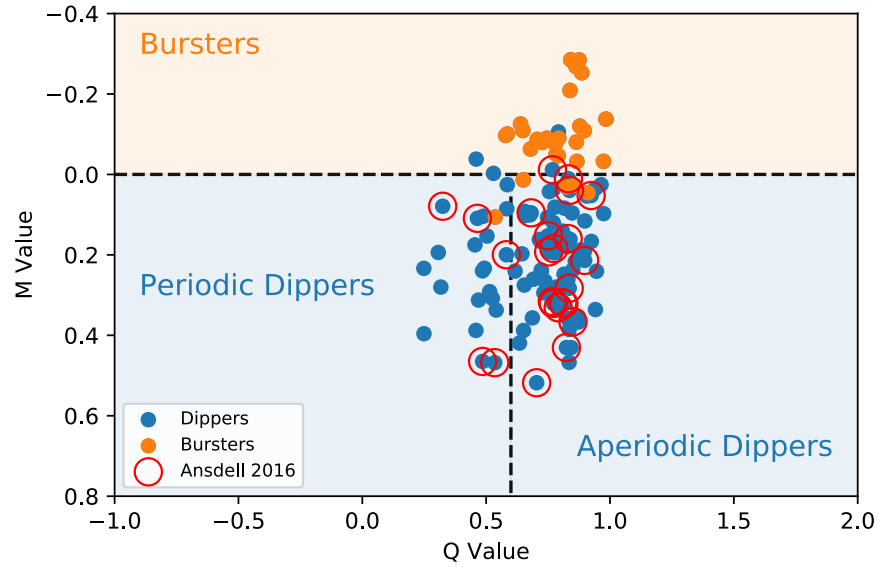


Figure 5.13: Distribution of dippers and bursters in Q and M space. Q tracks the periodicity of the light curve and M tracks the asymmetry of the light curve. Those targets that have been classified by eye as bursters have been highlighted in orange and targets that have been classified as dippers are in blue. Based on Cody et al. (2014) we use a Q value of 0.6 to distinguish periodic and aperiodic bursters.

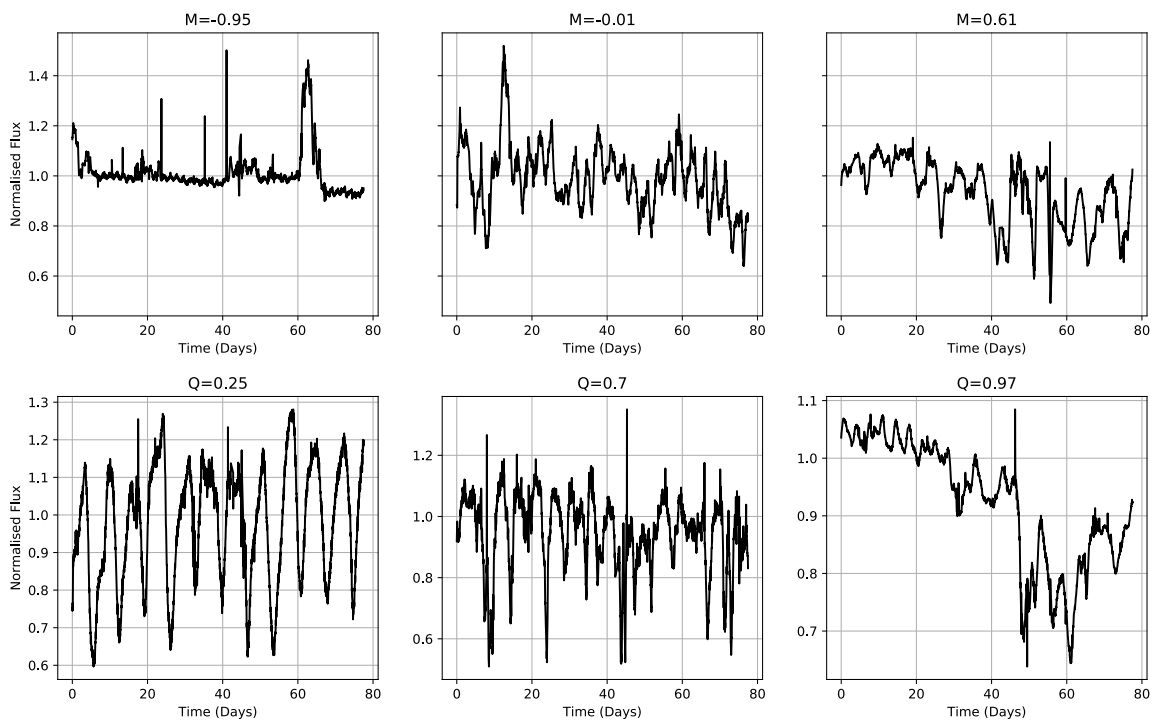


Figure 5.14: Examples of dippers from a range of M and Q statistic values. High Q values ($Q > 0.6$) indicate an aperiodic dipper while low Q values ($Q < 0.6$) indicate a periodic dipper. Negative M values indicate a star that mainly exhibits bursting while a positive M value indicates a star that is mostly dipping. In this work I chose not to have an intermediate class, though stars with $M \sim 0$ display roughly equal amounts of each behaviour.

5.6.2 Dip Parameters

Parameters such as the dip depth and duration are useful for characterising the behaviour of individual dippers. If the model of the inner edge of the disk obscuring the star is correct, the depth of the dip should relate to the amount of material obscuring the star. The duration should relate to the orbital distance from the star. To measure these parameters I firstly find all dips using the methods discussed in Section 5.4.3.2. I establish a background level using a Gaussian smoothing kernel at twice the period of the dipping behaviour with a maximum of 20 days. This is offset to the median level of the continuum as assessed by the GMM (see Section 5.4.3.2). This continuum level is shown in Figure 5.15. I find the depth of each event by finding the peak of the dip and ‘walking’ on either side until either this continuum is met or there is a turning point, as assessed by the gradient of the data. (This is performed on a slightly smoothed version of the data; a boxcar is used at a 25% of the period to smooth the data and remove any very short term variability.) These regions are shown in blue in Figure 5.15 for dips and orange for bursts. The duration of the dip is the width of the final allowed region. The dip depth is continuum level in that region less the minimum flux found in this region.

The final metric for each dipper target is then the median depth and median duration of all the dips that have been found. This is different to the approach from Ansdell et al. (2015), where the median level of the deepest 5 dips is used. This is designed to be more representative of the overall behaviour of the dipper.

This is not a perfect approach to searching for dips and bursts. Bursts and dips are sometimes confused, particularly in cases where there is a strong long term trend in the data. Some dips are also clearly the convolution of two or more events, which are harder to separate. While this method is not ideal, it provides statistics on the dipper population as a whole. Further efforts to fully model these stars more conclusively and physically could be undertaken in future.

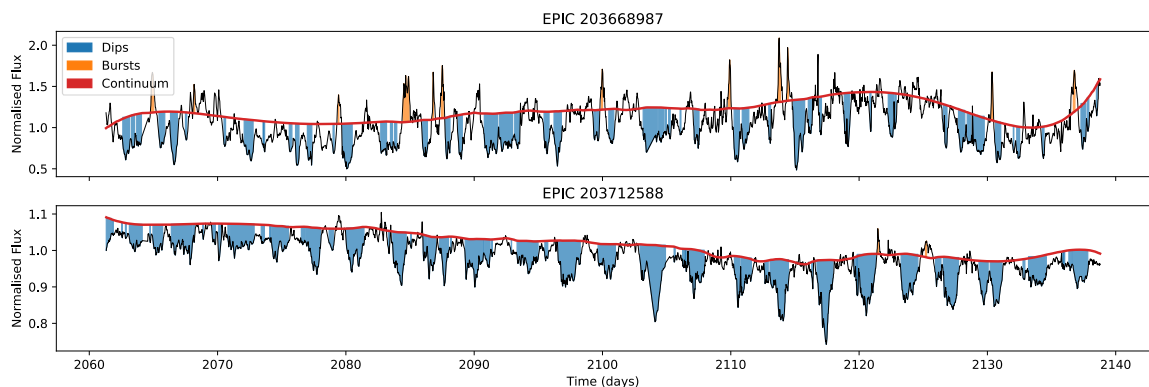


Figure 5.15: Example of the output of the dip depth and duration finding algorithm. Here the red line shows the continuum level, which is a simple 30 day smooth of the data after outliers have been removed. This is also offset to the continuum level as assessed by the GMM. Blue areas indicate features that have been labelled as dips, with the width and height of the area indicating the duration and depth of the dip. Orange areas have been labelled as bursts.

5.7 DIPPER CHARACTERISTICS

With a large sample of 95 dippers available it is possible to investigate basic properties using the distribution of dip characteristics and infrared excesses. Below I discuss some of the properties of the dippers in this sample in detail. I also investigate the cluster memberships of each target, the binary fraction in those clusters and discuss observations of their disks. In the dipper population there are a small num-

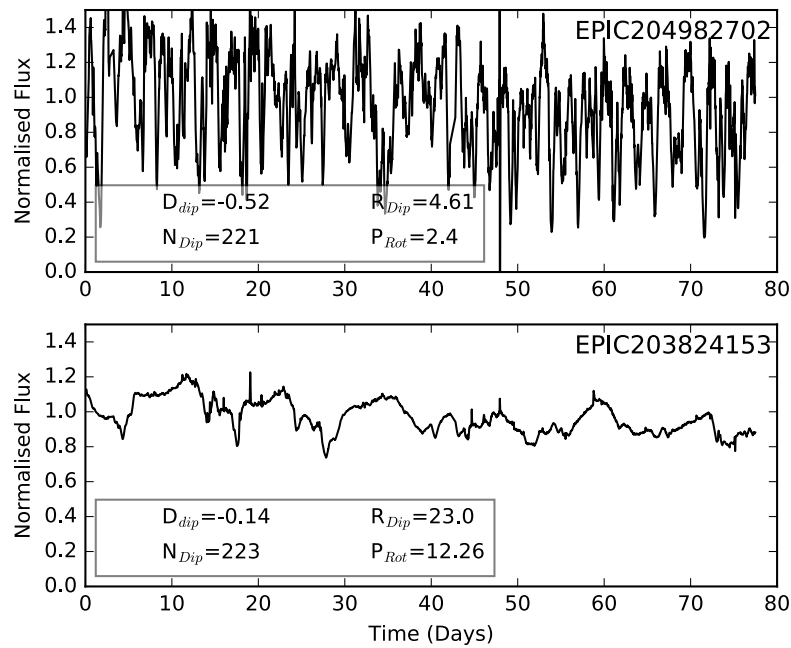


Figure 5.16: Example of two dipper targets that did not meet the criteria set out in Ansdell 2015. *Top*: The R_{dip} parameter here is slightly less than 5 as the dips are narrow and frequent. *Bottom*: The period of the dipping is approximately 12 days which is longer than the 10 day cut.

ber of candidates consistent with having evolved disks. These are further discussed in Section 5.20.

5.7.1 Comparison with Ansdell 2015

In Ansdell et al. (2015) dipper stars were defined by first smoothing with a high pass filter at 1 day and then measuring the following; the number of dips (N_{dip}), the average dip depth of the three deepest dips as measured from the normalised light curve (D_{dip}), the ratio of the dip depth to the standard deviation of the data (R_{dip}) and the rotation of the period of the star P_{rot} .

A dipper was then defined as a target with $N_{\text{dip}} > 5$, $D_{\text{dip}} > 0.07$, $R_{\text{dip}} > 5$ and P_{rot} to be less than 10. When I compare my sample of 95 dipper stars to this metric, 35% do not qualify. This is in many cases due to dippers being aperiodic, with no clear value for P_{rot} . It was found that the R_{dip} criteria clipped out a small number of dippers that were particularly symmetric, (flared as well as dipped). Two examples of dippers found by this work that do not qualify based on this metric are shown in Figure 5.16. I suggest that these criteria may be too strict and cut out valid dipper candidates.

In Ansdell et al. (2015) a positive correlation is seen between $E(K_s - W_2)$, a measure of dust content in the inner disk, and dip depth D_{Dip} . $E(K_s - W_2)$ encodes information about the amount of dust in the inner edge of the disk. In this work I have not obtained spectra for my objects and am unable to correct for reddening in all of my targets. Of my sample, 35 objects are observed in Luhman and Mamajek (2012) and have spectral types. I follow their procedure and use their classifications of spectral type to de-redden these 35 dippers. I use the A_V extinction coefficients from Ansdell et al. (2015) and the extinction law given in Cardelli, Clayton, and Mathis (1989) to correct 7 further dippers. The de-reddened values of K-W2 excess (labelled as

Table 5.7: Dippers as a function of each cluster. These cluster memberships are likely incomplete and several dippers were found not to be covered in any literature membership list, however are consistent in colour space with being members of one or both clusters.

	Upper Scorpius	ρ Ophiuchus
Number of Members	701	199
Number of Dippers	42	22
Percentage of Dippers	5.9% \pm 0.9%	11.0% \pm 2.3%
Number of Bursters	8	15
Percentage of Bursters	1.1% \pm 0.4%	7.5% \pm 1.9%

$E(K - W_2)$) are used in Figure 5.17. This figure contains 42 unique dipper stars that are able to be corrected for extinction. There is evidence of a correlation between dip depth and $E(K - W_2)$. A Spearman's rank test gives a correlation of 0.503 and a p-value of 0.0007. All dippers show an excess in $E(K - W_2)$ consistent with hosting a circumstellar disk. For comparison the lower panel of Figure 5.17 shows the same plot for all dipper and burster targets, with no de-reddening attempted. A correlation still persists. This suggests that dustier disks result in deeper dipping events. This supports the theory that the dips are due to dust obscuring the star at the inner edge of the disk.

Out of 25 dippers that are reported by Ansdell et al. (2015), 24 dippers are independently found in this work. In Ansdell et al. (2015), the search was performed by eye, whereas in this work I search using machine learning. Figure 5.18 shows the distributions of median depth and median duration for each target across the two samples, which show very similar distributions. This suggests the two samples are relatively similar and have similar completeness and biases. The method of machine learning does not seem to bias the result as compared with searching by eye. However, this does not exclude us from a further bias. Particularly, in general it is easier to find deeper dips as they are more easily distinguished from stellar noise. As we discount any targets with dips small enough to be explained with star spots, we may be under-representing the dippers at the smallest dip depths. Similarly, as our cadence is 30 minutes, we do not have the time resolution needed to observe shorter duration dips than 1.5 hours. We may be under-representing the sample of 'short period' dippers.

5.7.2 Comparing Dipper Samples By Cluster

Figure 5.19 shows the colour of all of the targets within Kepler Co2 with cluster members of Upper Scorpius and ρ Ophiuchus highlighted. All dippers are consistent with being members of either cluster and there is no evidence for dipper stars in the older background population.

I find that between the two clusters there is a modest difference between the occurrence rates of dippers as shown in Table 5.7, where occurrence rate is defined as the percentage of dippers in each cluster. In Upper Sco, (10 Myr), I find 5.9% \pm 0.9% were dipper stars and in ρ Oph, (1 Myr), an occurrence rate of 11.0% \pm 2.3%. Theory from works such as Alencar et al. (2010), McGinnis et al. (2015) and Bodman et al. (2016) suggest that the dipper phenomenon is due to the inner edge of circumstellar disks. As disks are known to evaporate as the system ages and transition into an evolved state, we might expect the dipper fraction to decrease with age. In these two clusters, I find only limited evidence that there is a difference between the dipper fraction as a function of age. As there are a low number of dippers in each cluster it is not possible to find any significant correlation with age or other cluster parameters. There are 22 dipper stars in my sample with an unknown membership, likely belonging

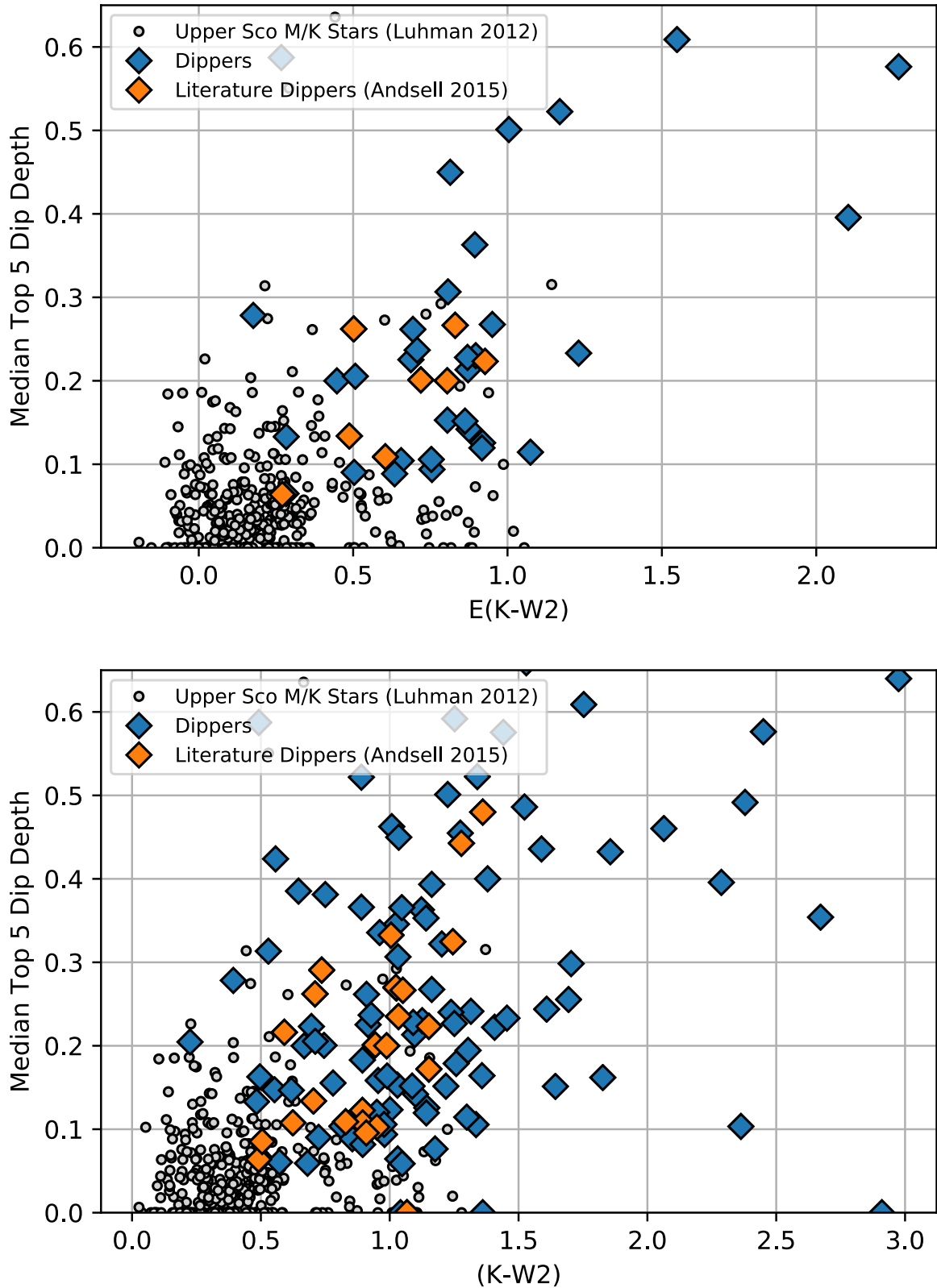


Figure 5.17: Average depth of the three deepest dips as a function of K-W2 excess corrected for extinction. Here blue diamond points indicate dipper stars found with the machine learning algorithm from this work and orange diamonds indicate dippers found in Andsell et al. (2015). Top: targets have been corrected for extinction using the procedure outlined in Luhman and Mamajek (2012). Bottom: All targets with no extinction correction.

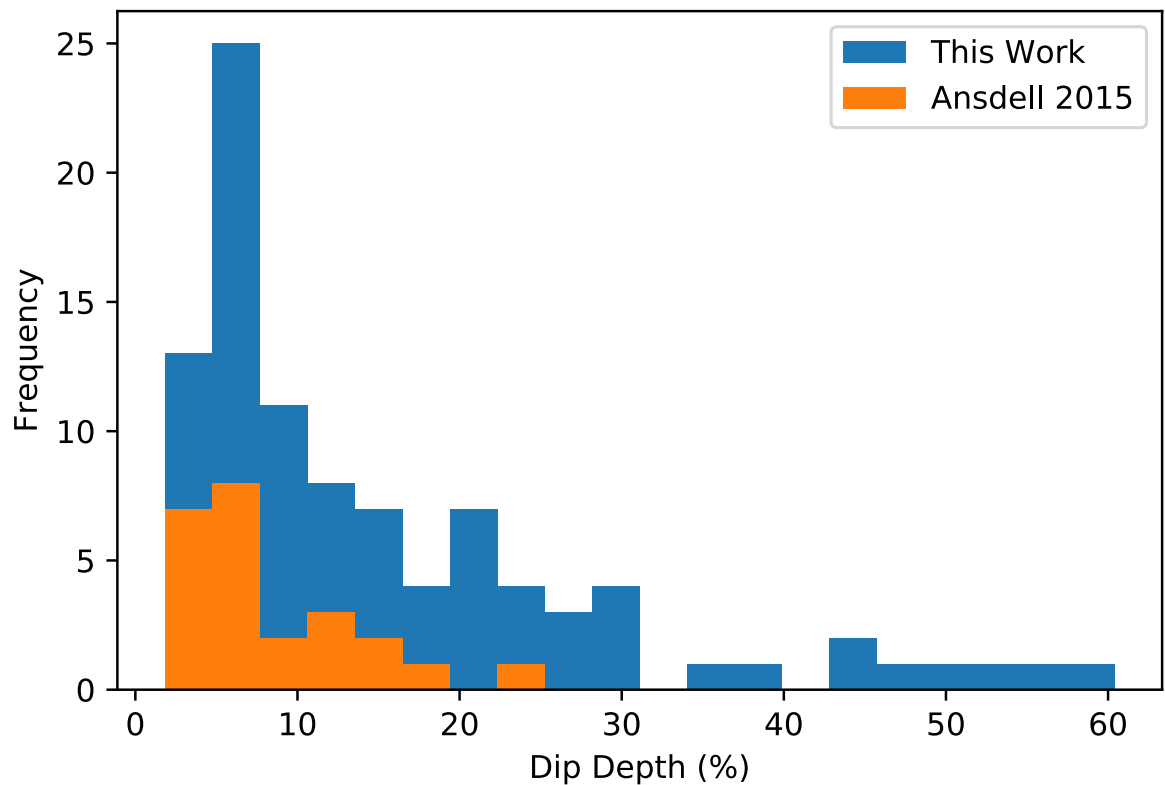
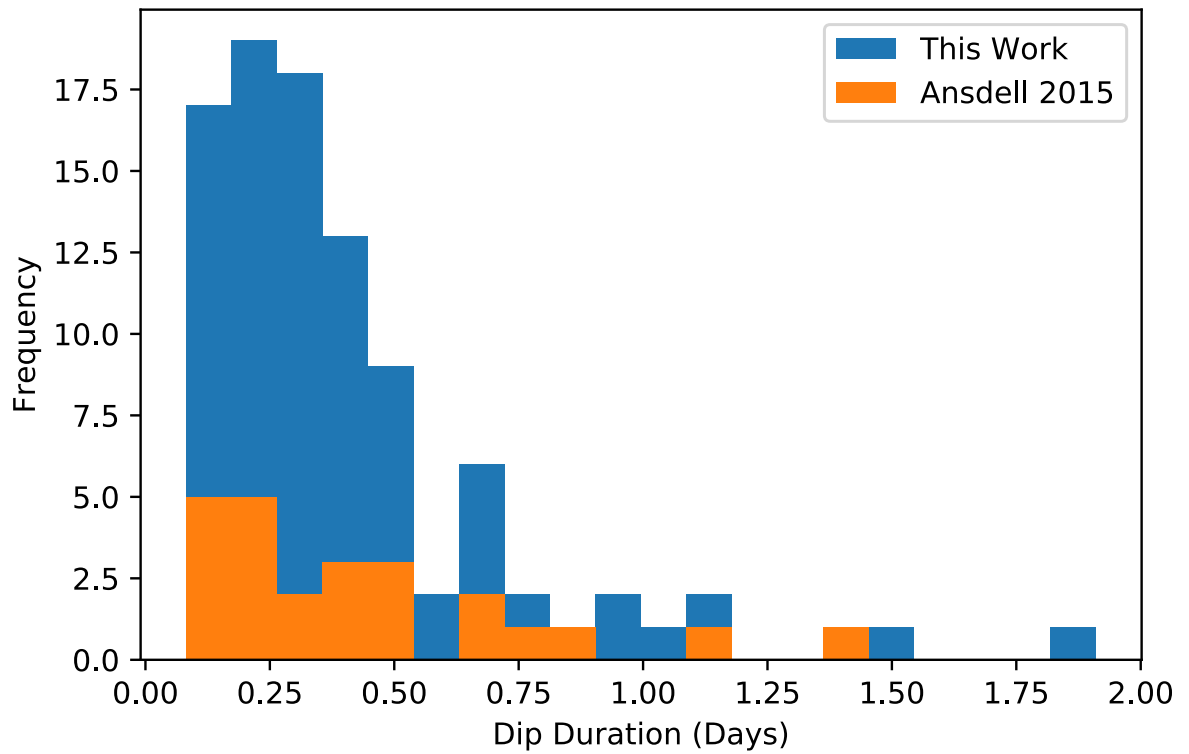


Figure 5.18: Distributions of dip depth and dip durations for all dipper targets. Blue: Dipping events found in this work using machine learning. Orange: Dipping events found in Ansdell et al. (2016). We see the two distributions are similar, suggesting there are no additional biases in these two parameters when machine learning is used.

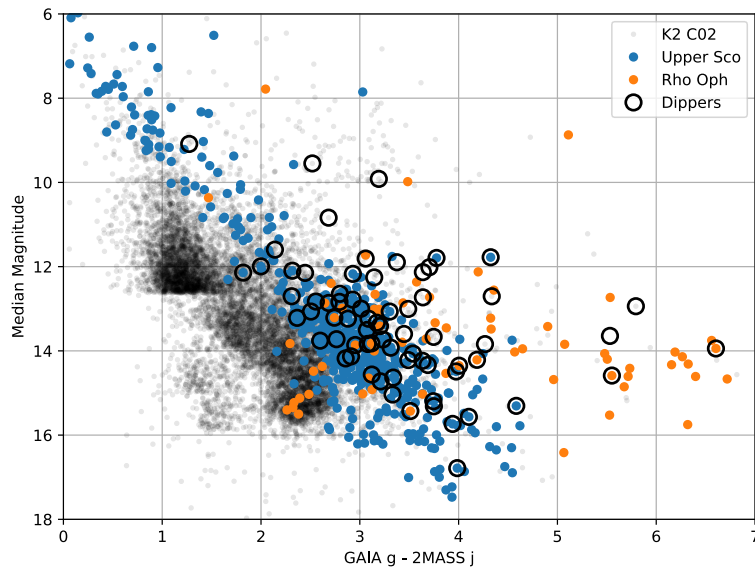


Figure 5.19: Median magnitude of light curves compared with g-j colour, with magnitudes from GAIA DR1 and 2MASS. Upper Sco and ρ Oph populations are easily distinguished and ρ Oph is seen to be redder as it is embedded in a cloud. At a magnitude of 18 the SNR of each target is too low to accurately find dipper stars. I find all candidates have an IR excess consistent with disk bearing stars.

to either cluster. With the release of parallax data from the GAIA mission in 2018 it will be possible to obtain better membership lists and more conclusively define the dipper fraction.

Cody et al. (2014) discusses the fraction of dippers out of the disk bearing population in NGC 2264. To compare Upper Sco and ρ Oph to their work I must first find out the fraction of stars that are disk bearing. Using the prescription in Cody et al. (2014) and Wilking et al. (2001) I identify the disk bearing stars as those with $\alpha > -1.6$ where $\alpha = d \log \lambda F_{\lambda} / d \log \lambda$, using K band photometry from 2MASS and W4 photometry from WISE. I then compare the fraction of dippers in the disk bearing stars for each cluster. All dippers found in this work meet the $\alpha > -1.6$ criteria, suggesting they all have disks.

Cody et al. (2014) have a sample of 1266 cluster members in NGC 2264. 162 were found to have both disks and high quality light curves. Of this sample 35 were found to be optical dippers. Table 5.8 shows the final dipper fraction for each of the three clusters. The average dipper fraction for disk bearing stars (for all dippers where alpha was obtainable) is $21.0\% \pm 5.5\%$. This is consistent with the finding for NGC 2264. Between the three clusters the dipper fraction in disk bearing stars is approximately 20%, regardless of age.

Table 5.9 shows the number of periodic and aperiodic dippers for each of the clusters. I have included the M and Q values for NGC2264 from Cody et al. (2014). Based on different choices in sigma clipping and smoothing, they are likely to be systematically offset. As there are small differences between the methods we might expect the two independent studies to produce slightly different values. The clusters themselves may also have different levels of periodic and aperiodic dippers. Despite this, I find that within errors the clusters have a similar split between aperiodic and periodic dippers. Approximately 25% of the dippers are periodic by this metric. The sample from Ansdell et al. (2016) also aligns well with the one in this work, suggesting we have similar completeness.

Table 5.8: Dipper fractions for the three clusters with well studied dipper populations. Upper Scorpius and ρ Ophiuchus have been added in this work. The dipper fraction quoted here is as a function of disk bearing stars only. The number of dipper stars is given in brackets next to the percentage.

Cluster	Age	Disk Fraction	Dipper Fraction
ρ Ophiuchus	0.1-1 Myr ^a	40.2% \pm 4.3%	20.1% \pm 4.3% (22)
NGC 2264	1-5 Myr ^b	12.8% \pm 1.0%	21.6% \pm 3.7% ^d (35)
Upper Scorpius	10 Myr ^c	26.7% \pm 2.0%	21.8% \pm 3.4% (42)

^a (Luhman and Rieke, 1999)

^b (Rebull et al., 2002) Dahm and E. (2008)

^c (Pecaut, Mamajek, and Bubar, 2011)

^d (Cody et al., 2014)

Table 5.9: The number of periodic and aperiodic dippers this work and the two other major works on dippers. Ansdell et al. (2015) uses the same data on the same cluster vets each target by eye. Cody et al. (2014) finds dippers in NGC 2264 using CoRoT. The classification system for these dippers are discussed above. Within errors, all three surveys find similar fractions of dippers being periodic and aperiodic.

	This Work	Ansdell et al. (2015)	Cody et al. (2014)
Cluster	Upper Sco/ ρ Oph	Upper Sco/ ρ Oph	NGC 2264
Periodic Dippers (%)	26.6% \pm 5.3%	21.7% \pm 9.7%	34.7% \pm 6.8%
Aperiodic Dippers (%)	68.1% \pm 8.5%	78.3% \pm 18.4%	65.3% \pm 9.3%

5.7.2.1 Multiplicity in ρ Ophiuchus

Work from Ratzka, Koehler, and Leinert (2005) discusses the multiplicity of systems in the ρ Oph region. In that work binaries are resolved down to a separation of 0.13". All binaries in their sample of ρ Oph had separations of more the 10 AU, with magnitude differences between the primary and secondary star of ≤ 2.5 magnitudes. Using this sample I can compare the fraction of dippers in binaries to the fraction of those outside of binaries. (This does not include very close binaries at narrower separations than 10 AU.)

Table 5.10 shows the binary fraction in ρ Oph for both bursters and dippers. There was no significant difference found between the binary fraction of the cluster and the dipper binary fraction, with both $\sim 30\%$. There is no significant evidence that binary systems influence the dipper phenomenon in any way. However, with such low number statistics and only limited data on binary systems in the cluster it is difficult to assess.

Table 5.10: Binary Fraction in ρ Oph. No difference is found between the binary fraction for dipper or burster stars.

	Binary	Non Binary	Binary Fraction
Number of Members	32	76	29.6% \pm 5.2%
Number of Dippers	5	11	31.3% \pm 13.9%
Number of Bursters	4	10	28.6% \pm 14.3%

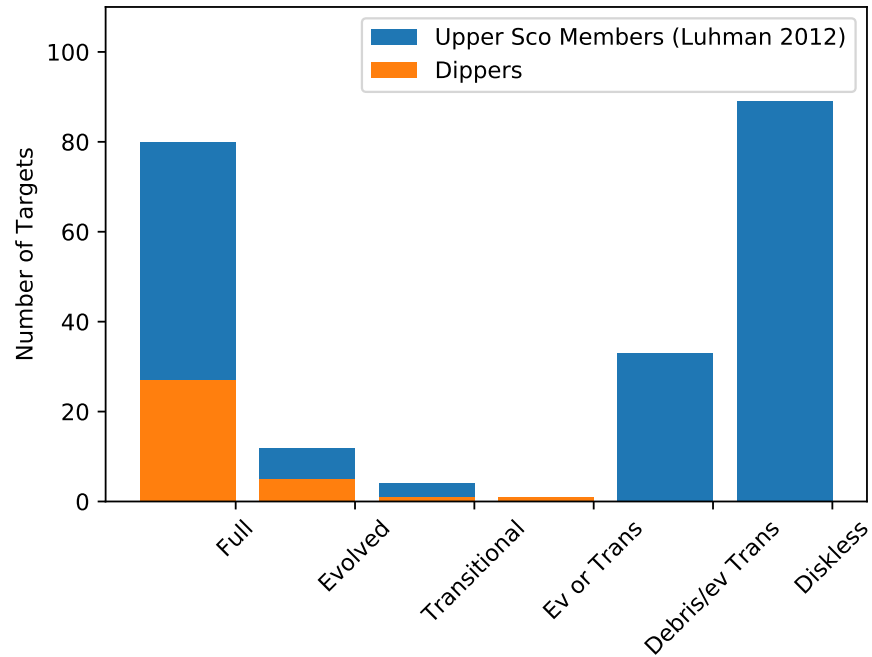


Figure 5.20: Dipper stars based on disk type as discussed in Barenfeld et al 2016, a survey of disks in Upper Sco, where Full indicates an IR excess and an SED that shows no clearing, Debris/Evolved Transition indicates an IR excess with some SED evidence of clearing and Evolved indicates no IR excess and no SED evidence of clearing. I find no dippers in systems with debris disks or later evolutions.

5.7.2.2 Disk Evolution

Luhman and Mamajek (2012) uses infrared excesses in K band and WISE photometry to distinguish the evolutionary stage of disk bearing stars in Upper Scorpius. They define disks as full (optically thick with no evidence in the SED of clearing), evolved (optically thin in the IR with no evidence in the SED of clearing) and transitional (with an SED showing evidence for gaps and holes). They also define debris/evolved transitional disks that are composed of second-generation dust and are considered to be the final stage of disk evolution. Figure 5.20 shows the distribution of these disk types in those targets that were observed both in Luhman and Mamajek (2012) and in K2 Co2. Debris disks and diskless stars are not found in the dipper population retrieved by this work. This supports the theory that the dipper phenomenon is caused by occultations by primordial dust in the disk.

Table 5.11 lists the 7 members of Upper Scorpius observed in Luhman and Mamajek (2012) shown to have evolved or transitional disks. (I find no dippers consistent with being diskless.) These dippers are also shown in Figure 5.21. Other dippers found here were either not observed in Luhman and Mamajek (2012) or are described as having “full” disks.

There are other dippers that have IR excesses consistent with being more evolved disks but were not observed in Luhman and Mamajek (2012). Of the 11 dipper targets consistent in colour space with being an evolved or transitional disk, none are distinct from the full disk dipper population in any of the features used to train the machine. They are consistent in period, dip depth and duty cycle with the full disk bearing dipper population.

Figure 5.22 shows a reproduction of Figure 2 from Luhman and Mamajek (2012) where the disk types of each target has been labelled. Here only targets that were also observed in K2 Co2 are shown. Dippers and bursters found by the machine learning algorithm and vetted by eye are plotted. The evolved dippers from Table 5.11 highlighted in green. For the majority of the dippers I have no spectral types

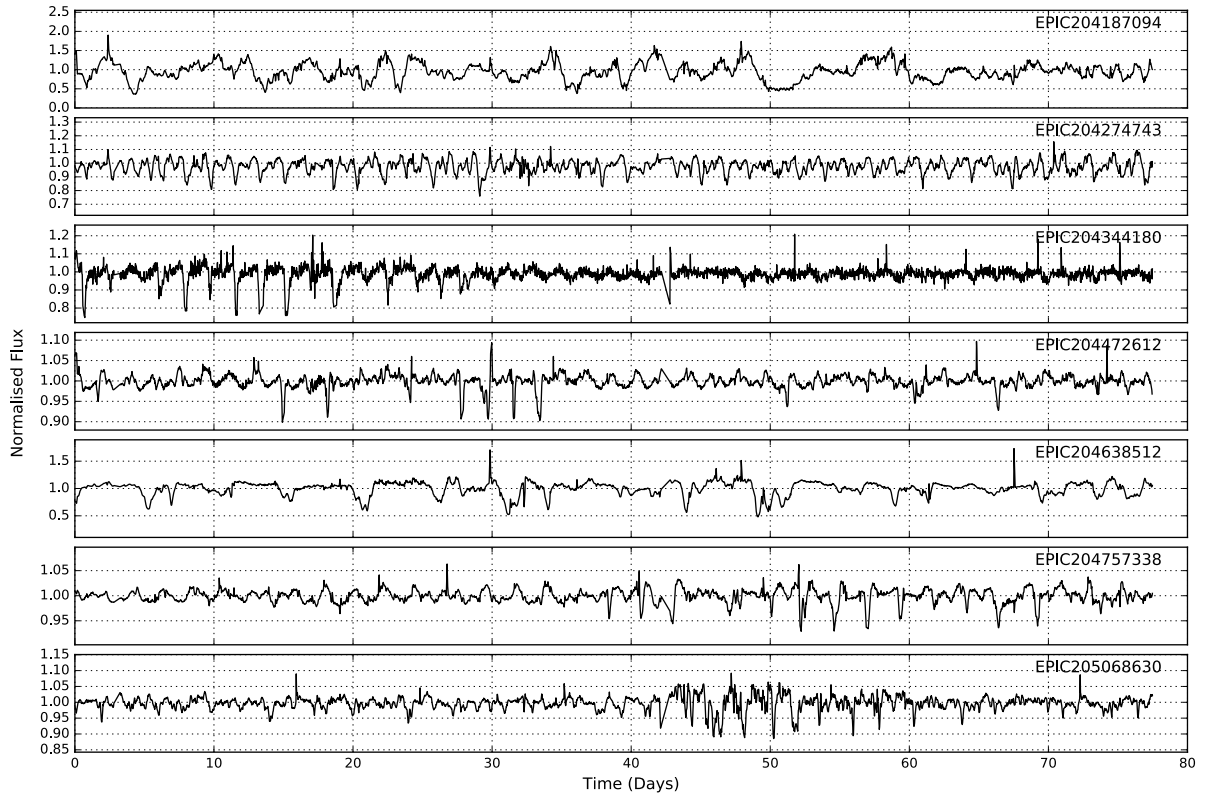


Figure 5.21: Light curves for evolved or transitional type dippers, as identified by Luhman and Mamajek (2012). These are indistinguishable from the rest of my dipper sample in any of the features used to train the machine. See also Table 5.11.

Table 5.11: Evolved or Transitional Disks as highlighted by Luhman and Mamajek (2012) that also exhibit dipper behaviour.

EPIC ID	RA	Dec	Disk Type
204187094	242.82956	-23.322251	evolved
204274743	239.37443	-22.978846	evolved
204344180	243.63696	-22.703707	ev or trans
204472612	242.14397	-22.198866	evolved
204638512	241.09023	-21.507916	transitional
204757338	241.86443	-20.995618	evolved
205068630	242.79566	-19.558912	evolved

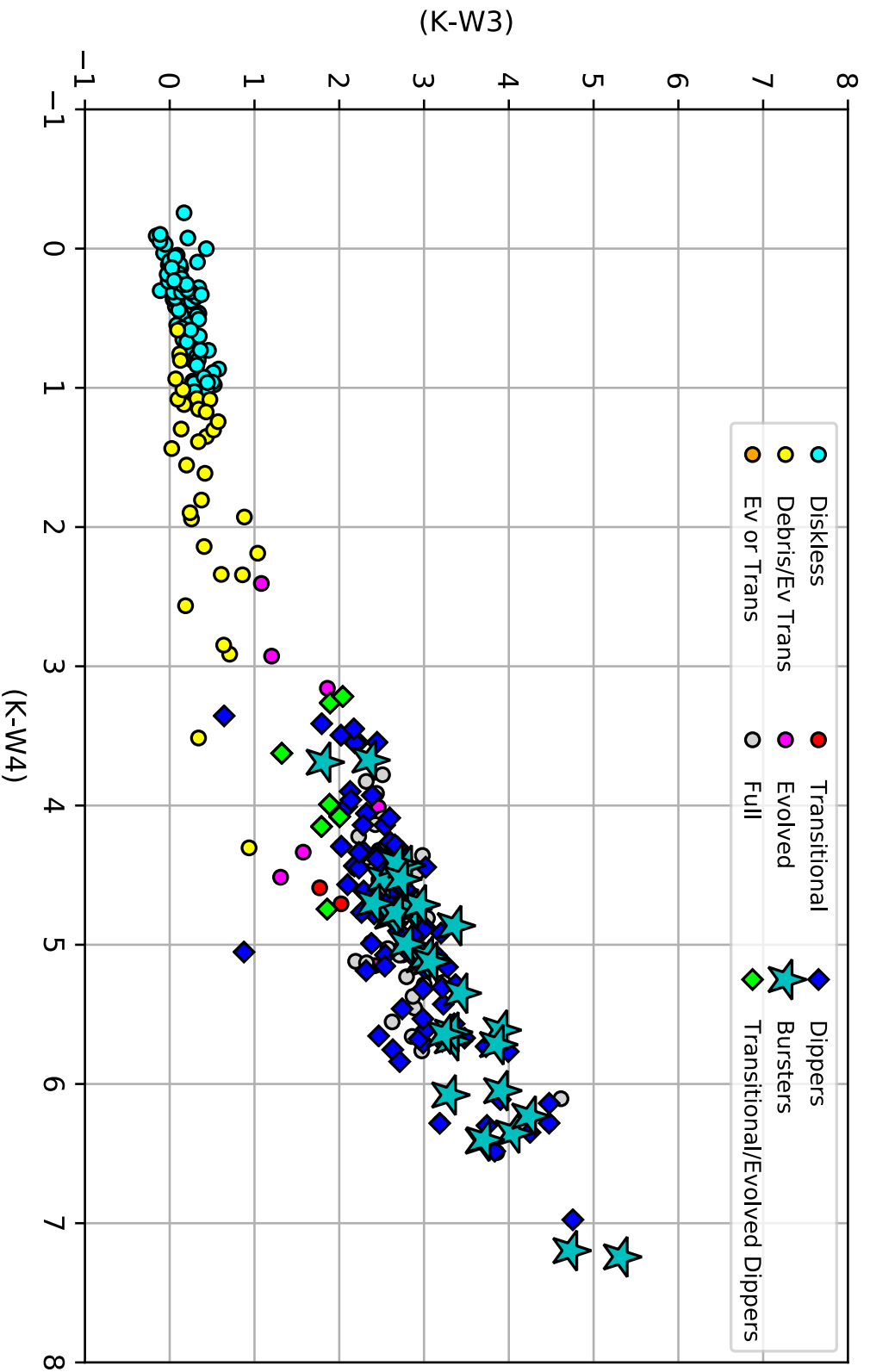


Figure 5.22: Disk types of dipper and burster stars found in this work where filled circles indicate disk types from Luhman and Mamajek (2012) in Upper Sco that were also observed in K2. Here colours are not corrected for reddening. Blue diamonds are all dippers found in this work with any membership, stars indicate bursters also with any membership which I expect to be an incomplete sample. Green diamonds indicate dippers that were also observed in Luhman and Mamajek (2012) that were found to have evolved or transitional disks given in Table 5.11. All green diamonds, blue diamonds and blue stars were added by this work, with all filled circles taken from Luhman and Mamajek (2012). The ML algorithm used here was insensitive to colour and so would be expected to find any more evolved dippers, were any to exist.

or reddening coefficients and so the targets in this Figure have not been corrected for reddening. This makes the classification of dippers into disk categories more difficult.

5.7.3 Orbital Distance to Inner Disk Edge

The dipper phenomenon is attributed to the dust at the inner edge of the circumstellar disk occultating the star in either warps or accretion streams. It is useful to understand the distribution of periods for these dipping events to better characterise the phenomenon. For most dippers a period can be estimated, either by using a Lomb-Scargle periodogram across the entire time series or selecting sections of the time series where dips repeat. In the worst cases it is possible to estimate the period by estimating the median time between successive dips.

Assuming Keplerian velocity, and using the known spectral types of these targets from Luhman and Mamajek (2012), Wilking, Gagné, and Allen (2008) and Ansdell et al. (2016), I can find an orbital separation from the host star. The orbital distance, assuming the the material orbits at a Keplerian rotation, is given by

$$D^3 \approx \left(\frac{GM P^2}{4\pi^2} \right) \quad (84)$$

where P is the orbital period, G is the gravitational constant and M is the mass of the star. The mass of the star is calculated from the model grid provided by Pecaut and Mamajek (2013). The temperature at this distance can be estimated using a blackbody relation.

$$T_{\text{sub}}^4 = \left(\frac{L}{16\pi\sigma D^2} \right) \quad (85)$$

where L is the luminosity of the star, σ is the Stephan Boltzman constant and D is the orbital distance.

Figure 5.23 shows the Keplerian radius of the material in AU (based on Equation 84) for each dipper target as a function of stellar luminosity, where the solid and dashed lines indicate a simple black body heating relation given in Eq 85. For aperiodic dippers the period has been estimated either using a lomb-scargle periodogram or the median separation between subsequent dips. The dipper population is notably cooler than the sublimation temperature with an average temperature of $1000\text{K} \pm 200\text{K}$.

This is similar to other findings for T Tauri stars. Eisner et al. (2007) shows using interferometry that low luminosity ($\lesssim 1 L_{\odot}$) T Tauri stars have wider inner disk edges than predicted by simple models. Millan-Gabet et al. (2006) also show the same result, that low luminosity T Tauri stars have larger sublimation radii compared with that estimated using a black body assumption. They suggest backwarming in the disk could increase the sublimation radius by a factor of two. They also note that smaller dust grains could cause the sublimation radius to increase. Muzerolle et al. (2003) suggest that the inner edge of the disk could be increased in T Tauri stars due to extra luminosity from accretion. If the dipper phenomenon can be attributed to the inner edge of the disk, some heating mechanism is required to push the inner edge of the disk further out.

Figure 5.23 shows that the dippers do not appear to follow a black-body temperature law. The Keplerian radius of the material is fairly constant across two orders of magnitude of stellar luminosity. Further work is needed to analyse whether this is due to small number statistics. (For example, the Keplerian radius for aperiodic dippers may be unreliable.) However, if this finding is robust, it may indicate that there is a characteristic distance for material being lifted out of the circumstellar disk that is independent of spectral type. This may be an indication that the interaction of the stellar magnetic field with the disk causes a warp at a characteristic distance, which obscures the stellar light and causes the dipping behaviour. Further work, both in the theoretical modelling of the disk and in observing this phenomenon as

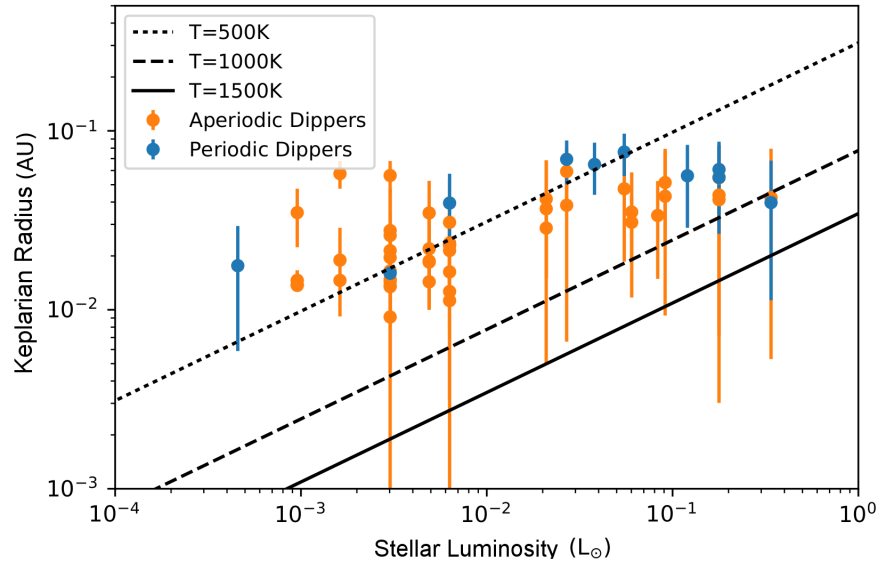


Figure 5.23: Inner disk edge in AU as a function of the luminosity of the star. I see dippers have systematically larger inner disk edge radii than predicted from a simple black body. Invoking backwarming or increased luminosity from accretion is likely to account for this additional heating.

a function of spectral type, is needed to better understand this trend. However, this work makes it clear that the use of observations of dipper stars is an important tool for observing this inner region and may give us a window into observing the effects of stellar magnetospheres.

5.7.3.1 Spectral Types of Dipper Stars

Stauffer et al. (2015) and Ansdell et al. (2016) find the dipper behaviour is limited to late-type M and K stars. Cody et al. (2014) presents 3 members of their sample as G type "quasi-periodic dippers" or "quasi-periodic symmetric". However, the criteria for selecting candidates in that work is different and all of these targets would not meet the criteria laid out by this work due to their low amplitude dips. Using the spectral types of the cluster members from the literature it is possible to predict how many FGK type stars would be observed if the phenomenon extended to these objects.

Luhman and Mamajek (2012) provides spectral types for their sample of 485 members of Upper Scorpius and Wilking, Gagné, and Allen (2008) provides spectral types for 124 members of ρ Ophiucus. Of these stars 53 were found to be dipper stars, (yielding a dipper fraction of $8.7\% \pm 3\%$ for the combined clusters with known spectral types).

Table 5.12 shows the expected number of dippers in each spectral type, if dipper fraction was not type dependent. I make the assumption that all stellar types are observed uniformly. Based on this, we see we would expect more observations of early-type stars. However, we are biased against high mass stars in our survey as they are likely to have longer period dips.

The period we would expect for a dipper around a larger star (were one to exist) is easy to calculate. As stellar mass increases the distance to the inner edge of the disk, the sublimation radius, will increase. If we assume the occulting material is at the sublimation radius then the period of the dips should increase as a function of spectral type. The distance to the inner edge of the disk can be estimated using the stellar parameters and the sublimation temperature of the dippers. (See Eqs. 84 and 85).

Table 5.12: Expected and observed number of dipper stars in Upper Sco and Rho Oph where spectral types have been determined in the works of Luhman and Mamajek (2012) and Barsony et al. (2012)

Spectral Type	Expected Dippers	Observed Dippers
B	2.2 ± 0.9	0
A	1.7 ± 0.7	0
F	0.9 ± 0.4	0
G	1.7 ± 0.7	0
K	5.2 ± 1.9	14
M	41.2 ± 14.0	39
L	0.1 ± 0.1	0

The sublimation temperature T_{sub} of dust in the disk is approximately 1300K-1600K as shown by Kobayashi et al. (2011) (depending on the species of dust). We would expect any dust on the inner edge of the disk to be $\lesssim T_{\text{sub}}$. In this case I use a sublimation temperature of $T_{\text{sub}} = 1000\text{K}$, which is found to be the average temperature for the dippers in this sample as discussed in Section 5.7.3 and shown in Figure 5.23.

Using the stellar models from Pecaut and Mamajek (2013) it is possible to calculate the expected period for early-type (BAFG) stars if the same dipper phenomenon were to continue into these spectral types. For G0 type stars I would expect a period 9.8 ± 5.6 days, for F0 type stars I would expect a period of 14.3 ± 8.1 days. As K2 Co2 is an 80 day long campaign I would expect G and F type dippers to be detectable, if they did indeed exist. However as shown in Table 5.12 there are low numbers of G-F type stars expected in this sample. For later A and B type stars I expect the rotation period at sublimation temperature to be $> 20 \pm 10$ days and too long to be detectable with K2 (if a detection limit of 4 occultations was imposed).

DISK LIFE TIMES AS A FUNCTION OF STELLAR TYPE As discussed in Kennedy and Kenyon (2009) and Carpenter et al. (2006), the disk life time varies as a function of spectral type. Larger stars evaporate their disks much more efficiently than smaller M and K stars. Using photometry from 2MASS and WISE and spectral type classifications from above we can see the different SED's of stars in each cluster. This is shown in Figure 5.24, which reproduces a similar figure from Carpenter et al. (2006). (The wavelength of each star has been offset by a random value to show the distribution.) Here dippers have been highlighted in orange, and bursters have been highlighted in green. We see that most large stars (F type through O type) do not have disks (with most being in the younger ρ Oph cluster).

Figure 5.25 shows also that larger stars do not have disks, including all stars in either cluster that have a spectral type from the literature. Dippers are highlighted in orange. Here, as above, W_1-W_3 excess is used to track the brightness of the disk dust around the star. Stars with high masses ($\gtrsim 1$ solar mass) mostly have no disks, as shown by the lack of bright, reddened stars. This shows that in these two clusters there may not be enough dusty, massive objects to test whether dippers can occur around larger stars.

Due to low number statistics with early-type stars with disks in Upper Sco and ρ Oph and the short and the 80 day integration time of K2, I am cannot rule out the possibility of F and G type dippers with this dataset with high significance.

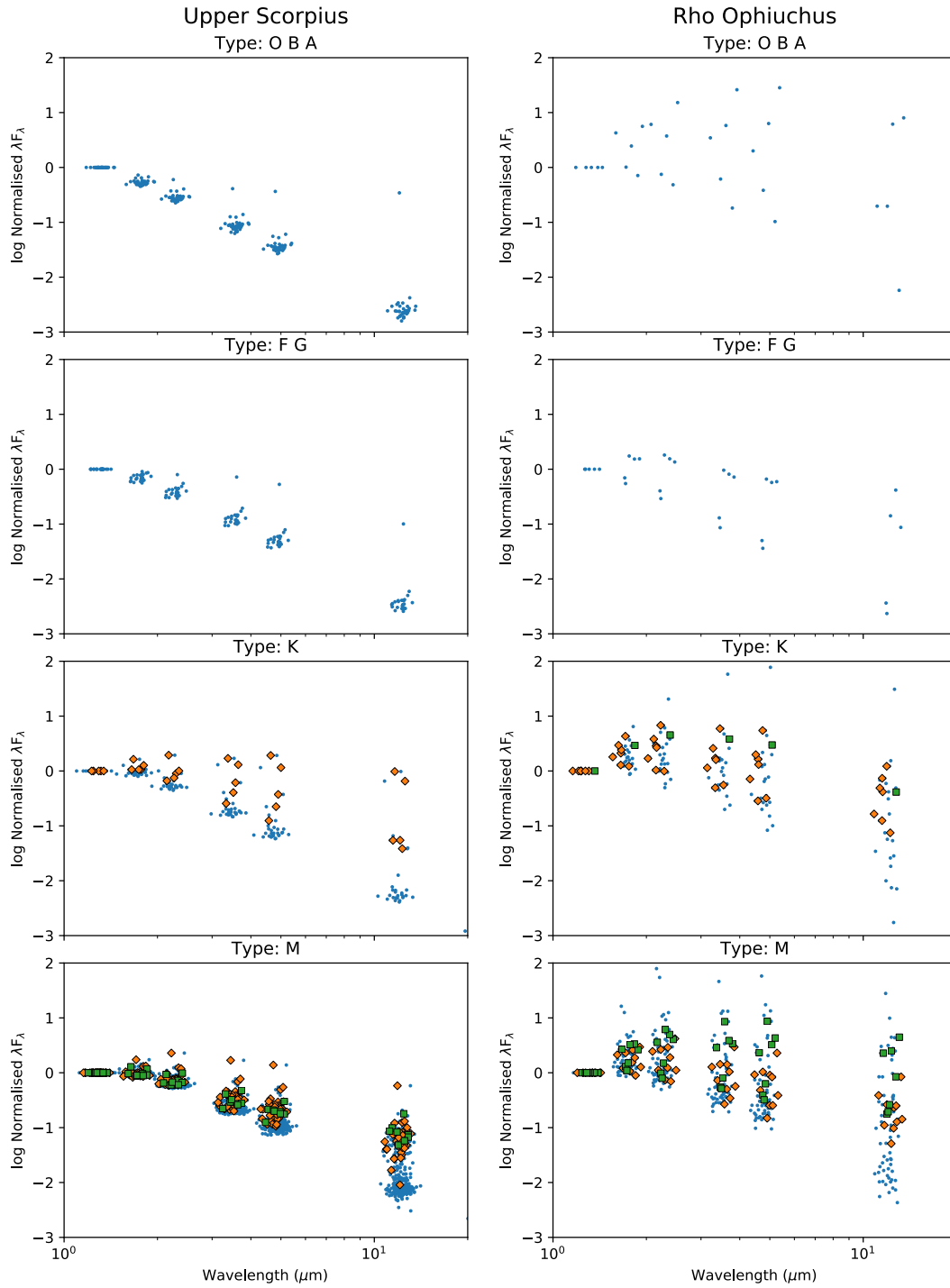


Figure 5.24: Reproduction of figure from Carpenter et al. (2006) showing the SED's of all Upper Scorpius and ρ Ophiuchus members as a function of spectral type, normalised to the j band flux. Here a random offset has been added in wavelength in order to distinguish populations. Dippers are highlighted in orange diamonds, bursters are highlighted in green squares. Disk bearing stars will have an excess of IR flux, causing their SED's to move higher in this plot. There are few F-O type stars showing disks in either cluster.

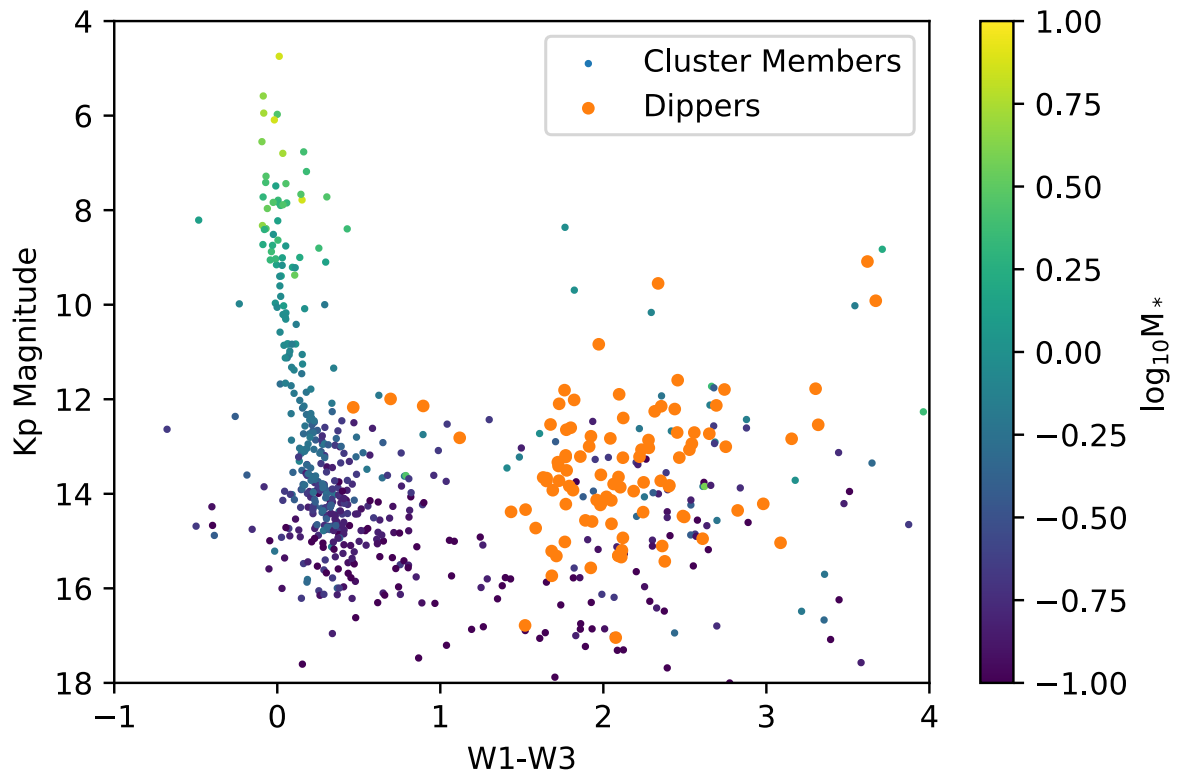


Figure 5.25: Magnitude of members of either young cluster as a function of $W1-W3$ excess, which is used to track the dust in the disk. Targets with a high $W1-W3$ excess host dusty disks. Using spectral types from the literature and models from Pecaut and Mamajek (2013) the masses of each target have been added. Dipper stars have been highlighted in orange. We see there is a lack of large stars with disks. As discussed in Kennedy and Kenyon (2009) and Carpenter et al. (2006) this is due to large stars evaporating their disks more efficiently than small M and K stars.

5.8 BURSTER STARS

A subset of the candidates flagged by the RF classifier were found to become brighter in bursting events very similar way to those found in Cody et al. (2014) and Stauffer et al. (2014). These were distinguished by eye from dippers and flagged as “burster” stars. This subset also contained targets that both dipped and bursted, referred to in Cody et al. (2014) as a symmetric morphology. An example of a burster target is given in Figure 5.26. All such stars were noted to have a significant infrared excess. These burst stars are otherwise indistinguishable from the dipper sample, they cluster in the same spaces of all other features.

In this work I do not train on a set of example bursters, since there are no other examples of burst stars in Upper Sco and ρ Oph with which to create a training class. Instead I serendipitously find burster stars in my classified dipper sample. This is largely because some of the training data have included dippers where the M statistic, amongst other features, showed shallow dipping events. This is either due to the relative symmetry of the light curve or because of a step function introduced in VJ2014 which reduces the apparent dipper signal. This has caused some burst stars with a symmetric morphology to be included in my final classified data set. The set of bursters in this work is likely incomplete and more could potentially be found in K2 Co2.

It would have been possible to iterate further and build a new burster class to find this type of object. I chose to have one, broad classification rather than split into two classes for two reasons: firstly the number of bursters is small (which may produce unreliable training). Secondly, there are some targets that are difficult to classify that both dip and flare. To ensure the dipper population is as clean as possible any cases where there was an equal amount of bursting events compared with dipping events (“symmetric morphology”) were added to the bursting class.

The bursts found in this sample do not resemble stellar flares, which are characterised as a sharp increase in flux with an exponential drop off. These events much more closely resemble the dipping behaviour in shape. Stauffer et al. (2014) suggests these events are accretion bursts, where mass falls onto the stellar photosphere over a short duration causing brightening events and hot spots. They show other candidates that are not bursting but may display a rotating hot spot from such an accretion mechanic.

The occurrence rate of burst stars for each cluster is $1.1\% \pm 0.4\%$ for Upper Sco (10 Myr) and $7.5\% \pm 1.9\%$ for ρ Oph (1 Myr) as shown in Table 5.7, though this may be an underestimate. If my incompleteness is the same for each cluster, which I expect, I find more burster stars in the younger ρ Oph cluster.

A full description of all targets, including whether they were classified by eye as burst or dipping, is given in in the Appendix 6.6.

5.9 SUMMARY

Dipper stars are a subclass of Classical T Tauri stars, so called because of their frequent occultations causing drops in flux of 10-50%. In this work I have used a Random Forest machine learning classification to find new dipper candidates in within K2 Campaign 2 using the literature dipper examples as a training set. I find there are 95 dipper targets in this field. I find that machine learning works excellently to distinguish this type of variable star, increasing the gains of finding dipper stars by eye in such a large dataset significantly, almost quadrupling the number of objects known in the field.

Infrared excesses have shown that all these candidates are likely split between the two young star clusters Upper Scorpius and ρ Ophiuchus. Comparing my candidates with known literature membership lists has allowed us to perform some statis-

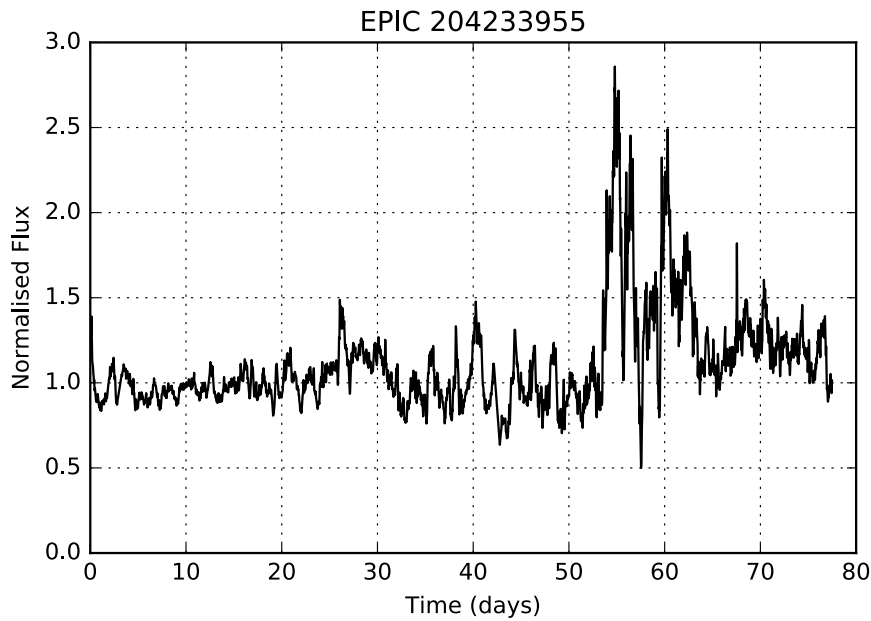


Figure 5.26: Example of a burst star from K2 Co2. Here I see the flux of the star doubles over a few days before returning to normal. The shape and duration of the burst event is inconsistent with stellar flares. 30 such object have been found in this work.

tics on the dipper fraction in each cluster leading to a dipper fraction of $5.9\% \pm 0.9\%$ for Upper Scorpius and $11.0\% \pm 2.3\%$ for ρ Ophiucus.

The machine learning algorithm built in this work uses 25 different, uncorrelated features based on light curve metrics only. I use a combination of standard light curve metrics, Gaussian Mixture Models and wavelet analysis to characterise the light curves. As my training sample is small the algorithm is iterated 200 times in order to ensure any classifications by the machine are robust despite a small number of training objects. From cross-validating my machine learning algorithm using scikit-learns ‘extra-tree-classifier’ I find that 86% of the dippers from the training sample are retrieved successfully. There is some confusion in the classifier, particularly between dippers and Beta Persei or Algol type eclipsing binaries.

I use information from all 200 runs to classify my final dipper sample. I calculate the probability of being in each class at each iteration and averaging them to find a final probability. To construct the dipper sample I take any targets that were classified as a dipper most frequently across the 200 iterations with a probability of 40% or greater, providing 229 objects. I check these targets by eye to remove any cases that are either poorly reduced in VJ2014 or could be explained by stellar variability. For completeness I also check any stars that have a probability of 20% or greater and find 4 additional objects out of 120 this way.

In this work I focus on building a machine that effectively classifies dipper stars only, not other types of variable star. I have found that by including other classifications I am able to improve my classification over having two simple classes (dipper or ‘non-dipper’). The addition of other variable types improves my classification probability by 18%.

I find disk bearing stars have dipper probability of $21.0\% \pm 5.5\%$ in both Upper Sco and ρ Oph. This is consistent with the findings from Cody et al. (2014), where a dipper fraction of $21.6 \pm 3.7\%$ was found in NGC 2264, a similar young cluster.

Of my sample 22 dippers were found to have no known membership. These are consistent in colour space with being a member of either cluster. In this work I have not attempted to assign memberships to them. With the released of parallax information from GAIA in 2018, the clusters should become much easier to distinguish.

This will not only allow us to establish the membership of these unknown dippers, but calculate a more accurate dipper fraction based on a more complete membership list.

¹¹⁸ Luhman and
Mamajek (2012);
Wilking, Gagné, and
Allen (2008)

Similarly to Ansdell et al. (2015) and Stauffer et al. (2015) I find the dipper phenomenon only in late-type (MK) stars. Based on spectral types from the literature¹¹⁸, I would expect to observe late-type stars in my sample (see Table 5.12). However, if we assume a rotation period consistent with the sublimation temperature at the inner edge of the disk, the 80 K2 campaigns may be too short to observe the dipper phenomenon in B and A type stars. Based on SED's using 2MASS and WISE photometry it is also likely that this larger stars have evaporated dust disks, which will prevent the possibility of them being dippers. Observations of younger clusters such as Taruas¹¹⁹ may allow us to test the possibility of F and G type dipper stars.

¹¹⁹ Kennedy and
Kenyon (2009)

Using work from Luhman and Mamajek (2012) I find that several of the dippers have evolved disk types (see Table 5.11 and Figure 5.21). These have smaller IR excesses than the rest of the population. These dippers are otherwise identical to the rest of the sample and are not distinguishable in any of the features used in this work. I find no debris disk or diskless stars to be dippers. This is consistent with the theory that the dipper phenomenon is caused by dust in primordial gas-rich disks occulting the star.

Using work from Ratzka, Koehler, and Leinert (2005), I find no evidence that the binary fraction between dippers and non-dippers in ρ Oph changes. This implies there is no effect on the dipper phenomenon by having a companion star at more than 10 AU.

I also find that 35% of my dipper sample does not meet the criteria set out in Ansdell et al. (2015), but are still clustered in the same feature space. Most of these objects were close to the cuts suggested in that work. (They have slightly longer periods or slightly smaller measurements of R_{dip} .) I suggest this metric may be too strict. Similar to Ansdell et al. (2015), I find evidence to support a correlation between IR excess and dip depth, as discussed in Section 5.7.1.

I find there are 30 burst type stars which exhibit brightening events on time scales of more than a day. These are inconsistent with stellar flares due to their shape, frequency and duration. This is a similar finding as in the NGC 2264 region, discussed in Cody et al. (2014) and Stauffer et al. (2014). As discussed in those works, bursting events are likely due to accretion in young disk bearing objects. These objects are likely incomplete in my survey as there is no specific training set for them. However, they otherwise cluster similarly in feature space as dipper stars. It would be possible to build up a separate training set for these objects and run the same classification algorithm to distinguish further examples of this class of object. I find bursting stars are more prevalent in the younger cluster, with Upper Scorpius containing $1.1\% \pm 0.4\%$ bursters and ρ Oph at $7.5\% \pm 1.9\%$ burster stars. This may suggest more unstable accretion in younger stars.

K2 will continue to make observations of young clusters in the coming years. Observations of the Pleiades and Hyades were taken in Campaign 4. Several clusters younger than 100 Myrs were observed in Campaign 9. New observations of the Taurus region scheduled for mid 2017. With this new data we will have an opportunity to study a new and important clusters to investigate if dipper fraction correlates with age. Finally, Upper Scorpius will also be revisited in Campaign 15, though coverage will be partial. This will allow us to follow up on several of the dippers found in this work.

By studying the populations of this class of young stellar object across clusters of different ages we will be able to understand more about this phenomenon. We will be able to test whether this mechanism is a transition stage in an evolving circumstellar disk, or whether this is ongoing accretion onto the star over the disk life time. I intend to extend this work by using this algorithm on other K2 Campaigns. This will include other large, young star clusters and investigate the prevalence of dipper and burst stars. By expanding my sample of dipper stars we are able to

understand more about disk dynamics in young stars, but also have a probe into the very inner region of the disk.

Part V

CONCLUSIONS

CONCLUSIONS

In this thesis I have investigated several aspects of exoplanet and time domain astronomy using readily available public data. I have tested the limits of atmospheric models, build a uniform analysis of exoplanet transmission spectra and classified young stars with machine learning, quadrupling the output from literature. I have used the wealth of data on exoplanets available, from K2, the enormous treasury programs from HST and several databases of molecular absorption data available. I have used these sources to perform independent and uniform analyses on light curves and spectra, and to investigate the limits of current exoplanet atmosphere models. I will summarise the findings of each of my projects here and discuss some of the applications and future avenues of study for this work.

In this work I have built sets of routines using C++, IDL and python to reduce and process these datasets. Where possible I will make the results of this work public, ensuring transparency and repeatability. By releasing these data products stellar and exoplanet atmosphere models can be further tested by other groups. I intend to release the molecular cross sections I have created with pressure broadening values so they can be used as inputs for exoplanet atmosphere models. I also intend to release a small applet to view each of the molecular features, so that wavelengths of interest for exoplanet observation can be easily found. This allows the bandpasses and resolutions of instruments to be matched for future missions, showing which molecular absorption features might be observable with each instrument. I also intend to release the stellar spectra I have created using the WFC3 observations, as they will potentially help to calibrate stellar models and are useful input spectra for synthesising exoplanet observations.

6.1 ATMOSPHERIC PRESSURE BROADENING

In the first part of this thesis I have presented my work with public molecular line lists. In this project I asked whether we were prepared for future observations of exoplanet atmospheres with JWST and beyond. One of the short falls of current models is the lack of pressure broadening at the molecular level. In this project I have quantified the magnitude of the effect of pressure broadening on atmospheric models across a range of temperatures and pressures. This investigation included many aspects of broadening, from the profile evaluation width to the effect of using a mean profile vs. a detailed line-by-line approach. I have also presented an optimal grid for calculating pressure broadening which provides significant speed gains over the standard in literature.

I have found that in general the effects of pressure broadening are small. Particularly, for hot exoplanets observed at low resolutions (such as hot Jupiters with HST WFC3) the effect of pressure broadening is negligible. However, for observations of cool, high pressure atmospheres ($T \lesssim 500\text{K}$ and $P \gtrsim 0.1$ atm) with JWST-like resolutions, some discrepancies will begin to show at the $\sim 5\%$ level. Such pressures and temperatures could be achieved in the atmospheres of smaller planets such as super-Earths (though as with all atmospheric observations a high signal-to-noise observation would be required for a detection). By omitting pressure broadening from atmospheric models our ability to measure abundances in exoplanet atmospheres will be limited the near future for cool, Earth-like planets. While these observations are currently unattainable, we must be prepared for a new age of exoplanet atmospheric observation with detailed pressure broadening parameters, particularly for H_2 and He broadening. As discussed in Chapter 2, these parameters are not cur-

rently available and will impact hot Jupiters primarily. For low temperature planets such as super-Earths and mini-Neptunes observed with $R=10^5$ (e.g. VLT/E-ELT) discrepancies can reach more than a factor of 2. This effect will compound with stratified atmospheres, complex temperature pressure profiles and multiple molecular absorbers.

In this project I have developed a grid of molecular absorption cross sections across a range of temperature and pressure space relevant for exoplanet atmospheres and ($T=300\text{K}-3500\text{K}$ and $P=0.001\text{ atm}-100\text{ atm}$). I have used this grid to investigate the impacts of pressure broadening on molecular cross sections and project the magnitude of discrepancies in exoplanet atmosphere models. These grids are high resolution and span a wide wavelength range ($\lambda = 0.3 - 20\mu\text{m}$ for most molecules). The grid could be combined with a simple 1D atmosphere model and temperature pressure gradient to create synthetic observations of exoplanet atmospheres for a range of resolutions and bandpasses. By using a 1D atmosphere model that combines layers of gas at different temperatures and pressures the effect of pressure broadening will be compounded. It would be possible using this approach to investigate if this compounded effect would be observable in the atmospheres of planets or cool stars and at what level transmission through a stratified atmosphere would effect a transmission spectrum from a synthetic planet if observed with instruments such as HST WFC3.

Measuring atmospheres of hotter targets, such as brown dwarfs, can be used to test exoplanet atmosphere models. Such targets can be used as test beds as the intermediate stage between stellar atmosphere and exoplanet atmosphere models. Their low density and cool surfaces ($T\sim 500\text{K}$ for Y and T dwarfs) make it possible for atmospheres to exist that are much more like exoplanets, with water vapour and clouds¹²⁰. Brown dwarfs are brighter than planets, allowing much higher signal to noise observations to be taken, making them possible with current technology with high resolution instruments. Observations with the VLT have been taken of brown dwarf atmospheres spectra, such as Luhman 16AB¹²¹ at resolutions of $R=100,000$. Based on my work in Chapter 2, this would be high enough to measure the pressure broadening of the H_2O and CH_4 molecules in the atmospheres of these brown dwarfs if the cloud deck in the atmosphere were low. I would be interested to apply the grid of molecular absorption cross sections produced here and a simple 1D model to these high resolution spectra, and find if pressure levels could be constrained in anyway for these two molecules.

¹²⁰ Buenzli
et al. (2015)

¹²¹ Buenzli
et al. (2015)

6.2 EXOPLANET IR SPECTRA

In the second chapter of this thesis I developed a bespoke pipeline to automatically and uniformly reduce HST WFC3 transmission spectra of atmospheres taken in spatial scan mode. I developed several new corrections for the data and improved on methods such as the divide OOT method¹²². By ensuring my pipeline is automatic my results are free from user choices and easily reproducible by other teams. I am able to create exoplanet transmission spectra uniformly and quickly, mitigating a range of difficult instrument systematics. This has enabled to me to create the largest sample of exoplanet transmission spectra to date using all available public spatial scan data (30 unique exoplanets) and meaningfully intercompare them.¹

Using literature spectra and atmospheric models I have been able to validate my reduction internally and externally, and have found that it produces consistent spectra. I have found that observations from different visits and using different scan directions produce the same spectrum within errors, suggesting my methods are robust. Finally, I have devised the out of transit test (OOT test) to check the quality

¹²² Berta et al. (2012)

¹Note added in Proof: While this work was in the final stages of proofing a similar publication was added to the arxiv. Tsiaras et al. (2017) presented a set of 30 exoplanet spectra take with WFC3 and fits each with a full atmospheric model. They note similar features, such as the absorption feature in Wasp-76b which they attribute to TiO. The analysis of the water feature height presented in this work remains unique.

of each dataset and remove candidates with high channel variability from the final sample.

I have created a spectral sequence of exoplanet transmission spectra from water-rich to water poor using a similar method to Sing et al. (2016). In my work I have no access to visible wavelengths and so measurements of hazes and cloud made in Sing et al. (2016) are not possible. Instead, I have been able to use the height of the water feature at $1.34\mu\text{m}$ to rank spectra in a sequence.

I have then used this dataset to relate the height of the water feature to the theoretical scale height of the planet. The scale height dictates the height of the atmosphere based on the planet density and equilibrium temperature. Less dense, warmer planets have larger scale heights. Using the scale height and the water absorption cross section from the previous chapter I am able to create a simple analytical model for the expected water feature height. This model is based on a uniform slab of optically thin gas with a size related to the scale height of the planet. This model predicts the height of the water feature with no assumptions of clouds, chemistry or temperature-pressure profiles and depends only on the equilibrium temperature of the planet and its density.

I find the theoretical height of the water feature predicted by this model correlates significantly with the observed water height. This shows that the exoplanet transmission spectra are well described by a simple absorption model that varies based only on their bulk parameters, without invoking complex atmospheric models. Not only does this suggest that there is a continuum of water absorption in the transmission spectral sequence but that the observations are showing true, astrophysical variation and these small signals cannot be attributed to noise or detector errors.

Using the theoretical water height as a function of planet temperature and density I have derived a list of 79 planets that would be appropriate to observe water with HST, given its signal to noise profile. Due to the width of the absorption cross section as a function of temperature high scale height, low temperature planets are ideal for observations with HST WFC3. I have found that there are 9 planets that are small, (< 1 Jupiter radius) and with small masses. This creates a large scale height, making them amenable to atmospheric observations while still being a smaller, more Earth-like planet. In particular I highlight Kepler-18b and c, both of which are small, low mass planets close in to their host star. Their combination of a large scale height and long orbital period ($\lesssim 14$ day), would make them ideal candidates for observations with this technique. Based on this relation I have recently proposed for HST WFC3 time to follow up these two objects. If awarded time, I intend to supplement this data with archival Spitzer data on these planets and Gemini N/GMOS data to make a comparison very similar to that done in Sing et al. (2016), analysing water content and hazes in two planets within a single system..

6.2.1 Stellar IR Spectra

Accurate stellar parameters are crucial to obtain mass and radius measurements for exoplanets and accurately characterise them. In my third chapter I discuss the impact of inaccurate stellar parameters, specifically on the mass and radii measurements of exoplanets from the previous chapter. In creating a pipeline to reduce exoplanet data I have been able to create high SNR spectra of their host stars. Using these high quality spectra I have tested state-of-the-art stellar spectral models and temperature retrieval.

I observe an average $160\text{K} \pm 30\text{K}$ offset between temperature values retrieved using WFC3 and literature values of stellar temperature. Literature values are derived either with optical photometry, measurements of absorption line widths or interferometry. A discrepancy would imply either an error in the data in the IR or an error in stellar atmosphere models in the IR. Using NICMOS data of standard star HD209458 I have shown that there is a 2-4% error in the sensitivity curve of WFC3, which I propose introduces an artificial slope in the data. This slope increases the

black body slope of the stars, causing temperature to be overestimated when compared to fits from literature. By comparing the standard star HD209458 to data from the NICMOS instrument in the same wavelength region I was able to remove this artificial slope.

On testing the data again I have also found there is a discrepancy between models and data in the near-IR for cool stars ($T \lesssim 3500\text{K}$). For cool stars such as GJ1214b this can result in decreasing the measured exoplanet radius by 30%. This would drive up the density of the planet, causing different composition models to fit better. In the case of GJ1214b this would cause a rocky model to fit the planet better, rather than a water rich model (based on composition models from Zeng, Sasselov, and Jacobsen (2016)). It is likely that this second discrepancy is due to errors in the models rather than the literature values, as models perform better in the optical than in the IR. Stellar atmosphere models also perform poorly for cool stars due to molecular absorption, in this case by water.

Cool, small stars are the focus of exoplanet surveys such as TRAPPIST and MEarth and so accurately representing these stars, (which often peak in the IR) is a priority. I propose that this data set could be used to test the accuracy of a range of stellar atmosphere models including the ATLAS models¹²³ and 3D models such as CO5BOLD¹²⁴. This sequence of stellar spectra could be used to find which is most accurate in the IR for cool stars with molecular absorbers. By combining these IR spectra with optical spectra (e.g. from HARPS) better estimates of the stellar temperatures could be achieved and compared with accepted literature values.

¹²³ Kurucz (1992)

¹²⁴ Freytag et al. (2012)

6.3 DIPPER STARS

In my final project I have used light curves from the K2 mission to find examples of young dipper stars using supervised machine learning. Dipper stars show irregular, large amplitude occultations which are attributed to dust from the circumstellar disk accreting onto the star¹²⁵. By studying such stars we are able to investigate how the disk interacts with the star and how the disk evolves. The mechanism behind this phenomenon is poorly understood and few examples of dippers are available in literature. Dipper stars present excellent opportunities to study the inner region of the circumstellar disk. This region will be greatly impacted by stellar winds and the magnetosphere and is likely to have complex structure. Other methods struggle to probe this small region. Finding more of these objects, particularly as a function of cluster age, will allow us to investigate how the disk behaves and dissipates. By finding more examples of dippers we can improve our understanding and find the limits of the behaviour, whether it correlates with stellar mass and at what age dippers are no longer present.

¹²⁵ Bodman et al. (2016)

Dipper stars were already known to have been present in the Upper Scorpius and ρ Ophiucius region as discussed by Ansdell et al. (2015) (and also present in young cluster NGC 2264¹²⁶). I have increased the known number of this object from 25 to 96 in Upper Sco and ρ Oph, and identified 30 examples of "bursting" objects in that region. Previously the data had been classified by eye, missing many key examples of the phenomenon. Using machine learning (ML) algorithms I have reduced the human bias in discovering these objects and find examples that would otherwise have been missed, either due to low amplitude dips or long periods. These objects are complicated and do not easily separate in one particular feature space, suggesting that a ML approach is warranted. By using a ML approach I am also able to estimate the completeness and contamination of the sample and estimate a dipper fraction, based on the number of dippers found per disk bearing star. I find a dipper fraction of $\sim 20\%$, which is within errors of the dipper fraction from young cluster NGC 2264.

¹²⁶ Cody et al. (2014)

In this project I have also been able to identify a related object, known as a burster star. This object clusters in all of the same parameter space as dipper stars, suggesting that they are related. Bursters have been theorised to be similarly young dusty

stars that are undergoing accretion bursts¹²⁷. By finding bursting objects using an unbiased ML approach I can lend weight to the theory that these are related objects.

The dippers found in this work behave similarly to those known in literature in Upper Sco and ρ Oph and also in NGC 2264 in terms of their dip depth and duration. They are all consistent with being M/K stars that are young with IR excesses indicative of a dusty circumstellar disk. It would have been possible to use infrared excess as observed by 2MASS and WISE as a feature in the ML algorithm to improve the accuracy of the retrieval. However, by omitting it the machine is more sensitive to any dustless dippers, where any to exist. All dippers found in this work show an IR excess. As this feature was not used to train the machine, this lends strength to my classification.

K2 has recently observed the Taurus region during Campaign 13, which will be released in August–October 2017. This will allow us to study a region known to host young T Tauri stars. If dipper stars can be found in this region we will be able to observe the dipper fraction as a function of age.

In Campaign 15 Upper Scorpius will be partially revisited, with data released in April 2018. In this revisit there will be 11 dipper and burster targets that will be re-observed. Figure 6.1 shows the overlap between these two campaigns, overlaid on a dust map to show where the cluster is most concentrated. This presents an excellent opportunity to follow up on these objects three years later and find if their modes of variability have changed; whether they are periodic still, whether their dip depths have changed or whether they still display dips and bursts.

Finally, burster objects present the opportunity to study material falling into the host star. By modelling both the dipping events and the brightness increase during the bursting events it may be possible to constrain the mass of infalling material from the disk. Combining this with observations of these objects as a function of age will allow us to begin to model the dissipation processes for these early disks, particularly for small stars.

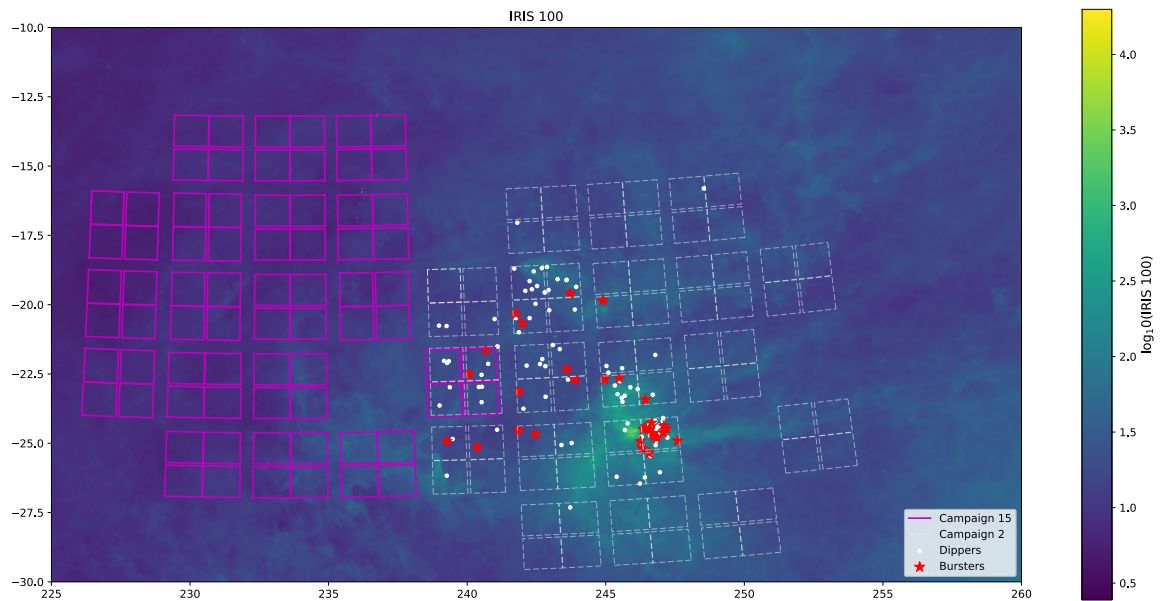


Figure 6.1: K2 Campaign 2 footprint on Upper Scorpius with bursters and dippers found in this work highlighted. Campaign 15 will partially revisit this region and is shown in magenta. Four of the modules will overlap with a previous visit and contain 13 targets found in this work to burst or dip. Unfortunately, much of Upper Scorpius is missed by this campaign.

6.4 FUTURE PROSPECTS

There are many current efforts in ground based observations of light curves in the hunt for exoplanets, both in large scale and small scale. Particularly NGTS and WASP will continue covering large fractions of the sky over long time scales. Unlike K2 data the cadence for this data is very short (~ 10 seconds), allowing much better sampling of light curve features. Observations of young dipper stars with such instruments would allow the shapes of the dips to be accurately measured to investigate the optical thickness and morphology of the accreting mass structures. With surveys such as these and continued observations from K2 it is an excellent time to use machine learning to classify variable stars, reducing the amount of human bias introduced to the process.

In the near future there will be brand new exoplanet discovery missions coming online, both on the ground and in space. Large missions such as TESS and PLATO will be able to not only increase the census we know of exoplanets but push to much smaller, rocky planets in an endeavour to find Earth-like planets around sun like stars. JWST will be able to characterise atmospheres in great detail with a host of near IR instruments and a large collecting area. In this new age, with ever smaller exoplanet signals, it becomes important to accurately reduce data and mitigate instrument systematics carefully.

There are other surveys that use the benefits of small stars to boost the transit signal. The TRAPPIST survey has already proved to be very successful and its follow on project SPECULOOS will allow us to find small planets around cool, small stars. In these cases we will rely heavily on models of cool stars from many aspects, including their size, their spectra and their activity. It becomes important to understand their parameters well.

With a wealth of new missions, new light curve and new transmission spectroscopy data available we will be inundated with exciting science. Thousands more planets will be discovered and analysed in great detail. To capitalise on this science we will begin to rely more on classification techniques from supervised machine learning not only to reduce the level of human bias, but to reduce the work load. I look forward to contributing to this new era of exoplanet discovery and characterisation in whatever small way I can.

Part VI

APPENDIX

6.5 APPENDIX A

In Chapter 3 I present an empirical relation between the scale height of a planet and the height of the water feature observed with WFC₃. Using this relation I have created a list of the optimal candidates to observe with HST WFC₃ with a strong water feature. These are given in Table 6.1.

Name	Scale Height	Temperature	Radius (R_{Jup})	Mass (M_{Jup})	Magnitude (V)	HST SNR
WASP-69b	687.0±0.2	961.0±22.0	1.057±0.047	0.26±0.017	9.87	80.5069
WASP-127b	2430.0±64.0	1400.0±30.0	1.37±0.04	0.18±0.02	10.15	70.8632
WASP-76b	1323.0±15.7	2183.0±43.0	1.83±0.06	0.92±0.03	9.5	56.9916
WASP-94 Ab	1749.0±19.8	1605.0±28.0	1.72±0.06	0.452±0.035	10.1	52.6032
WASP-79b	1398.0±72.8	1730.0±169.0	2.09±0.14	0.9±0.08	10.1	50.7125
WASP-20b	1577.0±0.3	1378.0±35.0	1.462±0.059	0.311±0.017	10.68	42.7882
WASP-131b	1338.0±17.4	1458.0±32.0	1.22±0.05	0.27±0.02	10.1	42.0159
WASP-74b	817.0±5.1	1916.0±39.0	1.56±0.06	0.95±0.06	9.7	41.7053
KELT-4 Ab	971.0±3.8	1822.0±27.0	1.699±0.046	0.902±0.06	9.98	40.9797
WASP-121b	1155.0±18.6	2359.0±53.0	1.865±0.044	1.183±0.064	10.44	39.8491
HAT-P-1b	730.0±5.0	1323.0±18.0	1.319±0.019	0.525±0.019	10.34	37.7765
WASP-62b	812.0±7.2	1438.0±37.0	1.39±0.06	0.57±0.04	10.3	36.1123
WASP-13b	1019.0±2.3	1514.0±34.0	1.389±0.045	0.477±0.044	10.42	34.2368
WASP-54b	1275.0±34.0	1782.0±66.0	1.653±0.09	0.636±0.025	10.42	33.815
WASP-52b	759.0±17.3	1301.0±35.0	1.27±0.03	0.46±0.02	12	32.7109
KELT-8b	1114.0±67.1	1677.0±67.0	1.86±0.18	0.867±0.065	10.833	32.3828
HAT-P-30b	690.0±16.7	1641.0±48.0	1.34±0.065	0.711±0.028	10.419	32.2934
WASP-17b	2402.0±27.1	1769.0±48.0	1.991±0.081	0.486±0.032	11.6	31.7458
WASP-39b	1075.0±7.1	1121.0±38.0	1.27±0.04	0.28±0.03	12.11	29.4111
WASP-49b	751.0±11.0	1373.0±39.0	1.115±0.047	0.378±0.027	11.36	28.4815
KELT-14b	772.0±0.7	1961.0±54.0	1.743±0.047	1.284±0.032	11	26.6713
HAT-P-26b	895.0±37.2	994.0±73.0	0.565±0.072	0.059±0.007	11.744	26.5179
WASP-126b	814.0±11.7	1486.0±70.0	0.96±0.1	0.28±0.04	10.8	26.4225
WASP-31b	1316.0±25.3	1574.0±38.0	1.549±0.05	0.478±0.029	11.7	26.1041
TrES-4b	2047.0±18.0	1798.0±48.0	1.838±0.081	0.494±0.035	11.592	25.8868
WASP-15b	1036.0±6.4	1654.0±38.0	1.428±0.077	0.542±0.05	11	25.8797
WASP-63b	1376.0±27.4	1536.0±56.0	1.43±0.1	0.38±0.03	11.2	24.7755
WASP-82b	818.0±18.3	2185.0±56.0	1.67±0.07	1.24±0.04	10.1	24.6795
KELT-6b	691.0±50.0	1318.0±60.0	1.18±0.11	0.442±0.019	10.418	24.366
WASP-67b	804.0±153.7	1036.0±18.0	1.4±0.3	0.42±0.04	12.5	23.9078
HAT-P-33b	1105.0±58.0	1780.0±32.0	1.686±0.045	0.762±0.101	11.188	23.4479
WASP-118b	1159.0±14.0	1726.0±40.0	1.44±0.036	0.514±0.02	11.02	23.3206
HAT-P-12b	695.0±12.7	958.0±22.0	0.959±0.029	0.211±0.012	12.84	23.2324
WASP-21b	849.0±36.5	1336.0±33.0	1.07±0.06	0.3±0.011	11.58	22.1291
HAT-P-18b	709.0±0.3	848.0±31.0	0.995±0.052	0.197±0.013	12.759	22.0615
WASP-139b	835.0±8.0	917.0±22.0	0.8±0.05	0.117±0.017	12.4	20.7725
WASP-88b	1514.0±44.2	1762.0±76.0	1.7±0.13	0.56±0.08	11.4	19.832
HAT-P-19b	737.0±8.9	1009.0±49.0	1.132±0.072	0.292±0.018	12.901	19.4336
WASP-12b	1056.0±15.0	2584.0±59.0	1.9±0.057	1.47±0.076	11.69	19.3128
WASP-113b	1033.0±19.3	1485.0±64.0	1.409±0.096	0.475±0.054	11.771	17.8281
WASP-78b	1081.0±93.5	1999.0±257.0	1.7±0.11	0.89±0.08	12	17.4059
HAT-P-40b	1432.0±11.0	1767.0±32.0	1.73±0.062	0.615±0.038	11.699	16.9226
WASP-90b	1291.0±38.9	1839.0±59.0	1.63±0.09	0.63±0.07	11.7	16.3816
WASP-48b	700.0±8.7	1958.0±60.0	1.396±0.051	0.907±0.085	11.72	15.4521
HAT-P-65b	2179.0±32.7	1931.0±55.0	1.89±0.13	0.527±0.083	13.145	14.0346
HAT-P-51b	1071.0±1.7	1189.0±28.0	1.293±0.054	0.309±0.018	13.44	13.7343
HAT-P-39b	1200.0±16.5	1749.0±60.0	1.571±0.108	0.599±0.099	12.422	13.582

WASP-142b	923.0±34.8	1990.0±75.0	1.53±0.08	0.84±0.09	12.3	13.1776
Kepler-78b	678.0±45.2	2217.0±42.0	0.105±0.014	0.006±0.001	11.551	12.5825
WASP-83b	672.0±10.5	1120.0±39.0	1.04±0.08	0.3±0.03	12.9	12.1857
Kepler-51c	3747.0±373.0	454.0±108.0	0.803±0.25	0.013±0.001	14.669	12.0111
Kepler-7b	1596.0±109.1	1607.0±10.0	1.622±0.013	0.441±0.043	12.885	11.5841
Kepler-12b	1752.0±103.6	1478.0±29.0	1.754±0.031	0.432±0.053	13.8	10.9982
K2-39b	1046.0±21.7	1855.0±93.0	0.732±0.098	0.158±0.031	10.832	10.6641
HATS-26b	1507.0±100.2	1921.0±69.0	1.75±0.21	0.65±0.076	12.955	10.6309
HATS-27b	1170.0±24.5	1655.0±86.0	1.5±0.2	0.53±0.13	12.766	10.4039
WASP-92b	829.0±11.8	1878.0±68.0	1.461±0.077	0.805±0.068	13.18	9.48616
CoRoT-1b	682.0±11.6	1900.0±43.0	1.49±0.08	1.03±0.12	13.6	9.15283
HAT-P-66b	1022.0±74.5	1901.0±63.0	1.59±0.16	0.783±0.057	12.993	8.97804
Kepler-18d	986.0±17.1	793.0±27.0	0.623±0.029	0.052±0.004	13.549	8.45964
HATS-8b	1216.0±61.1	1322.0±92.0	0.873±0.123	0.138±0.019	14.03	8.38614
HATS-31b	929.0±51.7	1826.0±99.0	1.64±0.22	0.88±0.12	13.105	8.21829
K2-107b	732.0±36.5	1780.0±83.0	1.44±0.15	0.84±0.08	12.92	7.83822
Kepler-36c	728.0±25.5	1016.0±11.0	0.328±0.005	0.025±0.002	11.866	6.96643
Kepler-8b	941.0±85.0	1664.0±52.0	1.416±0.053	0.59±0.13	13.9	6.50863
Kepler-18c	733.0±15.0	990.0±34.0	0.49±0.023	0.054±0.006	13.549	6.45995
Kepler-425b	683.0±133.1	1072.0±18.0	0.978±0.022	0.25±0.08	14.97	6.09235
HATS-11b	729.0±2.8	1632.0±58.0	1.51±0.078	0.85±0.12	14.018	5.93767
Kepler-41b	885.0±70.9	1789.0±35.0	1.29±0.02	0.56±0.08	14.465	5.85696
Kepler-427b	934.0±26.4	1075.0±79.0	1.23±0.21	0.29±0.09	14.42	5.6788
Kepler-426b	758.0±99.8	1302.0±21.0	1.09±0.03	0.34±0.08	15.073	5.30618

Table 6.1: Projected best candidates for HST WFC₃ observations of water features. Here scale height is derived from the mass of the planet, temperature of the star and orbital period of the planet as given by Nasa Exoplanet Archive with a μ value of 2. HST signal-to-noise ratio is based on an observation with WFC₃ G141 grism with an integration time of 50 seconds. Targets that have also been observed with HST spatial scan mode have been highlighted, though some have been removed from the reduction.

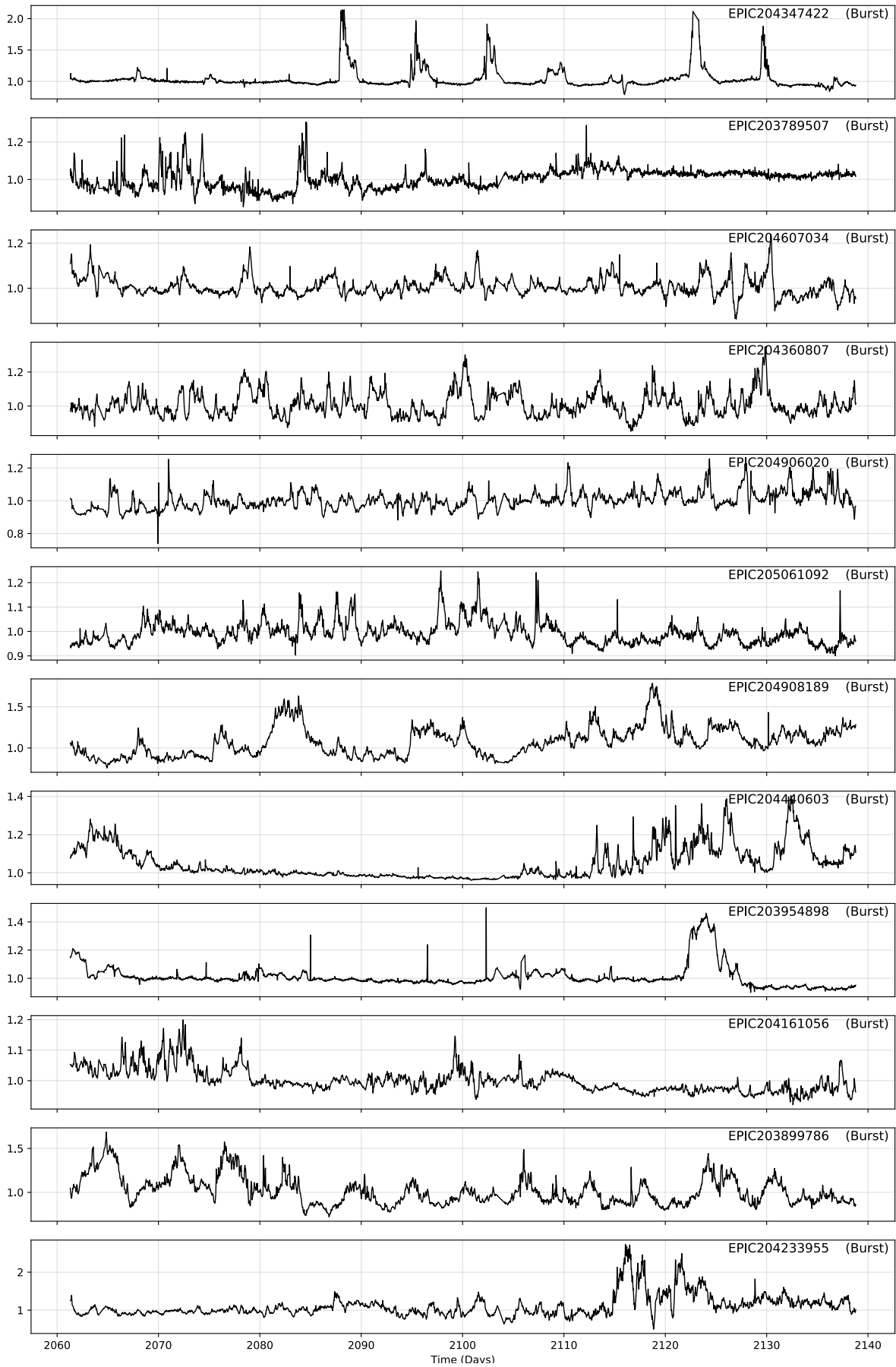


Figure 6.2: Light curves for Dippers and Bursters from Chapter 5 in normalised flux. These are ordered by M Stat and so start with the brightest ‘bursting’ targets ordered towards the deepest ‘dipping’. Dippers used to train the machine learning algorithm are highlighted in orange. 22 of these training candidates are taken from Ansdell et al. (2015) and Bodman et al. (2016). 18 are taken from the first iteration of this machine, see Section 5.4.2.1 for more detail.

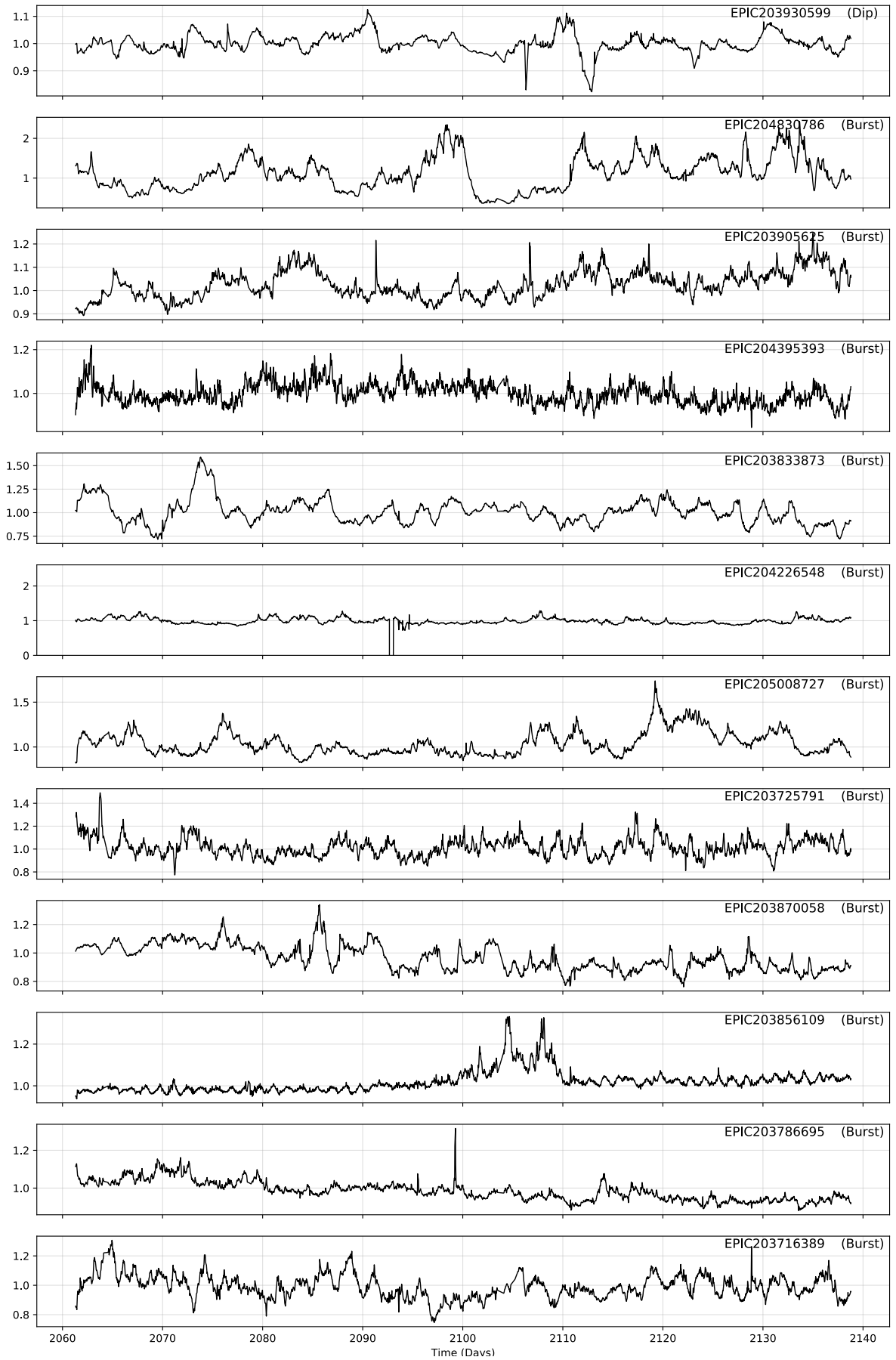


Figure 6.2: continued

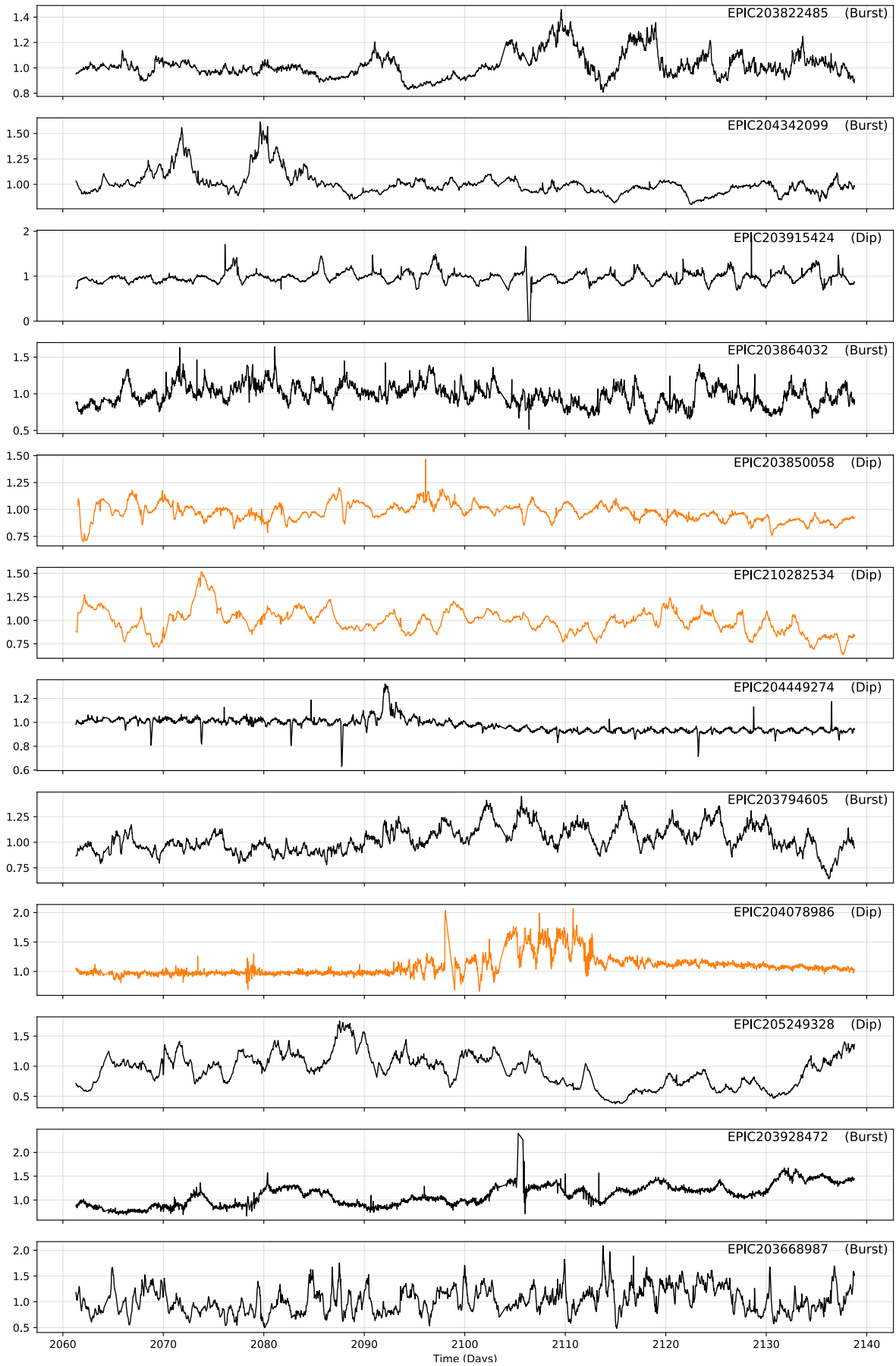


Figure 6.2: continued

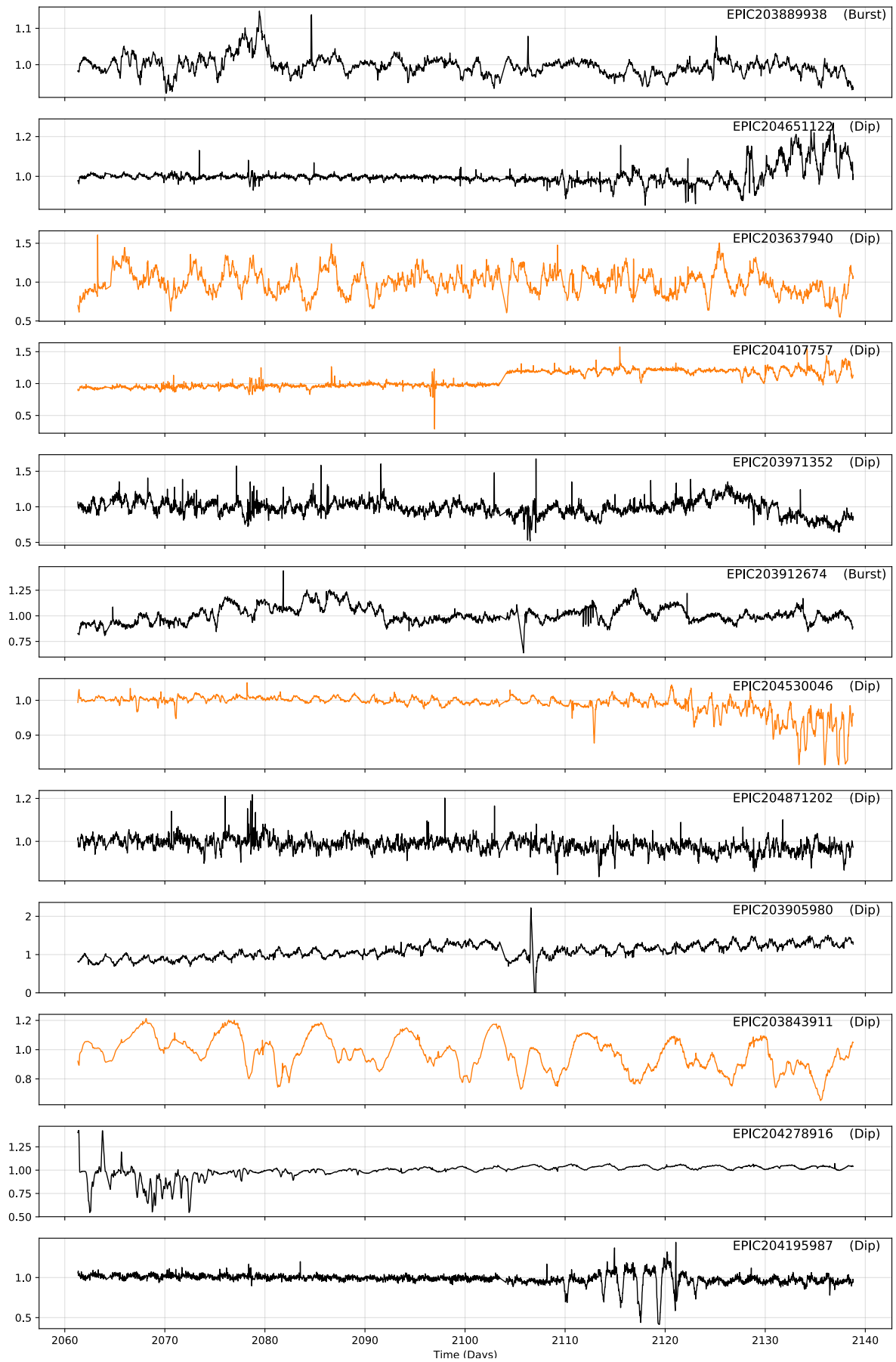


Figure 6.2: continued

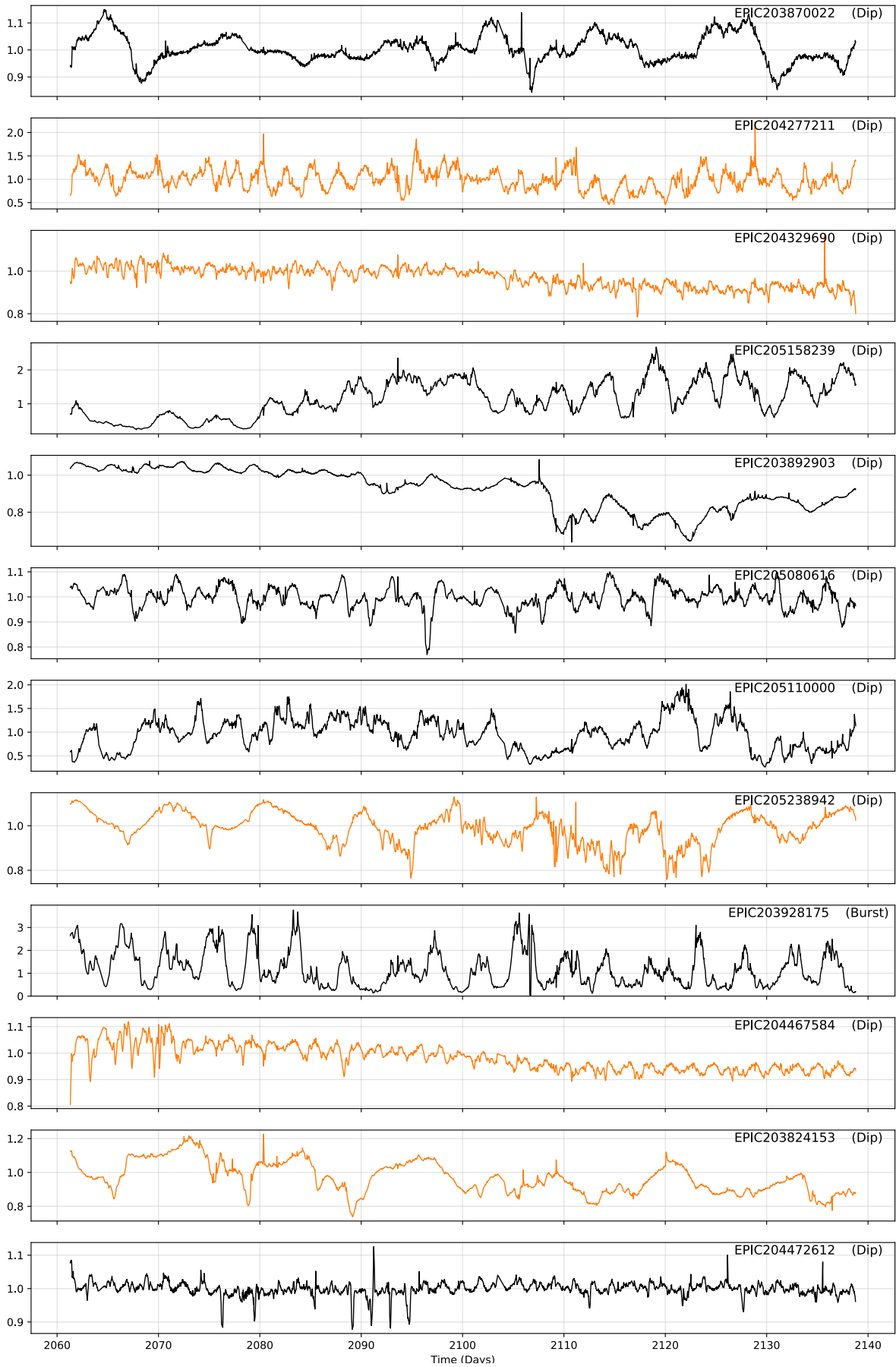


Figure 6.2: continued

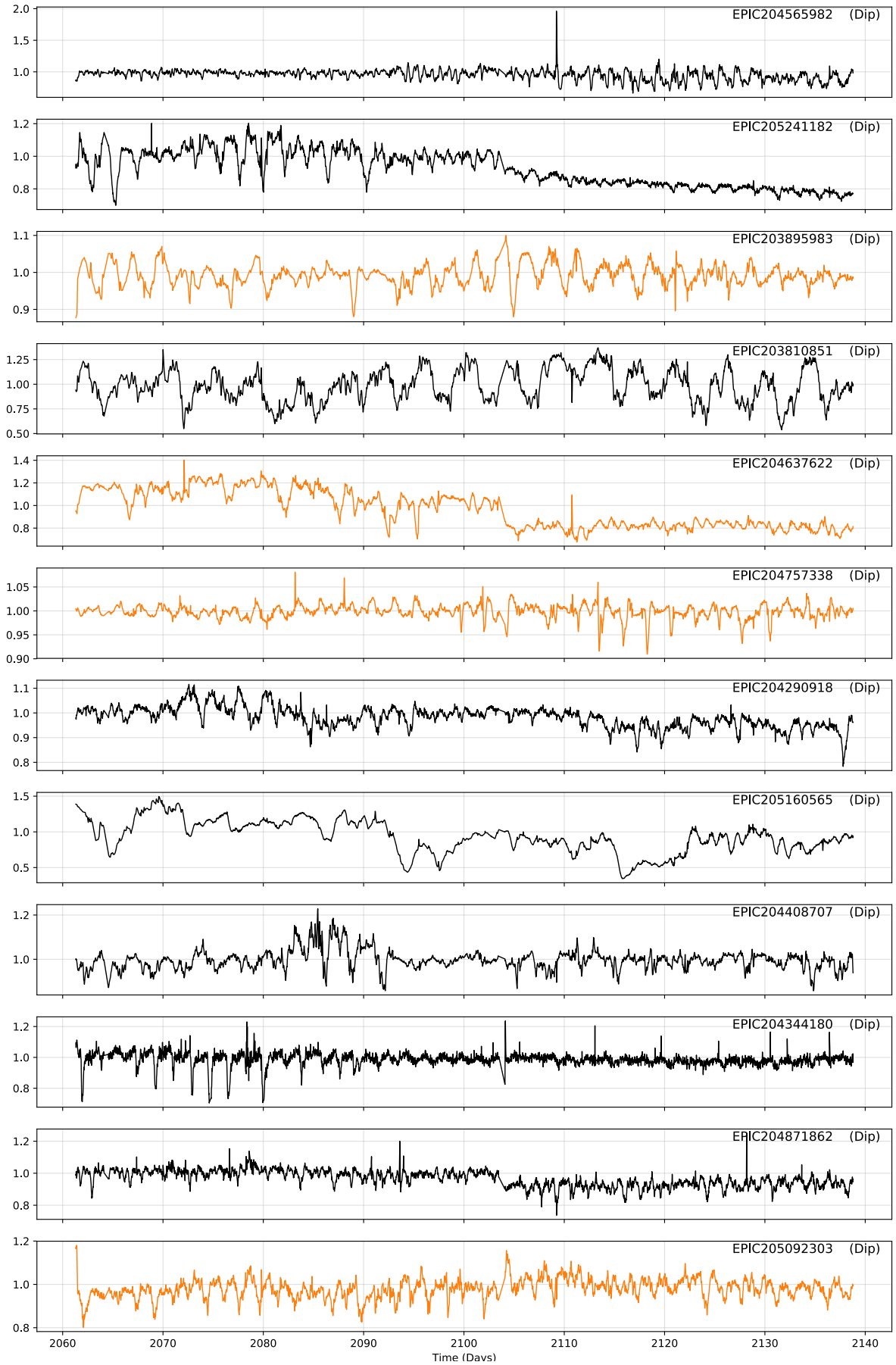


Figure 6.2: continued

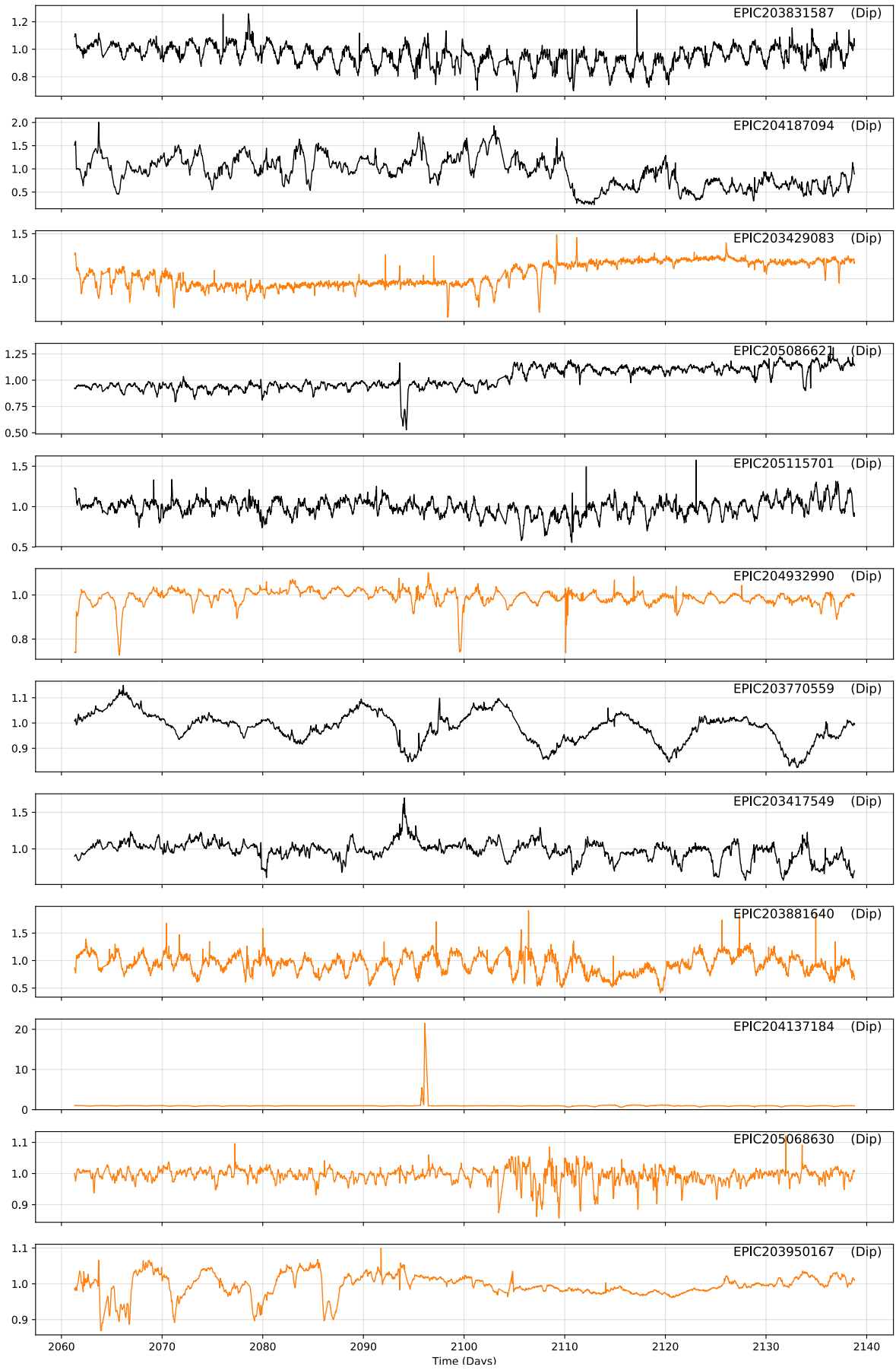


Figure 6.2: continued

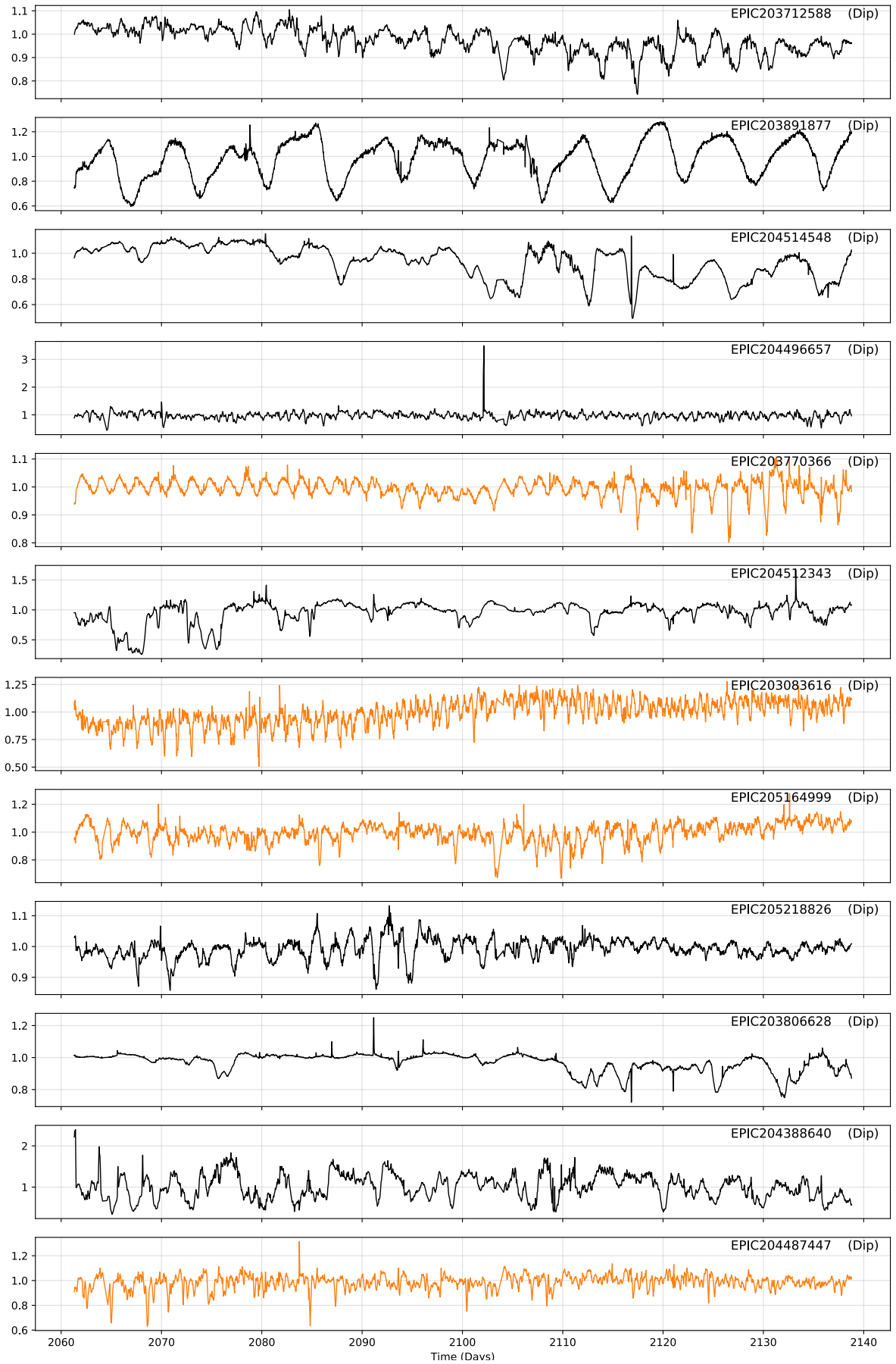


Figure 6.2: continued

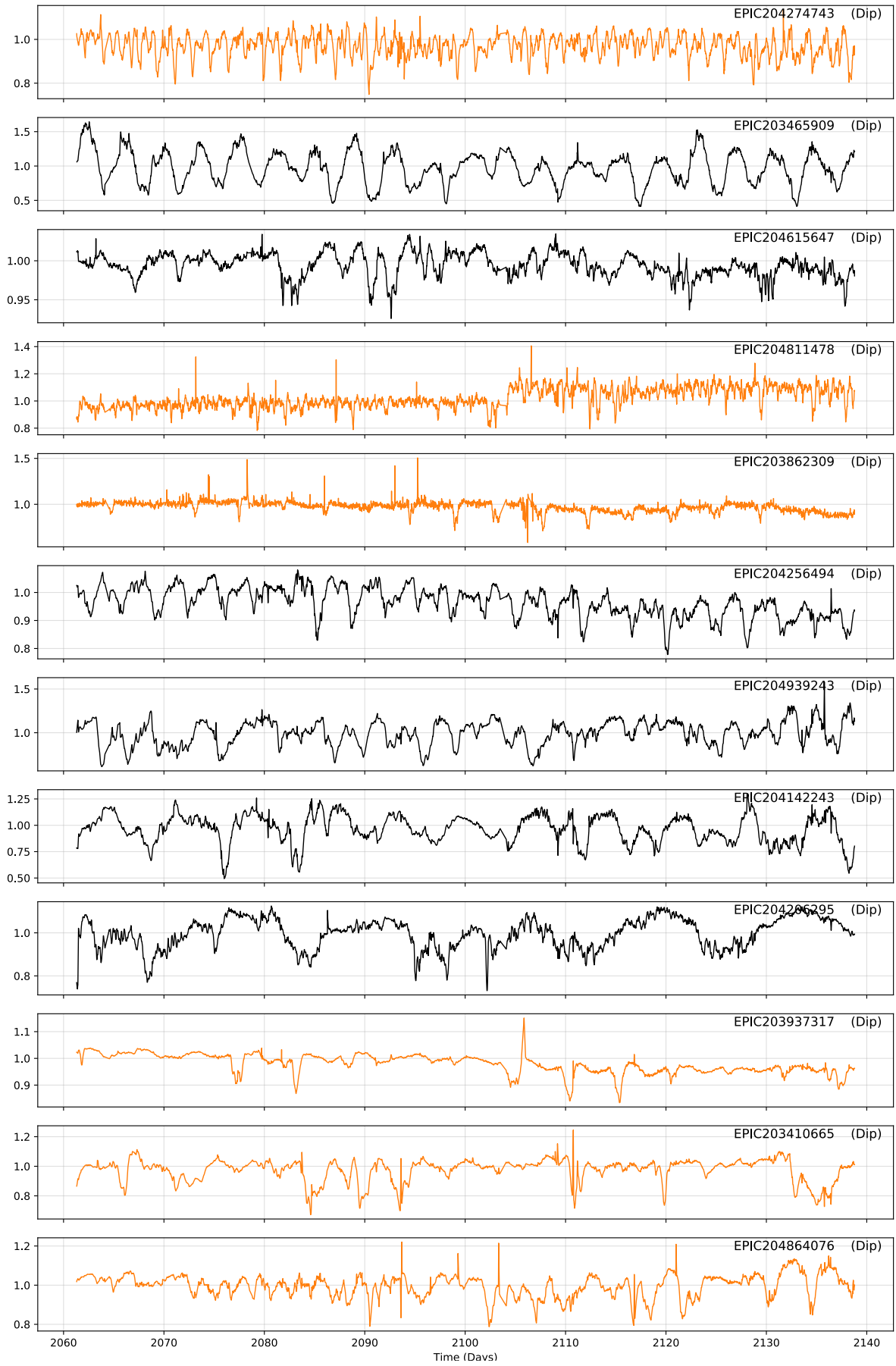


Figure 6.2: continued

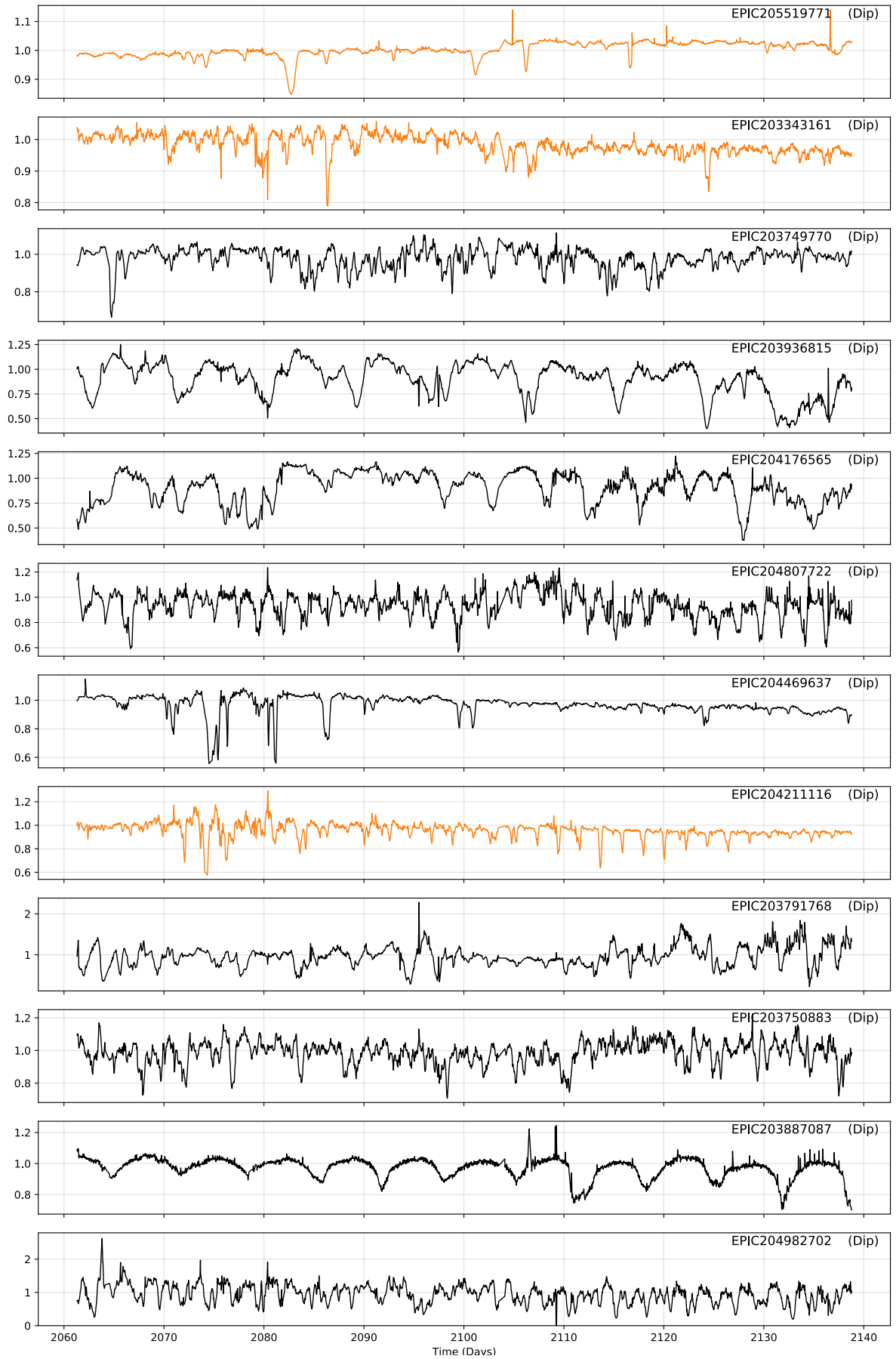


Figure 6.2: continued

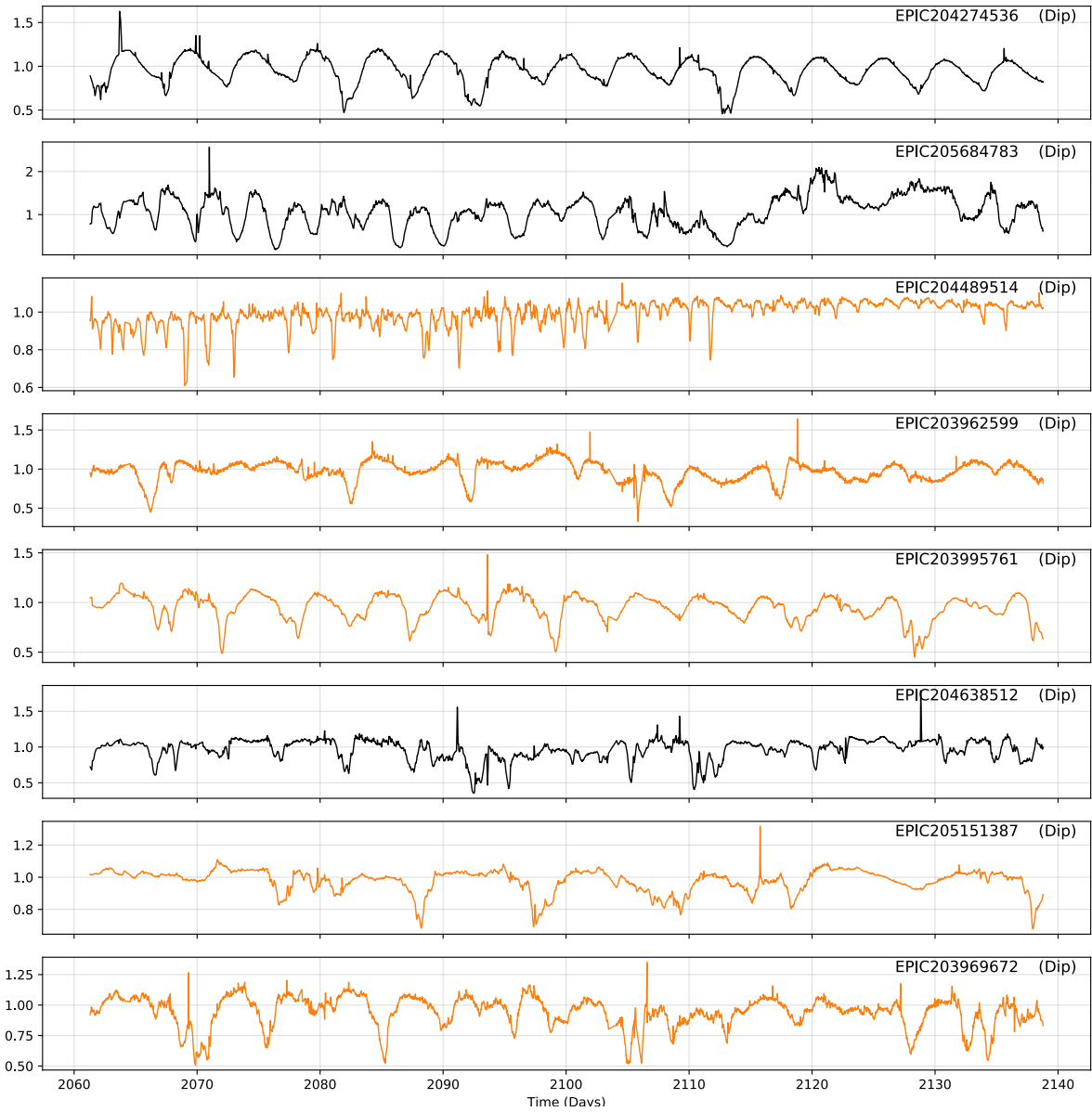


Figure 6.2: continued

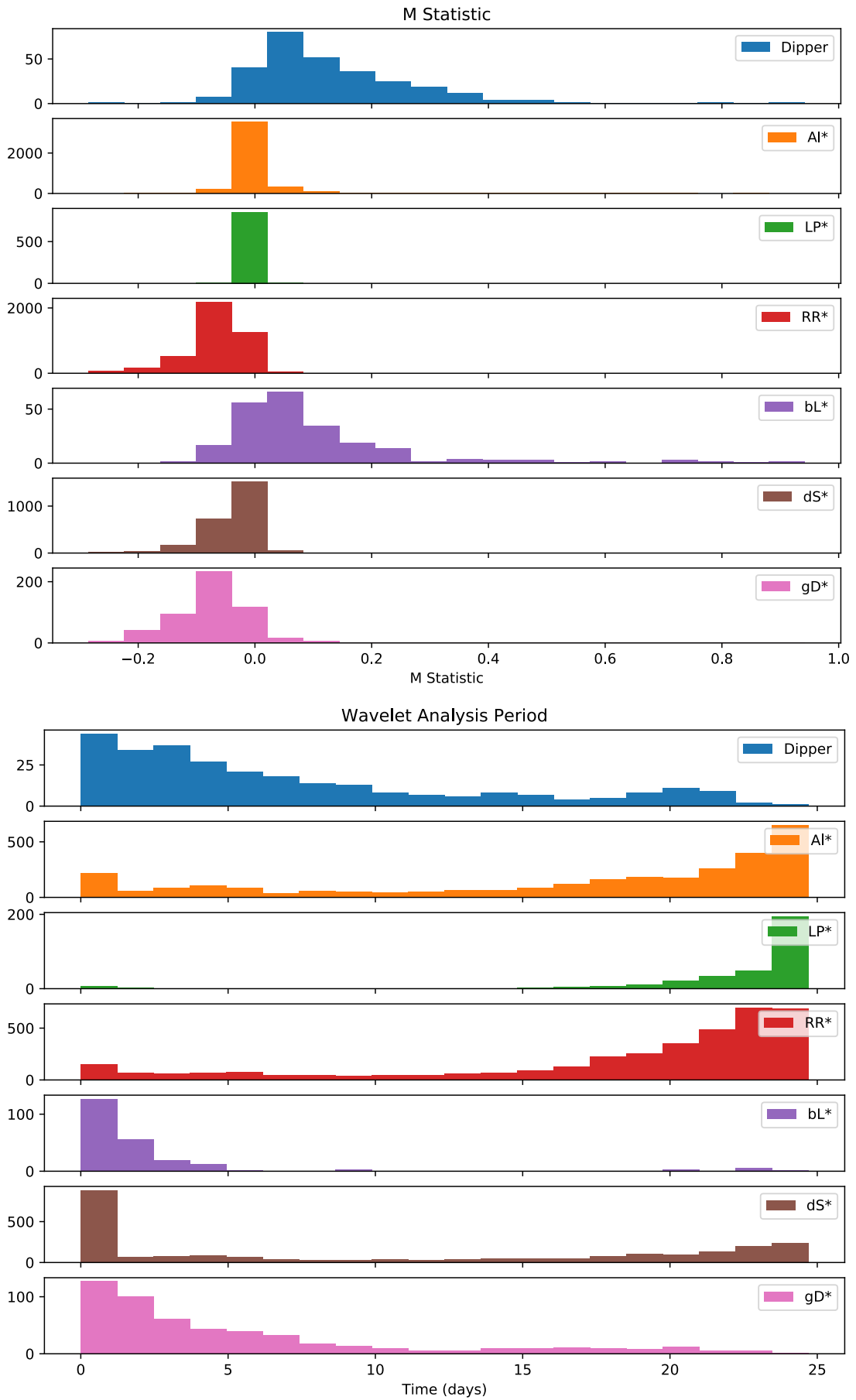


Figure 6.3: Plots showing the distributions of the top ten features for dipper analysis from the ML algorithm. Here each possible classification is shown. In this figure these are the final ML classifications after a iterating 200 times. Some of those classified in the dipper sample have since been discounted.

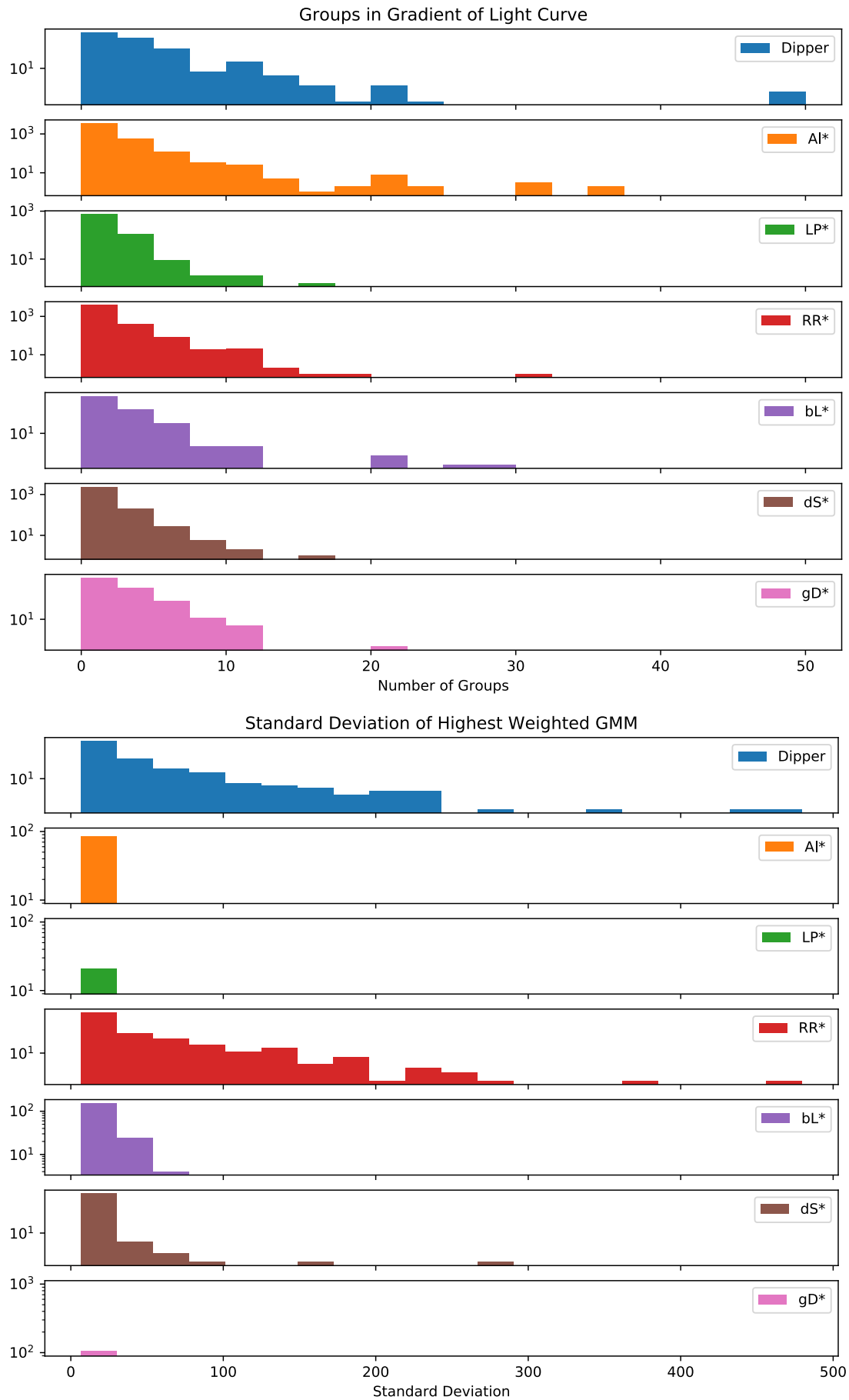


Figure 6.3: continued

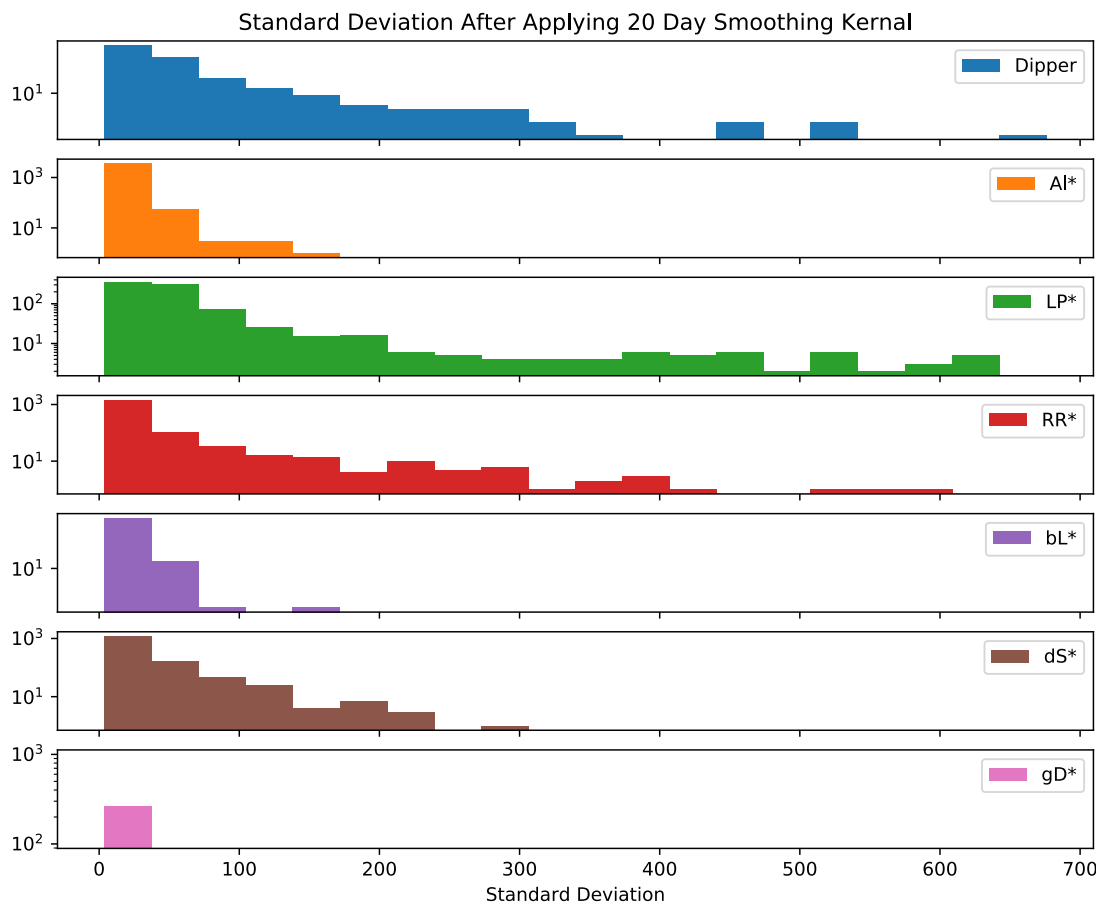
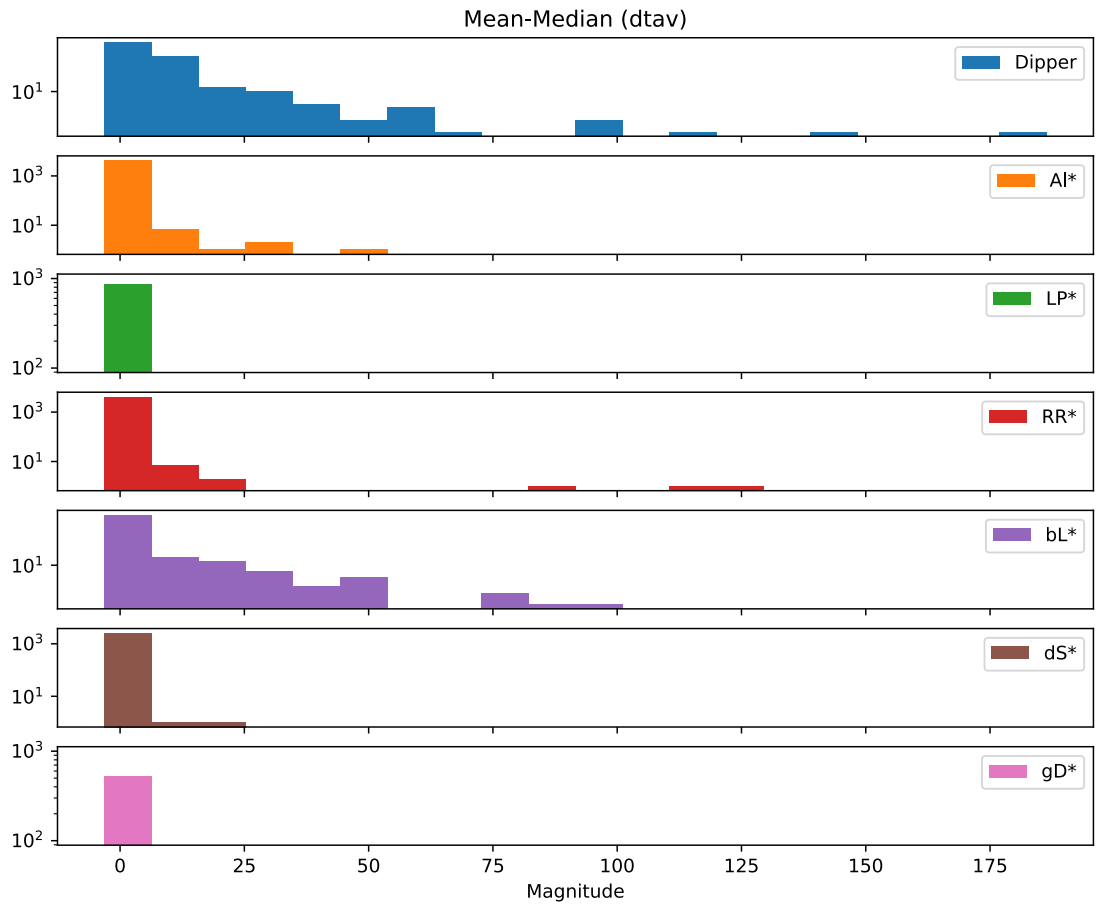


Figure 6.3: continued

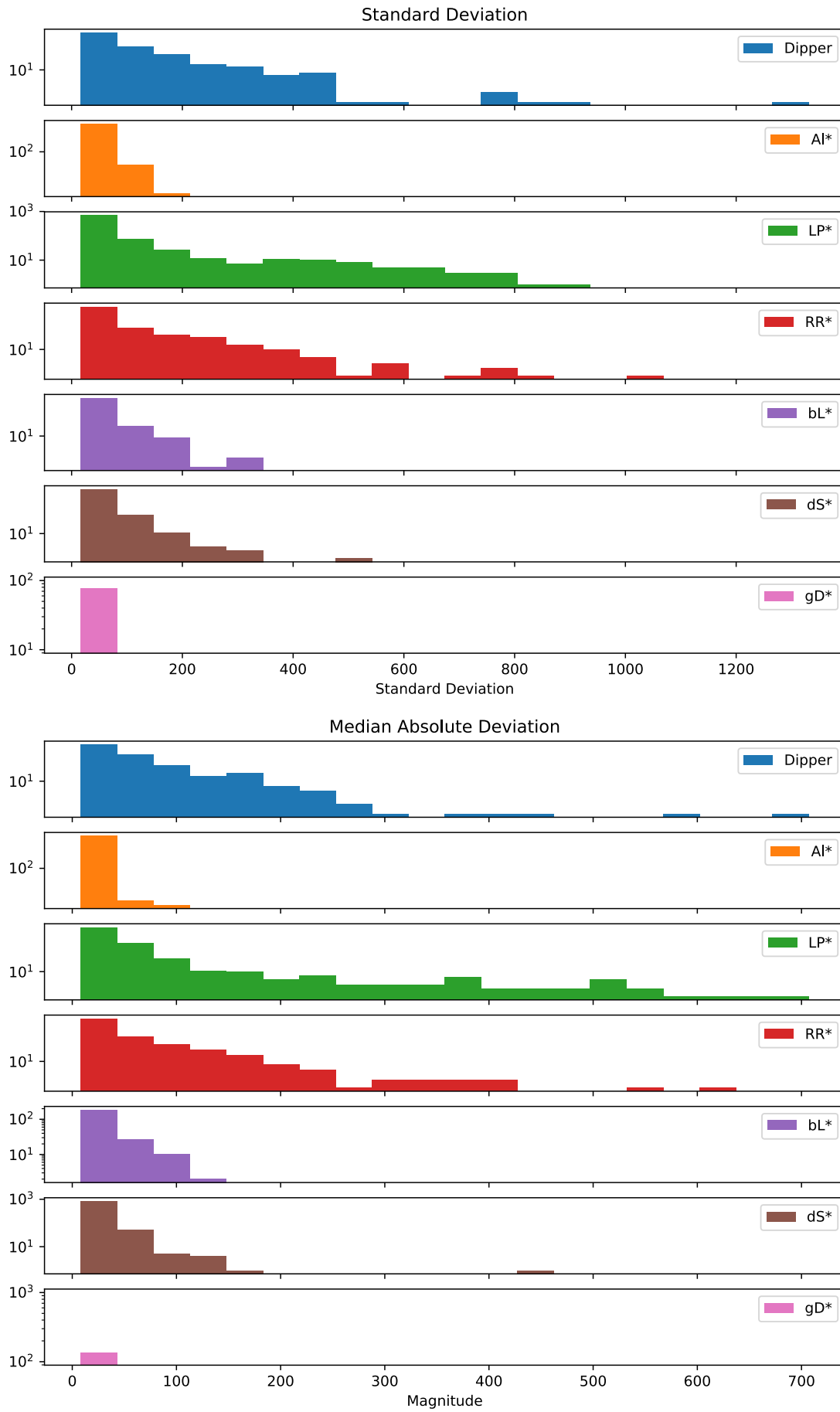


Figure 6.3: continued

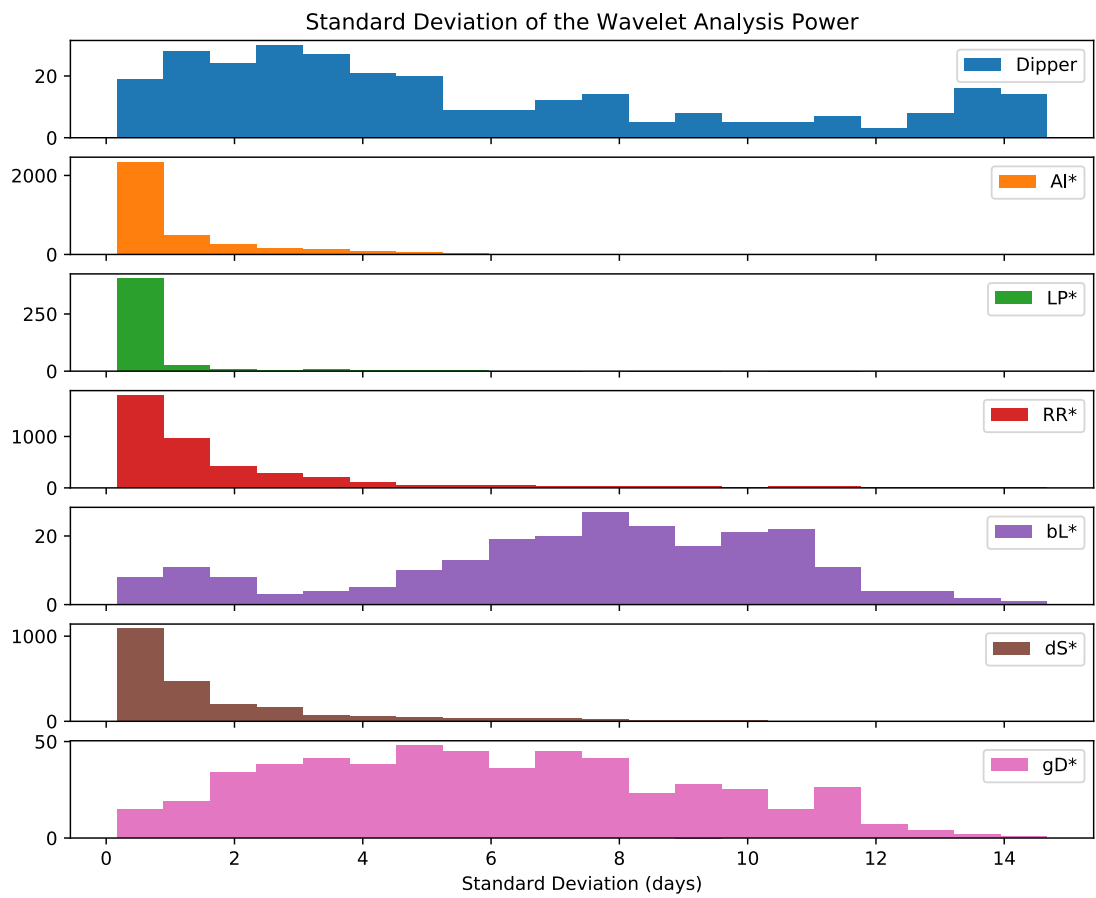
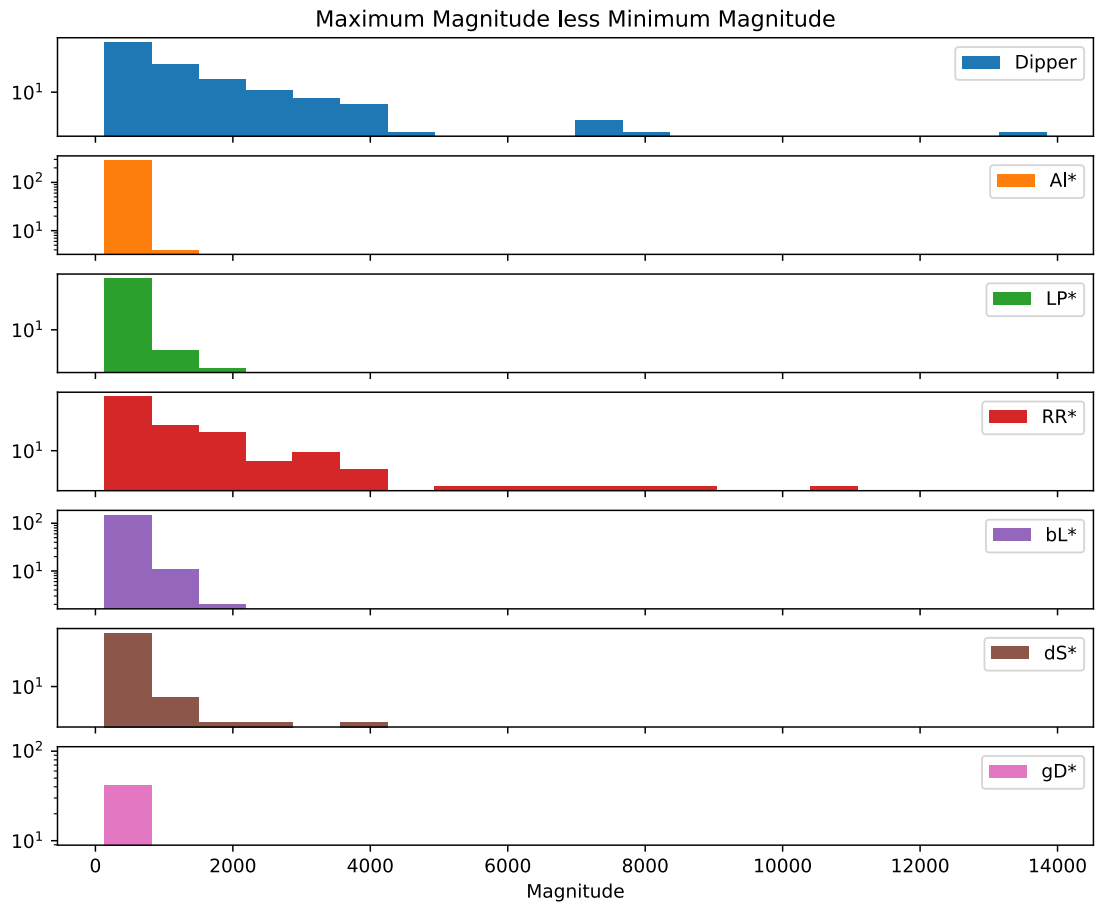


Figure 6.3: continued

BIBLIOGRAPHY

In:

- ALMA Partnership et al. (2015). "The 2014 ALMA Long Baseline Campaign: First Results from High Angular Resolution Observations toward the HL Tau Region." In: *ApJ* 808, L3, p. L3. DOI: [10.1088/2041-8205/808/1/L3](https://doi.org/10.1088/2041-8205/808/1/L3). arXiv: [1503.02649](https://arxiv.org/abs/1503.02649) [astro-ph.SR].
- Abramowitz, M. and I.A. Stegun (1964). *Handbook of Mathematical Functions*. Fifth. Dover: New York.
- Aigrain, S., S. T. Hodgkin, M. J. Irwin, J. R. Lewis, and S. J. Roberts (2015). "Precise time series photometry for the Kepler-2.0 mission." In: *Monthly Notices of the Royal Astronomical Society* 447(3), pp. 2880–2893. ISSN: 0035-8711. DOI: [10.1093/mnras/stu2638](https://doi.org/10.1093/mnras/stu2638). URL: <http://mnras.oxfordjournals.org/content/447/3/2880>.
- Aigrain, Suzanne, Hannu Parviainen, and Benjamin Pope (2016). "K2SC: Flexible systematics correction and detrending of K2 light curves using Gaussian Process regression." In: DOI: [10.1093/mnras/stw706](https://doi.org/10.1093/mnras/stw706). arXiv: [1603.09167](https://arxiv.org/abs/1603.09167). URL: <http://arxiv.org/abs/1603.09167><http://dx.doi.org/10.1093/mnras/stw706>.
- Akeson, R. L. et al. (2013a). "The NASA Exoplanet Archive: Data and Tools for Exoplanet Research." In: *PASP* 125, p. 989. DOI: [10.1086/672273](https://doi.org/10.1086/672273). arXiv: [1307.2944](https://arxiv.org/abs/1307.2944) [astro-ph.IM].
- Akeson, R. L. et al. (2013b). "The NASA Exoplanet Archive: Data and Tools for Exoplanet Research." In: *PASP* 125, p. 989. DOI: [10.1086/672273](https://doi.org/10.1086/672273). arXiv: [1307.2944](https://arxiv.org/abs/1307.2944) [astro-ph.IM].
- Alencar, S. H. P., P. S. Teixeira, M. M. Guimaraes, P. T. McGinnis, J. F. Gameiro, J. Bouvier, S. Aigrain, E. Flaccomio, and F. Favata (2010). "Accretion dynamics and disk evolution in NGC 2264: a study based on the Corot photometric observations." In: DOI: [10.1051/0004-6361/201014184](https://doi.org/10.1051/0004-6361/201014184). arXiv: [1005.4384](https://arxiv.org/abs/1005.4384). URL: <http://arxiv.org/abs/1005.4384><http://dx.doi.org/10.1051/0004-6361/201014184>.
- Alexander, R. D., C. J. Clarke, and J. E. Pringle (2006). "Photoevaporation of protoplanetary discs - I. Hydrodynamic models." In: *MNRAS* 369, pp. 216–228. DOI: [10.1111/j.1365-2966.2006.10293.x](https://doi.org/10.1111/j.1365-2966.2006.10293.x). eprint: [astro-ph/0603253](https://arxiv.org/abs/astro-ph/0603253).
- Anderson, D. R. et al. (2010). "WASP-31b: a low-density planet transiting a metal-poor, late-F-type dwarf star." In: DOI: [10.1051/0004-6361/201016208](https://doi.org/10.1051/0004-6361/201016208). arXiv: [1011.5882](https://arxiv.org/abs/1011.5882). URL: <http://arxiv.org/abs/1011.5882><http://dx.doi.org/10.1051/0004-6361/201016208>.
- Anglada-Escudé, Guillem, Bárbara Rojas-Ayala, Alan P Boss, Alycia J Weinberger, and James P Lloyd (2012). "GJ 1214b revised Improved trigonometric parallax, stellar parameters, orbital solution, and bulk properties for the super-Earth GJ 1214b." In: arXiv: [arXiv:1210.8087v3](https://arxiv.org/abs/1210.8087v3). URL: <https://arxiv.org/pdf/1210.8087.pdf>.
- Ansdell, M. et al. (2015). "Young "Dipper" Stars in Upper Sco and Rho Oph Observed by K2." In: p. 19. ISSN: 15384357. DOI: [10.3847/0004-637X/816/2/69](https://doi.org/10.3847/0004-637X/816/2/69). arXiv: [1510.08853](https://arxiv.org/abs/1510.08853). URL: <http://arxiv.org/abs/1510.08853>.
- Ansdell, M., E. Gaidos, J. P. Williams, G. Kennedy, M. C. Wyatt, D. M. LaCourse, T. L. Jacobs, and A. W. Mann (2016). "Dipper disks not inclined towards edge-on orbits." In: *MNRAS* 6(July), pp. 1–6. ISSN: 17453933. DOI: [10.1093/mnrasl/slw140](https://doi.org/10.1093/mnrasl/slw140). arXiv: [1607.03115](https://arxiv.org/abs/1607.03115). URL: <http://arxiv.org/abs/1607.03115>.
- Armitage, P. J. (2007). "Lecture notes on the formation and early evolution of planetary systems." In: *ArXiv Astrophysics e-prints*. eprint: [astro-ph/0701485](https://arxiv.org/abs/astro-ph/0701485).
- Armstrong, D. J. et al. (2015). "K2 Variable Catalogue II: Machine Learning Classification of Variable Stars and Eclipsing Binaries in K2 Fields 0-4." In: DOI: [10.1088/0000-0008/51/1/012001](https://doi.org/10.1088/0000-0008/51/1/012001).

- 1093/mnras/stv2836. arXiv: 1512.01246. URL: <http://arxiv.org/abs/1512.01246><http://dx.doi.org/10.1093/mnras/stv2836>.
- Armstrong, D. J. et al. (2016). “K2 variable catalogue - II. Machine learning classification of variable stars and eclipsing binaries in K2 fields 0-4.” In: *MNRAS* 456, pp. 2260–2272. DOI: [10.1093/mnras/stv2836](https://doi.org/10.1093/mnras/stv2836). arXiv: 1512.01246 [astro-ph.SR].
- Baglin, Annie and G. Hébrard Vauclair (2000). “The space stellar photometry mission COROT: Asteroseismology and search for extrasolar planets.” In: *Journal of Astrophysics and Astronomy* 21(3), pp. 319–322. ISSN: 0973-7758. DOI: [10.1007/BF02702417](https://doi.org/10.1007/BF02702417). URL: <http://dx.doi.org/10.1007/BF02702417>.
- Bakos, G. Á. et al. (2007). “HAT-P-1b: A Large-Radius, Low-Density Exoplanet Transiting One Member of a Stellar Binary.” In: *ApJ* 656, pp. 552–559. DOI: [10.1086/509874](https://doi.org/10.1086/509874). eprint: [astro-ph/0609369](https://arxiv.org/abs/astro-ph/0609369).
- Bakos, G. Á. et al. (2010). “HAT-P-11b: A SUPER-NEPTUNE PLANET TRANSITING A BRIGHT K STAR IN THE <i>KEPLER</i> FIELD.” In: *The Astrophysical Journal* 710(2), pp. 1724–1745. ISSN: 0004-637X. DOI: [10.1088/0004-637X/710/2/1724](https://doi.org/10.1088/0004-637X/710/2/1724). URL: <http://stacks.iop.org/0004-637X/710/i=2/a=1724?key=crossref.df7c8f80b81d64756b8d5f50f628122a>.
- Barber, R. J., J. Tennyson, G. J. Harris, and R. N. Tolchenov (2006). “A high-accuracy computed water line list.” In: *MNRAS* 368, pp. 1087–1094. DOI: [10.1111/j.1365-2966.2006.10184.x](https://doi.org/10.1111/j.1365-2966.2006.10184.x). eprint: [astro-ph/0601236](https://arxiv.org/abs/astro-ph/0601236).
- Barsony, M., K. E. Haisch, K. A. Marsh, and C. McCarthy (2012). “A Significant Population of Candidate New Members of the ρ Ophiuchi Cluster.” In: *Astrophysical Journal* 751, 22, p. 22. DOI: [10.1088/0004-637X/751/1/22](https://doi.org/10.1088/0004-637X/751/1/22). arXiv: 1206.4552 [astro-ph.GA].
- Barstow, J. K., S. Aigrain, P. G. J. Irwin, and D. K. Sing (2017). “A Consistent Retrieval Analysis of 10 Hot Jupiters Observed in Transmission.” In: *ApJ* 834, 50, p. 50. DOI: [10.3847/1538-4357/834/1/50](https://doi.org/10.3847/1538-4357/834/1/50). arXiv: 1610.01841 [astro-ph.EP].
- Batalha, N. M. et al. (2013). “Planetary Candidates Observed by Kepler. III. Analysis of the First 16 Months of Data.” In: *ApJS* 204, 24, p. 24. DOI: [10.1088/0067-0049/204/2/24](https://doi.org/10.1088/0067-0049/204/2/24). arXiv: 1202.5852 [astro-ph.EP].
- Batygin, K., P. H. Bodenheimer, and G. P. Laughlin (2016). “In Situ Formation and Dynamical Evolution of Hot Jupiter Systems.” In: *ApJ* 829, 114, p. 114. DOI: [10.3847/0004-637X/829/2/114](https://doi.org/10.3847/0004-637X/829/2/114). arXiv: 1511.09157 [astro-ph.EP].
- Bean, J. L., J.-M. Désert, A. Seifahrt, N. Madhusudhan, I. Chilingarian, D. Homeier, and A. Szentgyorgyi (2013). “Ground-based Transit Spectroscopy of the Hot-Jupiter WASP-19b in the Near-infrared.” In: *ApJ* 771, 108, p. 108. DOI: [10.1088/0004-637X/771/2/108](https://doi.org/10.1088/0004-637X/771/2/108). arXiv: 1303.1094 [astro-ph.EP].
- Berta, Z. K., J. Irwin, and D. Charbonneau (2013). “Constraints on Planet Occurrence around Nearby Mid-to-late M Dwarfs from the MEARTH Project.” In: *ApJ* 775, 91, p. 91. DOI: [10.1088/0004-637X/775/2/91](https://doi.org/10.1088/0004-637X/775/2/91). arXiv: 1307.3178 [astro-ph.EP].
- Berta, Z. K., D. Charbonneau, J. Désert, E. M. Miller-Ricci Kempton, P. R. McCullough, C. J. Burke, J. J. Fortney, J. Irwin, P. Nutzman, and D. Homeier (2012). “The Flat Transmission Spectrum of the Super-Earth GJ1214b from Wide Field Camera 3 on the Hubble Space Telescope.” In: *The Astrophysical Journal* 747, p. 35. ISSN: 1538-4357. DOI: [10.1088/0004-637X/747/1/35](https://doi.org/10.1088/0004-637X/747/1/35). arXiv: 1111.5621. URL: [http://adsabs.harvard.edu/cgi-bin/nph-data{_}query?bibcode=2012ApJ...747...35B{\&}link{_}type=ABSTRACT\\$\backslash\\$npapers://0be24a46-325a-4116-a3c6-fd8a3b614472/Paper/p11957](http://adsabs.harvard.edu/cgi-bin/nph-data{_}query?bibcode=2012ApJ...747...35B{\&}link{_}type=ABSTRACT\backslashnpapers://0be24a46-325a-4116-a3c6-fd8a3b614472/Paper/p11957).
- Birkby, J. L., R. J. de Kok, M. Brogi, E. J. W. de Mooij, H. Schwarz, S. Albrecht, and I. A. G. Snellen (2013). “Detection of water absorption in the day side atmosphere of HD 189733 b using ground-based high-resolution spectroscopy at 3.2 μ m.” In: *MNRAS* 436, pp. L35–L39. DOI: [10.1093/mnrasl/slt107](https://doi.org/10.1093/mnrasl/slt107). arXiv: 1307.1133 [astro-ph.EP].
- Birnstiel, T., M. Fang, and A. Johansen (2016). “Dust Evolution and the Formation of Planetesimals.” In: *Space Sci. Rev.* 205, pp. 41–75. DOI: [10.1007/s11214-016-0256-1](https://doi.org/10.1007/s11214-016-0256-1). arXiv: 1604.02952 [astro-ph.SR].

- Blecic, J., J. Harrington, and M. O. Bowman (2016). “B.” In: *ApJS* 225, 4, p. 4. DOI: [10.3847/0067-0049/225/1/4](https://doi.org/10.3847/0067-0049/225/1/4). arXiv: [1505.06392](https://arxiv.org/abs/1505.06392) [astro-ph.IM].
- Bloom, J S et al. (2011). “Automating Discovery and Classification of Transients and Variable Stars in the Synoptic Survey Era.” In: arXiv: [arXiv:1106.5491v1](https://arxiv.org/abs/1106.5491v1).
- Bodman, EvaH.L., AliceC. Quillen, Megan Ansdell, Michael Hippke, TabethaS. Boyajian, EricE. Mamajek, EricG. Blackman, Aaron Rizzuto, and Joel H. Kastner (2016). “Dippers and Dusty Disks Edges: A Unified Model.” In: *eprint arXiv:1605.03985*. URL: <http://adsabs.harvard.edu/abs/2016arXiv160503985B>.
- Bohlin, R. C. and A. U. Landolt (2015). “The CALSPEC Stars P177D and P330E.” In: *AJ* 149, 122, p. 122. DOI: [10.1088/0004-6256/149/4/122](https://doi.org/10.1088/0004-6256/149/4/122). arXiv: [1502.01754](https://arxiv.org/abs/1502.01754) [astro-ph.IM].
- Bonfils, X. et al. (2012). “A hot Uranus transiting the nearby M dwarf GJ3470. Detected with HARPS velocimetry. Captured in transit with TRAPPIST photometry.” In: DOI: [10.1051/0004-6361/201219623](https://doi.org/10.1051/0004-6361/201219623). arXiv: [1206.5307](https://arxiv.org/abs/1206.5307). URL: <http://arxiv.org/abs/1206.5307><http://dx.doi.org/10.1051/0004-6361/201219623>.
- Bonifacio, P., E. Caffau, H.-G. Ludwig, and M. Steffen (2011). “LTE model atmospheres MARCS, ATLAS and CO5BOLD.” In: *ArXiv e-prints*. arXiv: [1109.0717](https://arxiv.org/abs/1109.0717) [astro-ph.SR].
- Bouvier, J. et al. (2003). “Eclipses by circumstellar material in the T Tauri star AA Tau. II. Evidence for non-stationary magnetospheric accretion.” In: *Astronomy and Astrophysics, v.409, p.169-192 (2003)* 409, pp. 169–192. ISSN: 0004-6361. DOI: [10.1051/0004-6361:20030938](https://doi.org/10.1051/0004-6361:20030938). arXiv: [0306551](https://arxiv.org/abs/0306551) [astro-ph]. URL: <http://arxiv.org/abs/astro-ph/0306551><http://dx.doi.org/10.1051/0004-6361:20030938>.
- Boyajian, T. et al. (2015). “Stellar diameters and temperatures - VI. High angular resolution measurements of the transiting exoplanet host stars HD 189733 and HD 209458 and implications for models of cool dwarfs.” In: *MNRAS* 447, pp. 846–857. DOI: [10.1093/mnras/stu2502](https://doi.org/10.1093/mnras/stu2502). arXiv: [1411.5638](https://arxiv.org/abs/1411.5638) [astro-ph.SR].
- Boyajian, Tabetha S et al. (2008). “Interferometric Measurements with the CHARA Array.” In: arXiv: [arXiv:0804.2719v2](https://arxiv.org/abs/0804.2719v2). URL: <https://arxiv.org/pdf/0804.2719.pdf>.
- Braun, Kaspar von et al. (2011). “55 Cancri: Stellar Astrophysical Parameters, a Planet in the Habitable Zone, and Implications for the Radius of a Transiting Super-Earth.” In: DOI: [10.1088/0004-637X/740/1/49](https://doi.org/10.1088/0004-637X/740/1/49). arXiv: [1106.1152](https://arxiv.org/abs/1106.1152). URL: <http://arxiv.org/abs/1106.1152><http://dx.doi.org/10.1088/0004-637X/740/1/49>.
- Broggi, M., I. A. G. Snellen, R. J. de Kok, S. Albrecht, J. Birkby, and E. J. W. de Mooij (2012). “The signature of orbital motion from the dayside of the planet τ Boötis b.” In: *Nature* 486, pp. 502–504. DOI: [10.1038/nature11161](https://doi.org/10.1038/nature11161). arXiv: [1206.6109](https://arxiv.org/abs/1206.6109) [astro-ph.EP].
- Buenzli, E., D. Saumon, M. S. Marley, D. Apai, J. Radigan, L. R. Bedin, I. N. Reid, and C. V. Morley (2015). “Cloud Structure of the Nearest Brown Dwarfs: Spectroscopic Variability of Luhman 16AB from the Hubble Space Telescope.” In: *Astrophysical Journal* 798, 127, p. 127. DOI: [10.1088/0004-637X/798/2/127](https://doi.org/10.1088/0004-637X/798/2/127). arXiv: [1411.0003](https://arxiv.org/abs/1411.0003) [astro-ph.SR].
- Burke, C. J. et al. (2015). “Terrestrial Planet Occurrence Rates for the Kepler GK Dwarf Sample.” In: *ApJ* 809, 8, p. 8. DOI: [10.1088/0004-637X/809/1/8](https://doi.org/10.1088/0004-637X/809/1/8). arXiv: [1506.04175](https://arxiv.org/abs/1506.04175) [astro-ph.EP].
- Cameron, A. Collier et al. (2007). “WASP-1b and WASP-2b: two new transiting exoplanets detected with SuperWASP and SOPHIE.” In: *Monthly Notices of the Royal Astronomical Society* 375(3), pp. 951–957. ISSN: 1365-2966. DOI: [10.1111/j.1365-2966.2006.11350.x](https://doi.org/10.1111/j.1365-2966.2006.11350.x). URL: <http://dx.doi.org/10.1111/j.1365-2966.2006.11350.x>.
- Cardelli, Jason A., Geoffrey C. Clayton, and John S. Mathis (1989). “The relationship between infrared, optical, and ultraviolet extinction.” In: *The Astrophysical Journal* 345, p. 245. ISSN: 0004-637X. DOI: [10.1086/167900](https://doi.org/10.1086/167900). URL: <http://adsabs.harvard.edu/doi/10.1086/167900>.

- Carlos Rodrigo Enrique Solano, Amelia Bayo (2012). *SVO Filter Profile Service Version 1.0*. URL: <http://ivoa.net/documents/Notes/SVOFPS/index.html>.
- Carpenter, John M., Eric E. Mamajek, Lynne A. Hillenbrand, and Michael R. Meyer (2006). "Evidence for Mass-dependent Circumstellar Disk Evolution in the 5 Myr Old Upper Scorpius OB Association." In: *The Astrophysical Journal* 651(1), pp. L49–L52. ISSN: 0004-637X. DOI: [10.1086/509121](https://doi.org/10.1086/509121). URL: <http://stacks.iop.org/1538-4357/651/i=1/a=L49>.
- Casagrande, Luca, Laura Portinari, and Chris Flynn (2006). "Accurate fundamental parameters for Lower Main Sequence Stars." In: *Mon. Not. R. Astron. Soc* 000(0000), pp. 0–0. arXiv: [0608504v1](https://arxiv.org/abs/0608504v1) [arXiv:astro-ph]. URL: <https://arxiv.org/pdf/astro-ph/0608504.pdf>.
- Cassan, A. et al. (2012). "One or more bound planets per Milky Way star from microlensing observations." In: *Nature* 481(7380), pp. 167–169. ISSN: 0028-0836. DOI: [10.1038/nature10684](https://doi.org/10.1038/nature10684). URL: <http://www.nature.com/doi/10.1038/nature10684>.
- Chamberlain, J. W. (1978). *Theory of planetary atmospheres : an introduction to their physics and chemistry*.
- Chan, Tucker, Mikael Ingemyr, Joshua N. Winn, Matthew J. Holman, Roberto Sanchis-Ojeda, Gil Esquerdo, and Mark Everett (2011). "The Transit Light Curve project. XIV. Confirmation of Anomalous Radii for the Exoplanets TrES-4b, HAT-P-3b, and WASP-12b." In: DOI: [10.1088/0004-6256/141/6/179](https://doi.org/10.1088/0004-6256/141/6/179). arXiv: [1103.3078](https://arxiv.org/abs/1103.3078). URL: <http://arxiv.org/abs/1103.3078><http://dx.doi.org/10.1088/0004-6256/141/6/179>.
- Charbonneau, D. et al. (2009). "A super-Earth transiting a nearby low-mass star." In: *Nature* 462, pp. 891–894. DOI: [10.1038/nature08679](https://doi.org/10.1038/nature08679). arXiv: [0912.3229](https://arxiv.org/abs/0912.3229) [astro-ph.EP].
- Charbonneau, David, Timothy M. Brown, Robert W. Noyes, and Ronald L. Gilliland (2001). "Detection of an Extrasolar Planet Atmosphere." In: DOI: [10.1086/338770](https://doi.org/10.1086/338770). arXiv: [0111544](https://arxiv.org/abs/0111544) [astro-ph]. URL: <http://arxiv.org/abs/astro-ph/0111544><http://dx.doi.org/10.1086/338770>.
- Chazelas, B. et al. (2012). "NGTS: a robotic transit survey to detect Neptune and super-Earth mass planets." In: *Ground-based and Airborne Telescopes IV*. Vol. 8444. Proc. SPIE, 84440E. DOI: [10.1117/12.925755](https://doi.org/10.1117/12.925755).
- Chen, J. and D. Kipping (2017). "Probabilistic Forecasting of the Masses and Radii of Other Worlds." In: *ApJ* 834, 17, p. 17. DOI: [10.3847/1538-4357/834/1/17](https://doi.org/10.3847/1538-4357/834/1/17). arXiv: [1603.08614](https://arxiv.org/abs/1603.08614) [astro-ph.EP].
- Cody, Ann Marie et al. (2014). "CSI 2264: SIMULTANEOUS OPTICAL AND INFRARED LIGHT CURVES OF YOUNG DISK-BEARING STARS IN NGC 2264 WITH CoRoT and SPITZER EVIDENCE FOR MULTIPLE ORIGINS OF VARIABILITY." In: *The Astronomical Journal* 147(4), p. 82. ISSN: 0004-6256. DOI: [10.1088/0004-6256/147/4/82](https://doi.org/10.1088/0004-6256/147/4/82). arXiv: [1401.6582](https://arxiv.org/abs/1401.6582). URL: <http://arxiv.org/abs/1401.6582>.
- Coughlin, J. L. et al. (2014). "Contamination in the Kepler Field. Identification of 685 KOIs as False Positives via Ephemeris Matching Based on Q1–Q12 Data." In: *AJ* 147, 119, p. 119. DOI: [10.1088/0004-6256/147/5/119](https://doi.org/10.1088/0004-6256/147/5/119). arXiv: [1401.1240](https://arxiv.org/abs/1401.1240) [astro-ph.IM].
- Crossfield, I. J. M., T. Barman, B. M. S. Hansen, and A. W. Howard (2013). "Warm ice giant GJ 3470b. I. A flat transmission spectrum indicates a hazy, low-methane, and/or metal-rich atmosphere." In: *A&A* 559, A33, A33. DOI: [10.1051/0004-6361/201322278](https://doi.org/10.1051/0004-6361/201322278). arXiv: [1308.6580](https://arxiv.org/abs/1308.6580) [astro-ph.EP].
- Cubillos, P. E. (2016). "Characterizing Exoplanet Atmospheres: From Light-curve Observations to Radiative-transfer Modeling." In: *ArXiv e-prints*. arXiv: [1604.01320](https://arxiv.org/abs/1604.01320) [astro-ph.EP].
- Cubillos, P., J. Harrington, J. Blečić, M. M. Stemm, N. B. Lust, A. S. Foster, P. M. Rojo, and T. J. Loredo (2014). "Bayesian Atmospheric Radiative Transfer (BART): Model, Statistics Driver, and Application to HD 209458b." In: *AAS/Division for Planetary Sciences Meeting Abstracts*. Vol. 46. AAS/Division for Planetary Sciences Meeting Abstracts, p. 111.06.

- Dahm, S. E. and S. E. (2008). “The Young Cluster and Star Forming Region NGC 2264.” In: *Handbook of Star Forming Regions, Volume I: The Northern Sky ASP Monograph Publications, Vol. 4. Edited by Bo Reipurth, p.966 4, p. 966.* arXiv: 0808.3835. URL: <http://arxiv.org/abs/0808.3835>.
- Decin, L., P. W. Morris, P. N. Appleton, V. Charmandaris, L. Armus, and J. R. Houck (2004). “MARCS: Model Stellar Atmospheres and Their Application to the Photometric Calibration of the Spitzer Space Telescope Infrared Spectrograph (IRS).” In: *ApJS* 154, pp. 408–412. DOI: 10.1086/422884. eprint: astro-ph/0406104.
- Deming, D. et al. (2013a). “Infrared Transmission Spectroscopy of the Exoplanets HD 209458b and XO-1b Using the Wide Field Camera-3 on the Hubble Space Telescope.” In: *ApJ* 774, 95, p. 95. DOI: 10.1088/0004-637X/774/2/95. arXiv: 1302.1141 [astro-ph.EP].
- Deming, D. et al. (2013b). “Infrared Transmission Spectroscopy of the Exoplanets HD 209458b and XO-1b Using the Wide Field Camera-3 on the Hubble Space Telescope.” In: *Astrophysical Journal* 774, 95, p. 95. DOI: 10.1088/0004-637X/774/2/95. arXiv: 1302.1141 [astro-ph.EP].
- Demory, B.-O. et al. (2013). “Inference of Inhomogeneous Clouds in an Exoplanet Atmosphere.” In: *ApJ* 776, L25, p. L25. DOI: 10.1088/2041-8205/776/2/L25. arXiv: 1309.7894 [astro-ph.EP].
- Dodson-Robinson, S. E., D. Veras, E. B. Ford, and C. A. Beichman (2009). “The Formation Mechanism of Gas Giants on Wide Orbits.” In: *ApJ* 707, pp. 79–88. DOI: 10.1088/0004-637X/707/1/79. arXiv: 0909.2662 [astro-ph.EP].
- Dong, S. and Z. Zhu (2013). “Fast Rise of “Neptune-size” Planets (4–8 R_J) from P 10 to 250 Days Statistics of Kepler Planet Candidates up to 0.75 AU.” In: *ApJ* 778, 53, p. 53. DOI: 10.1088/0004-637X/778/1/53. arXiv: 1212.4853 [astro-ph.EP].
- Dressel, L. (2014). *Wide Field Camera 3 Instrument Handbook, Version 6.0.*
- Dubath, P. et al. (2011). “Random forest automated supervised classification of Hipparcos periodic variable stars.” In: DOI: 10.1111/j.1365-2966.2011.18575.x. arXiv: 1101.2406. URL: <http://arxiv.org/abs/1101.2406><http://dx.doi.org/10.1111/j.1365-2966.2011.18575.x>.
- Eastman, J., B. S. Gaudi, and E. Agol (2013). “EXOFAST: A Fast Exoplanetary Fitting Suite in IDL.” In: *PASP* 125, pp. 83–112. DOI: 10.1086/669497. arXiv: 1206.5798 [astro-ph.IM].
- Ehrenreich, D., X. Bonfils, C. Lovis, X. Delfosse, T. Forveille, M. Mayor, V. Neves, N. C. Santos, S. Udry, and D. Ségransan (2014). “Near-infrared transmission spectrum of the warm-Uranus GJ 3470b with the Wide Field Camera-3 on the Hubble Space Telescope.” In: *A&A* 570, A89, A89. DOI: 10.1051/0004-6361/201423809. arXiv: 1405.1056 [astro-ph.EP].
- Eisner, J. A., L. A. Hillenbrand, R. J. White, J. S. Bloom, R. L. Akeson, and C. H. Blake (2007). “Near-Infrared Interferometric, Spectroscopic, and Photometric Monitoring of T Tauri Inner Disks.” In: DOI: 10.1086/521874. arXiv: 0707.3833. URL: <http://arxiv.org/abs/0707.3833><http://dx.doi.org/10.1086/521874>.
- Esposito, M. et al. (2014). “The GAPS Programme with HARPS-N at TNG. III: The retrograde orbit of HAT-P-18b.” In: *Astronomy & Astrophysics, Volume 564, id.L13, 5 pp.* 564. ISSN: 0004-6361. DOI: 10.1051/0004-6361/201423735. arXiv: 1403.6728. URL: <http://arxiv.org/abs/1403.6728><http://dx.doi.org/10.1051/0004-6361/201423735>.
- Evans, T. M., D. K. Sing, H. R. Wakeford, N. Nikolov, G. E. Ballester, B. Drummond, T. Kataria, N. P. Gibson, D. S. Amundsen, and J. Spake (2016). “Detection of H₂O and Evidence for TiO/VO in an Ultra-hot Exoplanet Atmosphere.” In: *ApJ* 822, L4, p. L4. DOI: 10.3847/2041-8205/822/1/L4. arXiv: 1604.02310 [astro-ph.EP].
- Faedi, F. et al. (2011). “WASP-39b: a highly inflated Saturn-mass planet orbiting a late G-type star.” In: DOI: 10.1051/0004-6361/201116671. arXiv: 1102.1375. URL: <http://arxiv.org/abs/1102.1375><http://dx.doi.org/10.1051/0004-6361/201116671>.

- Faure, A., L. Wiesenfeld, B.J. Drouin, and J. Tennyson (2013). "Pressure broadening of water and carbon monoxide transitions by molecular hydrogen at high temperatures." In: *Journal of Quantitative Spectroscopy and Radiative Transfer* 116, pp. 79–86. ISSN: 0022-4073. DOI: <http://dx.doi.org/10.1016/j.jqsrt.2012.09.015>. URL: <http://www.sciencedirect.com/science/article/pii/S0022407312004268>.
- Fischer, J., R.R. Gamache, A. Goldman, L.S. Rothman, and A. Perrin (2003). "Total internal partition sums for molecular species in the 2000 edition of the {HITRAN} database." In: *Journal of Quantitative Spectroscopy and Radiative Transfer* 82(1?4). The {HITRAN} Molecular Spectroscopic Database: Edition of 2000 Including Updates of 2001., pp. 401–412. ISSN: 0022-4073. DOI: [http://dx.doi.org/10.1016/S0022-4073\(03\)00166-3](http://dx.doi.org/10.1016/S0022-4073(03)00166-3). URL: <http://www.sciencedirect.com/science/article/pii/S0022407303001663>.
- Fischer, P. D. et al. (2016). "HST Hot-Jupiter Transmission Spectral Survey: Clear Skies for Cool Saturn WASP-39b." In: *ApJ* 827, 19, p. 19. DOI: [10.3847/0004-637X/827/1/19](https://doi.org/10.3847/0004-637X/827/1/19). arXiv: [1601.04761](https://arxiv.org/abs/1601.04761) [astro-ph.EP].
- Flock, M., J. P. Ruge, N. Dzyurkevich, T. Henning, H. Klahr, and S. Wolf (2015). "Gaps, rings, and non-axisymmetric structures in protoplanetary disks. From simulations to ALMA observations." In: *A&A* 574, A68, A68. DOI: [10.1051/0004-6361/201424693](https://doi.org/10.1051/0004-6361/201424693). arXiv: [1411.2736](https://arxiv.org/abs/1411.2736) [astro-ph.EP].
- Foreman-Mackey, D., D. W. Hogg, and T. D. Morton (2014). "Exoplanet Population Inference and the Abundance of Earth Analogs from Noisy, Incomplete Catalogs." In: *ApJ* 795, 64, p. 64. DOI: [10.1088/0004-637X/795/1/64](https://doi.org/10.1088/0004-637X/795/1/64). arXiv: [1406.3020](https://arxiv.org/abs/1406.3020) [astro-ph.EP].
- Fraine, J., D. Deming, B. Benneke, H. Knutson, A. Jordán, N. Espinoza, N. Madhusudhan, A. Wilkins, and K. Todorov (2014). "Water vapour absorption in the clear atmosphere of a Neptune-sized exoplanet." In: *Nature* 513, pp. 526–529. DOI: [10.1038/nature13785](https://doi.org/10.1038/nature13785). arXiv: [1409.8349](https://arxiv.org/abs/1409.8349) [astro-ph.EP].
- Freedman, R. S., M. S. Marley, and K. Lodders (2008). "Line and Mean Opacities for Ultracool Dwarfs and Extrasolar Planets." In: *Astrophysical Journal, Supplement* 174, pp. 504–513. DOI: [10.1086/521793](https://doi.org/10.1086/521793). arXiv: [0706.2374](https://arxiv.org/abs/0706.2374).
- Freedman, R. S., J. Lustig-Yaeger, J. J. Fortney, R. E. Lupu, M. S. Marley, and K. Lodders (2014). "Gaseous Mean Opacities for Giant Planet and Ultracool Dwarf Atmospheres over a Range of Metallicities and Temperatures." In: *Astrophysical Journal, Supplement* 214, 25, p. 25. DOI: [10.1088/0067-0049/214/2/25](https://doi.org/10.1088/0067-0049/214/2/25). arXiv: [1409.0026](https://arxiv.org/abs/1409.0026) [astro-ph.EP].
- Fressin, F., G. Torres, D. Charbonneau, S. T. Bryson, J. Christiansen, C. D. Dressing, J. M. Jenkins, L. M. Walkowicz, and N. M. Batalha (2013). "The False Positive Rate of Kepler and the Occurrence of Planets." In: *ApJ* 766, 81, p. 81. DOI: [10.1088/0004-637X/766/2/81](https://doi.org/10.1088/0004-637X/766/2/81). arXiv: [1301.0842](https://arxiv.org/abs/1301.0842) [astro-ph.EP].
- Freytag, B., M. Steffen, H. G. Ludwig, S. Wedemeyer-Böhm, W. Schaffnerberger, and O. Steiner (2012). "Simulations of Stellar Convection with CO5BOLD." In: *J. Comput. Phys.* 231(3), pp. 919–959. ISSN: 0021-9991. DOI: [10.1016/j.jcp.2011.09.026](https://doi.org/10.1016/j.jcp.2011.09.026). URL: <http://dx.doi.org/10.1016/j.jcp.2011.09.026>.
- Gamache, R. R., A. L. Laraia, and J. Lamouroux (2011). "Half-widths, their temperature dependence, and line shifts for the HDO-CO₂ collision system for applications to CO₂-rich planetary atmospheres." In: *Icarus* 213, pp. 720–730. DOI: [10.1016/j.icarus.2011.03.021](https://doi.org/10.1016/j.icarus.2011.03.021).
- Gamache, R. R., R. Lynch, J. J. Plateaux, and A. Barbe (1997). "Halfwidths and line shifts of water vapor broadened by CO₂: measurements and complex Robert-Bonamy formalism calculations." In: *J. Quant. Spec. Radiat. Transf.* 57, pp. 485–496. DOI: [10.1016/S0022-4073\(96\)00148-3](https://doi.org/10.1016/S0022-4073(96)00148-3).
- Gamache, Robert R., Richard Lynch, and Steven P. Neshyba (1998). "New developments in the theory of pressure-broadening and pressure-shifting of spectral lines of H₂O: The complex Robert-Bonamy formalism." In: *Journal of Quantitative Spectroscopy and Radiative Transfer* 59(3?5). Atmospheric Spectroscopy Applications 96, pp. 319–335. ISSN: 0022-4073. DOI: <http://dx.doi.org/10.1016/S0022->

- 4073(97)00123-4. URL: <http://www.sciencedirect.com/science/article/pii/S0022407397001234>.
- Gamache, Robert R., Julien Lamouroux, Anne L. Laraia, Jean-Michel Hartmann, and Christian Boulet (2012). "Semiclassical calculations of half-widths and line shifts for transitions in the 30012?00001 and 30013?00001 bands of CO₂, I: Collisions with {N₂}" In: *Journal of Quantitative Spectroscopy and Radiative Transfer* 113(11). Three Leaders in Spectroscopy, pp. 976–990. ISSN: 0022-4073. DOI: <http://dx.doi.org/10.1016/j.jqsrt.2012.02.014>. URL: <http://www.sciencedirect.com/science/article/pii/S0022407312000738>.
- Gilliland, R. L. et al. (2010). "Kepler Asteroseismology Program: Introduction and First Results." In: *PASP* 122, p. 131. DOI: [10.1086/650399](https://doi.org/10.1086/650399). arXiv: [1001.0139](https://arxiv.org/abs/1001.0139) [astro-ph.SR].
- Gillon, M., E. Jehin, L. Delrez, P. Magain, C. Opitom, and S. Sohy (2013). "SPECULOOS: Search for habitable Planets Eclipsing ULtra-cOOl Stars." In: *Protostars and Planets VI Posters*.
- Gillon, M. et al. (2017). "Seven temperate terrestrial planets around the nearby ultracool dwarf star TRAPPIST-1." In: *Nature* 542, pp. 456–460. DOI: [10.1038/nature21360](https://doi.org/10.1038/nature21360). arXiv: [1703.01424](https://arxiv.org/abs/1703.01424) [astro-ph.EP].
- Grimm, S. L. and K. Heng (2015). "HELIOS-K: An Ultrafast, Open-source Opacity Calculator for Radiative Transfer." In: *ArXiv e-prints*. arXiv: [1503.03806](https://arxiv.org/abs/1503.03806) [astro-ph.EP].
- Gustafsson, B., B. Edvardsson, K. Eriksson, U. G. Jørgensen, Å. Nordlund, and B. Plez (2008). "A grid of MARCS model atmospheres for late-type stars. I. Methods and general properties." In: *A&A* 486, pp. 951–970. DOI: [10.1051/0004-6361:200809724](https://doi.org/10.1051/0004-6361/200809724). arXiv: [0805.0554](https://arxiv.org/abs/0805.0554).
- Harris, G. J., J. Tennyson, B. M. Kaminsky, Y. V. Pavlenko, and H. R. A. Jones (2006). "Improved HCN/HNC linelist, model atmospheres and synthetic spectra for WZ Cas." In: *MNRAS* 367, pp. 400–406. DOI: [10.1111/j.1365-2966.2005.09960.x](https://doi.org/10.1111/j.1365-2966.2005.09960.x). eprint: [astro-ph/0512363](https://arxiv.org/abs/astro-ph/0512363).
- Hartman, J. D. and G. Á. Bakos (2016). "VARTOOLS: A program for analyzing astronomical time-series data." In: *Astronomy and Computing* 17, pp. 1–72. DOI: [10.1016/j.ascom.2016.05.006](https://doi.org/10.1016/j.ascom.2016.05.006). arXiv: [1605.06811](https://arxiv.org/abs/1605.06811) [astro-ph.IM].
- Hartman, J. D. et al. (2010). "HAT-P-26b: A Low-Density Neptune-Mass Planet Transiting a K Star." In: DOI: [10.1088/0004-637X/728/2/138](https://doi.org/10.1088/0004-637X/728/2/138). arXiv: [1010.1008](https://arxiv.org/abs/1010.1008).
- Hartman, J. D. et al. (2011). "HAT-P-32b and HAT-P-33b: Two Highly Inflated Hot Jupiters Transiting High-Jitter Stars." In: DOI: [10.1088/0004-637X/742/1/59](https://doi.org/10.1088/0004-637X/742/1/59). arXiv: [1106.1212](https://arxiv.org/abs/1106.1212). URL: <http://arxiv.org/abs/1106.1212><http://dx.doi.org/10.1088/0004-637X/742/1/59>.
- Hartmann, Lee and Scott J. Kenyon (1996). "THE FU ORIONIS PHENOMENON ¹." In: *Annual Review of Astronomy and Astrophysics* 34(1), pp. 207–240. ISSN: 0066-4146. DOI: [10.1146/annurev.astro.34.1.207](https://doi.org/10.1146/annurev.astro.34.1.207). URL: <http://www.annualreviews.org/doi/10.1146/annurev.astro.34.1.207>.
- Haynes, K., A. M. Mandell, E. Sinukoff, N. Madhusudhan, A. Burrows, and D. Deming (2014). "Exoplanet Transit Spectroscopy of Hot Jupiters Using HST/WFC₃." In: *Exploring the Formation and Evolution of Planetary Systems*. Ed. by M. Booth, B. C. Matthews, and J. R. Graham. Vol. 299. IAU Symposium, pp. 266–270. DOI: [10.1017/S1743921313008533](https://doi.org/10.1017/S1743921313008533).
- Haynes, K., A. M. Mandell, N. Madhusudhan, D. Deming, and H. Knutson (2015). "Spectroscopic Evidence for a Temperature Inversion in the Dayside Atmosphere of Hot Jupiter WASP-33b." In: *ApJ* 806, 146, p. 146. DOI: [10.1088/0004-637X/806/2/146](https://doi.org/10.1088/0004-637X/806/2/146). arXiv: [1505.01490](https://arxiv.org/abs/1505.01490) [astro-ph.EP].
- Hebrard, G. et al. (2012). "WASP-52b, WASP-58b, WASP-59b, and WASP-60b: four new transiting close-in giant planets." In: DOI: [10.1051/0004-6361/201220363](https://doi.org/10.1051/0004-6361/201220363). arXiv: [1211.0810](https://arxiv.org/abs/1211.0810). URL: <http://arxiv.org/abs/1211.0810><http://dx.doi.org/10.1051/0004-6361/201220363>.
- Hedelt, P., P. von Paris, M. Godolt, S. Gebauer, J. L. Grenfell, H. Rauer, F. Schreier, F. Selsis, and T. Trautmann (2013). "Spectral features of Earth-like planets and

- their detectability at different orbital distances around F, G, and K-type stars." In: *A&A* 553, A9, A9. DOI: [10.1051/0004-6361/201117723](https://doi.org/10.1051/0004-6361/201117723). arXiv: [1302.5516](https://arxiv.org/abs/1302.5516) [astro-ph.EP].
- Hedges, Christina and Nikku Madhusudhan (2016). "Effect of Pressure Broadening on Molecular Cross Sections in Exoplanetary Atmospheres." In: 24(January), pp. 1–24. ISSN: 0035-8711. DOI: [10.1093/mnras/stw278](https://doi.org/10.1093/mnras/stw278). arXiv: [1602.00751](https://arxiv.org/abs/1602.00751).
- Heiter, U, P Jofré, B Gustafsson, A J Korn, C Soubiran, and F Thévenin (2015). "Gaia FGK benchmark stars: Effective temperatures and surface gravities." In: *A&A* 582. DOI: [10.1051/0004-6361/201526319](https://doi.org/10.1051/0004-6361/201526319). URL: <http://www.aanda.org/articles/aa/pdf/2015/10/aa26319-15.pdf>.
- Hellier, Coel et al. (2009). "An orbital period of 0.94?days for the hot-Jupiter planet WASP-18b." In: *Nature* 460(7259), pp. 1098–1100. ISSN: 0028-0836. DOI: [10.1038/nature08245](https://doi.org/10.1038/nature08245). URL: <http://www.nature.com/doi/10.1038/nature08245>.
- Hellier, Coel et al. (2010). "WASP-29b: A Saturn-sized transiting exoplanet." In: arXiv: [arXiv:1009.5318v1](https://arxiv.org/abs/1009.5318v1).
- Hellier, Coel et al. (2011). "WASP-43b: The closest-orbiting hot Jupiter." In: arXiv: [arXiv:1104.2823v1](https://arxiv.org/abs/1104.2823v1). URL: <https://arxiv.org/pdf/1104.2823.pdf>.
- Heng, K. and A. P. Showman (2015). "Atmospheric Dynamics of Hot Exoplanets." In: *Annual Review of Earth and Planetary Sciences* 43, pp. 509–540. DOI: [10.1146/annurev-earth-060614-105146](https://doi.org/10.1146/annurev-earth-060614-105146). arXiv: [1407.4150](https://arxiv.org/abs/1407.4150) [astro-ph.EP].
- Herbig, George H. and George H. (1960). "The Spectra of Be- and Ae-TYPE Stars Associated with Nebulosity." In: *The Astrophysical Journal Supplement Series* 4, p. 337. ISSN: 0067-0049. DOI: [10.1086/190050](https://doi.org/10.1086/190050). URL: <http://adsabs.harvard.edu/doi/10.1086/190050>.
- Herbst, W., D. K. Herbst, E. J. Grossman, and D. Weinstein (1994). "Catalogue of UBVRI photometry of T Tauri stars and analysis of the causes of their variability." In: *The Astronomical Journal* 108, p. 1906. ISSN: 00046256. DOI: [10.1086/117204](https://doi.org/10.1086/117204). URL: http://adsabs.harvard.edu/cgi-bin/bib/{_}query?1994AJ...108.1906H.
- Herbst, William (2012). "The Variability of Young Stellar Objects." In: 40.
- Hill, C., S. N. Yurchenko, and J. Tennyson (2013). "Temperature-dependent molecular absorption cross sections for exoplanets and other atmospheres." In: *Icarus* 226, pp. 1673–1677. DOI: [10.1016/j.icarus.2012.07.028](https://doi.org/10.1016/j.icarus.2012.07.028). arXiv: [1205.6514](https://arxiv.org/abs/1205.6514) [astro-ph.EP].
- Howard, A. W. et al. (2010a). "HAT-P-17b,c: A Transiting, Eccentric, Hot Saturn and a Long-period, Cold Jupiter." In: DOI: [10.1088/0004-637X/749/2/134](https://doi.org/10.1088/0004-637X/749/2/134). arXiv: [1008.3898](https://arxiv.org/abs/1008.3898). URL: <http://arxiv.org/abs/1008.3898http://dx.doi.org/10.1088/0004-637X/749/2/134>.
- Howard, Andrew W., John Asher Johnson, Geoffrey W. Marcy, Debra A. Fischer, Jason T. Wright, Gregory W. Henry, Howard Isaacson, Jeff A. Valenti, Jay Anderson, and Nikolai E. Piskunov (2010b). "The NASA-UC Eta-Earth Program: III. A Super-Earth orbiting HD 97658 and a Neptune-mass planet orbiting Gl 785." In: DOI: [10.1088/0004-637X/730/1/10](https://doi.org/10.1088/0004-637X/730/1/10). arXiv: [1011.0414](https://arxiv.org/abs/1011.0414). URL: <http://arxiv.org/abs/1011.0414http://dx.doi.org/10.1088/0004-637X/730/1/10>.
- Hu, R., S. Seager, and Y. L. Yung (2015). "Helium Atmospheres on Warm Neptune- and Sub-Neptune-sized Exoplanets and Applications to GJ 436b." In: *ApJ* 807, 8, p. 8. DOI: [10.1088/0004-637X/807/1/8](https://doi.org/10.1088/0004-637X/807/1/8). arXiv: [1505.02221](https://arxiv.org/abs/1505.02221) [astro-ph.EP].
- Huitson, C. M. et al. (2013). "An HST optical-to-near-IR transmission spectrum of the hot Jupiter WASP-19b: detection of atmospheric water and likely absence of TiO." In: *MNRAS* 434, pp. 3252–3274. DOI: [10.1093/mnras/stt1243](https://doi.org/10.1093/mnras/stt1243). arXiv: [1307.2083](https://arxiv.org/abs/1307.2083) [astro-ph.EP].
- Husser, T.-O., S Wende-von Berg, S Dreizler, D Homeier, A Reiners, T. Barman, and Peter H Hauschildt (2013). "Astrophysics A new extensive library of PHOENIX stellar atmospheres." In: *A&A* 553, A6. DOI: [10.1051/0004-6361/201219058](https://doi.org/10.1051/0004-6361/201219058).
- Jenkins, J. M. et al. (2010). "Overview of the Kepler Science Processing Pipeline." In: *ApJ* 713, pp. L87–L91. DOI: [10.1088/2041-8205/713/2/L87](https://doi.org/10.1088/2041-8205/713/2/L87). arXiv: [1001.0258](https://arxiv.org/abs/1001.0258) [astro-ph.EP].

- Jørgensen, U. G., P. Jensen, G. O. Sørensen, and B. Aringer (2001). “H₂O in stellar atmospheres.” In: *A&A* 372, pp. 249–259. DOI: [10.1051/0004-6361:20010285](https://doi.org/10.1051/0004-6361:20010285).
- Kataria, T., A. P. Showman, J. J. Fortney, K. B. Stevenson, M. R. Line, L. Kreidberg, J. L. Bean, and J.-M. Désert (2015a). “The Atmospheric Circulation of the Hot Jupiter WASP-43b: Comparing Three-dimensional Models to Spectrophotometric Data.” In: *ApJ* 801, 86, p. 86. DOI: [10.1088/0004-637X/801/2/86](https://doi.org/10.1088/0004-637X/801/2/86). arXiv: [1410.2382](https://arxiv.org/abs/1410.2382) [[astro-ph.EP](#)].
- Kataria, T., A. P. Showman, J. J. Fortney, K. B. Stevenson, M. R. Line, L. Kreidberg, J. L. Bean, and J.-M. Désert (2015b). “The Atmospheric Circulation of the Hot Jupiter WASP-43b: Comparing Three-dimensional Models to Spectrophotometric Data.” In: *ApJ* 801, 86, p. 86. DOI: [10.1088/0004-637X/801/2/86](https://doi.org/10.1088/0004-637X/801/2/86). arXiv: [1410.2382](https://arxiv.org/abs/1410.2382) [[astro-ph.EP](#)].
- Kataria, T., D. K. Sing, N. K. Lewis, C. Visscher, A. P. Showman, J. J. Fortney, and M. S. Marley (2016). “The Atmospheric Circulation of a Nine-hot-Jupiter Sample: Probing Circulation and Chemistry over a Wide Phase Space.” In: *ApJ* 821, 9, p. 9. DOI: [10.3847/0004-637X/821/1/9](https://doi.org/10.3847/0004-637X/821/1/9). arXiv: [1602.06733](https://arxiv.org/abs/1602.06733) [[astro-ph.EP](#)].
- Kennedy, G. M. and S. J. Kenyon (2009). “Stellar Mass Dependent Disk Dispersal.” In: *ApJ* 695, pp. 1210–1226. DOI: [10.1088/0004-637X/695/2/1210](https://doi.org/10.1088/0004-637X/695/2/1210). arXiv: [0901.2603](https://arxiv.org/abs/0901.2603) [[astro-ph.SR](#)].
- Kennedy, G. M., M. A. Kenworthy, J. Pepper, J. E. Rodriguez, R. J. Siverd, K. G. Stassun, and M. C. Wyatt (2017). “The transiting dust clumps in the evolved disk of the Sun-like UXor RZ Psc.” In: *ArXiv e-prints*. arXiv: [1701.06568](https://arxiv.org/abs/1701.06568) [[astro-ph.SR](#)].
- Kipping, D. M. (2010). “Investigations of approximate expressions for the transit duration.” In: *MNRAS* 407, pp. 301–313. DOI: [10.1111/j.1365-2966.2010.16894.x](https://doi.org/10.1111/j.1365-2966.2010.16894.x). arXiv: [1004.3819](https://arxiv.org/abs/1004.3819) [[astro-ph.EP](#)].
- Kipping, D. M. and E. Sandford (2016). “Observational biases for transiting planets.” In: *MNRAS* 463, pp. 1323–1331. DOI: [10.1093/mnras/stw1926](https://doi.org/10.1093/mnras/stw1926). arXiv: [1603.05662](https://arxiv.org/abs/1603.05662) [[astro-ph.EP](#)].
- Knutson, H. A., B. Benneke, D. Deming, and D. Homeier (2014a). “A featureless transmission spectrum for the Neptune-mass exoplanet GJ436b.” In: *Nature* 505, pp. 66–68. DOI: [10.1038/nature12887](https://doi.org/10.1038/nature12887). arXiv: [1401.3350](https://arxiv.org/abs/1401.3350) [[astro-ph.EP](#)].
- Knutson, H. A., D. Dragomir, L. Kreidberg, E. M.-R. Kempton, P. R. McCullough, J. J. Fortney, J. L. Bean, M. Gillon, D. Homeier, and A. W. Howard (2014b). “Hubble Space Telescope Near-IR Transmission Spectroscopy of the Super-Earth HD 97658b.” In: *ApJ* 794, 155, p. 155. DOI: [10.1088/0004-637X/794/2/155](https://doi.org/10.1088/0004-637X/794/2/155). arXiv: [1403.4602](https://arxiv.org/abs/1403.4602) [[astro-ph.EP](#)].
- Knutson, Heather A, Diana Dragomir, Laura Kreidberg, Eliza M R Kempton, P R McCullough, Jonathan J Fortney, Jacob L Bean, Michael Gillon, Derek Homeier, and Andrew W Howard (2008). “Hubble Space Telescope Near-IR Transmission Spectroscopy of the Super-Earth HD 97658b.” In: *The Astrophysical Journal* 794(2), p. 2008. DOI: [10.1088/0004-637X/794/2/155](https://doi.org/10.1088/0004-637X/794/2/155). arXiv: [1403.4602](https://arxiv.org/abs/1403.4602). URL: <http://arxiv.org/abs/1403.4602v2papers3://publication/uuid/36513317-B9E0-4E41-BF1A-70BE9D3380F4http://adsabs.harvard.edu/cgi-bin/nph-data{}query?bibcode=2014ApJ...794..155K{}link{}type=EJOURNALpapers3://publication/doi/10.1088/0004-637X/794/2/155>.
- Kobayashi, H., H. Kimura, S.-i. Watanabe, T. Yamamoto, and S. Müller (2011). “Sublimation temperature of circumstellar dust particles and its importance for dust ring formation.” In: *Earth, Planets, and Space* 63, pp. 1067–1075. DOI: [10.5047/eps.2011.03.012](https://doi.org/10.5047/eps.2011.03.012). arXiv: [1104.5627](https://arxiv.org/abs/1104.5627) [[astro-ph.EP](#)].
- Konopacky, Q. M., T. S. Barman, B. A. Macintosh, and C. Marois (2013). “Detection of Carbon Monoxide and Water Absorption Lines in an Exoplanet Atmosphere.” In: *Science* 339, pp. 1398–1401. DOI: [10.1126/science.1232003](https://doi.org/10.1126/science.1232003). arXiv: [1303.3280](https://arxiv.org/abs/1303.3280) [[astro-ph.EP](#)].
- Kozhurina-Platais, V, M Dulude, T Dahlen, and C Cox (2012). “SPACE TELESCOPE SCIENCE INSTITUTE WFC₃/UVIS and IR Multi-Wavelength Geometric Distortion.” In:

- Kreidberg, L. et al. (2014a). “A Precise Water Abundance Measurement for the Hot Jupiter WASP-43b.” In: *Astrophysical Journal* 793, L27, p. L27. DOI: [10.1088/2041-8205/793/2/L27](https://doi.org/10.1088/2041-8205/793/2/L27). arXiv: [1410.2255](https://arxiv.org/abs/1410.2255) [astro-ph.EP].
- Kreidberg, L. et al. (2014b). “A Precise Water Abundance Measurement for the Hot Jupiter WASP-43b.” In: *ApJ* 793, L27, p. L27. DOI: [10.1088/2041-8205/793/2/L27](https://doi.org/10.1088/2041-8205/793/2/L27). arXiv: [1410.2255](https://arxiv.org/abs/1410.2255) [astro-ph.EP].
- Kreidberg, L., J. L. Bean, J.-M. Désert, B. Benneke, D. Deming, K. B. Stevenson, S. Seager, Z. Berta-Thompson, A. Seifahrt, and D. Homeier (2014c). “Clouds in the atmosphere of the super-Earth exoplanet GJ1214b.” In: *Nature* 505, pp. 69–72. DOI: [10.1038/nature12888](https://doi.org/10.1038/nature12888). arXiv: [1401.0022](https://arxiv.org/abs/1401.0022) [astro-ph.EP].
- Kreidberg, L. et al. (2015). “A Detection of Water in the Transmission Spectrum of the Hot Jupiter WASP-12b and Implications for Its Atmospheric Composition.” In: *ApJ* 814, 66, p. 66. DOI: [10.1088/0004-637X/814/1/66](https://doi.org/10.1088/0004-637X/814/1/66). arXiv: [1504.05586](https://arxiv.org/abs/1504.05586) [astro-ph.EP].
- Kuntzschner, H, H Bushouse, M Kümmel, and J R Walsh (2009). “WFC3 SMOV proposal 11552 : Calibration of the G102 grism.” In: *Analysis*, pp. 1–29.
- Kuntzschner, H, M Kümmel, J R Walsh, and H Bushouse (2011). “Revised Flux Calibration of the WFC3 G102 and G141 grisms.” In: URL: <http://www.stsci.edu/hst/wfc3/documents/ISRs/WFC3-2011-05.pdf>.
- Kurucz, R. L. (1992). “Atomic and Molecular Data for Opacity Calculations.” In: *Rev. Mexicana Astron. Astrofis.* 23, p. 45.
- Lancon, A. and B. Rocca-Volmerange (1992). “A library of near-IR stellar spectra from 1.328 to 2.5 microns.” In: *A&AS* 96, pp. 593–612.
- Larson, R. B. (2003). “The physics of star formation.” In: *Reports on Progress in Physics* 66, pp. 1651–1697. DOI: [10.1088/0034-4885/66/10/R03](https://doi.org/10.1088/0034-4885/66/10/R03). eprint: [astro-ph/0306595](https://arxiv.org/abs/astro-ph/0306595).
- Lecavelier Des Etangs, A, F Pont, A Vidal-Madjar, and D Sing (2008). “Rayleigh scattering in the transit spectrum of HD 189733b.” In: *A&A* 481, pp. 83–86. DOI: [10.1051/0004-6361:200809388](https://doi.org/10.1051/0004-6361:200809388). URL: <http://www.aanda.org/articles/aa/pdf/2008/14/aa09388-08.pdf>.
- Li, G., I. E. Gordon, L. S. Rothman, Y. Tan, S.-M. Hu, S. Kassi, A. Campargue, and E. S. Medvedev (2015). “Rovibrational Line Lists for Nine Isotopologues of the CO Molecule in the X $^1\Sigma^+$ Ground Electronic State.” In: *Astrophysical Journal, Supplement* 216, 15, p. 15. DOI: [10.1088/0067-0049/216/1/15](https://doi.org/10.1088/0067-0049/216/1/15).
- Li, Z.-Y., R. Banerjee, R. E. Pudritz, J. K. Jørgensen, H. Shang, R. Krasnopolsky, and A. Maury (2014). “The Earliest Stages of Star and Planet Formation: Core Collapse, and the Formation of Disks and Outflows.” In: *Protostars and Planets VI*, pp. 173–194. DOI: [10.2458/azu_uapress_9780816531240-ch008](https://doi.org/10.2458/azu_uapress_9780816531240-ch008). arXiv: [1401.2219](https://arxiv.org/abs/1401.2219) [astro-ph.SR].
- Line, M. R. and V. Parmentier (2016). “The Influence of Nonuniform Cloud Cover on Transit Transmission Spectra.” In: *ApJ* 820, 78, p. 78. DOI: [10.3847/0004-637X/820/1/78](https://doi.org/10.3847/0004-637X/820/1/78). arXiv: [1511.09443](https://arxiv.org/abs/1511.09443) [astro-ph.EP].
- Line, M. R., H. Knutson, D. Deming, A. Wilkins, and J.-M. Desert (2013). “A Near-infrared Transmission Spectrum for the Warm Saturn HAT-P-12b.” In: *ApJ* 778, 183, p. 183. DOI: [10.1088/0004-637X/778/2/183](https://doi.org/10.1088/0004-637X/778/2/183). arXiv: [1310.4796](https://arxiv.org/abs/1310.4796) [astro-ph.EP].
- Line, M. R., K. B. Stevenson, J. Bean, J.-M. Desert, J. J. Fortney, L. Kreidberg, N. Madhusudhan, A. P. Showman, and H. Diamond-Lowe (2016). “No Thermal Inversion and a Solar Water Abundance for the Hot Jupiter HD 209458b from HST/WFC3 Spectroscopy.” In: *AJ* 152, 203, p. 203. DOI: [10.3847/0004-6256/152/6/203](https://doi.org/10.3847/0004-6256/152/6/203). arXiv: [1605.08810](https://arxiv.org/abs/1605.08810) [astro-ph.EP].
- Lodieu, N. (2013). “VizieR Online Data Catalog: UKIDSS GCS Upper Sco members (Lodieu, 2013).” In: *VizieR Online Data Catalog* 743.
- López-Morales, M. (2007). “On the Correlation between the Magnetic Activity Levels, Metallicities, and Radii of Low-Mass Stars.” In: *ApJ* 660, pp. 732–739. DOI: [10.1086/513142](https://doi.org/10.1086/513142). eprint: [astro-ph/0701702](https://arxiv.org/abs/astro-ph/0701702).

- Lovis, C. and D. Fischer (2010). "Radial Velocity Techniques for Exoplanets." In: *Exoplanets*. Ed. by S. Seager, pp. 27–53.
- Luger, Rodrigo, Eric Agol, Ethan Kruse, Rory Barnes, Andrew Becker, Daniel Foreman-Mackey, and Drake Deming (2016). "EVEREST: Pixel Level Decorrelation of K2 Light curves." In: DOI: [10.3847/0004-6256/152/4/100](https://doi.org/10.3847/0004-6256/152/4/100). arXiv: [1607.00524](https://arxiv.org/abs/1607.00524). URL: <http://arxiv.org/abs/1607.00524><http://dx.doi.org/10.3847/0004-6256/152/4/100>.
- Luhman, K. L. and E. E. Mamajek (2012). "The Disk Population of the Upper Scorpius Association." In: *Astrophysical Journal* 758, 31, p. 31. DOI: [10.1088/0004-637X/758/1/31](https://doi.org/10.1088/0004-637X/758/1/31). arXiv: [1209.5433](https://arxiv.org/abs/1209.5433).
- Luhman, K. L. and G. H. Rieke (1999). "Low-Mass Star Formation and the Initial Mass Function in the Rho Ophiuchi Cloud Core." In: DOI: [10.1086/307891](https://doi.org/10.1086/307891). arXiv: [9905286](https://arxiv.org/abs/9905286) [astro-ph]. URL: <http://arxiv.org/abs/astro-ph/9905286><http://dx.doi.org/10.1086/307891>.
- Madhusudhan, N. (2012). "C/O Ratio as a Dimension for Characterizing Exoplanetary Atmospheres." In: *Astrophysical Journal* 758, 36, p. 36. DOI: [10.1088/0004-637X/758/1/36](https://doi.org/10.1088/0004-637X/758/1/36). arXiv: [1209.2412](https://arxiv.org/abs/1209.2412) [astro-ph.EP].
- Madhusudhan, N., N. Crouzet, P. R. McCullough, D. Deming, and C. Hedges (2014a). "H₂O Abundances in the Atmospheres of Three Hot Jupiters." In: *Astrophysical Journal* 791, L9, p. L9. DOI: [10.1088/2041-8205/791/1/L9](https://doi.org/10.1088/2041-8205/791/1/L9). arXiv: [1407.6054](https://arxiv.org/abs/1407.6054) [astro-ph.EP].
- Madhusudhan, N., N. Crouzet, P. R. McCullough, D. Deming, and C. Hedges (2014b). "H₂O Abundances in the Atmospheres of Three Hot Jupiters." In: *ApJ* 791, L9, p. L9. DOI: [10.1088/2041-8205/791/1/L9](https://doi.org/10.1088/2041-8205/791/1/L9). arXiv: [1407.6054](https://arxiv.org/abs/1407.6054) [astro-ph.EP].
- Mancini, L. et al. (2014). "Physical properties of the WASP-67 planetary system from multi-colour photometry." In: *Astronomy & Astrophysics* 568, A127. ISSN: 0004-6361. DOI: [10.1051/0004-6361/201424106](https://doi.org/10.1051/0004-6361/201424106). URL: <http://www.aanda.org/10.1051/0004-6361/201424106>.
- Mandel, K. and E. Agol (2002). "Analytic Light Curves for Planetary Transit Searches." In: *ApJ* 580, pp. L171–L175. DOI: [10.1086/345520](https://doi.org/10.1086/345520). eprint: [astro-ph/0210099](https://arxiv.org/abs/astro-ph/0210099).
- Mandell, A. M., K. Haynes, E. Sinukoff, N. Madhusudhan, A. Burrows, and D. Deming (2013). "Exoplanet Transit Spectroscopy Using WFC3: WASP-12 b, WASP-17 b, and WASP-19 b." In: *ApJ* 779, 128, p. 128. DOI: [10.1088/0004-637X/779/2/128](https://doi.org/10.1088/0004-637X/779/2/128). arXiv: [1310.2949](https://arxiv.org/abs/1310.2949) [astro-ph.EP].
- Marley, M. S., A. S. Ackerman, J. N. Cuzzi, and D. Kitzmann (2013). "Clouds and Hazes in Exoplanet Atmospheres." In: *Comparative Climatology of Terrestrial Planets*. Ed. by S. J. Mackwell, A. A. Simon-Miller, J. W. Harder, and M. A. Bullock, pp. 367–391. DOI: [10.2458/azu_uapress_9780816530595-ch15](https://doi.org/10.2458/azu_uapress_9780816530595-ch15).
- Marois, Christian, Bruce Macintosh, Travis Barman, B Zuckerman, Inseok Song, Jennifer Patience, David Lafrenière, and René Doyon (2008). "Direct Imaging of Multiple Planets Orbiting the Star HR 8799." In: *Science* 322(5906), pp. 1348–1352. ISSN: 0036-8075. DOI: [10.1126/science.1166585](https://doi.org/10.1126/science.1166585). URL: <http://science.sciencemag.org/content/322/5906/1348>.
- Mayor, M. and D. Queloz (1995). "A Jupiter-mass companion to a solar-type star." In: *Nature* 378, pp. 355–359. DOI: [10.1038/378355a0](https://doi.org/10.1038/378355a0).
- Mayor, M. et al. (2003). "Setting New Standards with HARPS." In: *The Messenger* 114, pp. 20–24.
- Mazeh, T., T. Holczer, and S. Faigler (2016). "Dearth of short-period Neptunian exoplanets: A desert in period-mass and period-radius planes." In: *A&A* 589, A75, A75. DOI: [10.1051/0004-6361/201528065](https://doi.org/10.1051/0004-6361/201528065). arXiv: [1602.07843](https://arxiv.org/abs/1602.07843) [astro-ph.EP].
- McCaulliff, S. D., J. M. Jenkins, J. Catanzarite, C. J. Burke, J. L. Coughlin, J. D. Twicken, P. Tenenbaum, S. Seader, J. Li, and M. Cote (2015). "Automatic Classification of Kepler Planetary Transit Candidates." In: *ApJ* 806, 6, p. 6. DOI: [10.1088/0004-637X/806/1/6](https://doi.org/10.1088/0004-637X/806/1/6). arXiv: [1408.1496](https://arxiv.org/abs/1408.1496) [astro-ph.IM].
- McCullough, P. R., N. Crouzet, D. Deming, and N. Madhusudhan (2014). "Water Vapor in the Spectrum of the Extrasolar Planet HD 189733b. I. The Transit." In:

- Astrophysical Journal* 791, 55, p. 55. DOI: [10.1088/0004-637X/791/1/55](https://doi.org/10.1088/0004-637X/791/1/55). arXiv: [1407.2462](https://arxiv.org/abs/1407.2462) [astro-ph.SR].
- McCullough, P. and J. MacKenty (2012). *Considerations for using Spatial Scans with WFC3*. Tech. rep.
- McGinnis, Pauline T. et al. (2015). “CSI 2264: Probing the inner disks of AA Tau-like systems in NGC 2264.” In: DOI: [10.1051/0004-6361/201425475](https://doi.org/10.1051/0004-6361/201425475). arXiv: [1502.07692](https://arxiv.org/abs/1502.07692). URL: <http://arxiv.org/abs/1502.07692><http://dx.doi.org/10.1051/0004-6361/201425475>.
- Meru, F., S. P. Quanz, M. Reggiani, C. Baruteau, and J. E. Pineda (2014). “Long-lasting dust rings in gas-rich disks: sculpting by single and multiple planets.” In: *ArXiv e-prints*. arXiv: [1411.5366](https://arxiv.org/abs/1411.5366) [astro-ph.EP].
- Meru, Farzana and Matthew R. Bate (2010). “Exploring the conditions required to form giant planets via gravitational instability in massive protoplanetary discs.” In: *Monthly Notices of the Royal Astronomical Society* 406(4), p. 2279. DOI: [10.1111/j.1365-2966.2010.16867.x](https://doi.org/10.1111/j.1365-2966.2010.16867.x). eprint: [/oup/backfile/Content_public/Journal/mnras/406/4/10.1111/j.1365-2966.2010.16867.x/2/mnras0406-2279.pdf](http://oup/backfile/Content_public/Journal/mnras/406/4/10.1111/j.1365-2966.2010.16867.x/2/mnras0406-2279.pdf). URL: [+http://dx.doi.org/10.1111/j.1365-2966.2010.16867.x](http://dx.doi.org/10.1111/j.1365-2966.2010.16867.x).
- Mihalas, D., L. H. Auer, and B. R. Mihalas (1978). “Two-dimensional radiative transfer. I - Planar geometry.” In: *Astrophysical Journal* 220, pp. 1001–1023. DOI: [10.1086/155988](https://doi.org/10.1086/155988).
- Millan-Gabet, Rafael, Fabien Malbet, Rachel Akeson, Christoph Leinert, John Monnier, and Rens Waters (2006). “The Circumstellar Environments of Young Stars at AU Scales.” In: arXiv: [0603554](https://arxiv.org/abs/0603554) [astro-ph]. URL: <http://arxiv.org/abs/astro-ph/0603554>.
- Miller-Ricci Kempton, E. and E. Rauscher (2012). “Constraining High-speed Winds in Exoplanet Atmospheres through Observations of Anomalous Doppler Shifts during Transit.” In: *Astrophysical Journal* 751, 117, p. 117. DOI: [10.1088/0004-637X/751/2/117](https://doi.org/10.1088/0004-637X/751/2/117). arXiv: [1109.2270](https://arxiv.org/abs/1109.2270) [astro-ph.EP].
- Morales-Calderón, M. et al. (2011). “YSOVAR: the first sensitive, wide-area, mid-IR photometric monitoring of the ONC.” In: DOI: [10.1088/0004-637X/733/1/50](https://doi.org/10.1088/0004-637X/733/1/50). arXiv: [1103.5238](https://arxiv.org/abs/1103.5238). URL: <http://arxiv.org/abs/1103.5238><http://dx.doi.org/10.1088/0004-637X/733/1/50>.
- Mordasini, C., H. Klahr, Y. Alibert, W. Benz, and K.-M. Dittkriz (2010). “Theory of planet formation.” In: *ArXiv e-prints*. arXiv: [1012.5281](https://arxiv.org/abs/1012.5281) [astro-ph.EP].
- Morley, C. V., H. Knutson, M. Line, J. J. Fortney, D. Thorngren, M. S. Marley, D. Teal, and R. Lupu (2017). “Forward and Inverse Modeling of the Emission and Transmission Spectrum of GJ 436b: Investigating Metal Enrichment, Tidal Heating, and Clouds.” In: *AJ* 153, 86, p. 86. DOI: [10.3847/1538-3881/153/2/86](https://doi.org/10.3847/1538-3881/153/2/86). arXiv: [1610.07632](https://arxiv.org/abs/1610.07632) [astro-ph.EP].
- Muzerolle, James, Nuria Calvet, Lee Hartmann, and Paola D’Alessio (2003). “Unveiling the Inner Disk Structure of T Tauri Stars.” In: arXiv: [0310067v1](https://arxiv.org/abs/0310067v1) [arXiv:astro-ph].
- Nagasawa, M., S. Ida, and T. Bessho (2008). “Formation of Hot Planets by a Combination of Planet Scattering, Tidal Circularization, and the Kozai Mechanism.” In: *ApJ* 678, 498–508, pp. 498–508. DOI: [10.1086/529369](https://doi.org/10.1086/529369). arXiv: [0801.1368](https://arxiv.org/abs/0801.1368).
- Ngo, N. H., H. Tran, R. R. Gamache, and J. M. Hartmann (2012). “Pressure effects on water vapour lines: beyond the Voigt profile.” In: *Royal Society of London Philosophical Transactions Series A* 370, pp. 2495–2508. DOI: [10.1098/rsta.2011.0272](https://doi.org/10.1098/rsta.2011.0272).
- Nikolov, N. et al. (2014). “Hubble Space Telescope hot Jupiter transmission spectral survey: a detection of Na and strong optical absorption in HAT-P-1b.” In: *MNRAS* 437, pp. 46–66. DOI: [10.1093/mnras/stt1859](https://doi.org/10.1093/mnras/stt1859). arXiv: [1310.0083](https://arxiv.org/abs/1310.0083) [astro-ph.SR].
- Nikolov, N., D. K. Sing, N. P. Gibson, J. J. Fortney, T. M. Evans, J. K. Barstow, T. Kataria, and P. A. Wilson (2016). “VLT FORS2 Comparative Transmission Spectroscopy: Detection of Na in the Atmosphere of WASP-39b from the Ground.” In: *ApJ* 832, 191, p. 191. DOI: [10.3847/0004-637X/832/2/191](https://doi.org/10.3847/0004-637X/832/2/191). arXiv: [1610.01186](https://arxiv.org/abs/1610.01186) [astro-ph.EP].

- Olivero, J.J. and R.L. Longbothum (1977). "Empirical fits to the Voigt line width: A brief review." In: *Journal of Quantitative Spectroscopy and Radiative Transfer* 17(2), pp. 233–236. ISSN: 0022-4073. DOI: [http://dx.doi.org/10.1016/0022-4073\(77\)90161-3](http://dx.doi.org/10.1016/0022-4073(77)90161-3). URL: <http://www.sciencedirect.com/science/article/pii/0022407377901613>.
- Parks, J. R., P. Plavchan, R. J. White, and A. H. Gee (2014). "Periodic and Aperiodic Variability in the Molecular Cloud ρ Ophiuchus." In: *Astrophysical Journal, Supplement* 211, 3, p. 3. DOI: [10.1088/0067-0049/211/1/3](https://doi.org/10.1088/0067-0049/211/1/3). arXiv: [1309.5300](https://arxiv.org/abs/1309.5300) [astro-ph.SR].
- Partridge, H. and D. W. Schwenke (1997). "The determination of an accurate isotope dependent potential energy surface for water from extensive ab initio calculations and experimental data." In: *J. Chem. Phys.* 106, pp. 4618–4639. DOI: [10.1063/1.473987](https://doi.org/10.1063/1.473987).
- Parviainen, Hannu (2015). "PYTRANSIT: fast and easy exoplanet transit modelling in PYTHON." In: *MNRAS* 450(April), pp. 3233–3238. DOI: [10.1093/mnras/stv894](https://doi.org/10.1093/mnras/stv894). URL: <http://mnras.oxfordjournals.org/cgi/doi/10.1093/mnras/stv894>.
- Parviainen, Hannu and Suzanne Aigrain (2015). "ldtk: Limb Darkening Toolkit." In: *MNRAS* 453(4), pp. 3821–3826. DOI: [10.1093/mnras/stv1857](https://doi.org/10.1093/mnras/stv1857). URL: <http://mnras.oxfordjournals.org/lookup/doi/10.1093/mnras/stv1857>.
- Paunzen, E. and T. Vanmunster (2016). "Peranso - Light curve and period analysis software." In: *Astronomische Nachrichten* 337, p. 239. DOI: [10.1002/asna.201512254](https://doi.org/10.1002/asna.201512254). arXiv: [1602.05329](https://arxiv.org/abs/1602.05329) [astro-ph.IM].
- Pecaut, Mark J. and Eric E. Mamajek (2013). "Intrinsic Colors, Temperatures, and Bolometric Corrections of Pre-Main Sequence Stars." In: *The Astrophysical Journal Supplement, Volume 208, Issue 1, article id. 9, 22 pp. (2013)*. 208. ISSN: 0067-0049. DOI: [10.1088/0067-0049/208/1/9](https://doi.org/10.1088/0067-0049/208/1/9). arXiv: [1307.2657](https://arxiv.org/abs/1307.2657). URL: <http://arxiv.org/abs/1307.2657><http://dx.doi.org/10.1088/0067-0049/208/1/9>.
- Pecaut, Mark J., Eric E. Mamajek, and Eric J. Bubar (2011). "A Revised Age for Upper Scorpius and The Star-Formation History Among the F-Type Members of the Scorpius-Centaurus OB Association." In: DOI: [10.1088/0004-637X/746/2/154](https://doi.org/10.1088/0004-637X/746/2/154). arXiv: [1112.1695](https://arxiv.org/abs/1112.1695). URL: <http://arxiv.org/abs/1112.1695><http://dx.doi.org/10.1088/0004-637X/746/2/154>.
- Pedregosa, F. et al. (2011). "Scikit-learn: Machine Learning in Python." In: *Journal of Machine Learning Research* 12, pp. 2825–2830.
- Pepe, F. A. et al. (2010). "ESPRESSO: the Echelle spectrograph for rocky exoplanets and stable spectroscopic observations." In: *Ground-based and Airborne Instrumentation for Astronomy III*. Vol. 7735. Proc. SPIE, 77350F. DOI: [10.1117/12.857122](https://doi.org/10.1117/12.857122).
- Perryman, M., J. Hartman, G. Á. Bakos, and L. Lindgren (2014). "Astrometric Exoplanet Detection with Gaia." In: *ApJ* 797, 14, p. 14. DOI: [10.1088/0004-637X/797/1/14](https://doi.org/10.1088/0004-637X/797/1/14). arXiv: [1411.1173](https://arxiv.org/abs/1411.1173) [astro-ph.EP].
- Pirzkal, Nor, R Ryan, and G Brammer (2016). "Trace and Wavelength Calibrations of the WFC3 G102 and G141 IR Grisms." In: URL: <http://www.stsci.edu/hst/wfc3/documents/ISRs/WFC3-2016-15.pdf>.
- Plez, B. (2012). *Turbospectrum: Code for spectral synthesis*. Astrophysics Source Code Library. ascl: [1205.004](https://ascl.net/1205.004).
- Ratzka, T., R. Köhler, and C. Leinert (2005). "A multiplicity survey of the ρ Ophiuchi molecular clouds." In: *A&A* 437, pp. 611–626. DOI: [10.1051/0004-6361:20042107](https://doi.org/10.1051/0004-6361:20042107). eprint: [astro-ph/0504593](https://arxiv.org/abs/astro-ph/0504593).
- Ratzka, Thorsten, Rainer Koehler, and Christoph Leinert (2005). "A Multiplicity Survey of the Rho Ophiuchi Molecular Clouds." In: DOI: [10.1051/0004-6361:20042107](https://doi.org/10.1051/0004-6361:20042107). arXiv: [0504593](https://arxiv.org/abs/0504593) [astro-ph]. URL: <http://arxiv.org/abs/astro-ph/0504593><http://dx.doi.org/10.1051/0004-6361:20042107>.
- Rauer, H. et al. (2014). "The PLATO 2.0 mission." In: *Experimental Astronomy* 38, pp. 249–330. DOI: [10.1007/s10686-014-9383-4](https://doi.org/10.1007/s10686-014-9383-4). arXiv: [1310.0696](https://arxiv.org/abs/1310.0696) [astro-ph.EP].
- Read, M. J., M. C. Wyatt, and A. H. M. J. Triaud (2017). "Transit Probabilities in Secularly Evolving Planetary Systems." In: *ArXiv e-prints*. arXiv: [1703.10046](https://arxiv.org/abs/1703.10046) [astro-ph.EP].

- Rebull, L. M., R. B. Makidon, S. E. Strom, L. A. Hillenbrand, A. Birmingham, Brian M. Patten, B. F. Jones, H. Yagi, and Mark T. Adams (2002). "Circumstellar Disk Candidates Identified in NGC 2264." In: *The Astronomical Journal* 123(3), pp. 1528–1547. ISSN: 00046256. DOI: [10.1086/338904](https://doi.org/10.1086/338904). URL: <http://stacks.iop.org/1538-3881/123/i=3/a=1528>.
- Richards, Joseph W., Dan L. Starr, Nathaniel R. Butler, Joshua S. Bloom, John M. Brewer, Arien Crellin-Quick, Justin Higgins, Rachel Kennedy, and Maxime Rischard (2011). "On Machine-Learned Classification of Variable Stars with Sparse and Noisy Time-Series Data." In: DOI: [10.1088/0004-637X/733/1/10](https://doi.org/10.1088/0004-637X/733/1/10). arXiv: [1101.1959](https://arxiv.org/abs/1101.1959). URL: <http://arxiv.org/abs/1101.1959><http://dx.doi.org/10.1088/0004-637X/733/1/10>.
- Richards, Joseph W., Dan L. Starr, Adam A. Miller, Joshua S. Bloom, Nathaniel R. Butler, Henrik Brink, and Arien Crellin-Quick (2012). "CONSTRUCTION OF A CALIBRATED PROBABILISTIC CLASSIFICATION CATALOG: APPLICATION TO 50k VARIABLE SOURCES IN THE ALL-SKY AUTOMATED SURVEY." In: *The Astrophysical Journal Supplement Series* 203(2), p. 32. ISSN: 0067-0049. URL: <http://adsabs.harvard.edu/abs/2012ApJS...203...32R>.
- Rizzuto, A. C., M. J. Ireland, and A. L. Kraus (2015). "New Pre-main-Sequence Stars in the Upper Scorpius Subgroup of Sco-Cen." In: DOI: [10.1093/mnras/stv207](https://doi.org/10.1093/mnras/stv207). arXiv: [1501.07270](https://arxiv.org/abs/1501.07270). URL: <http://arxiv.org/abs/1501.07270><http://dx.doi.org/10.1093/mnras/stv207>.
- Roberts, L. C., M. Shao, G. Vasisht, B. M. Levine, F. F. Aguayo, J. Nichols, T. G. Lockhart, H. Knight, B. R. Oppenheimer, and S. Hinkley (2009). "Exoplanet Imaging at the Palomar 5-m: Enhancing the Contrast of the Project 1640 Coronagraph." In: *American Astronomical Society Meeting Abstracts #214*. Vol. 214. American Astronomical Society Meeting Abstracts, p. 704.
- Rojas-Ayala, Bárbara, Kevin R Covey, Philip S Muirhead, and James P Lloyd (2011). "Metallicity and Temperature Indicators in M dwarf K band Spectra: Testing New & Updated Calibrations With Observations of 133 Solar Neighborhood M dwarfs." In: arXiv: [arXiv:1112.4567](https://arxiv.org/abs/1112.4567). URL: <https://arxiv.org/pdf/1112.4567.pdf>.
- Rothman, L. S. et al. (1998). "The HITRAN Molecular Spectroscopic Database and HAWKS (HITRAN Atmospheric Workstation): 1996 Edition." In: *J. Quant. Spec. Radiat. Transf.* 60, pp. 665–710. DOI: [10.1016/S0022-4073\(98\)00078-8](https://doi.org/10.1016/S0022-4073(98)00078-8).
- Rothman, L. S., I. E. Gordon, R. J. Barber, H. Dothe, R. R. Gamache, A. Goldman, V. I. Perevalov, S. A. Tashkun, and J. Tennyson (2010). "HITEMP, the high-temperature molecular spectroscopic database." In: *J. Quant. Spec. Radiat. Transf.* 111, pp. 2139–2150. DOI: [10.1016/j.jqsrt.2010.05.001](https://doi.org/10.1016/j.jqsrt.2010.05.001).
- Rothman, L. S. et al. (2013). "The HITRAN₂₀₁₂ molecular spectroscopic database." In: *J. Quant. Spec. Radiat. Transf.* 130, pp. 4–50. DOI: [10.1016/j.jqsrt.2013.07.002](https://doi.org/10.1016/j.jqsrt.2013.07.002).
- Ryabchikova, T., N. Piskunov, R. L. Kurucz, H. C. Stempels, U. Heiter, Y. Pakhomov, and P. S. Barklem (2015). "A major upgrade of the VALD database." In: *Phys. Scr* 90(5), 054005, p. 054005. DOI: [10.1088/0031-8949/90/5/054005](https://doi.org/10.1088/0031-8949/90/5/054005).
- S. G. Johnson A. Cervellino, J. Wuttke (2012). *libcerf, numeric library for complex error functions*. <http://apps.jcns.fz-juelich.de/libcerf>.
- Sato, B. et al. (2012). "HAT-P-38b: A Saturn-Mass Planet Transiting a Late G Star." In: DOI: [10.1093/pasj/64.5.97](https://doi.org/10.1093/pasj/64.5.97). arXiv: [1201.5075](https://arxiv.org/abs/1201.5075). URL: <http://arxiv.org/abs/1201.5075><http://dx.doi.org/10.1093/pasj/64.5.97>.
- Sato, Bun'ei et al. (2005). "The N₂K Consortium. II. A Transiting Hot Saturn around HD 149026 with a Large Dense Core." In: *The Astrophysical Journal* 633(1), pp. 465–473. ISSN: 0004-637X. DOI: [10.1086/449306](https://doi.org/10.1086/449306). URL: <http://stacks.iop.org/0004-637X/633/i=1/a=465>.
- Schneider, J., C. Dedieu, P. Le Sidaner, R. Savalle, and I. Zolotukhin (2011). "Defining and cataloging exoplanets: the exoplanet.eu database." In: *A&A* 532, A79, A79. DOI: [10.1051/0004-6361/201116713](https://doi.org/10.1051/0004-6361/201116713). arXiv: [1106.0586](https://arxiv.org/abs/1106.0586) [astro-ph.EP].

- Schreier, Franz (2011). “Optimized implementations of rational approximations for the Voigt and complex error function.” In: *Journal of Quantitative Spectroscopy and Radiative Transfer* 112(6), pp. 1010–1025. ISSN: 0022-4073. DOI: <http://dx.doi.org/10.1016/j.jqsrt.2010.12.010>. URL: <http://www.sciencedirect.com/science/article/pii/S002240731000467X>.
- Schuler, Simon C., Davin Flateau, Katia Cunha, Jeremy R. King, Luan Ghezzi, and Verne V. Smith (2011). “Abundances of Stars with Planets: Trends with Condensation Temperature.” In: DOI: [10.1088/0004-637X/732/1/55](https://doi.org/10.1088/0004-637X/732/1/55). arXiv: [1103.0757](https://arxiv.org/abs/1103.0757). URL: <http://arxiv.org/abs/1103.0757><http://dx.doi.org/10.1088/0004-637X/732/1/55>.
- Seager, S. and D. Deming (2010). “Exoplanet Atmospheres.” In: *ARA&A* 48, pp. 631–672. DOI: [10.1146/annurev-astro-081309-130837](https://doi.org/10.1146/annurev-astro-081309-130837). arXiv: [1005.4037](https://arxiv.org/abs/1005.4037) [astro-ph.EP].
- Seager, S and D D Sasselov (2000). “THEORETICAL TRANSMISSION SPECTRA DURING EXTRASOLAR GIANT PLANET TRANSITS.” In: *THE ASTROPHYSICAL JOURNAL* 537, pp. 916–921.
- Sharp, C. M. and A. Burrows (2007). “Atomic and Molecular Opacities for Brown Dwarf and Giant Planet Atmospheres.” In: *Astrophysical Journal, Supplement* 168, pp. 140–166. DOI: [10.1086/508708](https://doi.org/10.1086/508708). eprint: [astro-ph/0607211](https://arxiv.org/abs/astro-ph/0607211).
- Showman, A. P., R. D. Wordsworth, T. M. Merlis, and Y. Kaspi (2013). “Atmospheric Circulation of Terrestrial Exoplanets.” In: *Comparative Climatology of Terrestrial Planets*. Ed. by S. J. Mackwell, A. A. Simon-Miller, J. W. Harder, and M. A. Bullock, pp. 277–326. DOI: [10.2458/azu_uapress_9780816530595-ch12](https://doi.org/10.2458/azu_uapress_9780816530595-ch12).
- Sing, D. K. et al. (2013). “HST hot-Jupiter transmission spectral survey: evidence for aerosols and lack of TiO in the atmosphere of WASP-12b.” In: *MNRAS* 436, pp. 2956–2973. DOI: [10.1093/mnras/stt1782](https://doi.org/10.1093/mnras/stt1782). arXiv: [1309.5261](https://arxiv.org/abs/1309.5261) [astro-ph.EP].
- Sing, D. K. et al. (2015). “HST hot-Jupiter transmission spectral survey: detection of potassium in WASP-31b along with a cloud deck and Rayleigh scattering.” In: *MNRAS* 446, pp. 2428–2443. DOI: [10.1093/mnras/stu2279](https://doi.org/10.1093/mnras/stu2279). arXiv: [1410.7611](https://arxiv.org/abs/1410.7611) [astro-ph.EP].
- Sing, D. K. et al. (2016). “A continuum from clear to cloudy hot-Jupiter exoplanets without primordial water depletion.” In: *Nature* 529, pp. 59–62. DOI: [10.1038/nature16068](https://doi.org/10.1038/nature16068). arXiv: [1512.04341](https://arxiv.org/abs/1512.04341) [astro-ph.EP].
- Slesnick, Catherine L., Lynne a. Hillenbrand, and John M. Carpenter (2008). “A Large Area Search for Low Mass Objects in Upper Scorpius. II. Age and Mass Distributions.” In: *The Astrophysical Journal* 688(1), pp. 377–397. ISSN: 0004-637X. DOI: [10.1086/592265](https://doi.org/10.1086/592265). arXiv: [0809.1436](https://arxiv.org/abs/0809.1436). URL: <http://stacks.iop.org/0004-637X/688/i=1/a=377>.
- Snellen, I. A. G., R. J. de Kok, E. J. W. de Mooij, and S. Albrecht (2010). “The orbital motion, absolute mass and high-altitude winds of exoplanet HD209458b.” In: *Nature* 465, pp. 1049–1051. DOI: [10.1038/nature09111](https://doi.org/10.1038/nature09111). arXiv: [1006.4364](https://arxiv.org/abs/1006.4364) [astro-ph.EP].
- Snellen, I. A. G., R. J. de Kok, R. le Poole, M. Brogi, and J. Birkby (2013). “Finding Extraterrestrial Life Using Ground-based High-dispersion Spectroscopy.” In: *ApJ* 764, 182, p. 182. DOI: [10.1088/0004-637X/764/2/182](https://doi.org/10.1088/0004-637X/764/2/182). arXiv: [1302.3251](https://arxiv.org/abs/1302.3251) [astro-ph.EP].
- Snellen, I. A. G., B. R. Brandl, R. J. de Kok, M. Brogi, J. Birkby, and H. Schwarz (2014). “Fast spin of the young extrasolar planet β Pictoris b.” In: *Nature* 509, pp. 63–65. DOI: [10.1038/nature13253](https://doi.org/10.1038/nature13253).
- Soubiran, C., J.-F. Le Campion, N. Brouillet, and L. Chemin (2016). “The PASTEL catalogue: 2016 version.” In: *A&A* 591, A118, A118. DOI: [10.1051/0004-6361/201628497](https://doi.org/10.1051/0004-6361/201628497). arXiv: [1605.07384](https://arxiv.org/abs/1605.07384) [astro-ph.SR].
- Soubiran, Caroline, Jean-François Le Campion, Nathalie Brouillet, and Laurent Chemin (2016). “The PASTEL catalogue: 2016 version.” In: *A&A* 591. DOI: [10.1051/0004-6361/201628497](https://doi.org/10.1051/0004-6361/201628497). URL: <http://www.aanda.org/articles/aa/pdf/2016/07/aa28497-16.pdf>.

- Spiegel, D. S., Z. Haiman, and B. S. Gaudi (2007). "On Constraining a Transiting Exoplanet's Rotation Rate with Its Transit Spectrum." In: *Astrophysical Journal* 669, pp. 1324–1335. DOI: [10.1086/521921](https://doi.org/10.1086/521921). arXiv: [0705.0004](https://arxiv.org/abs/0705.0004).
- Stauffer, John et al. (2014). "CSI 2264: Characterizing Accretion-Burst Dominated Light Curves for Young Stars in NGC 2264." In: DOI: [10.1088/0004-6256/147/4/83](https://doi.org/10.1088/0004-6256/147/4/83). arXiv: [1401.6600](https://arxiv.org/abs/1401.6600). URL: <http://arxiv.org/abs/1401.6600><http://dx.doi.org/10.1088/0004-6256/147/4/83>.
- Stauffer, John et al. (2015). "CSI 2264: CHARACTERIZING YOUNG STARS IN NGC 2264 WITH SHORT-DURATION PERIODIC FLUX DIPS IN THEIR LIGHT CURVES." In: *The Astronomical Journal* 149(4), p. 130. ISSN: 1538-3881. DOI: [10.1088/0004-6256/149/4/130](https://doi.org/10.1088/0004-6256/149/4/130). arXiv: [1501.06609](https://arxiv.org/abs/1501.06609). URL: <http://arxiv.org/abs/1501.06609>.
- Stephens, I. W., L. W. Looney, W. Kwon, M. Fernández-López, A. M. Hughes, L. G. Mundy, R. M. Crutcher, Z.-Y. Li, and R. Rao (2014). "Spatially resolved magnetic field structure in the disk of a T Tauri star." In: *Nature* 514, pp. 597–599. DOI: [10.1038/nature13850](https://doi.org/10.1038/nature13850). arXiv: [1409.2878](https://arxiv.org/abs/1409.2878).
- Stevenson, K. B. et al. (2014a). "Thermal structure of an exoplanet atmosphere from phase-resolved emission spectroscopy." In: *Science* 346, pp. 838–841. DOI: [10.1126/science.1256758](https://doi.org/10.1126/science.1256758). arXiv: [1410.2241](https://arxiv.org/abs/1410.2241) [astro-ph.EP].
- Stevenson, K. B., J. L. Bean, A. Seifahrt, J.-M. Désert, N. Madhusudhan, M. Bergmann, L. Kreidberg, and D. Homeier (2014b). "Transmission Spectroscopy of the Hot Jupiter WASP-12b from 0.7 to 5 μm ." In: *AJ* 147, 161, p. 161. DOI: [10.1088/0004-6256/147/6/161](https://doi.org/10.1088/0004-6256/147/6/161). arXiv: [1305.1670](https://arxiv.org/abs/1305.1670) [astro-ph.EP].
- Stevenson, K. B., M. R. Line, J. L. Bean, J.-M. Désert, J. J. Fortney, A. P. Showman, T. Kataria, L. Kreidberg, and Y. K. Feng (2017). "Spitzer Phase Curve Constraints for WASP-43b at 3.6 and 4.5 μm ." In: *AJ* 153, 68, p. 68. DOI: [10.3847/1538-3881/153/2/68](https://doi.org/10.3847/1538-3881/153/2/68). arXiv: [1608.00056](https://arxiv.org/abs/1608.00056) [astro-ph.EP].
- Swain, M., P. Deroo, G. Tinetti, M. Hollis, M. Tessenyi, M. Line, H. Kawahara, Y. Fujii, A. P. Showman, and S. N. Yurchenko (2013). "Probing the extreme planetary atmosphere of WASP-12b." In: *Icarus* 225, pp. 432–445. DOI: [10.1016/j.icarus.2013.04.003](https://doi.org/10.1016/j.icarus.2013.04.003). arXiv: [1205.4736](https://arxiv.org/abs/1205.4736) [astro-ph.EP].
- Tennyson, J. and S. N. Yurchenko (2012). "ExoMol: molecular line lists for exoplanet and other atmospheres." In: *MNRAS* 425, pp. 21–33. DOI: [10.1111/j.1365-2966.2012.21440.x](https://doi.org/10.1111/j.1365-2966.2012.21440.x). arXiv: [1204.0124](https://arxiv.org/abs/1204.0124) [astro-ph.EP].
- Thompson, S. E., F. Mullally, J. Coughlin, J. L. Christiansen, C. E. Henze, M. R. Haas, and C. J. Burke (2015). "A Machine Learning Technique to Identify Transit Shaped Signals." In: *ApJ* 812, 46, p. 46. DOI: [10.1088/0004-637X/812/1/46](https://doi.org/10.1088/0004-637X/812/1/46). arXiv: [1509.00041](https://arxiv.org/abs/1509.00041) [astro-ph.EP].
- Tinetti, G, P Deroo, M R Swain, C A Griffith, G Vasisht, L R Brown, C Burke, and P Mccullough (2010). "Probing the terminator region atmosphere of the Hot-Jupiter XO-1b with transmission spectroscopy." In: arXiv: [arXiv:1002.2434v1](https://arxiv.org/abs/1002.2434v1).
- Torrence, Christopher and Gilbert P. Compo (1998). "A Practical Guide to Wavelet Analysis." In: *Bulletin of the American Meteorological Society* 79, pp. 61–78.
- Torres, Guillermo (2007). "The Transiting Exoplanet Host Star GJ 436: A Test of Stellar Evolution Models in the Lower Main Sequence, and Revised Planetary Parameters." In: *The Astrophysical Journal* 671(1), pp. L65–L68. ISSN: 0004-637X. DOI: [10.1086/524886](https://doi.org/10.1086/524886). URL: <http://stacks.iop.org/1538-4357/671/i=1/a=L65>.
- Triaud, Amaury H. M. J. et al. (2013). "WASP-80b: a gas giant transiting a cool dwarf." In: DOI: [10.1051/0004-6361/201220900](https://doi.org/10.1051/0004-6361/201220900). arXiv: [1303.0254](https://arxiv.org/abs/1303.0254). URL: <http://arxiv.org/abs/1303.0254><http://dx.doi.org/10.1051/0004-6361/201220900>.
- Tsantaki, M, S G Sousa, V Zh Adibekyan, N C Santos, A Mortier, and G Israelian (2013). "Deriving precise parameters for cool solar-type stars Optimizing the iron line list." In: *A&A* 555. DOI: [10.1051/0004-6361/201321103](https://doi.org/10.1051/0004-6361/201321103). URL: <http://www.aanda.org/articles/aa/pdf/2013/07/aa21103-13.pdf>.
- Tsiaras, A., I. P. Waldmann, M. Rocchetto, R. Varley, G. Morello, M. Damiano, and G. Tinetti (2016a). "A New Approach to Analyzing HST Spatial Scans: The Trans-

- mission Spectrum of HD 209458 b." In: *ApJ* 832, 202, p. 202. DOI: [10.3847/0004-637X/832/2/202](https://doi.org/10.3847/0004-637X/832/2/202). arXiv: [1511.07796](https://arxiv.org/abs/1511.07796) [astro-ph.EP].
- Tsiaras, A. et al. (2016b). "Detection of an Atmosphere Around the Super-Earth 55 Cancri e." In: *ApJ* 820, 99, p. 99. DOI: [10.3847/0004-637X/820/2/99](https://doi.org/10.3847/0004-637X/820/2/99). arXiv: [1511.08901](https://arxiv.org/abs/1511.08901) [astro-ph.EP].
- Tsiaras, A. et al. (2017). "A population study of hot Jupiter atmospheres." In: *ArXiv e-prints*. arXiv: [1704.05413](https://arxiv.org/abs/1704.05413) [astro-ph.EP].
- Tsiaras, A., Waldmann, P., Rocchetto, M., Varley, R., Morello, G., Tinetti, G. (2015). "A new approach to analysing HST spatial scans: the transmission spectrum of HD 209458b." In: *eprint arXiv:1511.07796*. URL: <http://adsabs.harvard.edu/abs/2015arXiv151107796T>.
- Udry, S. and N. C. Santos (2007). "Statistical Properties of Exoplanets." In: *ARA&A* 45, pp. 397–439. DOI: [10.1146/annurev.astro.45.051806.110529](https://doi.org/10.1146/annurev.astro.45.051806.110529).
- Valenti, J. A. and N. Piskunov (1996). "Spectroscopy made easy: A new tool for fitting observations with synthetic spectra." In: *A&AS* 118, pp. 595–603.
- Vanderburg, Andrew and John Asher Johnson (2014). "A TECHNIQUE FOR EXTRACTING HIGHLY PRECISE PHOTOMETRY FOR THE TWO-WHEELED Kepler MISSION." In: arXiv: [arXiv:1408.3853v1](https://arxiv.org/abs/1408.3853v1).
- Varley, R., A. Tsiaras, and K. Karpouzas (2015). "Wayne - A Simulator for HST WFC3 IR Grism Spectroscopy." In: *ArXiv e-prints*. arXiv: [1511.09108](https://arxiv.org/abs/1511.09108) [astro-ph.IM].
- Wakeford, H. R. et al. (2013). "HST hot Jupiter transmission spectral survey: detection of water in HAT-P-1b from WFC3 near-IR spatial scan observations." In: *MNRAS* 435, pp. 3481–3493. DOI: [10.1093/mnras/stt1536](https://doi.org/10.1093/mnras/stt1536). arXiv: [1308.2106](https://arxiv.org/abs/1308.2106) [astro-ph.EP].
- Wakeford, H. R., D. K. Sing, T. Evans, D. Deming, and A. Mandell (2016). "Marginalizing Instrument Systematics in HST WFC3 Transit Light Curves." In: *ApJ* 819, 10, p. 10. DOI: [10.3847/0004-637X/819/1/10](https://doi.org/10.3847/0004-637X/819/1/10). arXiv: [1601.02587](https://arxiv.org/abs/1601.02587) [astro-ph.EP].
- Wakeford, H. R. et al. (2017). "HAT-P-26b: A Neptune-mass Exoplanet with Primordial Solar Heavy Element Abundance." In: *American Astronomical Society Meeting Abstracts*. Vol. 229. American Astronomical Society Meeting Abstracts, p. 401.01.
- Waters, L. B. F. M. and C. Waelkens (1998). "HERBIG A e /B e STARS." In: *Annual Review of Astronomy and Astrophysics* 36(1), pp. 233–266. ISSN: 0066-4146. DOI: [10.1146/annurev.astro.36.1.233](https://doi.org/10.1146/annurev.astro.36.1.233). URL: <http://www.annualreviews.org/doi/10.1146/annurev.astro.36.1.233>.
- Wilking, B. A., M. Gagné, and L. E. Allen (2008). "Star Formation in the ρ Ophiuchi Molecular Cloud." In: *Handbook of Star Forming Regions, Volume II*. Ed. by B. Reipurth, p. 351.
- Wilking, B. A., M. R. Meyer, T. P. Greene, and J. G. Robinson (2001). "The Star Forming History of Low Mass T Tauri Stars in the Vicinity of the Rho Ophiuchi Cloud." In: *American Astronomical Society, 199th AAS Meeting, id.156.07; Bulletin of the American Astronomical Society, Vol. 34, p.563* 34, p. 563.
- Wilkins, Ashlee N, Drake Deming, Nikku Madhusudhan, Adam Burrows, Heather Knutson, Peter Mccullough, and Sukrit Ranjan (2014). "THE EMERGENT 1.1-1.7 MICRON SPECTRUM OF THE EXOPLANET COROT-2B AS MEASURED USING THE HUBBLE SPACE TELESCOPE." In: arXiv: [arXiv:1401.4464v1](https://arxiv.org/abs/1401.4464v1).
- Williams, J. P. and L. A. Cieza (2011). "Protoplanetary Disks and Their Evolution." In: *ARA&A* 49, pp. 67–117. DOI: [10.1146/annurev-astro-081710-102548](https://doi.org/10.1146/annurev-astro-081710-102548). arXiv: [1103.0556](https://arxiv.org/abs/1103.0556) [astro-ph.GA].
- Wilson, P. A., D. K. Sing, N. Nikolov, A. Lecavelier des Etangs, F. Pont, J. J. Fortney, G. E. Ballester, M. López-Morales, J.-M. Désert, and A. Vidal-Madjar (2015). "GTC OSIRIS transiting exoplanet atmospheric survey: detection of potassium in HAT-P-1b from narrow-band spectrophotometry." In: *MNRAS* 450, pp. 192–200. DOI: [10.1093/mnras/stv642](https://doi.org/10.1093/mnras/stv642). arXiv: [1503.07165](https://arxiv.org/abs/1503.07165) [astro-ph.EP].

- Wolszczan, A. and D. A. Frail (1992). "A planetary system around the millisecond pulsar PSR1257 + 12." In: *Nature* 355, pp. 145–147. DOI: [10.1038/355145a0](https://doi.org/10.1038/355145a0).
- Wright, J. T. et al. (2011). "The Exoplanet Orbit Database." In: *PASP* 123, p. 412. DOI: [10.1086/659427](https://doi.org/10.1086/659427). arXiv: [1012.5676](https://arxiv.org/abs/1012.5676) [astro-ph.SR].
- Wright, J. T., G. W. Marcy, A. W. Howard, J. A. Johnson, T. D. Morton, and D. A. Fischer (2012). "The Frequency of Hot Jupiters Orbiting nearby Solar-type Stars." In: *ApJ* 753, 160, p. 160. DOI: [10.1088/0004-637X/753/2/160](https://doi.org/10.1088/0004-637X/753/2/160). arXiv: [1205.2273](https://arxiv.org/abs/1205.2273) [astro-ph.EP].
- Yurchenko, S. N., R. J. Barber, and J. Tennyson (2011). "A variationally computed line list for hot NH₃." In: *MNRAS* 413, pp. 1828–1834. DOI: [10.1111/j.1365-2966.2011.18261.x](https://doi.org/10.1111/j.1365-2966.2011.18261.x). arXiv: [1011.1569](https://arxiv.org/abs/1011.1569) [astro-ph.EP].
- Yurchenko, S. N. and J. Tennyson (2014). "ExoMol line lists - IV. The rotation-vibration spectrum of methane up to 1500 K." In: *MNRAS* 440, pp. 1649–1661. DOI: [10.1093/mnras/stu326](https://doi.org/10.1093/mnras/stu326). arXiv: [1401.4852](https://arxiv.org/abs/1401.4852) [astro-ph.EP].
- Zaghloul, M. R. (2007). "On the calculation of the Voigt line profile: a single proper integral with a damped sine integrand." In: *MNRAS* 375, pp. 1043–1048. DOI: [10.1111/j.1365-2966.2006.11377.x](https://doi.org/10.1111/j.1365-2966.2006.11377.x).
- Zaghloul, Mofreh R. and Ahmed N. Ali (2011). "Algorithm xxx: computing the Faddeyeva and Voigt functions." In: *CoRR* abs/1106.0151. URL: <http://arxiv.org/abs/1106.0151>.
- Zeng, L., D. D. Sasselov, and S. B. Jacobsen (2016). "Mass-Radius Relation for Rocky Planets Based on PREM." In: *ApJ* 819, 127, p. 127. DOI: [10.3847/0004-637X/819/2/127](https://doi.org/10.3847/0004-637X/819/2/127). arXiv: [1512.08827](https://arxiv.org/abs/1512.08827) [astro-ph.EP].
- Zhou, Yifan, Aniel Apai, Ben W P Lew, and Glenn Schneider (2017). "A PHYSICAL MODEL-BASED CORRECTION FOR CHARGE TRAPS IN THE HUBBLE SPACE TELESCOPE'S WIDE FIELD CAMERA 3 NEAR-IR DETECTOR AND APPLICATIONS TO TRANSITING EXOPLANETS AND BROWN DWARFS." In: arXiv: [arXiv:1703.01301v2](https://arxiv.org/abs/1703.01301v2). URL: <https://arxiv.org/pdf/1703.01301.pdf>.
- de Kok, R. J., M. Brogi, I. A. G. Snellen, J. Birkby, S. Albrecht, and E. J. W. de Mooij (2013). "Detection of carbon monoxide in the high-resolution day-side spectrum of the exoplanet HD 189733b." In: *A&A* 554, A82, A82. DOI: [10.1051/0004-6361/201321381](https://doi.org/10.1051/0004-6361/201321381). arXiv: [1304.4014](https://arxiv.org/abs/1304.4014) [astro-ph.EP].
- de Wit, J. et al. (2016). "A combined transmission spectrum of the Earth-sized exoplanets TRAPPIST-1 b and c." In: *Nature* 537, pp. 69–72. DOI: [10.1038/nature18641](https://doi.org/10.1038/nature18641). arXiv: [1606.01103](https://arxiv.org/abs/1606.01103) [astro-ph.EP].
- de Zeeuw, P. T., R. Hoogerwerf, J. H. J. de Bruijne, A. G. A. Brown, and A. Blaauw (1999). "A HIPPARCOS Census of the Nearby OB Associations." In: *AJ* 117, pp. 354–399. DOI: [10.1086/300682](https://doi.org/10.1086/300682). eprint: [astro-ph/9809227](https://arxiv.org/abs/astro-ph/9809227).